Modelling the Dayside Ionosphere of Titan: Application of Electron Degradation Model for Methane

Thesis submitted to

Cochin University of Science and Technology

In partial fulfillment of the requirements

for the award of

Doctor of Philosophy

in

Physics

Under the faculty of Sciences

by

Vrinda Mukundan

Space Physics Laboratory

Vikram Sarabhai Space Centre

Indian Space Research Organisation

Thiruvananthapuram

INDIA

April 2018

Dedicated to

God Almighty,

my mentor Dr. Bhardwaj,

my husband Vivek,

&

my family

Declaration

I hereby declare that the Ph.D. thesis work titled, **Modelling the Dayside Ionosphere of Titan: Application of Electron Degradation Model for Methane** is based on the original work carried out by me under the supervision of **Dr. Anil Bhardwaj**, at Space Physics Laboratory, Vikram Sarabhai Space centre, Thiruvananthapuram and has not been included in any other thesis submitted previously for the award of any degree.

April 2018 **Vrinda Mukundan**

भौतिक अनुसंधान प्रयोगशाला
(भारत सरकार, अंतरिक्ष विभाग की यूनिट)
नवरंगपुरा, अहमदाबाद - 380009, भारत

Physical Research Laboratory
(A Unit of Dept. of Space, Govt. of India)
Navrangpura, Ahmedabad - 380 009, India

फोन Phone: +91-79-26314855 फैक्स Fax: +91-79-26300374 ई-मेल E-mail: abhardwaj@prl.res.in / Bhardwaj_SPL@yahoo.com

डॉ. अनिल भारद्वाज, एफएनए, एफएएससी, एफएनएएससी
Dr. Anil Bhardwaj, FNA, FASc, FNASc
निदेशक/Director

March 26, 2018

CERTIFICATE

Certified that the thesis titled "**Modelling the Dayside Ionosphere of Titan: Application of Electron Degradation Model for Methane**" submitted by **Ms. Vrinda Mukundan (Reg. No. 4962)** in partial fulfilment for the award of degree of Doctor of Philosophy to Cochin University of Science and Technology is an authentic record of research work carried out by her under my supervision at Space Physics Laboratory, Vikram Sarabhai Space Centre, Thiruvananthapuram and has not been included in any other thesis submitted previously for the award of any degree.

डॉ. अनिल भारद्वाज / Dr. Anil Bhardwaj
(शोध-प्रबंध पर्यवेक्षक / Thesis Supervisor)

भौतिक अनुसंधान प्रयोगशाला
(भारत सरकार, अंतरिक्ष विभाग की यूनिट)
नवरंगपुरा, अहमदाबाद - 380009, भारत

Physical Research Laboratory
(A Unit of Dept. of Space, Govt. of India)
Navrangpura, Ahmedabad - 380 009, India

फोन Phone: +91-79-26314855 फैक्स Fax: +91-79-26300374 ई-मेल E-mail: abhardwaj@prl.res.in / Bhardwaj_SPL@yahoo.com

डॉ. अनिल भारद्वाज, एफएनए, एफएएससी, एफएनएएससी
Dr. Anil Bhardwaj, FNA, FASc, FNASc
निदेशक/Director

March 26, 2018

Certificate

Certified that all the relevant corrections and modifications suggested by the audience during the Pre-synopsis seminar and recommended by the Doctoral Committee of **Ms. Vrinda Mukundan (Reg. No. 4962)** have been incorporated in this thesis.

डॉ. अनिल भारद्वाज / Dr. Anil Bhardwaj
(शोध-प्रबंध पर्यवेक्षक / Thesis Supervisor)

Acknowledgements

I shall begin with the God Almighty; without His will I would have never found the right path. Thank You for granting me the wisdom, health and strength to undertake this research task and enabling me to its completion.

I express my sincere gratitude to my mentor Dr. Anil Bhardwaj. He has been a constant source of great enthusiasm, encouragement, sound advice, and a treasury of scientific ideas. I remain amazed that despite his busy schedule he was always available whenever I had a question about my research/writing. I would have been lost without him. He gave me the freedom to work in my own way but steered me in the right direction whenever he thought I needed it and taught me to persevere despite hardships. I could not have imagined having a better advisor and mentor for my Ph.D study.

I sincerely thank Dr. Radhika Ramachandran, Director, Space Physics Laboratory, for her encouragement in my research work and her valuable suggestions as the Academic committee chairman.

I thank the members of Doctoral committee and Academic committee of SPL, Dr. Rajeev, Dr. Prabha, Dr. Geetha Ramkumar, Dr. Tarun Pant, Dr. Rajkumar Choudhary, Dr. Suresh Raju, Dr. Suresh Babu, Dr. K. Kishore, Dr. D. B. Subrahamanyam, Dr. Satheesh Thampi, and Dr. Vipin Yadav, for their feedback and suggestions. I also thank the CUSAT research committee members and Central Level Monitoring Committee members of VSSC for critically evaluating my work every year.

All the faculty members of SPL have been very supportive and helpful at various phases of my research and I do hereby acknowledge all of them. The support provided by the administrative staff of SPL, especially Ms. Susheela and Ms. Sisira, is gratefully acknowledged.

The gratitude, admiration and love that I feel for Dr. Dhanya is beyond words. Rather than a colleague, she was more like my family. She has been generously helpful whenever I approached her, let the problem be personal or professional. Thank you Chechi for all those enlightening scientific discussions and more importantly, for being a wonderful friend.

My special thanks to Dr. Sonal Jain and Dr. Raghuram for their encouragement and invaluable guidance which has really helped me in my research.

In my daily work I have been blessed with a friendly and cheerful group of fellow students. I thank God for bringing a special group of friends into my life, Roshny, Suneeth, Sneha, and Kavitha, the people who loved, supported, guided, and prayed for me regardless of the circumstances. I will always remember all those stimulating discussions and all the fun we have had in the last five years. I would also like to acknowledge all the research scholars of SPL for adding colours to my research life.

Words cannot express the feelings that I have for my family. I am forever indebted to my parents for their unconditional love and the sacrifices they have made to support me. I would not be where I am today without your care and support. I am also thankful to my sister Meera for being the most adorable sister

who was always there for me through all the rough times of my life . To my little nephew Balu and my brother-in-law Reghunath; thank you for the sunshine you both brought into our family.

Finally, I would like to acknowledge the most important person in my life - my husband Vivek. These past five years have not been an easy ride, both academically and personally. There were times when everything seemed hopeless. It was only because of his constant encouragement (and sometimes a kick up my backside when I needed one) that ultimately made it possible for me to see this work through to the end. I truly thank Vivek for being my best friend and soul mate.

Contents

Preface . . . xvii
Publications and Conference presentations . . . xix
List of Figures . . . xxi
List of Tables . . . xxvii

1 Introduction **1**
1.1 Relevance of electron impact studies in planetary atmospheres . . . 3
1.2 Titan - the Saturnian moon . . . 5
1.2.1 The Cassini-Huygens mission . . . 7
1.3 The Ionosphere . . . 8
1.3.1 Photochemistry on the dayside of Titan′s ionosphere . . . 9
1.3.2 Negative ions . . . 11
1.4 Previous modelling studies . . . 13
1.4.1 Positive ions . . . 13
1.4.2 Negative ions . . . 17
1.5 Motivation for this study . . . 18
1.6 Photochemical model for the dayside ionosphere . . . 20
1.7 Thesis Structure . . . 21

2 Electron energy degradation model in gases using Monte Carlo method: Application to xenon **25**
2.1 Introduction . . . 25
2.2 Monte Carlo Method . . . 27
2.3 Electron energy degradation model using Monte Carlo method . . . 30
2.4 Monte Carlo model for electron degradation in xenon gas . . . 32
2.5 Cross Sections . . . 33
2.5.1 Total Elastic cross sections . . . 34
2.5.2 Differential elastic cross sections . . . 36
2.5.3 Ionization cross sections . . . 36
2.5.4 Excitation cross sections . . . 37
2.5.5 Total cross sections . . . 39
2.6 Model Results . . . 40
2.6.1 Yield Spectrum . . . 40
2.6.2 Mean energy per ion pair . . . 42
2.6.3 Secondary electron energy distribution . . . 44
2.6.4 Efficiency . . . 45
2.7 Summary . . . 46

3 Monte Carlo model for electron degradation in methane gas 49
3.1 Introduction . . . 49
3.2 Monte Carlo model for electron degradation in methane gas . . . 50
3.3 Cross Sections . . . 51
3.3.1 Total Elastic cross sections . . . 51
3.3.2 Differential elastic cross sections (DCS) . . . 51
3.3.3 Attachment . . . 51
3.3.4 Vibrational Excitation . . . 53
3.3.5 Ionization . . . 57
3.3.6 Dissociation . . . 58
3.3.7 Emission . . . 58
3.3.8 Total cross sections . . . 59
3.4 Results . . . 60
3.4.1 Yield Spectrum . . . 60
3.4.2 Mean energy per ion pair . . . 61
3.4.3 Secondary Electron production . . . 63
3.4.4 Efficiency . . . 63
3.5 Summary . . . 66

4 Photochemical model for the dayside ionosphere of Titan 69
4.1 Introduction . . . 69
4.2 Model description . . . 69
4.3 Model inputs . . . 71
4.3.1 Solar flux . . . 71
4.3.2 Neutral densities . . . 72
4.3.3 Cross sections . . . 74
4.3.4 Electron temperature . . . 75
4.3.5 Reaction rate coefficients . . . 76
4.4 Model results . . . 76
4.4.1 Photoelectron production rate . . . 76
4.4.2 Photoelectron flux . . . 78
4.4.3 Volume Production Rates . . . 80
4.4.3.1 Impact of high resolution N_2 photo cross sections on volume production rate calculations . . . 82
4.4.4 Photochemical equilibrium model . . . 85
4.5 Impact of model input parameters on the calculated ion and electron densities . . . 91
4.5.1 Impact of photoelectron flux . . . 92
4.5.2 N_2^+ ion production rates . . . 96
4.5.3 Electron Temperature . . . 98
4.5.4 HCN density . . . 101
4.5.5 Dissociative electron recombination coefficient (DRC) of $C_2H_5^+$ and CH_5^+ . . . 103
4.5.6 Additional reactions proposed by *Westlake et al.* [2012] . . . 104
4.5.7 NH_3 density . . . 105
4.5.8 Solar flux models . . . 107
4.6 Summary . . . 108

5 Modelling the negative ion chemistry on Titan's dayside ionopshere 111

5.1 Introduction 111
5.2 Formation and destruction processes of anions 112
5.3 Model inputs 117
5.3.1 Solar flux 117
5.3.2 Neutral Densities 117
5.3.3 Cross sections 117
5.3.4 Reaction rate coefficients 118
5.4 Results and Discussion 118
5.4.1 H^- and CH_2^- 119
5.4.2 CN^- and C_3N^- 122
5.4.3 C_4H^- and C_5N^- 124
5.4.4 C_2H^- and C_6H^- 126
5.4.5 O^- and OH^- 127
5.5 Comparison of model results with the recent observations 129
5.6 Conclusion 131

6 Summary and future scope **133**
6.1 Future Scope 135

Appendix A Reactions and Rate Coefficients **137**

References **145**

Thesis advisor
Anil Bhardwaj

Author
Vrinda Mukundan

**Modelling the Dayside Ionopshere of Titan:
Application of Electron Degradation Model for Methane**

Preface

Titan, the Saturnian moon, is a very unique body in the solar system due to its many intriguing features, such as a thick atmosphere, presence of liquid bodies on the surface, the complex geological processes, etc. Much was not known about Titan until the Cassini-Huygens spacecraft, which was a dedicated mission for Saturn and its satellite systems, visited Titan. The mission revealed before us an unusual atmosphere which is largely composed of heavy organic molecules and nitrogen bearing compounds. The instruments, such as the Ion Neutral Mass Spectrometer (INMS), Langmuir Probe (LP), Ion Beam Spectrometer (IBS), etc measured the plasma composition of the upper atmosphere and unveiled an ionosphere which is the home for a plethora of charged particles, including positive ions, negative ions, and free electrons. These plasma particles are the byproducts of a complex photochemistry, which is initiated by the photoionization of the major atmospheric neutrals N_2 and CH_4 and the subsequent reactions of these photoionization products with the background neutral gases.

In this thesis a model is developed to study the photochemistry taking place in the dayside ionosphere of Titan and to calculate the density profiles of positive ions, negative ions and free electrons. Electron impact processes contribute significantly to the ionospheric chemistry. To understand the interaction of electrons with atmospheric gases, energy deposition model is required. In the present thesis an electron energy degradation model is developed to study the interaction of electrons with CH_4, the gas which plays a crucial role in controlling the photochemistry. The output of the degradation model is used for the calculation of ion production rates due to electron impact, which is subsequently used for computing plasma densities. These profiles are finally compared with the observations made by the instruments onboard Cassini.

A brief introduction of the work carried out in this thesis is presented in Chapter 1. In Chapter 2, energy deposition models are described and a Monte Carlo model for studying electron energy degradation in an atomic gas xenon is presented. Chapter 3 deals with the Monte Carlo model for electron energy deposition in a molecular gas methane. Chapter 4 and 5 present modelling the photochemistry in the dayside upper atmosphere of Titan. A summary of the thesis and the future scope of the present work is reported in Chapter 6.

Publications:

1. Anil Bhardwaj and **Vrinda Mukundan** (2015), Monte Carlo model for electron degradation in methane gas, *Planetary and Space Science*, *111*, 34 – 43, doi:10.1016/j.pss.2015.03.008.

2. **Vrinda Mukundan** and Anil Bhardwaj (2016), Monte Carlo model for electron degradation in xenon gas, *Proceedings of Royal Society A, 472*, 20150727, doi:10.1098/rspa.2015.0727.

3. **Vrinda Mukundan** and Anil Bhardwaj (2018), Dayside ionosphere of Titan: Impact on calculated plasma densities due to variations in the model parameters, *Icarus*, *299*, 222 – 239, doi:10.1016/j.icarus.2017.07.022.

4. **Vrinda Mukundan** and Anil Bhardwaj (2018), A model for negative ion chemistry in Titan's ionosphere, *The Astrophysical Journal, 856*, 168 – 179, doi:10.3847/1538-4357/aab1f5 .

Conference Presentations:

1. **Vrinda Mukundan** and Anil Bhardwaj (2014), Monte Carlo model for electron degradation in methane gas, *20^{th} National Conference on Atomic and Molecular Physics (NCAMP–XX)*, Indian Institute of Space Science and Technology, Trivandrum, 9–12 December.

2. **Vrinda Mukundan** and Anil Bhardwaj (2016), Monte Carlo model for electron degradation in planetary atmospheric gases: Methane and Xenon, *19^{th} National Space Science Symposium (NSSS–2016)*, Vikram Sarabhai Space Center, Trivandrum, 9–12 February.

3. **Vrinda Mukundan** and Anil Bhardwaj (2016), Calculation of ion production rates and electron densities for Titan's sunlit upper atmosphere, *19^{th} National Space Science Symposium (NSSS–2016)*, Vikram Sarabhai Space Center, Trivandrum, 9–12 February.

4. **Vrinda Mukundan** and Anil Bhardwaj (2017), Calculation of ion production rates and electron densities for the dayside ionosphere of Titan, *29^{th} Kerala Science Congress (KSC–2017)*, Mar Thoma College, Pathanamthitta, 28–30 January.

5. **Vrinda Mukundan** and Anil Bhardwaj (2017), Photochemical model for the dayside ionosphere of Titan, *Commonwealth Science Conference 2017*, Singapore, 12–15 June.

6. **Vrinda Mukundan** and Anil Bhardwaj (2017), Photochemical modelling on the dayside ionosphere of Titan, *Meeting on the scientific outcomes of Cassini-Huygens mission*, Physical Research Laboratory, Ahmedabad, 13 September.

List of Figures

1.1 Variation of solar radiation, neutral density and ionization rate with altitude (Taken from *Kallenrode* [2004]). 2
1.2 The image of Titan taken by Cassini. Blue layer represents the atmosphere and detached hazes (Image credit: NASA/JPL-Caltech). 5
1.3 A schematic figure showing the growth of molecular ions leading to the formation of organic particles. Figure taken from *Waite et al.* [2007]. . . 8
1.4 The ion-neutral reaction scheme in Titan′s ionosphere, taken from *Richard et al.* [2015]. 9
1.5 Ion spectrum recorded by Cassini INMS during T5 flyby of Titan (Figure taken from *Vuitton et al.* [2007]). 11
1.6 Energy–time spectrogram recorded by ELS and the corresponding actuator angle during the T40 flyby of the Cassini orbiter. The vertical spikes systematically occur when the ram angle is 0° (taken from *Vuitton et al.* [2009]). 12
1.7 Photochemical model for calculating the plasma densities. 20

2.1 Flowchart showing Monte Carlo simulation for the electron degradation in atomic gas. It shows flow only up to secondary electrons; subsequent electrons (tertiary, quaternary, etc.) are also followed in the similar manner in the simulation. 29
2.2 Electron impact ionization cross sections for Xe. Cross sections up to five ionization states are shown here. 34
2.3 Energy level diagram of Xe for the excited states $5p^5 6s$ and $5p^5 6p$. Image taken from *Srivastava* [2007] 37
2.4 Electron impact cross sections for elastic and inelastic processes of Xe . . 41
2.5 Yield spectra for different incident energies. Red curve shows numerical yield spectra obtained using the model. Analytical Yield Spectrum (AYS), calculated using equation (2.14), is represented by blue curves. To separate the curves for better clarity, yield spectrum for 10000, 4000, 1000, 500 and 50 eV are shown after multiplying with scaling factors 2000, 300, 80 and 20 and 5, respectively. 42
2.6 Mean energy per ion pair for ions Xe^+, Xe^{2+}, Xe^{3+}, Xe^{4+}, Xe^{5+} and neutral Xe (shown as total). Symbols show the values calculated using numerical yield spectrum for Xe. 43

2.7 Energy distribution of secondary electrons for incident energies 100 eV, 1 keV and 10 keV. Y axis shows the number of secondary electrons produced per incident primary electron. Dotted and dashed curves show distribution of tertiary and quaternary electrons, respectively, for an incident energy of 10 keV. Inset shows the energy distribution of secondary, tertiary and quaternary electrons for an incident energy of 10 keV zoomed in the lower energy range of 10 to 50 eV. 44
2.8 Efficiencies of various ionization processes. Symbols represent the efficiencies calculated using numerical yield spectra and solid lines are efficiencies calculated using AYS. 45
2.9 Efficiencies of various levels in the (a) 1s configuration (b) 2p configuration (c) remaining excitation channels. Symbols represent the efficiencies calculated using numerical yield spectra and solid lines are efficiencies calculated using AYS. 47
2.10 Efficiencies of ionization and excitation processes. Symbols represent the efficiencies calculated using numerical yield spectra and solid lines are efficiencies calculated using AYS. 48

3.1 Flowchart showing Monte Carlo simulation for electron degradation in molecular gas. It shows flow only up to secondary electrons; subsequent electrons (tertiary, quaternary, etc.) are also followed in the similar manner in the simulation. Excitation involves vibrational, rotational, and electronic excitations and are not shown separately. 52
3.2 Cross sections for elastic and inelastic processes for e-CH_4 collisions. $\nu_{1,3}$ and $\nu_{2,4}$ are the cross sections for stretching and bending vibration modes, respectively. 53
3.3 Electron impact cross sections of CH_4 for various ionization and dissociation channels. 57
3.4 Electron impact cross sections for H Lyman and H Balmer emissions. . . 59
3.5 Electron impact cross sections of CH_4 for CH band and various CI line emissions. 60
3.6 Yield spectra for different incident energies. Solid curve shows numerical yield spectra obtained using the model. Analytical Yield Spectrum (AYS), calculated using equation (3.2), is represented by dashed curves. Dotted curve shows improved AYS, obtained by summing equations (3.2) and (3.4). Yield Spectrum for 10000, 5000, 1000, 100 and 50 eV are shown after multiplying with scaling factors 9000, 1000, 100 and 30 and 1, respectively 61
3.7 Mean energy per ion pair for ions CH_4^+, CH_3^+, CH_2^+, CH^+, C^+, H_2^+, H^+, and neutral CH_4 (shown as total). Symbols shows the values calculated using numerical yield spectrum for CH_4^+ and neutral CH_4 62
3.8 Energy Distribution of secondary electrons for incident energies 100 eV, 1 keV and 10 keV. Verical axis shows the number of secondary electrons produced per incident primary electron. Dotted and dashed curves show distribution of tertiary and quaternary electrons, respectively, for an incident energy of 1000 eV. The inset shows the energy distribution of secondary, teritary and quaternary electrons for an incident energy of 10 keV by zooming in the lower energy range. 63

3.9 Efficiencies of various ionization processes. Symbols represent the efficiencies that are calculated using numerical yield spectra and solid lines are efficiencies calculated using AYS. 64
3.10 Efficiencies of various dissociation channels. Symbols represent the efficiencies that are calculated using numerical yield spectra and solid lines are efficiencies calculated using AYS. 65
3.11 Efficiencies of various emission channels. Symbols represent the efficiencies that are calculated using numerical yield spectra and solid lines are efficiencies calculated using AYS. 66
3.12 Efficiencies of various loss channels. Symbols represent the efficiencies that are calculated using numerical yield spectra and solid lines are efficiencies calculated using AYS. Vibrational efficiencies are calculated using numerical yield spectrum only. 67

4.1 The High resolution EUV flux model for Aeronomic Calculation (HEUVAC) model solar flux at 1 AU on 5 January 2008. 72
4.2 The density profiles of the major atmospheric species N_2, CH_4, and H_2 used in the model. The symbols show the profile measured by the INMS during T40 flyby. 73
4.3 The density profiles of 15 minor species used in the model. 73
4.4 Photon impact cross sections of N_2 and CH_4 used in the model. 74
4.5 Electron impact cross sections of N_2 used in the model. 74
4.6 Electron temperature profile measured during T40 flyby. The solid line shows the linear fit for the electron temperature that is used in the current model. 75
4.7 Calculated primary photoelectron energy spectra at three different altitudes of 900, 1000 and 1100 km, for a SZA of 37^o. 77
4.8 The altitude of unit optical depth for a SZA of 37° at different wavelengths in Titan's atmosphere. 77
4.9 Calculated photoelectron flux at three different altitudes of 900, 1000 and 1100 km, for a SZA of 37^o. 78
4.10 Calculated photoelectron flux at 1020 km compared with Cassini CAPS observation (obtained from *Richard et al.* [2015]) and calculations of *Lavvas et al.* [2011] and *Richard et al.* [2015] for the T40 flyby. 80
4.11 Volume production rates of the major primary ions N_2^+, N^+, CH_4^+, and CH_3^+ due to photon impact (black line) and photoelectron impact (red line) at a SZA of 37°. Blue line indicates the total ion production rates (photon + photoelectron). 83
4.12 Total volume production rates of the minor primary ions CH_2^+, CH^+, C^+, H_2^+, and H^+ at a SZA of 37°. 84
4.13 Volume production rates of major primary ions N_2^+, N^+, CH_4^+ and CH_3^+ calculated for a SZA of 60^o. The symbols stars and open squares show the calculations of *Richard et al.* [2015] and *Lavvas et al.* [2011], respectively. 84

4.14 (a) Production rate of CH_4^+ and CH_3^+ ions for a SZA of 37°. Solid curves and dashed curves show the profiles obtained using low resolution (LR) and high resolution (HR) N_2 photoabsorption cross sections, respectively. (b) Comparison between CH_4^+ production rates calculated by *Lavvas et al.* [2011] (blue lines) and current model (red lines) at a SZA of 60^o. (c) Comparison between the low resolution (10 Å bins) photoabsorption cross sections of N_2 used by *Lavvas et al.* [2011] and by the current model. . . 85
4.15 The reaction pathways of the major primary ions and terminal ions. The approximate percentage contribution to total production or loss for each reaction at altitudes near the ionospheric (∼1100 km) peak is indicated in parentheses. 87
4.16 Calculated density profiles of three major ions, $HCNH^+$, $C_2H_5^+$ and CH_5^+, for a SZA of 37^o, compared with INMS observations for T40 flyby and model calculations of *Westlake et al.* [2012], *Richard et al.* [2015] and *Dobrijevic et al.* [2016]. 88
4.17 Density profiles of minor ions calculated using photochemical model for T40 flyby condition. 89
4.18 Calculated electron density profile for T40 flyby of Titan, compared with Cassini RPWS/LP observations and model calculations of *Vigren et al.* [2013], *Westlake et al.* [2012] and *Dobrijevic et al.* [2016]. 90
4.19 Calculated electron density profile for various Titan flybys compared with Cassini RPWS/LP observations. 91
4.20 Calculated photoelectron flux at 1074 km compared with calculations of *Vigren et al.* [2016] and with Cassini CAPS observation (obtained from *Vigren et al.* [2016]). The dashed line indicates the case when the photoelectron flux is reduced by a factor of 3.0 92
4.21 (a) Production rates of the major primary ions N_2^+, N^+, CH_4^+, and CH_3^+ due to electron impact. Solid curves show the electron impact production rate obtained in the standard case and dashed curves shows the production rates obtained when photoelectron flux is reduced by a factor of 3.0. (b) Total ion production rates due to photon and photoelectron impact. Solid blue curve shows the total ion production rates (photon + photoelectron) in the standard case and dashed blue curve shows the one obtained when the photoelectron flux is reduced by a factor of 3. Same is the case with the red curves which shows total ion production rates by electron impact. 93
4.22 Density profiles of electrons and the major ions, $HCNH^+$, $C_2H_5^+$, and CH_5^+. Symbols show the Cassini observations. Solid red curve is the profile obtained in the standard case and dashed red curve shows the calculated density when the photoelectron flux is reduced by a factor of 3.0. 94

4.23 Comparison of volume production rate of N_2^+ calculated using the current study (solid red curve) with that of *Sagnières et al.* [2015] and *Madanian et al.* [2016]. Solid black curve and crosses show the calculation of *Sagnières et al.* [2015], using solar energy deposition model (SED) model and empirical model, respectively. Similarly, solid blue curve and open squares represent calculations of *Madanian et al.* [2016]. Red dashed curve shows the case where our calculated production rate values are adjusted to match with the empirical calculations of *Madanian et al.* [2016]. 96
4.24 Density profiles of electrons and major ions, $HCNH^+$, $C_2H_5^+$, and CH_5^+, calculated using the empirical production rate of N_2^+. Solid curves show the standard case profiles. The dashed curves show the profiles obtained when our calculated production rate values of N_2^+ are adjusted to match with the empirical calculations of *Madanian et al.* [2016]. 97
4.25 (a) Electron Temperature profiles used for testing model sensitivity. The symbols circles and squares represents the T_e measured by Langmuir probe during the T40 inbound and outbound conditions, respectively. Electron temperature of *Richard et al.* [2011] (from *Westlake et al.* [2012]) has been extrapolated from 1060-1000 km. Extrapolated region is represented by dotted line. (b) Electron density profile calculated using different electron temperatures profiles. 99
4.26 Electron density profile calculated for the dayside flybys T48, T86, T95 and T104. Solid red curves shows the standard case profiles and blue dashed curves show the profiles obtained when the RPWS/LP measured electron temperature is reduced by a factor of 5 for each flyby. 100
4.27 HCN density profiles used for different model runs. Symbols represent the density measured by INMS during the inbound leg of T41 flyby. . . . 101
4.28 Density profiles of electron and major ions, $HCNH^+$, $C_2H_5^+$ and CH_5^+, obtained using different density profiles of HCN shown in Figure 4.27. Case 1: HCN density measured during the inbound part of the T41 flyby fitted linearly. Case 2: Dayside average mixing ratio profile of HCN as given by *Cui et al.* [2016]. Case 3: Reducing the density of HCN used in standard case by a factor of 3. 102
4.29 Density profiles of major ions and electrons obtained by varying the dissociative recombination coefficient (DRC) of CH_5^+ and $C_2H_5^+$. Black circles represents the INMS observations. Red solid curve indicates the profile calculated in the standard case. Green dashed curve represent case 1 where the DRC of CH_5^+ and $C_2H_5^+$ is increased by a factor 5. Blue dotted curves show case 2 where the DRC of CH_5^+ and $C_2H_5^+$ is increased by a factor 10. 103
4.30 Density profiles of $HCNH^+$ and electron obtained by adding theoretical reactions proposed by *Westlake et al.* [2012]. Solid circles and open squares represent RPWS/LP measured electron density and INMS measured $HCNH^+$ density, respectively. Red and blue curves show the calculated density profiles of electron and $HCNH^+$ with solid lines representing the standard case profiles and dashed lines representing the profiles obtained when the theoretical reactions were included. 105

4.31 NH_3 densities used in the standard case along with the modelled profiles of *Dobrijevic et al.* [2016] (Case 1) and *Yelle et al.* [2010] (Case 2). The profiles for NH_4^+, $HCNH^+$, and electrons obtained by using each of these NH_3 profiles are also shown. 106
4.32 Comparison between S2K, SEE and HEUVAC solar flux models for 5 January 2008. The magnitude of the ratio between the solar fluxes is indicated on the right side vertical axis. The horizontal line shows the point where the ratio S2K/HEUVAC and SEE/HEUVAC equals 1. 107
4.33 Electron density profile obtained using three different solar flux models. . 108

5.1 Dissociative electron attachment cross sections used in the model. References are given in Table 5.1 114
5.2 Photodetachment cross sections of anions calculated using Miller-Threshold law. 115
5.3 The density profiles of 10 negative ions calculated in the present model, along with the total anion density. 119
5.4 The density profiles of (a) H^- and (b) CH_2^- calculated using the current model compared with the calculations of *Vuitton et al.* [2009] and *Dobrijevic et al.* [2016]. 123
5.5 The density profiles of (a) CN^- and (b) C_3N^- calculated using the current model compared with the calculations of *Vuitton et al.* [2009] and *Dobrijevic et al.* [2016]. In the bottom panel, symbols connected by solid line shows the profile of C_3N^- obtained when electron density was reduced by half to nullify the effect of overestimation in the electron density. See the text for more details. 124
5.6 The density profiles of (a) C_4H^- and (b) C_5N^- calculated using the current model compared with the calculations of *Vuitton et al.* [2009] and *Dobrijevic et al.* [2016]. In the top panel, symbols connected by solid line shows the profile of C_3N^- obtained when electron density was reduced by half to nullify the effect of overestimation in the electron density. See the text for more details. 126
5.7 The density profiles of (a) C_2H^- and (b) C_6H^- calculated using the current model compared with the calculations of *Vuitton et al.* [2009] and *Dobrijevic et al.* [2016]. 127
5.8 The density profiles of (a) O^- and (b) OH^- calculated using the current model compared with the calculations of *Vuitton et al.* [2009]. 128
5.9 The relative model density profiles of the anions CN^-, C_2H^- (top panel), and C_3N^- and C_4H^- (bottom panel) compared with the profiles obtained by *Desai et al.* [2017] at the mass peaks 25.8-26.0 u/q and 49-50.1 m/q during the ingress and egress of the T40 flyby 130

List of Tables

1.1 Ionospheres in the Solar System 3
1.2 Physical parameters of Titan 6

2.1 Elastic differential cross section for xenon (in units of 10^{-16} cm^2 sr^{-1}) . . 35
2.2 Fitting parameters for ionization cross sections of xenon. Notation 1E5 means 1×10^5 38
2.3 Parameters to calculate excitation cross sections of Xe. For all levels, $a_j = b_j = 1$ 40
2.4 Mean energy per ion pair (w-value) for neutral and different ionization states of xenon for incident energies 300 eV and 10 keV. 43

3.1 Elastic differential cross sections for CH_4 in units of cm^2. Value inside the bracket indicates a linearly extrapolated value. Notation 1E-18 implies 1 x 10^{-18} 54
3.2 Parameters for CH_4^+, CH_3^+ and CH_2^+ ionization cross section (equation (3.1)) 58
3.3 Mean energy per ion pair (w-value) for neutral and different ionization states of methane for incident energies 100 eV and 10 keV. 62

4.1 List of neutrals and ions included in the model 86
4.2 Information on the Cassini flybys used in our study 91
4.3 A comparison between empirically calculated production rate of N_2^+ by *Madanian et al.* [2016] and the values calculated using the present model 95

5.1 List of dissociative electron attachment processes considered in the model. 114
5.2 Major production and loss processes of anions at 1100 km and their relative contribution. 120

A.1 List of ion-neutral reactions considered in the model 137
A.2 Dissociative recombination rate coefficients used in the model (from *Richard* [2013]) 141
A.3 List of anion-neutral reactions considered in the model 142

Chapter 1

Introduction

Atmospheres of different bodies in our solar system host an electrified region where a substantial number of atmospheric particles are in a charged state. This region is known as ionosphere. *Schunk and Nagy* [2009] defines ionosphere as "the region where significant number of free thermal (< 1 eV) electrons and ions are present". In Earth's atmosphere, the presence of an electrically conducting layer was established when it was observed that the radio waves, while propagating through the atmosphere, get reflected back to the surface from $\sim$80 km altitude [*Breit and Tuve*, 1925; *Appleton and Barnett*, 1925]. Present understanding of the ionospheric processes confirms that these gaseous ions and free electrons not only affect the electrical properties of the atmosphere but also play an important role in the atmospheric chemistry [*Rees*, 1972].

There are two basic processes that cause the formation of an ionosphere; photoionization and impact ionization. The energetic solar ultraviolet (UV) radiation ionizes the atmospheric neutrals, resulting in the generation of ions and free electrons. This process is called photoionization. The electrons produced via photoionization, called photoelectrons, can also ionize, provided they have sufficient energy. Other sources of ionization are galactic cosmic rays, solar wind particles, energetic particles precipitating into the atmosphere, etc.

$$\mathrm{A} + \mathrm{h}\nu \rightarrow \mathrm{A}^+ + \mathrm{e}^- \text{ (Photoionization)}$$
$$\mathrm{A} + \mathrm{e}^* \rightarrow \mathrm{A}^+ + \mathrm{e}^- \text{ (Impact ionization)}$$

Here e^* represents an energetic electron. The plasma thus produced in the atmosphere is found to have profound impact in determining the characteristics of the atmosphere as they undergo several processes, like chemical reactions, transport under the influence of electric and magnetic fields, wave disturbances, etc. Understanding these processes require information on different parameters, viz., solar UV radiation, variations in the solar activity and the properties of the atmosphere such as neutral composition, atmospheric density, temperature, etc.

All it needs for a solar system body to have an ionosphere are an atmosphere where sufficient neutral particles are present to get ionized and solar UV radiation to cause

the ionization of the neutrals. As the solar radiation propagates down through the atmosphere, more neutrals are available to get ionized since the atmospheric density increases with decreasing altitude. However, the intensity of the radiation attenuates as it penetrates deeper and deeper which can reduce the rate of ionization. At the altitude where the product of solar flux and neutral density maximizes, the ionization rate and hence the plasma density will be maximum. Thus, the general behaviour of the ionosphere is that the plasma density increases with decreasing altitude, reaches a maximum and shows a gradual decrease afterwards [*Schunk and Nagy*, 2009](see Figure 1.1).

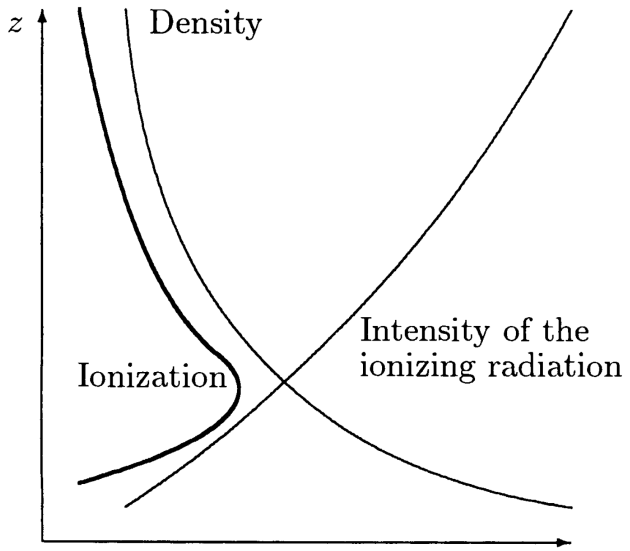

Figure 1.1: Variation of solar radiation, neutral density and ionization rate with altitude (Taken from *Kallenrode* [2004]).

The chemical reactions involving the primary products of the photoionization process plays a major role in deciding both the neutral and ionic composition of the upper atmosphere. Some of the reactions that occur in the ionospheric region are:

$XY + h\nu/e^- \rightarrow XY^+ + e^-$ (photon/electron impact ionization)

$X^+ + Y \rightarrow Y^+ + X$ (charge exchange)

$XY + e^- \rightarrow X^- + Y$ (dissociative electron attachment)

$X^+ + e^- \rightarrow X + h\nu$ (radiative recombination)

$X^+ + Y^- \rightarrow$ neutral products (ion-ion recombination)

$X^+ + Y \rightarrow$ products (ion-neutral reactions)

$X^- + h\nu \rightarrow X + e^-$ (photodetachment)

$XY^+ + h\nu \rightarrow X + Y$ (dissociative recombination)

Even though the composition of the ionosphere is largely determined by the major atmospheric gas, chemical reactions that occur in the ionospheric region also play an important role in determining the constituents. For example, in the Martian atmosphere, even though abundant neutral gas is CO_2, the dominant ion in the ionosphere is not CO_2^+ but O_2^+ (and O^+ at higher altitudes) which is formed through different chemical reactions [*Fox*, 2004]. Table 1.1 summarises the properties of different ionospheres in the solar system.

Table 1.1: Ionospheres in the Solar System

	Mean Distance from Sun (AU)†	Major atmospheric gases	Major ions	Peak plasma density (cm^{-3})	Altitude of ionospheric peak (km)	References
Venus	0.7	CO_2, N_2	O_2^+, NO^+, O^+	10^5	140	*Fox* [2004]
Earth	1.0	N_2, O_2	O^+, O_2^+, NO^+	10^6	300	*Banks et al.* [1976]
Mars	1.5	CO_2, N_2	O_2^+, CO_2^+, O^+	10^5	130	*Fox* [2004]
Jupiter	5.2	H_2, He	H^+, H_3^+	10^5	1800	*Hinson et al.* [1997]
Saturn	9.5	H_2, He	H^+, H_3^+	10^4	1800	*Nagy et al.* [2009]
Uranus	19.1	H_2, He	H^+, H_3^+	10^4	2000	*Bergstralh et al.* [1991]
Neptune	30.0	H_2, He	H^+, H_3^+	10^3	2000	*Lyons* [1995]

†1 AU = Mean Sun-Earth distance $\sim 1.49 \times 10^{11}$ m

1.1 Relevance of electron impact studies in planetary atmospheres

Planetary atmospheres are endlessly exposed to solar radiation. The ionization of the atmospheric gases caused by the high energy UV photons ensures that electrons are always available in the atmosphere to interact with the neutrals. Other sources of ionization can be different energetic particles of solar or magnetospheric origin. These high energy particles collide with the atmospheric neutrals and can ionize or excite the species. Depending on their energy, the cascade of secondary electrons, created by the ionization,

also can lead to further ionization or excitation. At lower energies, the electron collision can also result in de-excitation, ion-electron recombination, dissociation, or attachment to form negative ions. Such electron-neutral interactions can initiate different processes that could play a vital role in determining the physical and chemical properties of the atmosphere. For example, the ions and radicals produced by electron impact ionization/dissociation can lead to further chemical reactions which would ultimately determine the composition of the atmosphere. Excited species generated via electron impact excitation can undergo radiative decay which appears as atmospheric emissions such as airglow and aurora. Electron impact ionization also contributes to the formation of ionospheric layer in planetary atmospheres. A quantitative understanding of such phenomena is possible only with a thorough knowledge of electron collision processes.

Extensive research has been done on electron impact on N_2 and O_2 in Earth's atmosphere. It is the fragments produced from the photon and electron impact with these neutral gases that dominates the D and E region of Earth's ionosphere [*Rees*, 1972]. Electron collision results in the rotational and vibrational excitation of N_2 and O_2 and excitation of fine structure levels of atomic oxygen. At high altitudes, the photoelectrons also collide with the ambient thermal electrons resulting in significantly high electron temperature [*Banks*, 1969]. For auroral emissions also, electron-neutral collisions are the root cause. The high energy electrons of magnetospheric origin enter into atmosphere in the high latitude region by getting transported along the magnetic field lines. These electrons enter deep into the atmosphere where they collide with the molecules and excite them. They get de-excited by emitting radiation which we observe as aurora [*Chamberlain*, 1961].

Electron impact processes are important not only in Earth's atmosphere, but also in the atmosphere of all solar system bodies. The E and F region of the Martian ionosphere is primarily produced via photon and electron impact ionization [*Haider et al.*, 2009]. The study of *Bhardwaj and Jain* [2013] showed that electron impact on CO, followed by the electron and photon impact dissociation of CO_2, are the major source mechanism for Cameron band emissions in Venusian atmosphere. *Bhardwaj and Gladstone* [2000] and *Grodent* [2015] discussed in detail the role of electron–neutral interaction in causing auroral emissions in the giant planets atmospheres. The photochemistry in the upper atmosphere of these gas giants are also largely influenced by electron collision processes [*Strobel*, 2004]. The significance of electron impact ionization in cometary atmosphere was highlighted by the studies of *Cravens et al.* [1987] and *Bhardwaj et al.* [1990, 1996].

The present thesis aims at understanding the photochemistry on the dayside ionosphere of the satellite Titan, which is initiated by photon and electron collision processes with the atmospheric neutrals. The photoionization produces photoelectrons which lose their energy through a series of collisions with the neutral gases. The electron-neutral interaction leads to ionization, dissociation, or excitation of the target particles. The

byproducts of this collision process subsequently lead to a complex ion-neutral chemistry. This thesis aims at modelling the energy degradation process of electrons in gases, the results of which are applied for studying the photochemistry in the upper atmosphere of Titan. The current chapter gives a brief introduction to Titan and it's upper atmospheric photochemistry leading to the formation of ionosphere.

1.2 Titan - the Saturnian moon

Titan, the largest among the 62 moons of Saturn, is the second largest satellite in our solar system, dominated in size only by Ganymede, the satellite of Jupiter. It is even larger than the planet Mercury and the dwarf planet Pluto. Titan is the only satellite in the solar system that has a substantial atmosphere. The atmospheric pressure is ∼1.5 bar, which is 50% higher than what we experience on Earth [*Fulchignoni et al.*, 2005]. As the gravity of Titan is not strong enough to tightly hold this thick atmosphere, the atmosphere extends to very high altitudes (∼2000 km). Figure 1.2 shows an image of Titan taken by the Cassini Huygens mission (described later). The blue thin layer is the high altitude atmosphere surrounding Titan. Some physical and atmospheric parameters of Titan are listed in Table 1.2.

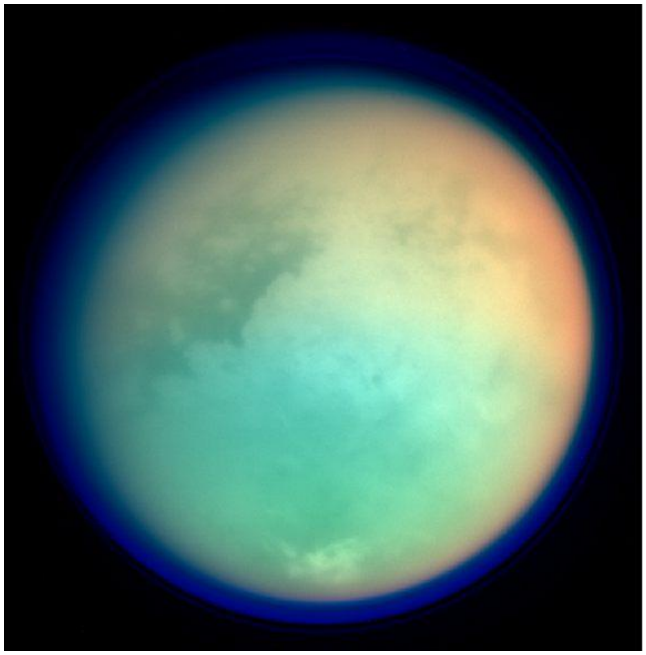

Figure 1.2: The image of Titan taken by Cassini. Blue layer represents the atmosphere and detached hazes (Image credit: NASA/JPL-Caltech).

Much was not known about Titan's atmosphere until the Voyager spacecraft visited the satellite. The UV spectrometer onboard the Voyager 1 confirmed that similar to Earth, the most abundant gas in the atmosphere of Titan is molecular nitrogen [*Strobel and Shemansky*, 1982]. Subsequent observations, space missions, and theoretical studies have largely improved our understanding of Titan's atmosphere [*Coustenis*, 2008; *Brown*

et al., 2009]. N_2 constitutes about 90-95% of the atmosphere, followed by methane (3-4%) and a few tenths of percent of H_2. In addition, the atmosphere harbours a suit of hydrocarbon and nitrogen bearing compounds (C_2H_2, C_2H_4, C_4H_2, C_6H_6, HCN, HC_3N, CH_3CN, etc) whose concentration range from 0.1 to 1000 ppm [*Hörst*, 2017]. Even though minor, these trace gases have received significant attention over the past few years. These heavy carbon and nitrogen bearing compounds point to an atmosphere where a complex organic chemistry is actively in progress [*Vuitton et al.*, 2014]. They are formed as the byproducts of a chain of reactions initiated by the interaction of solar UV photons and other energetic particles with the major gases N_2 and CH_4, and are the source of the aerosol and haze layer that shroud Titan, giving the satellite its brownish-orange appearance [*Lavvas et al.*, 2008, 2009, 2013].

Table 1.2: Physical parameters of Titan

Parameter	Value
Distance from Sun	9.5 AU
Distance from Saturn	1.23×10^6 km (20 Saturn radii)
Mass	1.34×10^{23} kg
Equatorial diameter	5150 km
Surface gravity	1.35 m/s^2
Escape velocity	2.64 km/s
Atmospheric pressure	1.5 bar
Surface Temperature	94 K
Atmospheric bulk composition	N_2, CH_4
Orbital period around Saturn	15.95 Earth days
Length of a day	15 Earth days
Length of an year	30 Earth years

The sophisticated chemistry taking place in the Saturnian moon have implications for our planet Earth. Theories suggest that the primordial Earth possessed an oxygen-less atmosphere with CH_4, N_2, H_2, H_2O, and NH_3 as the major constituents. The presence of a large variety of organic compounds is also suggested. As per recent studies, even the primitive atmosphere was dominated by N_2 [*Feulner*, 2012]. The chemistry that occurred in this primordial atmosphere finally led to the formation of biological molecules [*Miller and Urey*, 1959]. With a nitrogen-dominated atmosphere where a significant amount of CH_4 is also present, analogies can be made between the current organic chemistry of Titan and the pre-biotic chemistry that existed on Earth [*Coustenis*, 2015]. Several organic compounds such as hydrogen cyanide (HCN), cyanoacetylene

(HC_3N) and cyanogen (C_2N_2), which are formed as a byproduct of the chemistry, were the molecules which played an important role in Earth's pre-biotic chemistry [*Raulin and Gpcos Team*, 2006]. It has been established that the thick orange coloured haze particles called tholins and other organic aerosols, which are found to be present in plenty in Titan's atmosphere, can lead to the formation of biological molecules under appropriate conditions [*Neish et al.*, 2010; *Coustenis and Encrenaz*, 2013; *Palmer et al.*, 2017]. Thus, the studies on Titan′s chemistry might give us clue on the chemistry that led to the formation of life on Earth.

In addition to its thick atmosphere, Titan also posses many other intriguing features. Even though a satellite, all the processes that occur on an Earth-like planet, like wind, rain, volcanism, storm, tectonic activity, etc, take place on Titan [*Müller-Wodarg et al.*, 2014]. Similar to Earth's hydrological cycle, there is a methane cycle, with methane clouds, rain, and seas [*Jonathan and Atreya*, 2008]. Liquid bodies have been observed on the surface of this Saturnian moon and studies revealed that these lakes are composed of methane and other hydrocarbons [*Cordier et al.*, 2009]. All these features make Titan a fascinating body in the solar system.

1.2.1 The Cassini-Huygens mission

The Cassini-Huygens mission was a joint venture of NASA and ESA, to study the Saturn and its satellite systems exclusively. The mission was launched on 15 October 1997, and after its voyage for almost 7 years, it reached Saturn on 14 January 2005. Although the mission was meant for studying the entire Saturnian system, Titan was a priority target. Cassini was an orbiter which went around Saturn and it had several targeted flybys with Titan. Huygens was a probe which plunged into Titan's atmosphere and made in-situ measurements of several atmospheric parameters [*Matson et al.*, 2002]. The principal objectives of the Cassini-Huygens mission with respect to Titan were to measure the abundance of the atmospheric constituents, the horizontal and vertical distribution of the trace gases, the prevailing atmospheric conditions, like winds, general circulation, global temperature, seasonal effects, etc, the topography and composition of surface, and to investigate the properties of the upper atmosphere, to scrutinise the ionization and its impact on the neutral species. The mission carried 18 scientific instruments, 12 on the orbiter and 6 on the probe, collecting both remote sensing and in-situ data.

Cassini′s first flyby with Titan occurred on 26 October 2004 which was named as Ta encounter. The subsequent flybys were labelled as Tb, Tc, T3, T4, T5, etc. The last flyby, T126, was on 15 April 2017. During Tc, the Huygens probe was inserted into Titan′s atmosphere. Throughout its decent, the instruments onboard the probe measured lower atmospheric parameters of Titan. The upper atmospheric region, especially above 900 km, was explored by the instruments onboard the orbiter.

During the closest flyby T70, the orbiter went still deeper into the atmosphere with the altitude of closest approach (CA) being 880 km. After thirteen years of exploration, the mission ended on 15 September 2017 by plunging the Cassini spacecraft into Saturn's atmosphere.

1.3 The Ionosphere

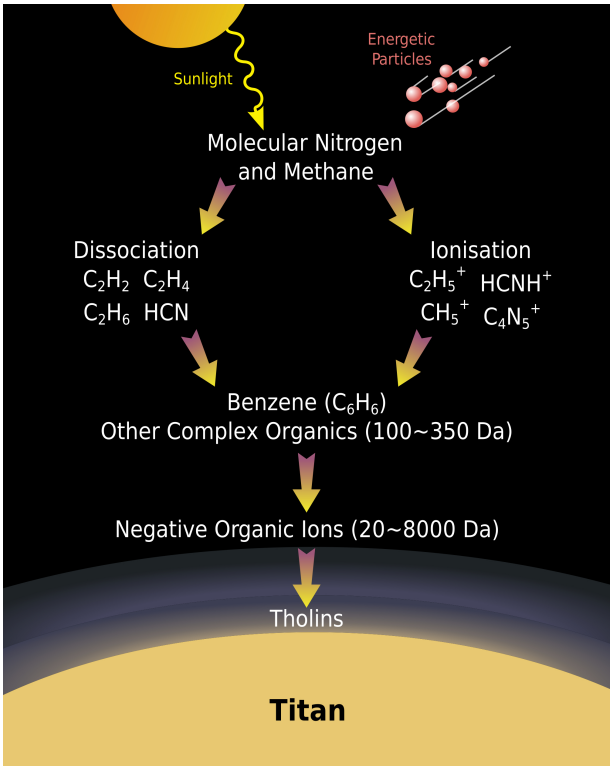

Figure 1.3: A schematic figure showing the growth of molecular ions leading to the formation of organic particles. Figure taken from *Waite et al.* [2007].

An ionosphere on Titan was first seen by the radio occultation experiment during Voyager-1 flyby [*Bird et al.*, 1997]. However, it was believed that the ionosphere is composed of a few low mass positive ions and did not have much to do with the neutral composition of the atmosphere [*Keller et al.*, 1998; *Wilson and Atreya*, 2004]. The Cassini-Huygens mission revolutionised these ideas. Cassini observations revealed the Titan′s ionosphere to be the most complex one, both chemically and dynamically. The Langmuir Probe (LP) instrument which was a part of the Radio and Plasma Wave Science (RPWS) experiment detected the presence of a substantial number of ionospheric electrons [*Wahlund et al.*, 2005]. The quadrupole mass spectrometer, named as Ion Neutral Mass Spectrometer (INMS), measured the ion and neutral composition of the upper atmosphere (>900 km). Positive ion composition was reported by INMS and it revealed the presence of heavy nitrile and hydrocarbon ions [*Wahlund et al.*, 2009]. The ionosphere is also found to host a suite of negative ions, an unexpected discovery

made by the Cassini Plasma Spectrometer-Electron Spectrometer (CAPS-ELS) [*Coates et al.*, 2007]. Further studies based on these observations suggested that these heavy molecular ionic species could be the precursors for the formation of larger molecules, aerosols, and haze particles (tholins) observed in Titan's atmosphere [*Imanaka et al.*, 2004; *Waite et al.*, 2007; *Lavvas et al.*, 2009]. It was found that the molecular growth could be triggered by the reactions involving anions, cations and radicals (see Figure 1.3). The neutral species such as benzene and ammonia are formed in the atmosphere as the byproducts of the chemistry [*Vuitton et al.*, 2008; *Yelle et al.*, 2010]. This established the role played by the ionosphere in Titan's atmospheric chemistry.

1.3.1 Photochemistry on the dayside of Titan′s ionosphere

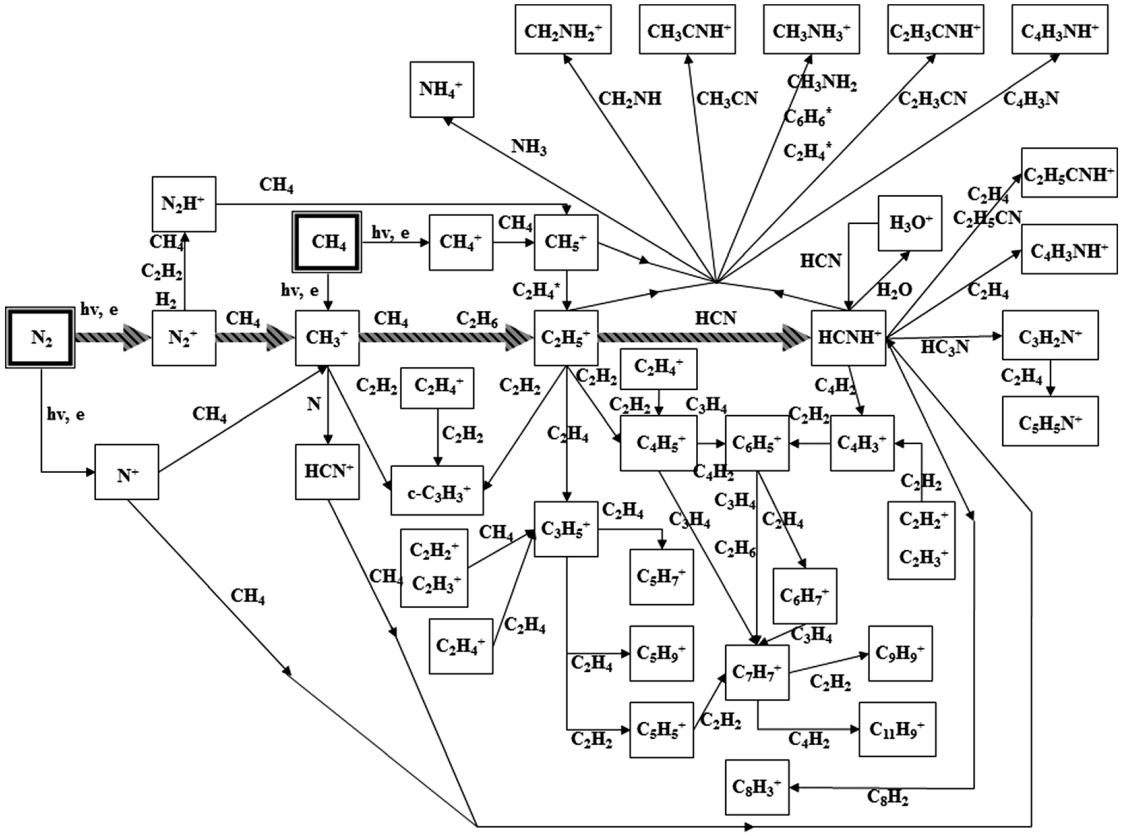

Figure 1.4: The ion-neutral reaction scheme in Titan′s ionosphere, taken from *Richard et al.* [2015].

Chemical reactions occurring in Titan′s ionosphere can be classified into two: neutral-neutral reactions and ion-neutral reactions. The current thesis focuses on the latter. On the sunlit side of Titan′s ionosphere, the main sources of ionization are solar photons and photoelectrons [*Galand et al.*, 2010]. The solar EUV photons impinging on the upper

atmosphere ionize the abundant neutral gases N_2 and CH_4:

$$\begin{aligned} N_2 + h\nu &\rightarrow N_2^+ + e^- \\ &\rightarrow N^+ + N + e^- \\ CH_4 + h\nu &\rightarrow CH_4^+ + e^- \end{aligned} \tag{1.1}$$

The ions, viz. CH_3^+, CH_2^+, CH^+, C^+, H_2^+, and H^+ also can be formed by the photoionization of CH_4. The photoelectrons generated can make collisions with N_2 and CH_4 and result in further ionization. The N_2^+ and N^+ ions are nonreactive with N_2 and go on to react further with methane and other hydrocarbons present in the atmosphere.

$$\begin{aligned} N_2^+ + CH_4 &\rightarrow CH_3^+ + N_2 + H \\ &\rightarrow CH_2^+ + N_2 + H_2 \\ N^+ + CH_4 &\rightarrow CH_3^+ + NH \\ &\rightarrow CH_4^+ + N \end{aligned} \tag{1.2}$$

These hydrocarbon ions immediately start reacting with the background neutral gases, thus resulting in a complex chemistry. The ion-molecule reactions take place at a faster rate (10^{-9} cm^3 s^{-1}) as compared to neutral-neutral reactions (10^{-11} cm^3 s^{-1}). New neutral and ionic species are formed as the result of these reactions. The ions can get converted to neutrals through ion-electron recombination reactions. The ions which do not recombine with electrons continue to react with the neutrals, like C_2H_2, C_2H_4, NH_3, C_2H_6, HCN, etc, until the formation of the product ions that are nonreactive with the neutral gases in the atmosphere. The sole loss process through which these ions are removed from the atmosphere is the ion-electron recombination. These terminal ions accumulate over time relative to more reactive ions. The neutral molecules formed in this process diffuse to lower altitudes and contribute to the molecular abundance. As the molecules diffuse to the lower atmosphere, they condense and finally form an aerosol layer in the stratosphere. This aerosol layer is identified as the Titan′s characteristic haze.

Figure 1.4 shows the ion-neutral reaction pathways in the dayside ionosphere. As indicated by the figure, the entire chain of reactions starts with the photon and photoelectron impact ionization of N_2 and CH_4. The most abundant terminal ions that are formed in the ionosphere as the byproducts of this chemistry are $HCNH^+$, $C_2H_5^+$, and CH_5^+ [*Cravens et al.*, 2009], in the order of their abundance. In addition, many other hydrocarbon ions are also formed like $CHCCNH^+$, HCN^+, CH_3CNH^+, $C_3H_5^+$, c-$C_3H_3^+$, etc. Figure 1.5 shows the ion spectrum recorded by INMS during the T5 flyby of Cassini. The ionization process also results in the formation of thermal electrons. In-situ measurements of Titan′s ionosphere have shown that Titan possesses a Chapman ionosphere with the peak electron density of ∼2500-3000 cm^{-3} at altitude between 1050-1200 km [*Wahlund et al.*, 2005].

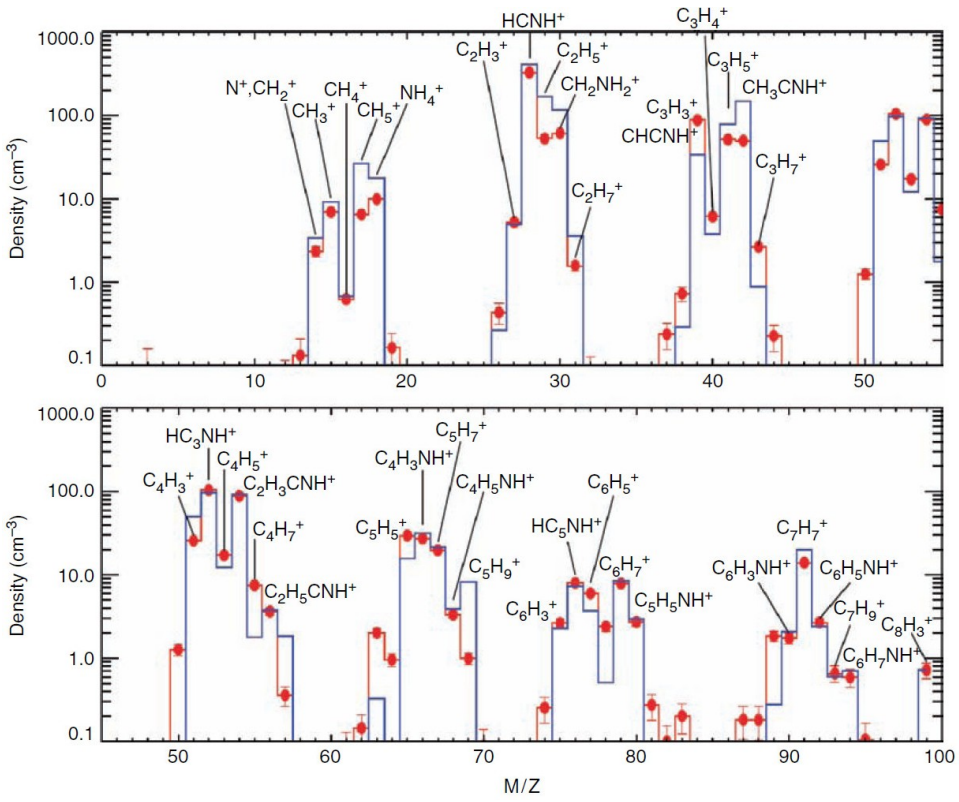

Figure 1.5: Ion spectrum recorded by Cassini INMS during T5 flyby of Titan (Figure taken from *Vuitton et al.* [2007]).

1.3.2 Negative ions

Negative ions have been reported to be present in dark clouds, circumstellar envelopes, cometary comae, etc (see *Millar et al.* [2017] and references therein). However, anions were least expected in the ionospheric region of Titan as all the models in the pre-Cassini period predicted that negative ions could be present only in the lower atmosphere (<400 km) [*Molina-Cuberos et al.*, 2000; *Bakes et al.*, 2002; *Borucki et al.*, 2006]. So, it came as a surprise when the CAPS-ELS instrument detected the presence of negative ions in the ionosphere of Titan [*Coates et al.*, 2007; *Waite et al.*, 2007]. Whenever the actuating instrument was oriented in the spacecraft direction, spikes were seen in the recorded spectrogram, which were attributed to negative ions (see Figure 1.6). Anions were detected during all those flybys for which the spacecraft altitude was low enough and the spacecraft orientation was favourable [*Coates et al.*, 2009, 2010]. This confirmed that the negative ions are a permanent feature of Titan's ionosphere. From the measured energy, the mass of the negative ions was calculated by assuming that the velocity of these cold thermal ions is equal to the spacecraft velocity. The mass of a singly charged negative ion is calculated as $m = 2E/v_{sc}^2$, where E is the observed energy and v_{sc} is the spacecraft velocity which was typically ∼6 km/s. The studies of *Coates et al.* [2007] and *Waite et al.* [2007] reported the presence of heavy anions having masses in the range 8000

to 10000 amu/q. During T16 flyby, negative ions as heavy as 13,800 amu/q were seen. The maximum density reported was ∼100 cm^{-3}. Using data from 34 flybys, *Wellbrock et al.* [2013] presented the density trends of negative ions of seven different mass groups (12-30, 30-55, 55-95, 95-130, 130-190, 190-652, and 625+ m/q) and reported the altitudes at which each of these mass groups showed maximum density. They concluded that the average altitudes at which each of these mass groups showed maximum density decrease with increasing ion mass.

Vuitton et al. [2009] made the first attempt to model the negative ion chemistry in Titan's ionosphere. They considered different possible production and loss processes of anions and identified dissociative electron attachment (DEA) to neutral molecules and associative detachment with radicals as the major production and loss mechanisms, respectively. The three peaks observed by the CAPS-ELS instrument at m/q = 22±4, 44±8, and 82±14, were identified as CN^-, C_3N^-, and C_5N^-, respectively. CN^- was suggested as the most dominant low mass anion in Titan's ionosphere.

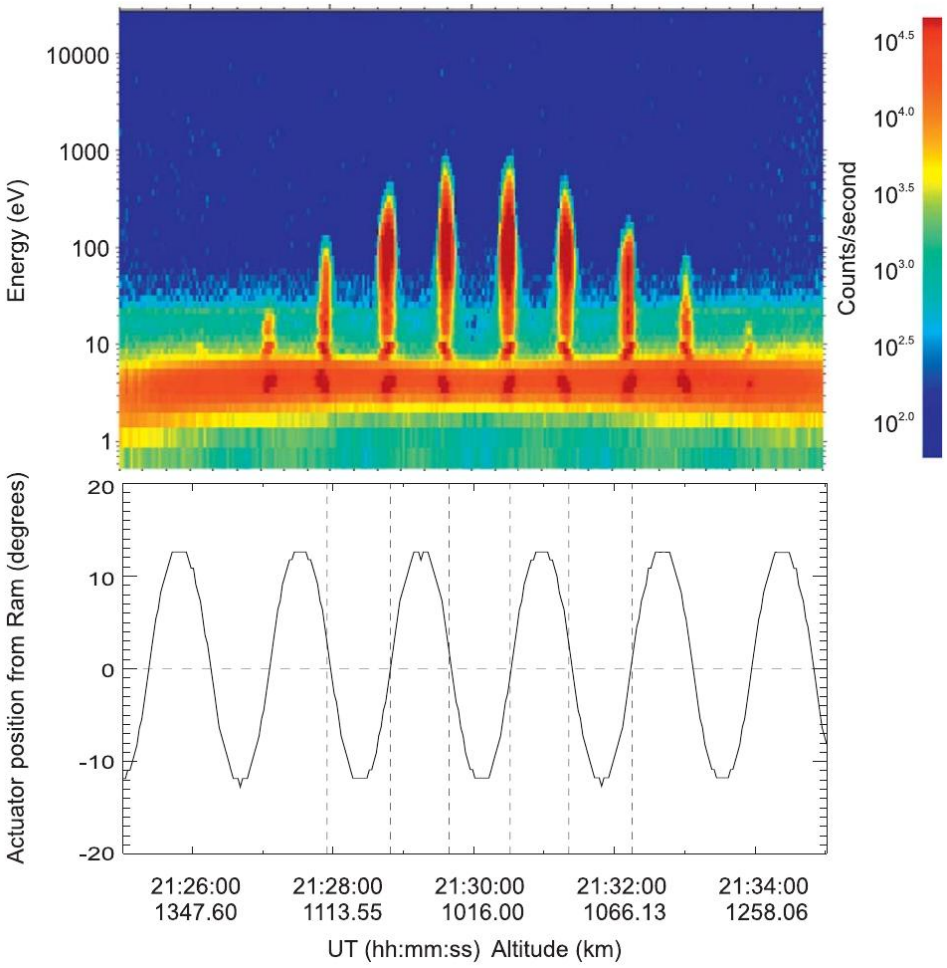

Figure 1.6: Energy–time spectrogram recorded by ELS and the corresponding actuator angle during the T40 flyby of the Cassini orbiter. The vertical spikes systematically occur when the ram angle is 0° (taken from *Vuitton et al.* [2009]).

Pre-Cassini studies, such as *Lebonnois et al.* [2002] and *Wilson and Atreya* [2003], suggested that the thick organic aerosol/haze layer, observed in the stratospheric region (50–250 km) of Titan is mainly formed through the stratospheric neutral chemistry. Using observations from Cassini Ultraviolet Imaging Spectrograph (UVIS), *Liang et al.* [2007] reported the detection of haze particles at ionospheric altitudes, consistent with the observations of heavy anions in this region. This suggested that the molecular growth starts at still higher altitudes. The anions, together with the positive ions undergo a series of chemical reactions and processes and simple molecules get converted to heavy organic macro molecules and eventually drift downward to form the haze layer in Titan′s atmosphere [*Waite et al.*, 2007, 2008]. A recent study by *Desai et al.* [2017] also suggest that the carbon chain anions could be the precursors for larger aerosols observed in Titan. They reported that the low mass carbon chain anions were observed to get depleted as heavier particles undergo rapid growth.

1.4 Previous modelling studies

1.4.1 Positive ions

The evolution of modelling studies in Titan's ionosphere can be classified as pre-Cassini and post-Cassini. Most of the pre-Cassini models were developed with the intention of providing aid to the interpretation of data from the upcoming mission. These studies suggested a complex and active organic chemistry in the ionospheric region and predicted the presence of many hydrocarbon and nitrile molecules, ions and free electrons.

The one dimensional model of *Ip* [1990] described in detail the ion-neutral chemistry in the ionosphere of Titan. As the measured density profiles of the neutrals in the atmosphere were not available, they used the modelled profiles of the neutral species by *Yung et al.* [1984]. The major ionization sources that were considered in the model were solar photons and energetic magnetospheric electrons. Their model suggested N_2^+, CH_3^+, $C_2H_5^+$, and H_2CN^+ as dominant ions in the upper atmosphere. They also suggested the presence of significant amounts of CH_5^+, N_2H^+, $C_2H_2^+$, and $C_2H_3^+$ near the ionospheric peak. By applying Chapman theory, the ionospheric peak was determined to be at $\sim$1200 km, with a peak electron density of 5000 cm^{-3} which was in agreement with the upper limit set by the Voyager-1 radio occultation data [*Lindal et al.*, 1983].

Keller et al. [1992] developed a one dimensional photochemical model which considered an elaborate list of ion-neutral reactions. In this study also, the background neutral atmosphere was based on the model of *Yung et al.* [1984]. A key finding of this model was that the major source of ionization on the dayside ionosphere is solar photons and photoelectrons and not the magnetospheric electrons as suggested by *Ip* [1990], even though they could be a dominant source on the nightside. For a solar zenith angle (SZA)

of 60° they calculated the density profiles of ions and electrons. The major ion was found to be H_2CN^+, followed by $C_2H_5^+$, CH_5^+, and HCN^+ and many other hydrocarbon ions of the form $C_nH_m^+$. The peak electron density obtained was 3030 cm^{-3} at an altitude of 1175 km.

The model of *Fox and Yelle* [1997] included more than 600 reactions and predicted the density profiles of 32 neutral species and 35 ions. They used the modelled profiles of N_2 and CH_4 from *Strobel et al.* [1992] and the mixing ratio profiles of C_2H_2, C_2H_4, C_2H_6, and C_4H_2 were taken from *Yung et al.* [1984]. Agreeing with the previous models, solar photons and photoelectrons were taken as the major source of ionization. In contrast with the findings of *Ip* [1990] and *Keller et al.* [1992], the model suggested that $HCNH^+$ could not be the dominant ion. The reactions of $HCNH^+$ with the neutrals NH_3, C_4H_2, and HC_3N which had reaction rate coefficient of the order of 10^{-9} cm^3 s^{-1} increased the loss rate of the ion, thus demoting it from the position of dominant ion. The difference between the neutral densities adopted by *Fox and Yelle* [1997] and the previous models also might have contributed to this conclusion. As per *Fox and Yelle* [1997], the hydrocarbon ions of the form $C_xH_y^+$ and $C_xH_yN_z^+$ would dominate near the ionospheric peak. For a SZA of 60°, they obtained a peak electron density of 7500 cm^{-3}.

Keller et al. [1998] updated their previous model [*Keller et al.*, 1992] by taking into account the newly measured reaction rate coefficients by *Anicich and McEwan* [1997] and added more neutral and ion species into their model. In addition to the model neutral atmosphere of *Yung et al.* [1984] and *Yung* [1987], this model also considered the recent model atmosphere by *Toublanc et al.* [1995]. *Keller et al.* [1998] agreed with the results of *Fox and Yelle* [1997] in that the hydrocarbon ions could be very important near the ionospheric peak; but they again suggested $HCNH^+$ as the dominant ion even after including the additional loss reactions considered by *Fox and Yelle* [1997]. *Keller et al.* [1998] explained the lower abundance of $HCNH^+$ in the model of *Fox and Yelle* [1997] as due to the underestimation in the production rate and overestimation in the loss rate of the ion which in turn occurred due to the difference in the neutral profiles of HCN and C_4H_2 adopted in their study. However, the peak electron density obtained by *Fox and Yelle* [1997] and *Keller et al.* [1998] were in agreement. A drawback of the updated model of *Keller et al.* [1998] was that only a few nitrogen-bearing molecules were included in the chemical network and hence most of the ions which they identified using the model were hydrocarbons.

The model of *Banaszkiewicz et al.* [2000] supported the findings of *Keller et al.* [1998]. They used the more recent neutral atmosphere of *Lara et al.* [1996] and calculated the densities of 55 ions. The ion density profiles that they obtained were in closer agreement with *Keller et al.* [1998] than those by *Fox and Yelle* [1997]. CH_5^+ and $C_2H_5^+$ were suggested as the dominant ions after $HCNH^+$. For a SZA of 30° the peak electron density that they obtained was ∼6000 cm^{-3}. *Wilson and Atreya* [2004] developed a

model in which the main focus was on understanding the coupling between neutral and ion chemistry. The model included updated reaction rate coefficients and cross sections. In agreement with the previous models, *Wilson and Atreya* [2004] predicted $HCNH^+$ as the dominant ion and estimated a peak electron density to be ∼4200 cm^{-3} for a SZA of 60°.

A new era in the ionospheric models of Titan began when the Cassini-Huygens reached the Saturnian system in January 2005. Till then, many crucial inputs to the models such as neutral atmosphere and temperature were based on the modelled values of *Yung et al.* [1984]; *Toublanc et al.* [1995]; *Strobel et al.* [1992]; *Gan et al.* [1992] etc. The only possible way to validate the model results was to compare with the previous model calculations. But once Cassini started making flybys with Titan, models could use measured atmospheric parameters as inputs and could validate the model results by comparing with the observations.

The first model that came out in this row was by *Cravens et al.* [2005] who modelled the conditions of Titan′s ionosphere during the Ta encounter and calculated the electron densities. They used N_2 and CH_4 profiles measured by INMS during the flyby. The chemistry scheme employed was the same as that of *Keller et al.* [1998]. Solar photons and magnetospheric electrons were included as the major source of ionization. The study concluded that during the ingress of Ta, which was on the dayside, solar radiation is the major source and during the outbound which was on near nightside, magnetospheric electrons made some contribution. Since INMS ion density measurements were not available during this flyby, *Cravens et al.* [2005] could compare their results only with the RPWS measured electron densities and reasonable agreement was seen. But, for the SZA between 80° and 90° and when the solar photons were considered as the major ionization source, the model predicted density was about 30% less than the observation. Also, the altitude of ionospheric peak predicted by the model was located below the altitude of closest approach of spacecraft for the dayside.

When the modelled mass spectrum of *Keller et al.* [1998] at an altitude of 1055 km was compared with the INMS measured ion mass spectrum during the T5 flyby, it was observed that the even mass ion densities are poorly or not reproduced by the model, though a good match was seen at odd masses. Even masses represent protonated nitrile species and odd masses represent protonated hydrocarbons. This suggested the necessity of adding more reactions including nitrogen-bearing molecules into the chemical reaction schemes existed till then. This was done in the models of *Vuitton et al.* [2006, 2007]. They used the updated list of reactions and rate coefficients from *Anicich et al.* [2006] and *McEwan and Anicich* [2007]. The mass spectrum generated by these models well reproduced the INMS mass spectrum for T5 flyby. Even so, the generated spectrum gave only a snapshot of the ionosphere, calculating densities for only a particular altitude, instead of a profile.

The ionosphere model of *Robertson et al.* [2009] used the neutral densities and electron temperature from Cassini measurements for two flybys; one on dayside (T17) and other on both dayside and nightside (T18). They used the same set of ion-neutral reactions by *Vuitton et al.* [2007]. Ionization sources considered were solar photons and photoelectrons as this was found to be sufficient for producing electron density in agreement with the observations. For both the flybys, the modelled electron and the total ion densities had reasonable agreement with the observations at altitudes above 1100 km. Below this height, the model values were significantly higher than LP observations.

Westlake et al. [2012] calculated the ion densities for the T40 flyby by using a photochemical model and an empirical model. In photochemical modelling, the production rates of the primary ions N_2^+, N^+, CH_4^+, CH_3^+, etc, are calculated and subsequently used them as input for simulating the ion-neutral chemistry. In empirical modelling, the ion densities are calculated by using the production and loss rates of the ions inferred from the INMS data. Both these models could sufficiently reproduce the density of hydrocarbon ions, but overestimated the density of the major ion $HCNH^+$. This overestimation also affected the calculated abundance of the second and third most abundant ions, $C_2H_5^+$ and CH_5^+ as the chemistry of these three ions are highly interlinked. They demonstrated that electron temperatures play a crucial role in determining the densities of the ions and suggested using electron temperature profiles that converge to the neutral temperature at lowest altitudes. They also analysed various production and destruction processes of $HCNH^+$ and found that a significant loss process is needed to cause the destruction of the ion. They suggested that the loss process must be with C_2H_2, C_2H_4, and H_2, having reaction rate coefficients 5 x 10^{-11}, 6 x 10^{-13} and 2 x 10^{-11} cm^3 s^{-1}, respectively, resulting in the formation of the ions HC_3NH^+, $C_3H_3NH^+$ and $CH_2NH_2^+$. But there was no experimental evidence that such reactions could exist.

Vigren et al. [2013] modelled the dayside ionosphere with the aim of calculating the electron number density profile. The study concentrated on four dayside flybys: T40, T41, T42, and T48. The production rate of electrons was calculated using a solar energy deposition model. The only loss process for the electrons that was considered was the dissociative recombination reactions. Using the laboratory-measured dissociative recombination rate coefficients of different ions present in Titan, they derived an effective recombination rate. This, along with RPWS/LP measured electron temperature and calculated electron production rate, was used to determine the plasma density for the photochemical equilibrium condition. Even though the altitude of peak plasma density matched with the observations, the predicted number densities were nearly a factor 2 higher than the measurements in the altitude range 1050-1200 km. They suggested that, other than dissociative recombination reaction, there may be an important loss process for the electrons and the reactions associated with negative ions may be important for the thermal electron balance in Titan's ionosphere.

To understand whether the overestimation in electron density is caused by the over estimation in production rates, *Richard et al.* [2015] calculated the ion production rates using a photochemical model as well as an empirical model which was based on INMS observations. The production rates of the major primary ions N_2^+, CH_4^+, and CH_3^+ obtained using the two methods were in good agreement. They concluded that the exaggerated plasma density is not caused by overproduction, but might be due to some insufficient electron-ion recombination, other chemistry like ion-molecule reactions, or the contributions of negative ions to the total charge. Model of *Dobrijevic et al.* [2016] which included the coupling between the neutral and ionic species from lower atmosphere up to the ionosphere also over-predicted the electron number densities. They suggested that to improve the chemical scheme of Titan's atmosphere a more precise assessment of the uncertainty factors for some rate constants is required. In addition, they established the requirement of a better evaluation of the uncertainty factors for photolysis rates including photodissociation and photoionization.

1.4.2 Negative ions

The first model which looked into the presence of anions in Titan was by *Capone et al.* [1976]. They studied cosmic ray induced ionization in the lower atmosphere of Titan (<400 km) and included only two anions in the model; H^- and CH_3^-. The major production and loss process were assumed to be three–body electron attachment and photodetachment, respectively. The study concluded that in the lower ionosphere, induced by cosmic ray ionization, the ratio of anion to cation density is only of the order of 10^{-4} and anion chemistry was supposed to be unimportant. The parametric model of *Molina-Cuberos et al.* [2000] studied the abundance of electrophilic species in Titan and calculated the densities of negative ions and electrons. They showed that when the fractional abundance of electrophillic species becomes $\sim 10^{-11}$, the density of negative ions become significantly high at lower altitudes (<40 km) and could be even more than electron density, thus affecting the electrical properties of the lower atmosphere. *Borucki et al.* [2006] studied the charging of aerosol in the lower atmosphere and considered the influence of negative ions. The formation of negatively charged polycyclic aromatic hydrocarbons (PAH^-) through collisional charging with anions and their loss through photodetachment was investigated. All these lower atmosphere models considered the formation of negatively charged particles either through three–body electron attachment or through the collisional charging of aerosols. The presence of anions in the upper atmosphere was ignored as the former process is inefficient in this region and aerosols were not expected to be present at >500 km.

The photochemical models of *Vuitton et al.* [2009] and *Dobrijevic et al.* [2016] are the only models to date that have studied the negative ion chemistry in Titan's ionosphere. Based on their electron affinity and gas phase acidity, *Vuitton et al.* [2009] chose eleven

anions, CN^-, C_3N^-, C_5N^-, C_4H^-, C_6H^-, C_2H^-, CH_3^-, CH_2^-, H^-, OH^-, and O^-, as the possible candidates. The production processes considered were Radiative Electron Attachment (REA), DEA, and ion–pair formation and the loss processes include photodetachment, ion–ion recombination, and ion–neutral associative detachment. The density profiles were calculated for the altitude range 700-1400 km. They attributed the two major peaks observed by CAPS/ELS at m/q = 22±4 and 44±8 to CN^- and C_3N^-, respectively. The peak densities obtained for these ions were 1 cm^{-3} for CN^- and 0.1 cm^{-3} for C_3N^-. As per their calculations, the third most abundant anion should be C_5N^- (m/q = 82±14). The hydrocarbon anions C_4H and C_6H were also found to be contributing significantly to the total anion densities at lower altitudes. There was only negligible contribution from all other anionic species. They identified the DEA and associative detachment with the radicals H and CH_3, as the most important production and loss process of anions.

Dobrijevic et al. [2016], using a one dimensional coupled ion-neutral model, calculated the density profiles of positive ions, negative ions, and neutral species for Titan's atmosphere and studied how the uncertainties in the reaction rate coefficients influence the model results. They updated the DEA cross sections used by *Vuitton et al.* [2009] and calculated the densities of the negative ions CN^-, C_3N^-, H^-, C_2H^-, C_3^-, and C_4H^-. For each of the calculated species, they studied the propagation of uncertainty on chemical rate constants and performed multiple Monte-Carlo runs to obtain a statistical set of mole fraction profiles as a function of altitude. For every calculated anion density profile, they presented a global mean number density profile obtained using the unperturbed rate constants as well as the intervals containing 50% and 90% of the density profiles. The anions, viz. C_5N^-, C_6H^-, CH_3^-, CH_2^-, OH^-, and O^-, were not considered in the study of *Dobrijevic et al.* [2016], the reason which they attribute either to the low abundance of the corresponding neutral species from which these anions are produced or the very low rate constant involved. The updated cross sections largely changed the chemistry scheme through which the anions get produced/removed from Titan's ionosphere. As per their model, the most abundantly produced anion in Titan's ionosphere is H^- which forms through the DEA of CH_4. These hydride anions then quickly get converted to CN^- and C_2H^-. However, the calculations of *Dobrijevic et al.* [2016] also showed that the two most abundant anions in Titan's ionosphere are CN^- and C_3N^-, which agrees with the model results of *Vuitton et al.* [2009].

1.5 Motivation for this study

As indicated in section 1.4.1, a number of models have been developed to study the ion-neutral chemistry on the dayside of Titan′s ionosphere. But none of them was able to reproduce the observed electron density. At the peak, the modelled electron density is about a factor of 2 to 3 larger than the Cassini measurements. The possible reasons

for this discrepancy are investigated in the current thesis. Literature survey suggests that there are inconsistencies in various input parameters that could affect the model computed plasma density which have not been addressed so far. A detailed assessment of model parameters, such as solar flux, neutral atmosphere, reaction rate coefficients, etc, affecting the production and loss of ions and electrons is the main objective of this study. This is very important in understanding the ion chemistry and the controlling parameters of plasma density in the ionosphere of Titan. Some of the recent studies [*Sagnières et al.*, 2015; *Vigren et al.*, 2016] showed that there is an overestimation in the modelled photoelectron flux and N_2^+ ion production rates and this could be the reason for the disagreement between observations and model results. This issue is also addressed in the current study. In addition to the positive ion chemistry, we have also modelled the chemistry of negative ions. Most of the existing models dealt only with positive ion chemistry and anion chemistry was not addressed. Anions, recently discovered by the Cassini mission, are important in Titan's ionosphere as they can initiate further molecular growth through chemical and physical processes leading to the formation of complex organics as suggested by recent studies. There have only been two models [*Vuitton et al.*, 2009; *Dobrijevic et al.*, 2016] which discussed the chemistry of negative ions in the upper atmosphere. There have been updates on reaction rate coefficients and dissociative electron attachment cross sections after the model of *Vuitton et al.* [2009]. Even though *Dobrijevic et al.* [2016] have used these updated coefficients and cross sections in their model, they limited their discussion to a few selected anions. Hence a study which explores the complete anion chemistry scheme using the updated parameters is required. We model the chemistry of all the negative ions proposed by *Vuitton et al.* [2009] in the ionospheric region using state-of-the-art cross sections and rate coefficients to understand what changes the updated parameters could cause to the existing modelled anion profiles. A recent study by *Desai et al.* [2017] reported for the first time the profiles of negative ions derived from CAPS-ELS observations during dayside flybys. This gives the opportunity to validate the model results by comparing with observations which has not been done before.

Methane gas is an important constituent in the atmosphere of Titan and other outer solar system atmospheres. The electron–methane interactions in these atmospheres influences many upper atmospheric phenomena including the ionospheric chemistry. The photochemistry of Titan's atmosphere is largely controlled by the photoionization and photodissociation products of methane even though methane constitutes only about 3-4% of the atmosphere. Hence it is essential to understand the electron-methane interaction. We begin with an energy deposition model using Monte Carlo technique to understand how the electron energy is distributed among various loss channel like ionization, dissociation, excitation, etc, while making collisions with the methane molecules. The output of the simulation is a distribution function called yield spectrum which

embodies information about the degradation process and can be used for studying the aeronomical processes in planetary atmospheres. Yield spectrum is then used to calculate photoelectron flux in Titan's ionosphere to investigate their interaction with atmospheric neutrals leading to further photochemistry in Titan.

1.6 Photochemical model for the dayside ionosphere

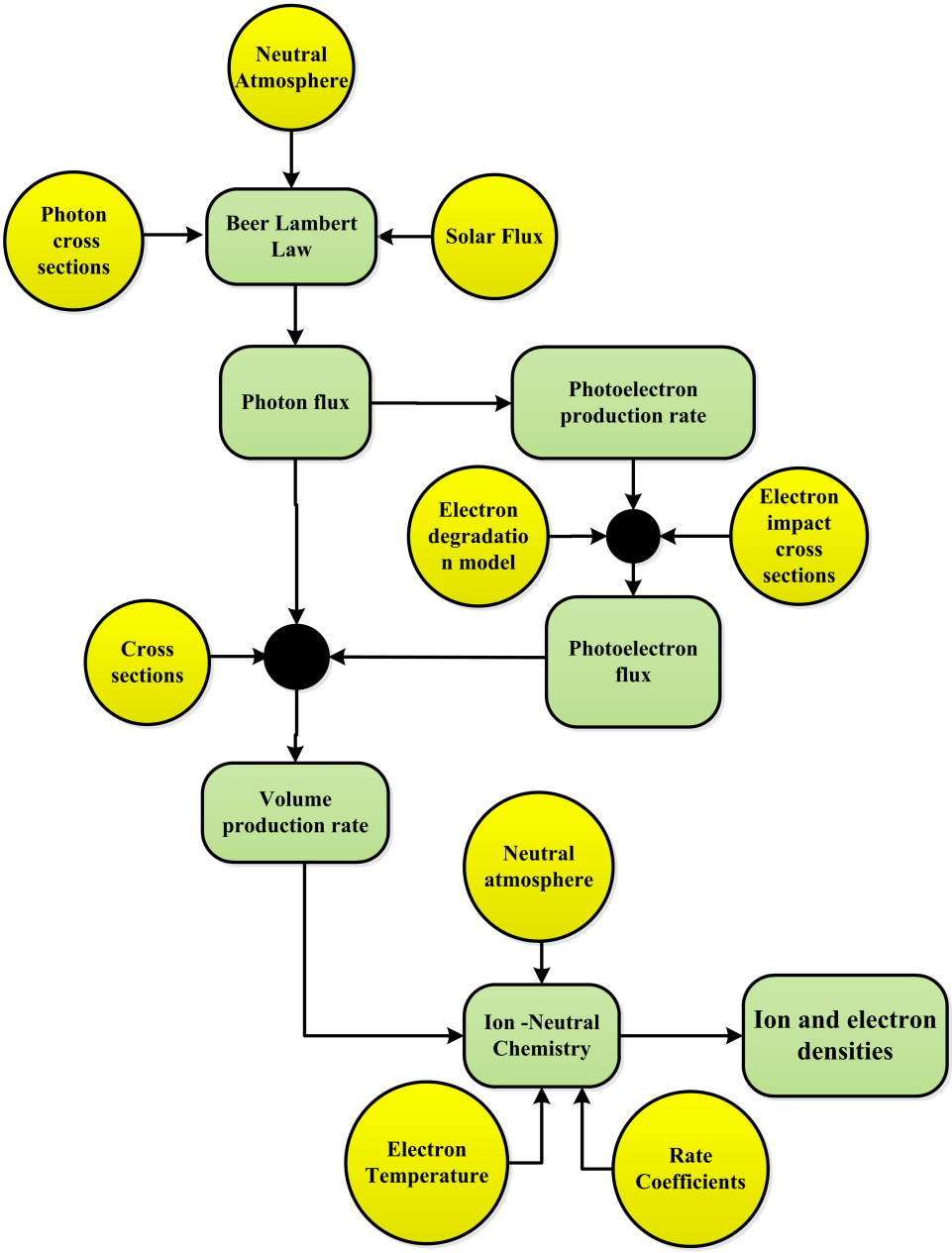

Figure 1.7: Photochemical model for calculating the plasma densities.

Figure 1.7 shows the general structure of the photochemical model that has been developed for studying the chemistry on the dayside ionosphere of Titan. The major sources of ionization on the dayside are photons and photoelectrons. Hence, it is essential to know how much photon flux and photoelectron flux is available at each

altitude to ionize the neutrals. The photon flux is calculated using Beer-Lambert law which describes the attenuation of solar flux as it passes through the atmosphere. The inputs required are solar UV radiation reaching the top of the atmosphere, the density profiles of the major neutral constituents N_2 and CH_4, and their photoabsorption cross sections. Calculated photon flux is subsequently used to obtain the ionization rate or the photoelectron production rate. Photoionization cross sections is an essential input for the calculation. Once photoelectrons are generated in the atmosphere, they immediately start colliding with the background gases and degrade their energy. To calculate the final steady-state photoelectron flux, it is important to know how the primary photoelectrons will degrade their energy. Among the various available techniques for studying the electron energy degradation in an atmosphere, the current study makes use of the Analytical Yield Spectra (AYS) approach which is obtained as the output of a Monte Carlo simulation model for electron energy degradation in gases. Using AYS, the steady-state photoelectron flux is calculated. The volume production rate of the major primary ions due to photon and photoelectron impact is determined. This is used as input to the model which includes the ion-neutral chemistry. The production and destruction reactions of various ions are taken in the model to calculate the number density profiles of different ionic species and electrons.

1.7 Thesis Structure

In this thesis, a one-dimensional photochemical model is developed for studying the ion-neutral chemistry on the dayside ionophere of Titan. The model calculates the density profiles of the major positive, negative ions and free thermal electrons. The model results are then compared with the observations. The organisation of thesis is as follows:

- **Chapter 2 - Electron energy degradation model in gases using Monte Carlo method: Application to xenon.** This chapter introduces the electron degradation models in gases. A review of available techniques for studying electron energy degradation in planetary atmospheres is presented. The Monte Carlo method used in the present study is discussed in detail. An energy deposition model is presented for studying degradation of electrons with energy $\leq$10 keV in the atomic gas xenon. Electron-xenon interactions find practical applications in several areas such as gas lasers, gamma ray detectors, gas counters, ion-thrusters, etc. A thorough review of the electron impact cross sections for e-Xe collisions, which forms the primary input to the energy deposition model along with the information on the selection of cross sections for model calculations, is presented in detail. The output of the simulation is the numerical yield spectrum which is a basic distribution function that contain information regarding the degradation

process and can be used to calculate the yield of any excited or ionized states. The numerical yield spectra are then fitted analytically, thus generating analytical yield spectra (AYS). Using yield spectrum, mean energy per ion pair and efficiencies of the ionization and excitation processes are calculated. The model results are compared with the values available in literature to validate the calculations. The AYS derived using the Monte Carlo model can be used to calculate steady-state electron flux in those mediums where e-Xe interactions take place as well as to calculate excitation rates or emission intensities.

- **Chapter 3 - Monte Carlo model for electron energy degradation in methane gas.** The chapter deals with the Monte Carlo model for electron energy deposition in a molecular gas methane, a gas which plays a crucial role in the photochemistry of Titan' atmosphere. The molecular targets add more intricacies to electron degradation process by introducing additional energy loss channels such as neutral dissociation, dissociative electron attachment, dissociative ionization, dissociative excitation etc. For modelling Titan's photochemistry, it is essential to understand how the electron will distribute its energy among these various loss channels while making collisions with the methane molecule. The electron impact cross sections for e-CH_4 collisions are used as input to the model. The numerical yield spectrum is analytically fitted, thus generating AYS. Mean energy per ion pair and efficiencies are calculated. The AYS presented in this chapter is used to calculate steady-state photoelectron fluxes in the atmosphere of Titan and is presented in the subsequent chapter.

- **Chapter 4 - Photochemical model for the ionosphere of Titan: Modelling the chemistry of Titan′s ionosphere.** A one-dimensional photochemical model for steady-state photochemical equilibrium condition is developed for the dayside ionosphere of Titan. An energy deposition model is developed which describes the absorption of solar UV radiation using Beer Lambert law. The initial inputs to the model are solar UV radiation reaching the top of the atmosphere, the altitudinal distribution of the neutral constituents and the photoabsoption cross sections. The attenuated solar flux, thus obtained is used for calculating photoelectron production rate, which is subsequently used in the calculation of steady-state photoelectron flux by employing the analytical yield spectrum approach. The ion production rates due to photon and photoelectron impact are calculated and are used as input to the model which includes ion-neutral chemistry. The production and destruction reactions of various ions are taken in the model to calculate the number density profiles of different ionic species and electrons. The model calculations are compared with Cassini observations. The possible reasons for the disagreement between modelled and observed plasma densities are explored by

performing an extensive analysis of model input parameters. Model calculations suggest that a more significant role is played by the plasma loss processes, rather than the production processes, in causing the disagreement.

- **Chapter 5 - Chemistry of negative ions in the ionosphere of Titan.** This chapter presents the chemistry of negative ions in the upper atmosphere region of Titan. The photochemical model presented in the previous chapter is extended by including the reactions of anions. Negative ion density profiles are computed using the most recent cross sections for dissociative electron attachment process and rate coefficients of ion-neutral reactions of anions. These are compared with the modelled profiles available in literature to understand the impact of the updated parameters on model calculations. Updated profiles obtained using the current model are also compared with the relative densities of anions which are reported recently based on observations. The model results are found to be consistent with the observations, based on which the current study could suggest the possible anions which could produce the observed relative density profiles.

A summary of the thesis and the future scope of the work is presented in Chapter 6.

Chapter 2

Electron energy degradation model in gases using Monte Carlo method: Application to xenon

2.1 Introduction

The collision of an electron with a neutral (atom or molecule) can be elastic or inelastic in nature. Although the elastic collision changes the direction, it does not change the energy of the electron. In the inelastic collision, some energy of the incident electron is used to ionize or excite the target neutral. When the target is a molecule, additional energy loss processes, such as dissociation and attachment, are also possible. If the remaining energy of the electron is sufficient to make further inelastic collisions, it will keep on colliding with the background gases until its energy is completely degraded. This process is referred to as electron energy degradation. Such processes are of great importance in understanding phenomena such as electron beam propagation in the atmosphere, population inversion process in a large group of gas lasers, optical emissions occurring in the upper atmosphere like aurora and airglow, etc [*Trajmar et al.*, 2006; *Sorokin*, 1986; *Campbell and Brunger*, 2009; *Bhardwaj and Gladstone*, 2000].

The photoelectrons generated in planetary atmospheres degrade their energy by colliding with neutral constituents of the atmosphere. Different techniques have been used to study the problem of electron energy degradation in atmospheres, viz. diffusion transport method, two-stream method, the multi-stream method, solution of Boltzmann transport equation, Fokker-Planck diffusion equation, continuous slowing down approximation, and discrete energy bin method.

The method by *Nisbet* [1968] and *Swartz* [1972], called diffusion transport method, used the concept of diffusion theory and solved a set of continuity equations for calculating flux of photoelectrons. This method required the calculation of diffusion coefficient for electrons passing through the atmospheric gases and needs information of the photoelectron pitch angle distribution and the details of collisional scattering. The two-

stream method used by *Banks and Nagy* [1970] assumed that the movement of electrons can occur only in two directions; either parallel or antiparallel to the geomagnetic field lines. In this case, the transport equation yields only an upward or downward flux. This method has been used widely for calculating the photoelectron fluxes in different planetary ionospheres, like Titan [*Gan et al.*, 1992], Venus [*Chen and Nagy*, 1978], Jupiter [*Waite et al.*, 1983] etc, and also in cometary ionospheres [*Korosmezey et al.*, 1987]. In reality, electrons can get scattered over a wide range of angles in the atmosphere. The multi-stream method used by *Oran and Strickland* [1978] took into account the fact that electrons can get scattered in any direction. The transport equations were solved for a pre-selected number of directions to represent anisotropic scattering and transport of electrons.

For studying the thermalisation of low energy electrons and their transport, *Mantas and Bowhill* [1975] used a method based on Boltzmann equations. Photoelectron flux was calculated by considering different processes, viz. transport, secondary electron production, energy degradation caused by the excitation of the neutrals to higher energy states and also the energy transfer to the ambient electron gas. Interaction of auroral electron with the atmosphere was studied by *Walt et al.* [1969] using the Fokker-Planck diffusion equation. They described electron energy degradation, their angular scattering through collisions and also the influence of Earth's magnetic field upon the pitch angle distribution. The method of *Walt et al.* [1969] had the drawback that the electron energy loss process was treated as a continuous phenomenon which is an erroneous concept at energies less than 500 eV. At these low energies, the discrete nature of energy loss process become important. The continuous nature of energy loss process at high energies was used in the method called Continuous Slowing Down Approximation (CSDA) used by *Green and Barth* [1965, 1967] and *Stolarski and Green* [1967]. The electron energy is degraded continuously from incident to cut-off with the assumption that the only significant loss processes are the excitation and ionization of the target particle. Even though this method could give reliable results on the population of excited states [*Heaps and Green*, 1974], it has got the disadvantage of ignoring the discrete nature of energy loss process which becomes very relevant at low energies. *Banks et al.* [1974] used a modified approach in which the energy loss at high energies (>500 eV) was treated as a continuous process and studied using Fokker-Planck method of *Walt et al.* [1969]. At low energies (<500 eV) the discrete energy loss technique of *Banks and Nagy* [1970] and *Nagy and Banks* [1970] was used.

Peterson [1969] introduced a method which takes into account the discrete nature of energy loss in each collision. In this method, the energy range from the incident energy to the lowest value is divided in to a number of equally spaced bins. The initial energy of the electron will be fractionally redistributed into lower energy bins as controlled by various cross sections. The topmost bin will be emptied once the energy of all the

electrons in the bin is redistributed to lower energy bins. This process continues until all bins of interest are empty. This technique has been used for electron energy degradation studies in H_2 [*Cravens et al.*, 1975] and in N_2 [*Fox and Victor*, 1988].

2.2 Monte Carlo Method

Simulation models can be classified into two; deterministic models and stochastic models. Deterministic models are mathematical models in which outputs are precisely determined. For such models, a unique input leads to a unique output. For stochastic models, a unique input can lead to a different output for each model run which occur due to the random nature of the modelled process. For such processes, a single simulation gives only one possible result. Multiple trial runs have to be performed to estimate the probability distribution of possible outcomes. Monte Carlo method is a statistical method used to approximate the probability of outcomes of a stochastic process.

To appreciate the applicability of this simulation technique for studying the problem of electron energy degradation and thus to calculate photoelectron flux in the atmosphere, consider the interaction of an electron with neutrals. It may collide elastically with the target or it may suffer inelastic collisions. Inelastic collisions can result in different possibilities, viz. ionization or excitation. In case of molecular targets, there exist additional channels, viz. dissociation, dissociative ionization, and electron attachment. The electron-neutral collision will continue until the energy of the electron is completely degraded. During each collision, the electron can perform any of the above mentioned processes. Another electron of same energy and initial conditions may follow a different sequence of processes. This kind of random process can be simulated numerically by calculating the probabilities of various possible occurrences for an electron. The sum of these probabilities will be unity. In order to reach a decision on which process has happened after each collision, Monte Carlo method uses random numbers distributed uniformly on the interval (0, 1) of real numbers. The decision is reached by comparing the probabilities with the random number. After each collision, new energy and direction is assigned to the electron. This sampling process is repeated until the collision process is terminated by some condition. Each new electron is treated similarly. A large number of such trials produces a frequency distribution for different processes from which their probability distributions can be derived. Probabilities can be calculated for different directions of scattering as well. Such probability distributions can finally give information on how the electron will degrade its energy while making collisions with the background gases. Even though time consuming, at some levels Monte Carlo simulation is found to be the most realistic simulation possible for studying electron energy deposition [*Solomon*, 2001]. The energy loss process of electrons is actually discrete in nature and this nature is exactly captured in the Monte Carlo model. As the method makes use of probabilistic decision making techniques, the accuracy of the

result largely depends on the number of simulations carried out.

Monte Carlo method was used to calculate the photoelectron flux in Earth's atmosphere by *Cicerone and Bowhill* [1970, 1971] and in cometary atmosphere by *Ashihara* [1978]. The study of energy deposition of auroral electrons in Earth's upper atmosphere by *Solomon* [1993] also employed the same method. A Monte Carlo model was constructed by *Singhal and Bhardwaj* [1991] for studying how the photoelectrons get energised under the influence of an electric field and subsequently used the results for studying the electroglow emissions from Uranus. Using the same method *Bhardwaj and Singhal* [1993] described the energization and energy degradation of low energy protons in an H_2 atmosphere in the presence of parallel electric field for studying the optically thin H Lyman alpha production on the outer planets. The method has also been used for sputtering studies [*Pospieszalska and Johnson*, 1996; *Johnson et al.*, 2000] as well as for the energy deposition of ring current [*Noël*, 1997]. The model of *Shematovich et al.* [2008] which studied the dayglow emissions in Martian atmosphere used Monte Carlo technique to study electron transport. The energy deposition model for solar energetic particle precipitating into the atmosphere of Mars by *Jolitz et al.* [2017] and the aeronomic model for the upper atmosphere of Jupiter by *Ionov et al.* [2017] also employed Monte Carlo technique.

Green and coworkers extensively used Monte Carlo method for studying the problem of electron energy degradation in various gases [*Jackman and Green*, 1979; *Green and Singhal*, 1979; *Singhal et al.*, 1980; *Singhal and Green*, 1981; *Singhal et al.*, 1983; *Green et al.*, 1985]. They introduced the concept of yield spectrum which is a basic distribution function that contain information regarding the degradation process and can be used to calculate the yield of any ionized or excited states [*Green et al.*, 1977a, b]. The analytical representation of numerical yield spectra is referred to as Analytical Yield Spectra (AYS). As AYS accurately represents numerical yield, the use of AYS reduces the computational time drastically as compared to the generation of numerical yield spectrum using Monte Carlo model. *Green et al.* [1977a] developed AYS for the gases Ar, H_2, H_2O, O_2, N_2, CO, CO_2 and He. Further studies of *Jackman and Green* [1979]; *Green and Singhal* [1979]; *Singhal et al.* [1980]; *Singhal and Green* [1981]; *Singhal and Bhardwaj* [1991]; *Bhardwaj and Singhal* [1993]; *Bhardwaj and Michael* [1999]; *Bhardwaj and Jain* [2009]; *Bhardwaj and Mukundan* [2015]; *Mukundan and Bhardwaj* [2016], etc. extended this approach to other gases. The AYS has been extensively used in the calculation of photoelectron fluxes, auroral electron fluxes and volume excitation/emission rates in various atmospheres [*Haider and Singhal*, 1983; *Singhal and Haider*, 1984; *Singhal and Haider*, 1986; *Bhardwaj and Singhal*, 1990; *Bhardwaj and Michael*, 1999; *Bhardwaj and Jain*, 2009; *Bhardwaj and Raghuram*, 2011, 2012].

A detailed description of the Monte Carlo model for electron energy degradation in atomic gases is presented in the next section.

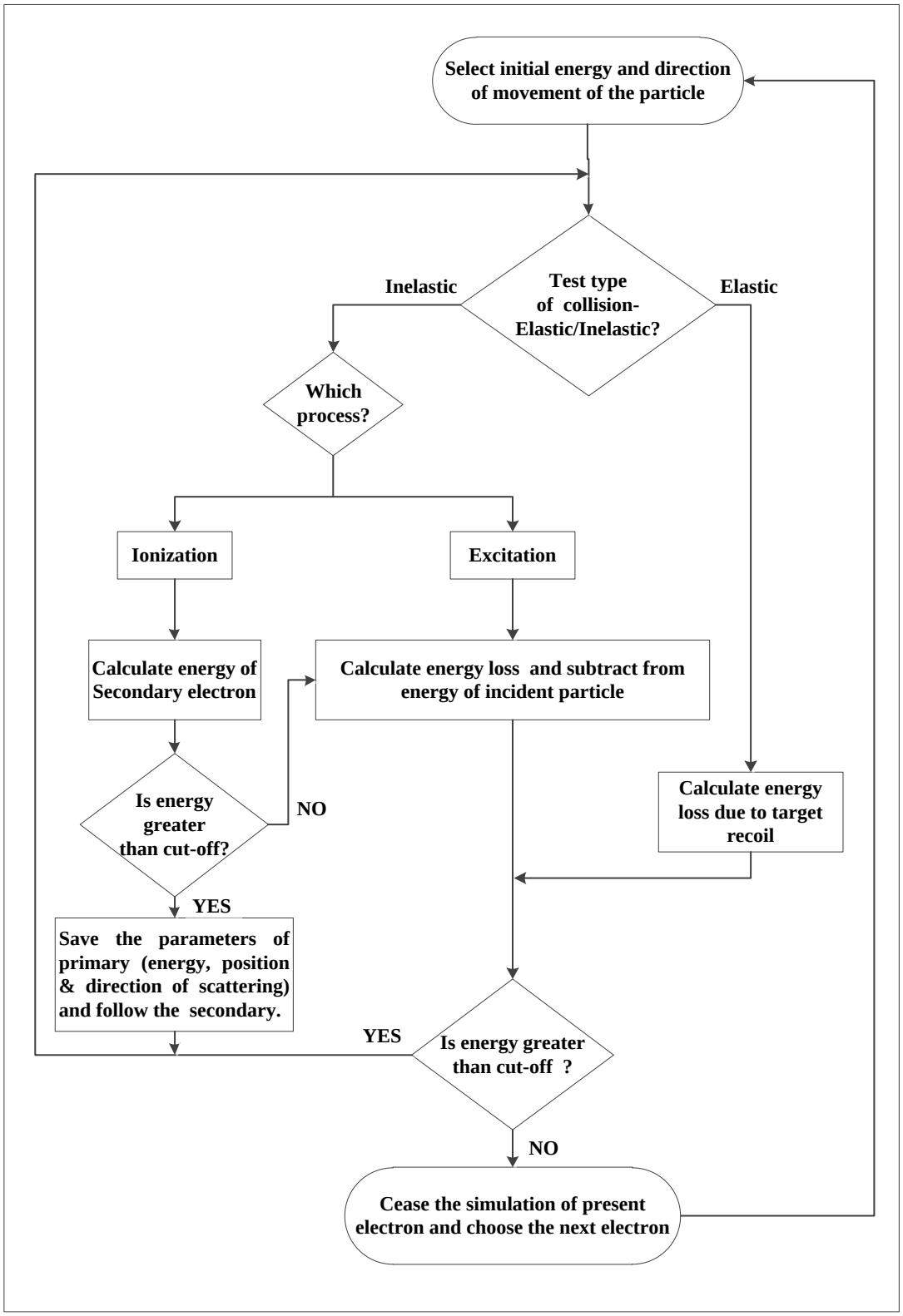

Figure 2.1: Flowchart showing Monte Carlo simulation for the electron degradation in atomic gas. It shows flow only up to secondary electrons; subsequent electrons (tertiary, quaternary, etc.) are also followed in the similar manner in the simulation.

2.3 Electron energy degradation model using Monte Carlo method

In the Monte Carlo simulation, the energy loss process of the electron is treated in a discrete manner. For carrying out the degradation by means of discrete steps, the electron is followed as it undergoes successive collisions. To accomplish the energy degradation in a convenient way, the energy range from the incident energy to cut off energy is divided into a number of bins. Whenever an electron makes an inelastic collision, the collision event is recorded in the corresponding energy bin. This process is continued and the particle, its secondary, tertiary, etc. are followed until the energy falls below an assigned cut off value. In the present simulation, the energy bin size is taken as 1 eV throughout the energy range. The cutoff energy is set as equal to the minimum energy required by the electron to make an inelastic collision with the target gas. In other words, it is the lowest threshold of all the inelastic processes.

Figure 2.1 shows the flow diagram of Monte Carlo simulation for the electron degradation. The simulation starts by fixing the energy of the incident electron. The direction of movement of electron (θ, ϕ) is assumed to be isotropic and is decided using the random numbers R_1 and R_2 as

$$\theta = \cos^{-1}(1 - 2R_1), \tag{2.1}$$

$$\phi = 2\pi R_2 \tag{2.2}$$

The distance that the electron has to travel before the collision is calculated as

$$S = -\log(1 - R_3)/N\sigma_T, \tag{2.3}$$

where R_3 is another random number, N is the number density of the gas (equal to 10^{10} cm^{-3}) and σ_T is the total scattering cross section (elastic + inelastic). Next, decision has to be made on the type of collision. The probabilities of the elastic and inelastic events, P_{el} (σ_{el}/σ_T) and P_{in} (σ_{in}/σ_T), where σ_{el} and σ_{in} are the elastic and inelastic cross sections, are calculated and compared with a new random number R_4. Elastic collision occurs if $P_{el} \geq R_4$. The energy loss in elastic collisions ΔE due to target recoil is calculated as

$$\triangle E = \frac{m^2v^2}{m+M} - \frac{m^2vV_1\cos\delta}{m+M}, \tag{2.4}$$

where

$$V_1 = v\left[\frac{m\cos\delta}{m+M} + \frac{[M^2 + m^2(\cos\delta - 1)]^{1/2}}{m+M}\right].$$

Here δ is the scattering angle in the laboratory frame, v and m are, respectively, the velocity and mass of the incident electron, and M is the mass of the target particle. The scattering angle δ is determined by using differential elastic cross sections which are fed

numerically into the model. The energy lost in the collision is then subtracted from the incident electron energy. After the collision, the deflection angle relative to the direction (θ,ϕ) is obtained by

$$\begin{aligned}
\cos\theta'' &= \cos\theta\cos\theta' - \sin\theta\sin\theta'\cos\phi', \\
\cos\phi'' &= (\cos\theta\cos\phi\sin\theta'\sin\phi' - \sin\phi\sin\theta'\sin\phi' + \sin\theta\cos\phi\cos\theta')/\sin\theta'', \\
\sin\phi'' &= (\cos\theta\cos\phi\sin\theta'\cos\phi' - \cos\phi\sin\theta'\sin\phi' + \sin\theta\sin\phi\cos\theta')/\sin\theta''.
\end{aligned} \tag{2.5}$$

Here θ', ϕ' are the scattering angles.

If an inelastic collision occurs, the collision event is recorded in the appropriate energy bin corresponding to the energy of the particle. It is further decided whether it is an excitation or ionization event. In case of ionization event, the energy of secondary electron has to be calculated as it can also initiate further inelastic collisions, provided it has sufficient energy. The secondary electron energy is calculated as [*Green and Sawada*, 1972]:

$$T = \frac{\Gamma_S\ E_v}{E_v + \Gamma_B}[\tan(RK_1 + (R-1)K_2)] + T_S - \left[\frac{T_A}{E_v + T_B}\right], \tag{2.6}$$

where

$$K_1 = \tan^{-1}\left\{\left[\frac{(E_v - I)}{2} - T_S + \frac{T_A}{(E_v + T_B)}\right] \Big/ \frac{\Gamma_S\ E_v}{(E_v + \Gamma_B)}\right\},$$

$$K_2 = \tan^{-1}\left\{\left[T_S - \frac{T_A}{(E_v + T_B)}\right] \Big/ \frac{\Gamma_S\ E_v}{(E_v + \Gamma_B)}\right\}.$$

Here E_v is the incident electron energy; Γ_S, Γ_A, T_A, T_B, and T_S are the fitting parameters, R is a random number, and I is the ionization threshold. If this energy is greater than that of the cut off energy then the secondary electron has to be followed. In order to follow the secondary electron, the parameters of the primary electron, i.e. the energy remaining in the primary, its position and direction of movement are first saved in suitable variables. Secondary electron is then followed in the same method as the primary electron. Once the energy of the secondary is completely degraded, the saved parameters of the primary electron are retrieved and its degradation is continued. Similarly, tertiary, quaternary, etc., electrons are followed in the simulation.

For all inelastic collisions, the collision event is recorded in the corresponding energy bin so that the information on the total number of collisions that occur in each energy bin can be obtained, after the simulation is complete. This is used for calculating the yield spectrum. The number of secondary, tertiary, quaternary, etc., electrons produced during ionization events are also stored in the corresponding energy bins which is used to determine their energy distribution. The angle and direction of movement of electron after each ionization and excitation event are calculated using differential elastic cross sections as described in equation (2.5). After each inelastic collision, appropriate energy

is subtracted from the particle energy. If the remaining energy is higher than the cutoff energy, it is again followed in the simulation. The simulation is made for a monoenergetic beam of 10^6 electrons; each and every electron is followed in a collision-by-collision manner until its energy falls below the assigned cutoff value.

In the following section, the application of Monte Carlo model for electron energy degradation is depicted by studying the interaction of electron with the atomic gas xenon.

2.4 Monte Carlo model for electron degradation in xenon gas

Xenon (Xe) is a widely studied atom due to its inert nature and simple ground state atomic structure. The inert nature of xenon makes it possible to study the pristine environment of the early solar system whose traces have been removed by other reactive elements [*Verchovsky and Sephton*, 2005]. Noble gases are valuable probes of extraterrestrial environments. Their abundances as well as isotopic compositions are indicators of various processes such as stellar events prior to solar system formation and radioactive decay. Hence, their study is vital to understand the sequence of events that led to the formation and subsequent evolution of the solar system. There are various missions that studied xenon in planetary atmospheres. For example, Galileo mass spectrometer reported a relative abundance of 2.6±0.5 times solar ratios in Jovian atmosphere [*Mahaffy et al.*, 2000]. Pioneer Venus Sounder Probe Neutral Mass Spectrometer measured an upper limit for xenon in Venusian atmosphere as 120 ppb [*Donahue et al.*, 1981]. In Earth's atmosphere xenon is a trace gas, having a concentration of 87 ppb [*Fleagle and Businger*, 1980].

Electron collision with Xe has a wide range of application. In x-ray and gamma ray detectors, Xe gas counters have been commonly used. In both these detectors, interaction of radiation with Xe atoms results in the production of electrons. Among the various methods of amplifying the obtained skimp signal, a commonly used approach is electron acceleration in which the accelerated electrons excite the xenon atoms through inelastic collisions leading to the production of secondary scintillation, i.e. the emission of detectable light in the vacuum ultraviolet region [*Knoll*, 2000]. The same technique is used in flash lamps which produce high intensity white light for a short duration. The excited atoms, created by electron-atom collisions, can de-excite by emitting in different wavelengths whose combined effect will give the appearance of white light emission. Electron bombardment technique with xenon is also used in ion thrusters which is an evolving technology in the field of rocket propulsion. Here, electrically accelerated Xe ions, created using electron impact, are emitted at high speed as exhaust and this will push the spacecraft forward. Efficiency of this kind of ion thrusters are found to be

higher than that of conventional chemical propulsion methods and has been used in NASA's missions Deep Space-1 [*Rayman et al.*, 1999] and DAWN [*Rayman et al.*, 2006]. The utmost use of xenon gas for such purposes will be possible only through a thorough understanding of properties associated with microscopic collision processes.

The electron collision process in xenon was studied earlier by *Date et al.* [2003] using Monte Carlo method. *Rachinhas et al.* [1999] studied the absorption of electrons with energies $\leq$ 200 keV in xenon using Monte Carlo simulation technique. They calculated mean energy per ion pair (w-value) and Fano factor in the energy range 20-200 keV and studied the influence of electric field on the results. Absorption of x-ray photons and the drift of resulting electrons under the influence of an applied electric field in xenon was studied by *Dias et al.* [1993], by using Monte Carlo technique. A 3D Monte Carlo method was used by *Santos et al.* [1994] to study the drift of electrons in xenon and to calculate various physical properties such as electroluminescence, drift velocities, etc.

In the present study, a Monte Carlo model for the local degradation of electrons with energy in the range 9-10000 eV in neutral xenon gas is developed to understand how the energy of the incident electron will be distributed among various loss channels, like ionization and excitation while it is making collisions with neutral xenon atoms. To make an inelastic collision with a xenon atom, an electron should have a minimum energy of 8.315 eV as it is the lowest threshold of all the inelastic processes. The cutoff energy is set as 9 eV since the energy bin size in the model is 1 eV. Modelling the electron energy degradation primarily requires a set of electron impact excitation and ionization cross sections for the atom. These cross sections are essential for electron energy deposition schemes and are presented in detail in Section 2.5. Using the model, numerical yield spectra is generated which is fitted analytically to obtain AYS. This is discussed in Section 2.6.1. The obtained secondary electron energy distribution, the calculation of efficiency of excitation and ionization processes, and the calculated mean energy per ion pair are presented in Section 2.6 . The summary of the chapter is given in Section 2.7.

2.5 Cross Sections

Cross sections for elastic and various inelastic processes form the primary input to the energy deposition model. A thorough review of the electron impact cross sections for e-Xe collisions is presented in this section along with the information on the selection of cross sections for model calculations. The selected cross sections are fitted using simple analytical equations. It is these analytically fitted form of cross sections that are used as input to the Monte Carlo model. These analytical cross sections represent the actual measured/calculated cross sections at all energies and thus facilitate the use of cross sections as input to the model.

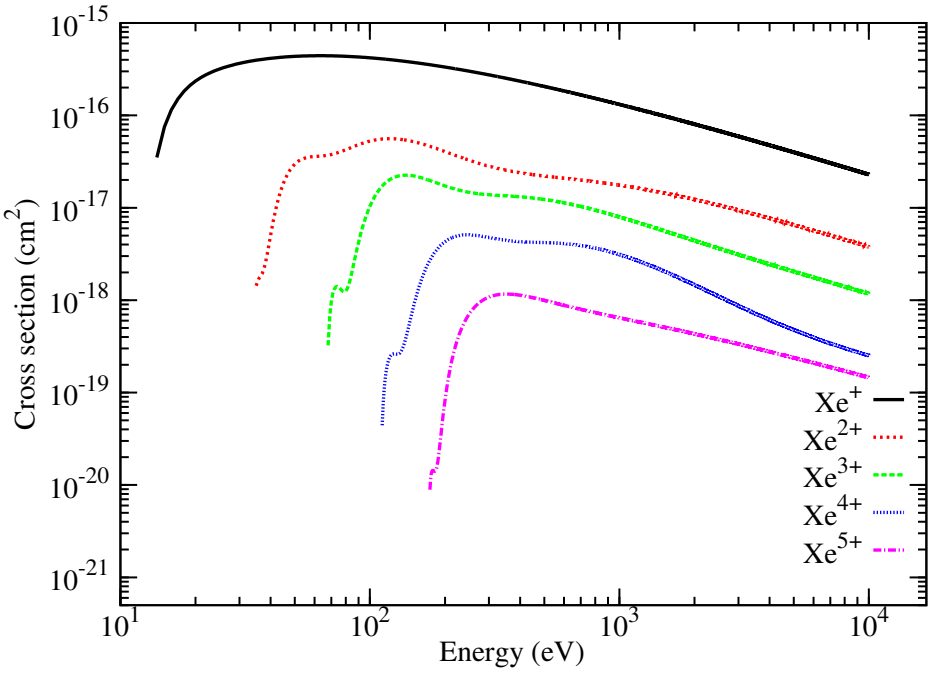

Figure 2.2: Electron impact ionization cross sections for Xe. Cross sections up to five ionization states are shown here.

2.5.1 Total Elastic cross sections

Total elastic scattering cross sections for Xe have been measured or calculated by many authors, like *Mayol and Salvat* [1997], *Gibson et al.* [1998], *Adibzadeh and Theodosiou* [2005], *Vinodkumar et al.* [2007] and *McEachran and Stauffer* [2014]. The present model used the analytically fitted theoretical cross sections of *McEachran and Stauffer* [2014] which are calculated using a relativistic optical potential method. These cross sections are in good agreement with the measured values of *Mayol and Salvat* [1997] and also with the theoretical values of *Adibzadeh and Theodosiou* [2005] and *Vinodkumar et al.* [2007] in the energy range 50-1000 eV. However, at energies between 15 eV and 50 eV, the cross sections of *Vinodkumar et al.* [2007] are lower with a maximum deviation of 50% at 30 eV. Calculations by *McEachran and Stauffer* [2014] is higher than the cross sections of *Gibson et al.* [1998] and *Adibzadeh and Theodosiou* [2005] at 1-10 eV. The maximum deviation (25%) is found at 6 eV. In the current model, the analytical fit of *McEachran and Stauffer* [2014] is extended to 10 keV to calculate the cross section at higher energies, even though the authors have mentioned that the analytical fit is valid only up to 2.5 keV. This extension is valid as it agrees with the cross sections calculated by *Garcia et al.* [2002] for the energy 50 eV to 10 keV using a scattering potential method.

Table 2.1: Elastic differential cross section for xenon (in units of 10^{-16} cm^2 sr^{-1}) .

Energy	Angle (degree)									
(eV)	0	10	20	30	40	50	60	70	80	
5	23.40	17.40	12.00	7.52	4.49	3.00	2.72	2.97	3.06	
10	37.40	27.60	19.30	12.4	7.11	3.70	1.89	1.10	0.801	
100	43.40	11.10	1.28	0.237	0.694	0.434	0.0487	0.055	0.229	
500	61.00	8.66	1.29	0.446	0.170	0.106	0.106	0.0827	0.0318	
1000	70.70	5.71	0.78	0.249	0.125	0.0752	0.0455	0.0282	0.0236	
Energy	Angle (degree)									
(eV)	90	100	110	120	130	140	150	160	170	180
5	2.570	1.560	0.499	0.0024	0.663	2.55	5.35	8.31	10.6	11.4
10	0.643	0.503	0.414	0.473	0.773	1.29	1.99	2.70	3.23	3.43
100	0.238	0.120	0.077	0.116	0.0896	0.00531	0.106	0.558	1.15	1.42
500	0.006	0.042	0.100	0.111	0.0557	0.00815	0.0692	0.260	0.479	0.576
1000	0.0282	0.031	0.0233	0.00821	0.00247	0.0254	0.00832	0.161	0.229	0.255

2.5.2 Differential elastic cross sections

The direction in which electron is scattered after each collision is calculated using differential elastic scattering cross sections (DCS). For the present work, DCS of *Adibzadeh and Theodosiou* [2005] is used, in which values for the energy range 1-1000 eV are given for a finer energy grid (1 eV). These values are in good agreement with the DCS values of *McEachran and Stauffer* [1984] and *Sienkiewicz and Baylis* [1989]. For energies greater than 1000 eV, linearly extrapolated values of differential cross sections are used, as measurements are not available. DCS values at a few energies are shown in Table 2.1. These cross sections are not analytically fitted and are fed numerically into the model.

2.5.3 Ionization cross sections

Both single and multiple ionization cross sections of xenon have been measured by *Schram* [1966], *Nagy et al.* [1980], *Stephan and Märk* [1984], *Wetzel et al.* [1987], *Lebius et al.* [1989], *Krishnakumar and Srivastava* [1988], *Almeida* [2002], and *Rejoub et al.* [2002]. Up to 1000 eV, we have used the recent measurements of *Rejoub et al.* [2002] which are in good agreement with the work of *Rapp and Englander-Golden* [1965], *Schram* [1966], *Nagy et al.* [1980] and *Stephan and Märk* [1984]. At energies greater than 1000 eV, measurement of *Schram* [1966] has been used as it is the only available measurement at higher energies. These cross sections are fitted using empirical formula of *Krishnakumar and Srivastava* [1988];

$$\sigma_p(E) = \frac{1}{IE}[A\ ln\frac{E}{I} + \sum_{i=1}^{N} B_i(1 - \frac{I}{E})^i] \tag{2.7}$$

where A and B_i are fitting coefficients, I is the ionization threshold, E is the electron energy and i is the number of terms N required to fit the data. Fitting parameters had to be adjusted as the cross sections of *Krishnakumar and Srivastava* [1988] are higher than that measured by *Rejoub et al.* [2002] and *Schram* [1966] by about 20% at the maximum. The fitting parameters used in the present study are given in Table 2.2.

The current model considers only up to the fifth ionization state of xenon. Higher states have very low ionization cross sections and the total yield will remain more or less the same even if they are taken into account. Ionization cross sections used in the model are shown in Figure 2.2. These partial ionization cross sections are then used to calculate gross ionization cross section as

$$\sigma_{gross} = \sigma^+ + 2\sigma^{2+} + 3\sigma^{3+} + 4\sigma^{4+} + 5\sigma^{5+} \tag{2.8}$$

As xenon is a gas that is capable of multiple ionization, total ionization cross section will be the charge weighted sum of partial ionization cross sections [*Rapp and Englander-*

Golden, 1965]. It is this gross ionization cross section that is used in the model.

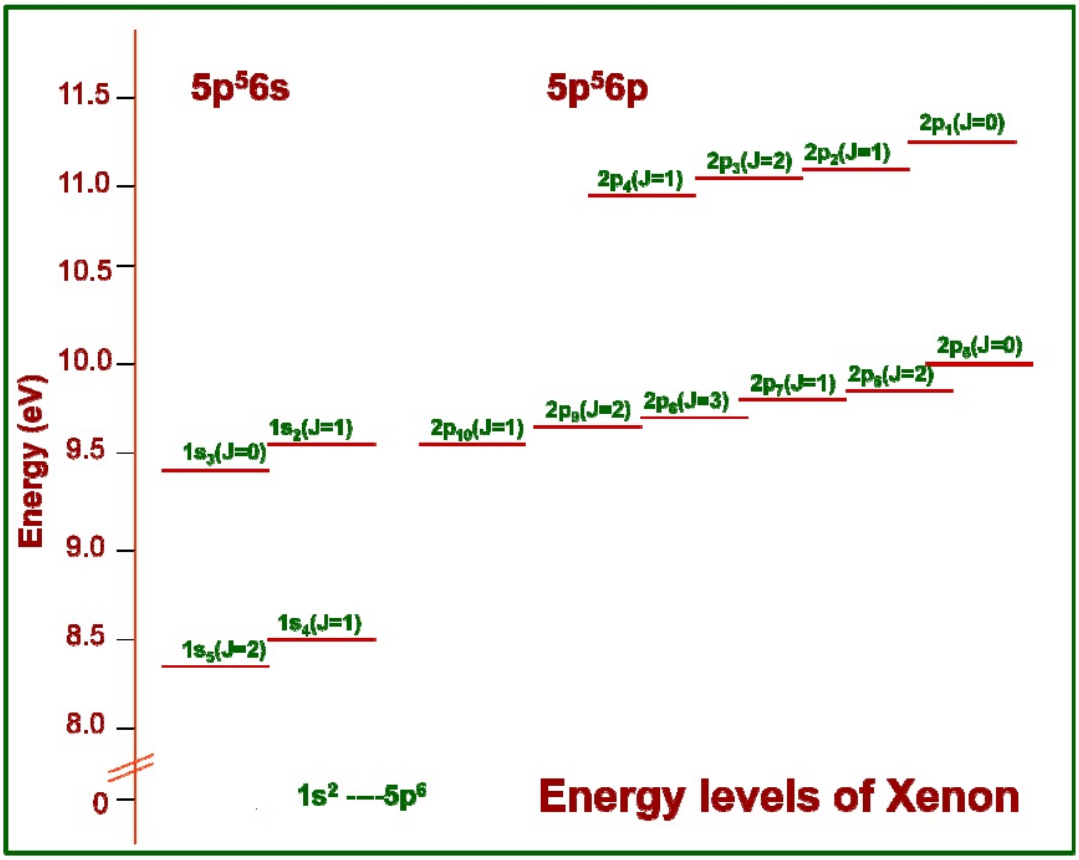

Figure 2.3: Energy level diagram of Xe for the excited states $5p^5 6s$ and $5p^5 6p$. Image taken from *Srivastava* [2007]

2.5.4 Excitation cross sections

Xenon (Z = 54) has a ground state configuration of $5p^6$. Electron impact excitation can result in configurations, like $5p^5 ns$, $5p^5 np$, $5p^5 nd$ etc. Each of these excited configurations will be composed of different levels which occur due to the coupling between the core angular momentum J_c and the angular momentum of the excited electron. For example, the $5p^5 6s$ configuration is composed of four levels which are represented as $1s_2$, $1s_3$, $1s_4$ and $1s_5$ (in the decreasing order of energy) in Paschen notation with J values 1, 0, 1 and 2, respectively (see Figure 2.3). Excitation cross sections for the various excitation levels of Xe are available in the literature. However, individual cross sections of various levels in each configuration have not been calculated.

Table 2.2: Fitting parameters for ionization cross sections of xenon. Notation 1E5 means 1×10^5

	I (eV)	A	B_1	B_2	B_3	B_4	B_5	B_6	B_7	B_8
Xe^+	12.12	5.1810E5	-5.5272E5	4.3084E5	-1.0138E6	4.3057E5	-	-	-	-
Xe^{2+}	33	2.0E5	-1.9897E5	1.4518E6	-2.8675E7	2.1198E8	-7.046E8	1.1679E9	-9.4364E8	2.9592E8
Xe^{3+}	65	2.2868E5	-3.2675E5	5.4044E6	-5.7805E7	2.5296E8	-4.9809E8	4.4934E8	-1.5128E8	-
Xe^{4+}	110	1.8596E5	-1.6909E5	8.7999E5	-1.2579E7	5.1109E7	-4.9230E7	-7.8086E7	1.6624E8	-7.8863E7
Xe^{5+}	172	7.1585E4	-4.8096E4	6.5617E6	6.5617E6	-1.5531E7	1.4689E7	-4.9586E6	-	-

Cross sections for the excitation into $5p^5 7p$ levels from the ground level as well as from the $5p^5 6s$ levels of xenon were measured by *Jung et al.* [2009]. *Sharma et al.* [2011] theoretically calculated the cross sections for the excitation into the $5p^5 7p$ levels. Excitation cross section from the ground state to the $5p^5 6s$ level was measured by *Fons and Lin* [1998]. *Puech and Mizzi* [1991] reported cross sections for the 13 excited levels of xenon where the excitation cross sections for the forbidden and allowed transitions were calculated separately. They made use of Born-Bethe approximation to calculate the cross sections at high incident electron energies and a low energy modifier to extend the calculations down to threshold energies. These semi-empirical expressions which are valid from threshold to relativistic energies are used in the current model. Excitation cross section for an allowed level is calculated as

$$\sigma_j = \frac{8\pi a_0^2 R^2}{mc^2\beta^2}\frac{F_{oj}}{W_j}[ln(\frac{\beta^2}{1-\beta^2}\frac{mc^2\beta^2}{2W_j}) - \beta^2] \tag{2.9}$$

where a_o is the Bohr radius, R the Rydberg constant, m the rest mass of electron and β is the velocity of incident electron in units of light velocity c. W_j is the excitation threshold of the j^{th} level and F_{oj} is the oscillator strength. For forbidden states, cross sections are calculated as

$$\sigma_j = \frac{8\pi a_0^2 R}{mc^2\beta^2}F_j \tag{2.10}$$

where F_j is a constant. To calculate cross sections at energies near threshold region, equations (2.9) and (2.10) have to be multiplied by a low energy modifier

$$B_j = \frac{[1-(\frac{2W_j}{mc^2\beta^2})^{a_j}]^{b_j}}{(mc^2\beta^2)^{c_j}} \tag{2.11}$$

where a_j, b_j and c_j are fitting parameters. Values of these parameters for the different excitation levels are shown in Table 2.3. Cross sections for various excitations are added together to obtain total excitation cross section.

2.5.5 Total cross sections

Total inelastic cross section is calculated by adding total excitation cross section and gross ionization cross section. These total inelastic cross sections and elastic cross sections are added up to obtain total scattering cross sections. Our calculated total scattering cross sections are in good agreement with values of *Kurokawa et al.* [2011], *Zecca et al.* [1991] and *Vinodkumar et al.* [2007]. Figure 2.4 shows various cross sections that are used in our model.

Table 2.3: Parameters to calculate excitation cross sections of Xe. For all levels, a_j = b_j=1

Level	W_j(eV)	$F_{oj}(F_j)$	c_j
$1s_5$	8.315	53.7	2.0
$1s_4$	8.437	0.26	0.0
$1s_3$	9.447	27.0	2.0
$1s_2$	9.570	0.19	0.0
$2p_{10}$	9.580	2.57	1.0
$2p_9 + 2p_8$	9.706	4.89	1.0
$2p_7 + 2p_6$	9.809	2.54	1.0
$3d_5$	9.917	0.01	0.0
$3d_6 + 2p_5 + 3d_4 + 3d_3 + 3d_4^{'} + 3d^{''} + 3d_1$	10.11	20.0	1.0
$3d_2$	10.40	0.395	0.0
$2s_5 + 2s_4$	10.59	0.097	0.0
$2p_4 + 2p_3 + 2p_2 + 2p_1$	11.0	5.0	1.0
$(3s\text{-}9s)_{allowed}$	11.7	0.689	0.0

2.6 Model Results

2.6.1 Yield Spectrum

Yield spectrum, U(E, E_0), for an incident electron energy E_0 and spectral energy E, is defined as the number of discrete energy loss events that happened in an energy interval E and E+ΔE.

$$U(E, E_0) = \frac{N(E)}{\triangle E}, \tag{2.12}$$

where N(E) is the number of inelastic collisions and $\triangle E$ is the energy bin width, which is 1 eV in the current model. The generation of numerical yield spectrum requires large computational time as each and every electron has to be followed including the secondaries, tertiaries, etc. For practical purposes, the analytically fitted form of numerical yield spectrum, called AYS, simplify the application by substantially reducing the computational time. The numerical yield spectrum, obtained as the output of the model, can be represented in an analytical form as [*Bhardwaj and Michael*, 1999]

$$U(E, E_0) = U_a(E, E_0)\ H(E_0 - E - E_m) + \delta(E_0 - E), \tag{2.13}$$

where H is the Heavyside function, E_m is the minimum threshold of the processes considered, and $\delta(E_0 - E)$ the Dirac delta function which accounts for the collision at

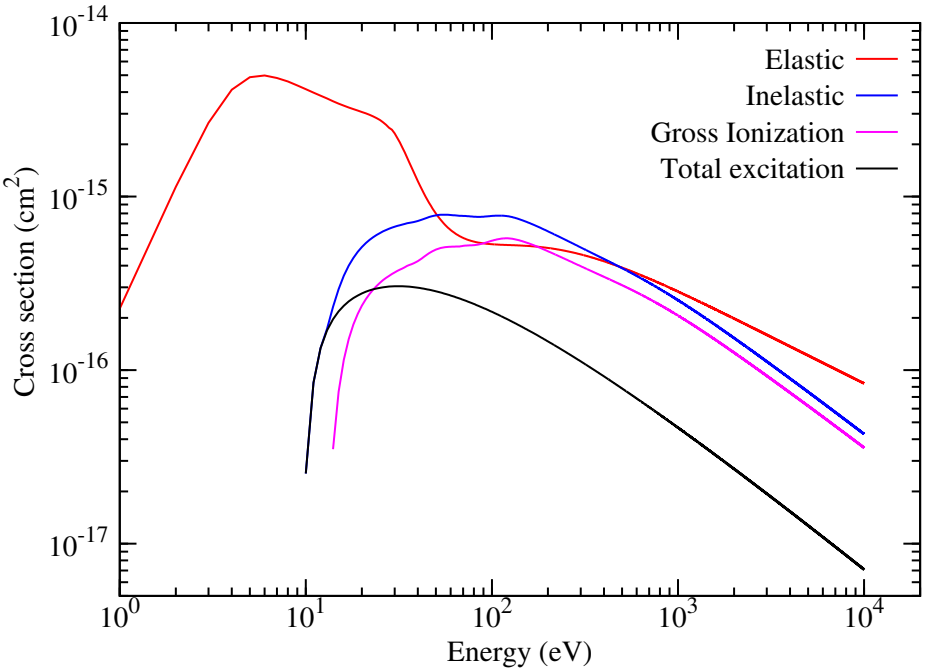

Figure 2.4: Electron impact cross sections for elastic and inelastic processes of Xe

source energy E_0. *Green et al.* [1977a] have given a simple analytical representation for $U_a(E, E_0)$ as

$$U_a(E, E_0) = A_1 \xi_0^s + A_2(\xi_0^{1-t}/\epsilon^{3/2+r}) \tag{2.14}$$

where $\xi = E_0/1000$ and $\epsilon = E/I$ (I is the lowest ionization threshold), and A_1, A_2, t, r, and s are fitting parameters. The fitting parameters for xenon gas obtained are $A_1 = 0.035$, $A_2 = 1.75$, $t = 0.0$, $r = -0.065$, and $s = -0.085$.

Figure 2.5 shows numerical yield spectrum as well as AYS for five different incident electron energies. Rapid oscillations seen in the yield spectrum at energies close to the incident electron energy are not taken into account in our analytical fit. These oscillations occur due to the fact that energy loss processes are discrete in nature. For an electron having incident energy E_0, an inelastic collision with threshold energy E_m will bring the energy down to a value of E_0 - E_m. No energy value in the region between E_0 and E_0 - E_m can be acquired by the electron. This is known as Lewis effect [*Douthat*, 1975]. The heavyside function in equation (2.13) accounts for the Lewis effect.

The yield spectrum can be used for calculating the population (J) of any state j, which is the number of inelastic events of type j caused by an electron while degrading its energy from E_0 to cut off as

$$J_j(E_0) = \int_{W_{th}}^{E_0} U(E, E_0)\, P_j(E)\, dE. \tag{2.15}$$

Here W_{th} is the threshold for the j^{th} process; $P_j(E)$ is the probability of the j^{th} process at energy E, which can be calculated as $P_j(E) = \sigma_j(E)/\sigma_{in}(E)$; $\sigma_{in}(E)$ is the total inelastic collision cross section at energy E. This is useful to determine various properties of the

gas, like mean energy per ion pair and efficiencies of different loss channels which are described in the following sections.

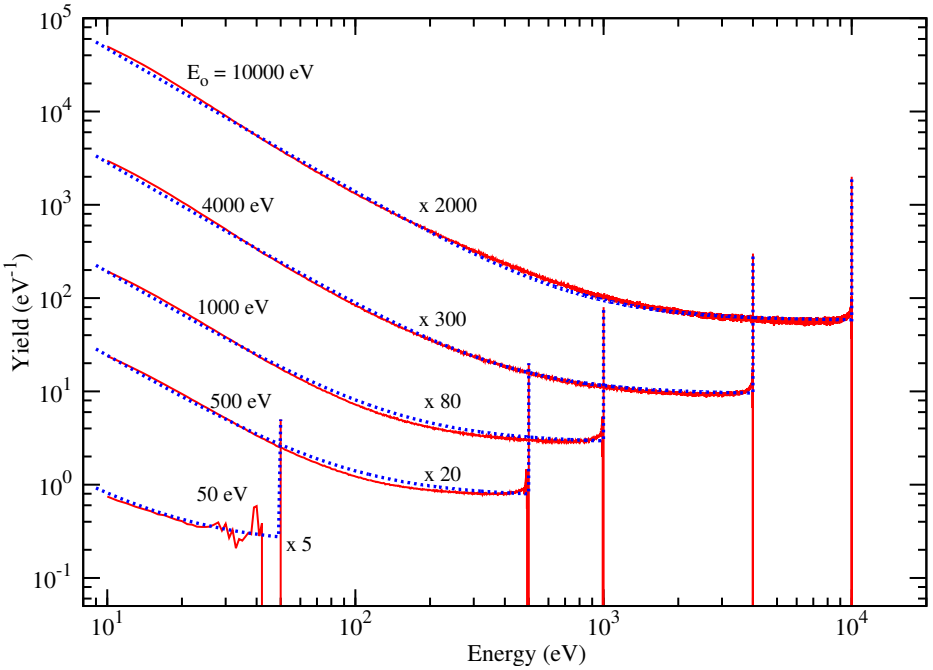

Figure 2.5: Yield spectra for different incident energies. Red curve shows numerical yield spectra obtained using the model. Analytical Yield Spectrum (AYS), calculated using equation (2.14), is represented by blue curves. To separate the curves for better clarity, yield spectrum for 10000, 4000, 1000, 500 and 50 eV are shown after multiplying with scaling factors 2000, 300, 80 and 20 and 5, respectively.

2.6.2 Mean energy per ion pair

Mean energy per ion pair, also known as w-value, is defined as the average energy spent by an electron to produce an electron-ion pair after its energy is completely dissipated. Its reciprocal gives the efficiency with which a particle can ionize the gas, and is a typical feature of the target species considered. The w-value for an incident electron energy E_0 is calculated as

$$w(E_0) = E_0/J(E_0), \tag{2.16}$$

where $J(E_0)$ is the population of the ionization events. Figure 2.6 shows the mean energy per ion pair value calculated for neutral xenon and for the various ionization channels of Xe. At high incident electron energies w approaches a constant value. As the incident electron energy decreases, ionization population also decreases since excitation process starts dominating due to their higher cross section at these energies. Thus w increases as the incident particle energy decreases. This behaviour of w agrees well with the previous calculations of *Combecher* [1980], *Date et al.* [2003], *Dayashankar* [1982] and *Dias et al.* [1993].

Table 2.4: Mean energy per ion pair (w-value) for neutral and different ionization states of xenon for incident energies 300 eV and 10 keV.

	E_0 = 300 eV	E_0 = 10 keV
Xe	23.2 eV	22 eV
Xe^+	29.3 eV	29.9 eV
Xe^{2+}	369.9 eV	286.6 eV
Xe^{3+}	1.1 keV	878.3 eV
Xe^{4+}	5.4 keV	3.4 keV
Xe^{5+}	43 keV	9.5 keV

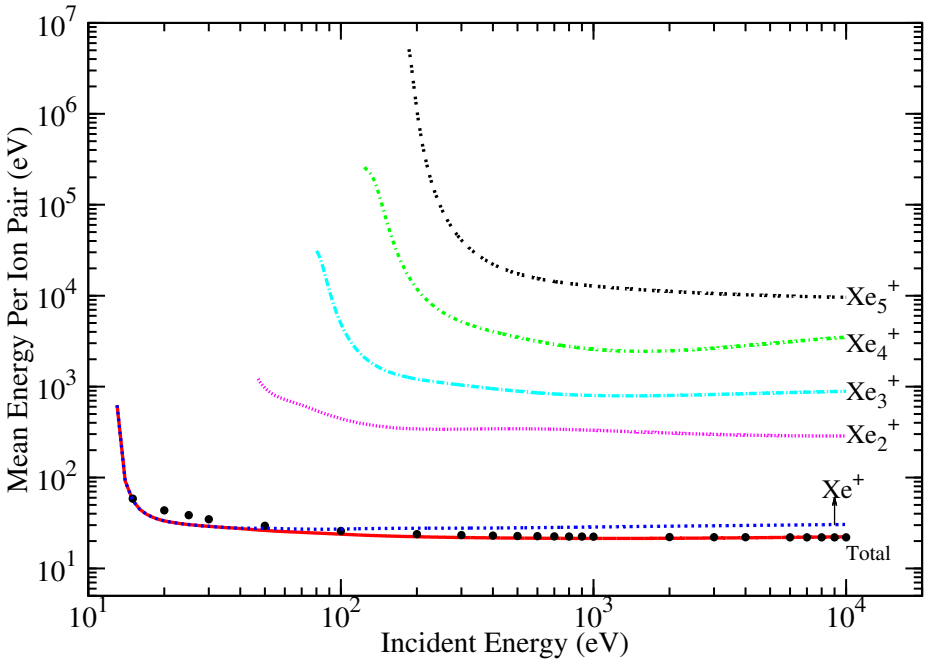

Figure 2.6: Mean energy per ion pair for ions Xe^+, Xe^{2+}, Xe^{3+}, Xe^{4+}, Xe^{5+} and neutral Xe (shown as total). Symbols show the values calculated using numerical yield spectrum for Xe.

Mean energy per ion pair calculated for neutral xenon and its various ionization states at two different incident energies, 10 keV and 300 eV are shown in Table 2.4. *Date et al.* [2003] reported a w-value of 21.7 eV at 10 keV. *Combecher* [1980] measured w-value for electrons in xenon and obtained a value of 22 eV for high energy electrons. *Dias et al.* [1993] obtained a value of 22 eV at 10 keV, while *Dayashankar* [1982] calculated a value of 23.1 eV for energy >200 eV. The value of mean energy per ion pair calculated using our model is in good agreement with those reported previously.

2.6.3 Secondary electron energy distribution

Secondary electrons generated during ionization can also cause inelastic collisions, provided they have sufficient energy. These electrons can have a maximum energy of (E-I)/2, where E is the energy of the primary electron and I is the ionization threshold. The energy of secondary electrons are calculated using equation (2.6). If this energy is greater than that of the cutoff energy, then it is also followed in the same manner as that of the primary. Similarly, tertiary, quaternary, etc electrons are also followed in the Monte Carlo simulation. The energy distribution of secondary electrons for different incident electron energies is shown in Figure 2.7. Also shown in the same figure is the distribution of tertiary and quaternary electrons for an incident energy of 10 keV. It is clear from the figure that during degradation, an electron with 10 keV energy, will produce at least one secondary or tertiary electron whose energy is >10 eV (<34 eV), which is sufficient to cause further inelastic collisions.

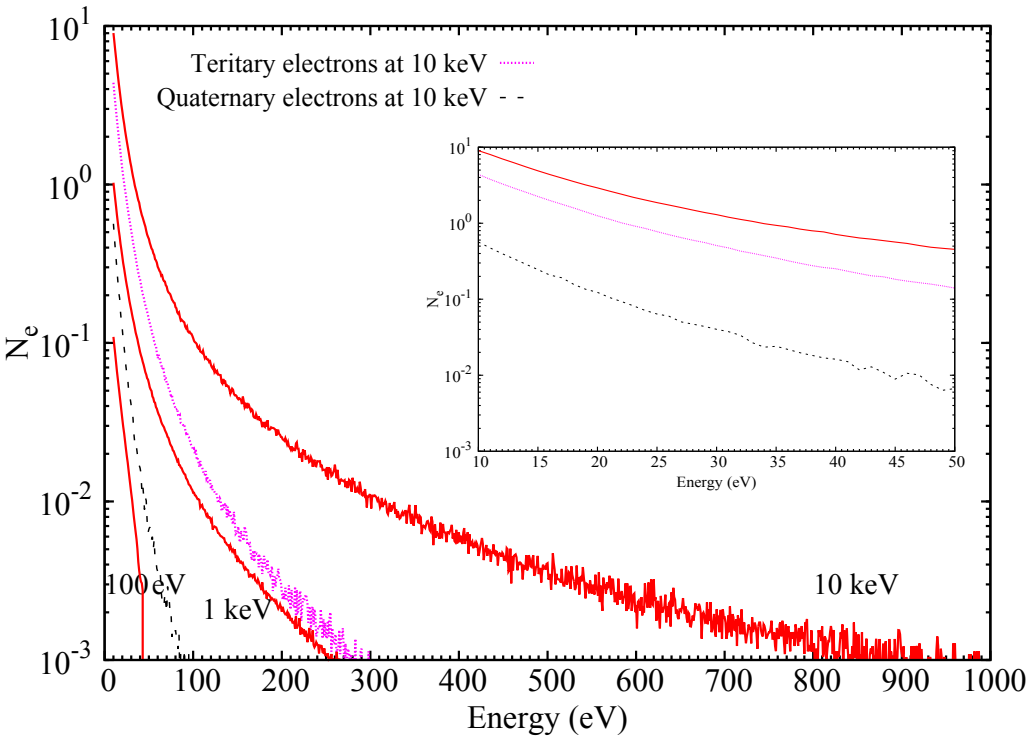

Figure 2.7: Energy distribution of secondary electrons for incident energies 100 eV, 1 keV and 10 keV. Y axis shows the number of secondary electrons produced per incident primary electron. Dotted and dashed curves show distribution of tertiary and quaternary electrons, respectively, for an incident energy of 10 keV. Inset shows the energy distribution of secondary, tertiary and quaternary electrons for an incident energy of 10 keV zoomed in the lower energy range of 10 to 50 eV.

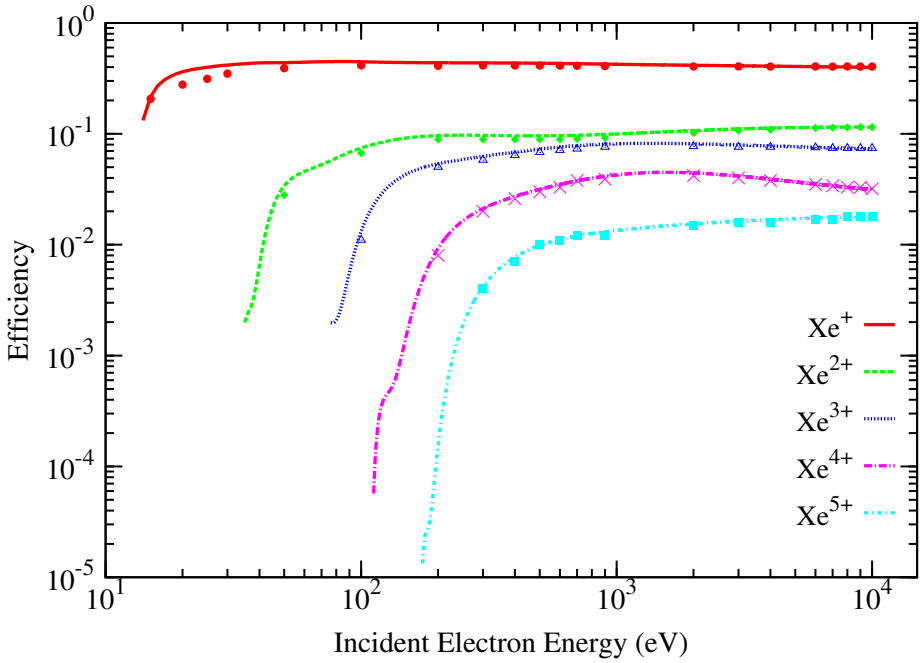

Figure 2.8: Efficiencies of various ionization processes. Symbols represent the efficiencies calculated using numerical yield spectra and solid lines are efficiencies calculated using AYS.

2.6.4 Efficiency

During the degradation process, the electron energy is distributed among various inelastic processes. Efficiency of a process gives information on what fraction of the incident energy is used for a particular process after the electron has completely degraded its energy. The efficiency, $\eta_j(E_0)$, of the j^{th} process at the incident energy E_0 can be obtained as

$$\eta_j(E_0) = \frac{W_{th}}{E_0} J_j(E_0) \tag{2.17}$$

where W_{th} is the threshold for the j^{th} process.

Figure 2.8 shows the efficiencies of the various ionization channels. Efficiencies are calculated using both numerical yield as well as analytical yield and are compared with each other. A good match is observed between the values obtained using the two methods. Throughout the energy range, Xe^+ ionization channel is found to have the maximum efficiency due to its high cross section. At 10 keV, Xe^+ has an efficiency of 40.5%. Xe^{2+}, Xe^{3+}, Xe^{4+} and Xe^{5+} have efficiencies of 11.5%, 7.4%, 3.2% and 1.8%, respectively.

Efficiencies of various levels in the 1s configuration are shown in Figure 2.9(a). For an incident electron energy of 10 keV, ~10% of the energy is spent in the 1s configuration. As seen in the figure, the allowed excitation $1s_4$ has the highest efficiency throughout the energy range with a value of 4.5% at 10 keV and the lowest efficiency is for the

forbidden excitation $1s_3$ with 0.4% efficiency. The other two excitations $1s_2$ and $1s_5$, have efficiencies 2.3% and 2.9%, respectively. Figure 2.9(b) shows the efficiencies of 2p configuration. The $2p_9$+$2p_8$ level has an efficiency of 1.6% at 10 keV and is the highest among various levels in 2p configuration. Out of ∼4% efficiency of 2p configuration at 10 keV, 0.9% is channeled in to $2p_{10}$ level, 0.8% into $2p_7$+$2p_6$ and 0.8% into $2p_4$+$2p_3$+ $2p_2$+$2p_1$ levels. Efficiencies of remaining excitation channels are shown in Figure 2.9(c). The $3d_5$ level has a very low efficiency of 0.1% at 10 keV. A combination of various forbidden levels, $3d_6$+$2p_5$+$3d_4$+$3d_3$+$3d_4$+$3d''$+$3d_1$, has an efficiency of 4.7%. The upper allowed excitation levels (3s-9s) consume around 5.9% of the incident electron energy. The $3d_2$ and $2s_5$+$2s_4$ levels have efficiencies of 4% and 1% at 10 keV, respectively.

Figure 2.10 shows how the incident electron energy is divided among ionization and excitation processes. From 50 eV onwards, ionization is the dominant inelastic process. More than 50% of incident energy is spent into ionization at these energies. Above 1000 eV, ionization efficiency attains a constant value of ∼64%. Excitation dominates at energies less than 30 eV. In the energy range where only elastic and excitation collision can occur, excitation efficiency is found to be around ∼90%, which is consistent with the results of *Dias et al.* [1993] and *Santos et al.* [1994]. At incident electron energies of 10 keV around 30% of the energy is spent on excitation events.

2.7 Summary

We have developed a Monte Carlo model for degradation of electrons with energy ≤10 keV in neutral xenon gas. Electron impact cross sections for elastic and various inelastic processes were compiled based on the recent experimental and theoretical studies. Analyticaly fitted form of these cross sections are used as input data to the model. The numerical yield spectrum calculated using Monte Carlo simulation is analytically represented through Equation (2.14), thus generating analytical yield spectrum. A good agreement is observed between numerical yield spectrum and AYS. From these results the mean energy per ion pair and the efficiency of inelastic processes have been calculated. The value of mean energy per ion pair is 22 eV for an incident energy of 10 keV which is consistent with the values obtained in earlier studies of *Date et al.* [2003], *Dias et al.* [1993], *Combecher* [1980], and *Dayashankar* [1982]. Secondary electron energy distribution is shown in Figure 2.7. Efficiency calculations showed that ionization process dominates for incident energies >50 eV and is found to have an efficiency of ∼65% at 10 keV. Efficiency of excitation is ∼30% at 10 keV incident energy. Our results are consistent with the previous calculations of *Santos et al.* [1994] and *Dias et al.* [1993].

Results presented in this chapter will be useful to understand the electron energy degradation process in xenon. The AYS derived using the Monte Carlo model can be used to calculate steady state electron flux in a medium like planetary atmospheres

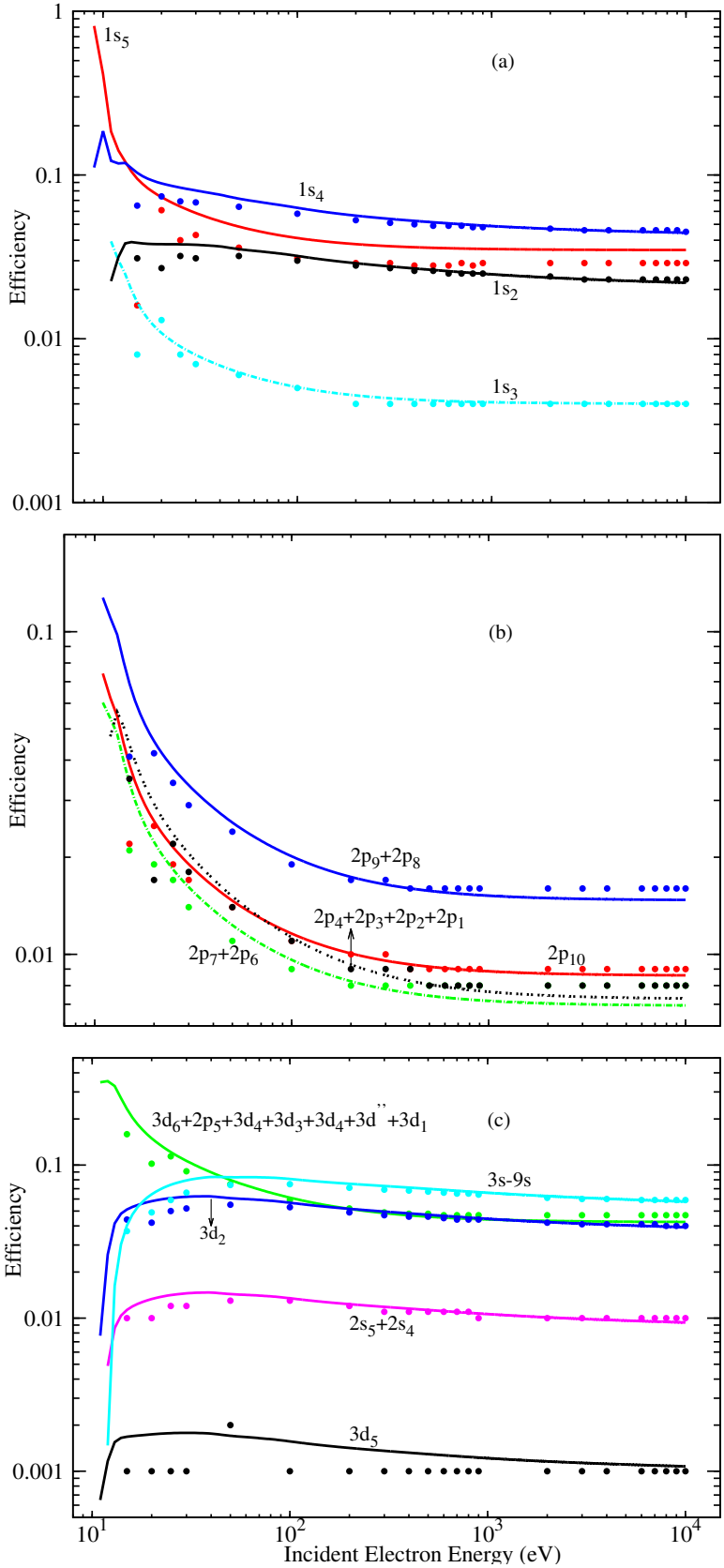

Figure 2.9: Efficiencies of various levels in the (a) 1s configuration (b) 2p configuration (c) remaining excitation channels. Symbols represent the efficiencies calculated using numerical yield spectra and solid lines are efficiencies calculated using AYS.

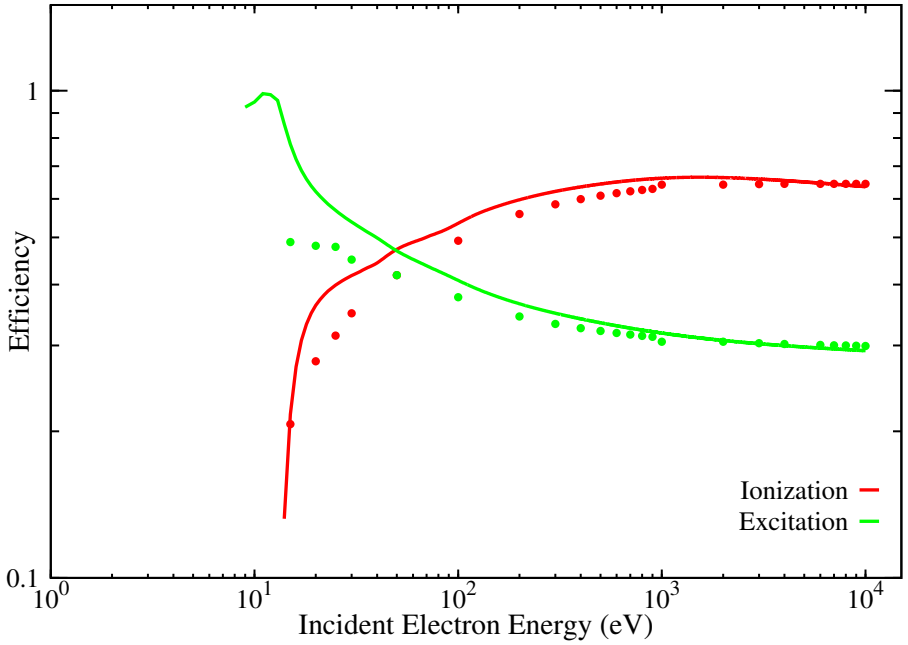

Figure 2.10: Efficiencies of ionization and excitation processes. Symbols represent the efficiencies calculated using numerical yield spectra and solid lines are efficiencies calculated using AYS.

[*Bhardwaj and Micheal*, 1999; *Bhardwaj and Singhal*, 1990], ion thrusters etc. as well as to calculate excitation rates or emission intensities [*Bhardwaj and Raghuram*, 2012; *Jain and Bhardwaj*, 2015]. Efficiencies can be used to calculate volume production rate multiplying by electron production rate and integrating over energy.

The electron energy degradation in a molecular gas methane is presented in the subsequent chapter.

Chapter 3

Monte Carlo model for electron degradation in methane gas

3.1 Introduction

When an electron collides with an atom, there are only two possible inelastic processes; the atom can either get ionized or it can get excited to higher energy levels. This is not the case when the collision partner is a molecule. The simple fact that a molecule consists of at least two atoms causes electron-molecule collisions to be much more sophisticated than electron-atom collisions. Additional energy loss processes are introduced into inelastic processes. The molecular excitations can be rotational, vibrational, or electronic in nature. As an extreme case of vibration, the molecule can get dissociated into fragments. In addition to the dissociation of a molecule into neutral ground-state fragments (neutral molecular dissociation), dissociation can also be combined with other inelastic processes resulting in dissociative excitation, dissociative ionization, and dissociative electron attachment. Thus, molecular targets add more intricacies to electron collision processes.

All atmospheres in the solar system are dominated by molecular gases, such as N_2, CO_2, O_2, CO, H_2O, H_2, CH_4, SO_2, etc. Free electrons are produced in these atmospheres from many sources, such as photoionization, electrons of solar or magnetospheric origin, cosmic ray ionization, etc. Nearly all atmospheric processes are ultimately the result of the interaction of photons and electrons with the molecular gases in the atmosphere. Energetic electrons can ionize or dissociate the neutral molecules, and a cascade of secondary electrons are generated, which in turn can cause ionization, dissociation, excitation and heating. The ability of a molecule to dissociate adds the possibility that the collision process generates new species, which are often much more reactive as well as chemically and physically very different from the parent molecule. These by-products can initiate further reactions which largely influence the atmospheric chemistry and planetary aeronomy processes, such as aurora and dayglow, etc [*Campbell and Brunger*, 2016].

An energy deposition model for electron-molecule collisions is presented in this chapter. Methane has been chosen as the target molecule due to its relevance in planetary atmospheres (see section 3.2). The Monte Carlo model for e-CH_4 collisions is presented in Section 3.2. The results of the simulation are presented in Section 3.4. The AYS calculated in this chapter will be used for calculating photoelectron flux in Titan's atmosphere which is discussed in the subsequent chapters.

3.2 Monte Carlo model for electron degradation in methane gas

Methane is the simplest hydrocarbon present in the solar system [*Mueller-Wodarg et al.*, 2008]. It is an important constituent in the atmospheres of the outer solar system planets Jupiter, Saturn, Uranus, and Neptune, and also in the atmospheres of satellites Titan and Triton [*Gregersen*, 2010]. The New-Horizons mission confirmed the presence of this hydrocarbon gas in the atmosphere of the dwarf-planet Pluto [*Gladstone et al.*, 2016]. Even though methane is only a minor gas in these atmospheres, it is vital in controlling many of the atmospheric processes. Methane is a well-mixed gas in the homospheres of Jupiter and Saturn and causes infrared absorption in these atmospheres. In Uranus and Neptune, it condenses as ice [*McFadden et al.*, 2006]. The bluish appearance of these planets is caused by the presence of CH_4 in the atmosphere as methane absorbs radiations of red wavelength. In the satellite Titan, Cassini-Huygens mission found regions of low radar reflectivity which are interpreted as lakes. These lakes are believed to be composed of methane and other hydrocarbon gases [*Cordier et al.*, 2009].

In the outer solar system atmospheres, CH_4 plays a key role in ionospheric photochemistry. Collision of solar photons or photoelectrons with methane molecules causes the neutral dissociation or ionization of the molecule which in turn leads to the generation of simple hydrocarbon radicals and ions. The subsequent reactions caused by these radicals and ions, either with themselves or with methane and other background gases, cause the production of higher order hydrocarbons, be it alkanes, alkenes or alkynes [*Banaszkiewicz et al.*, 2000; *Strobel*, 2004]. The heavy hydrocarbons can lead to polymerization and result in the production of UV-dark haze in Jupiter's polar region [*Singhal et al.*, 1992]. In Titan's upper atmosphere, heavy hydrocarbon ions are detected which is a byproduct of methane photochemistry [*Coates et al.*, 2007; *Wahlund et al.*, 2009]. Hydrogen cyanide, an important precursor for the formation of amino acids and proteins, is formed from those reactions for which methane acts as a precursor [*Romanzin et al.*, 2005]. The hydrocarbon abundance in the atmospheres of the planets Uranus and Neptune is also an outcome of the methane photochemistry [*Summers and Strobel*, 1989; *Romani et al.*, 1993].

There are several loss processes through which the electron can degrade its energy

while colliding with methane molecule. Figure 3.1 shows the modified flowchart for the Monte Carlo model for electron-molecule collisions. As mentioned previously, the additional loss channels, viz., neutral dissociation, dissociative ionization, electron attachment, and vibrational and electronic excitations have been incorporated into the model. All other equations used for calculating different parameters, like energy loss after each collision, the direction of scattering, the energy of secondary electrons, etc, remain the same as that discussed in Chapter 2. The electron impact cross sections for e-CH_4 collisions form the major input to the model. In the following section, a review of the electron impact cross sections for methane is presented with the information on the selection of cross sections for model calculations. These cross sections are fitted analytically using appropriate empirical equations. The analytical equation and the fitting parameters used for each cross section are also discussed.

3.3 Cross Sections

3.3.1 Total Elastic cross sections

Total elastic scattering cross section for methane has been measured by *Boesten and Tanaka* [1991], *Bundschu et al.* [1997], *Iga et al.* [1999], and *Kanik et al.* [1993]. All these measurements are in good agreement with each other. Measurements of *Boesten and Tanaka* [1991] in the energy range 1.5-100 eV was fitted using analytical formula by *Shirai et al.* [2002]. At energies above 100 eV, data from *Kanik et al.* [1993] is used for fitting. This analytically fitted form of elastic cross section is used in the current study and is shown in Figure 3.2.

3.3.2 Differential elastic cross sections (DCS)

The DCS for e-CH_4 collision has been measured by many workers. Values of DCS used in the present work are given in Table 3.1. In the low energy range of 3 to 15 eV, DCS measurements of *Mapstone and Newell* [1992] are used. However, DCS value at 5 and 10 eV are taken from *Cho et al.* [2008]. Cross sections for energies between 20 to 100 eV also are taken from *Cho et al.* [2008]. From 200 to 500 eV, measurements of *Iga et al.* [1999] and at 700 eV measurements of *Sakae et al.* [1989] are used. Since DCS measurements are not available for CH_4 for energies greater than 700 eV, linearly extrapolated values of cross sections are used.

3.3.3 Attachment

Dissociative electron attachment process of CH_4 results in the production of H^- and $CH_2{}^-$ ions. Cross section for this process was measured by *Sharp and Dowell* [1967] and *Rawat et al.* [2008]. Former cross sections were analytically fitted by *Shirai et al.* [2002], which are used in the present work and is shown in Figure 3.2.

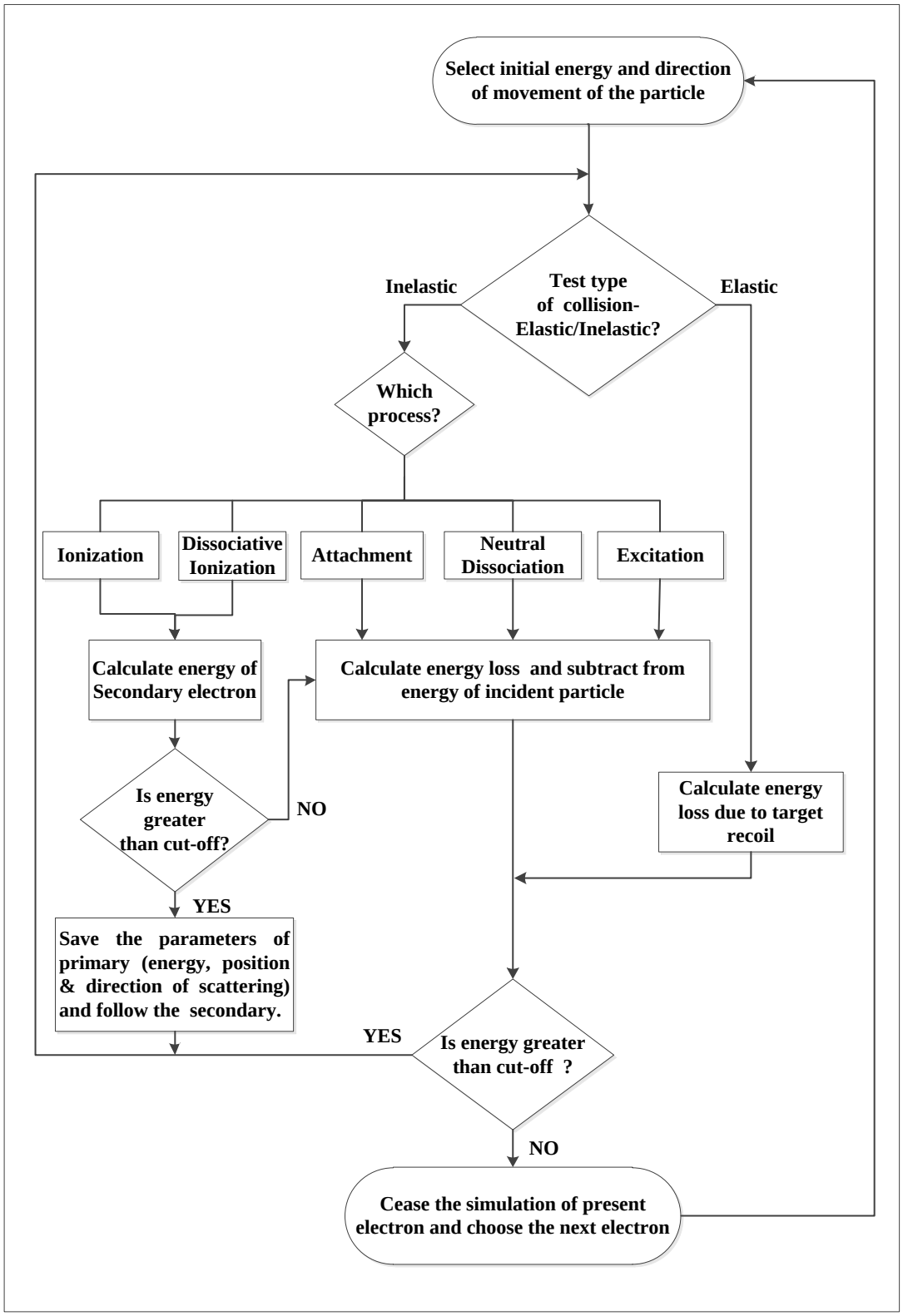

Figure 3.1: Flowchart showing Monte Carlo simulation for electron degradation in molecular gas. It shows flow only up to secondary electrons; subsequent electrons (tertiary, quaternary, etc.) are also followed in the similar manner in the simulation. Excitation involves vibrational, rotational, and electronic excitations and are not shown separately.

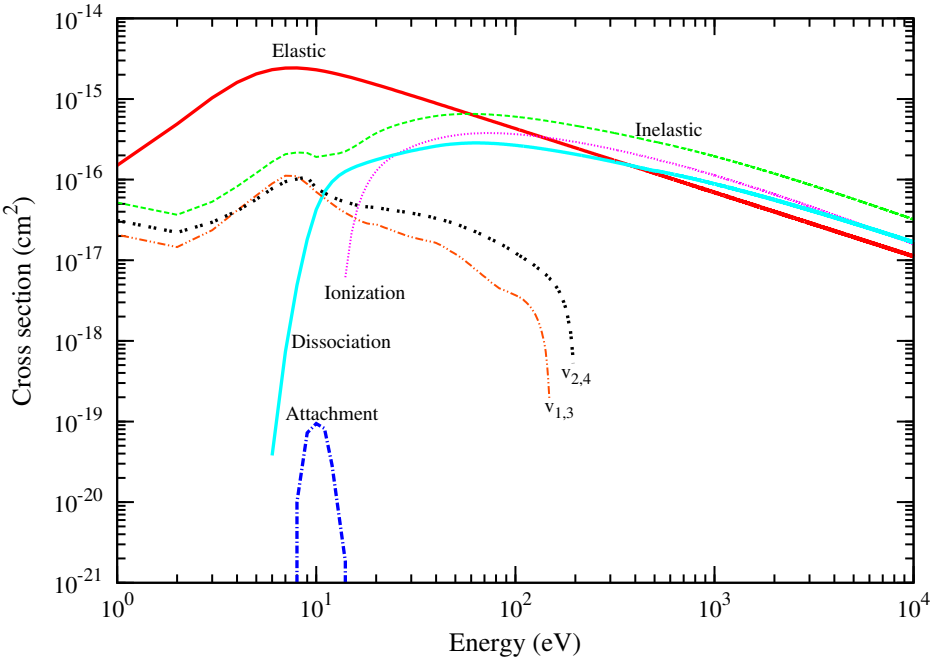

Figure 3.2: Cross sections for elastic and inelastic processes for e-CH_4 collisions. $\nu_{1,3}$ and $\nu_{2,4}$ are the cross sections for stretching and bending vibration modes, respectively.

3.3.4 Vibrational Excitation

Methane molecule is found to have four normal modes of vibration: ν_1 with threshold energy 0.362 eV, ν_2 with 0.190 eV, ν_3 with 0.374 eV and ν_4 with 0.162 eV. But it is difficult to resolve these modes experimentally as they have very close transition energies. Hence, experimental data are available for the combined cross sections for symmetric ν_1 and antisymmetric ν_3 stretching vibrations ($\nu_{1,3}$), and symmetric ν_2 and antisymmetric ν_4 bending vibrations ($\nu_{2,4}$) of CH_4.

Shyn [1991] measured vibrational excitation cross sections for methane at 5.0, 7.5, 10.0 and 15 eV. *Tawara* [1992] measured cross sections in the energy range 0.16-100 eV. DCS values in the 0.6 to 5.4 eV range, measured by *Bundschu et al.* [1997], were integrated to obtain the integral cross section. Vibrational excitation cross sections used in the current study are taken from *Davies et al.* [1988] in which cross section values are given for a larger energy range; 0.450 to 100 eV for $\nu_{1,3}$ mode, and 0.162 to 150 eV for $\nu_{2,4}$ mode. The values of *Davies et al.* [1988] and *Tawara* [1992] agree well at energies 10-100 eV but differ at low energies by about 50%. In this low energy range, good agreement is found when the values were compared with that of *Bundschu et al.* [1997]. Measurements of *Shyn* [1991] are found to be lower than the values of *Davies et al.* [1988] by ∼50%. Vibrational cross section used in this study is shown in Figure 3.2.

Table 3.1: Elastic differential cross sections for CH_4 in units of cm^2. Value inside the bracket indicates a linearly extrapolated value. Notation 1E-18 implies 1 x 10^{-18}

Energy	Angle (degree)								
(eV)	0	10	20	30	40	50	60	70	80
4.2	(5.70E-17)	(6.40E-17)	(7.10E-17)	7.80E-17	8.50E-17	1.11E-16	1.19E-16	1.14E-16	1.01E-16
5	(8.23E-16)	(6.09E-16)	3.91E-16	1.75E-16	1.32E-16	1.28E-16	1.39E-16	1.48E-16	1.39E-16
6	(3.19E-16)	(2.73E-16)	(2.27E-16)	1.81E-16	1.35E-16	1.42E-16	1.30E-16	1.42E-16	1.38E-16
7.9	(7.32E-16)	(6.04E-16)	(4.76E-16)	3.48E-16	2.20E-16	1.80E-16	1.43E-16	1.39E-16	1.32E-16
10	9.65E-16	(8.03E-16)	6.40E-16	4.88E-16	3.51E-16	2.12E-16	1.77E-16	1.14E-16	0.86E-16
15.4	(7.65E-16)	(6.29E-16)	(4.93E-16)	3.57E-16	2.21E-16	1.75E-16	1.08E-16	6.50E-17	5.00E-17
20	(1.20E-15)	9.45E-16	6.91E-16	4.55E-16	2.69E-16	1.34E-16	0.83E-16	0.53E-16	0.36E-16
30	(0.39E-15)	10.07E-16	6.25E-16	3.36E-16	1.60E-16	0.75E-16	0.40E-16	0.27E-16	0.18E-16
50	(1.45E-15)	9.22E-16	3.98E-16	1.80E-16	0.70E-16	0.29E-16	0.18E-16	0.10E-16	0.07E-16
100	(1.41E-15)	8.01E-16	1.95E-16	0.44E-16	0.19E-16	0.09E-16	0.04E-16	0.03E-16	0.02E-16
200	(1.14E-15)	5.51E-16	1.03E-16	3.34E-17	1.51E-17	8.20E-18	5.20E-18	3.80E-18	3.20E-18
300	(9.29E-16)	4.26E-16	7.26E-17	2.56E-17	1.12E-17	6.20E-18	3.80E-18	2.60E-18	1.80E-18
400	(6.76E-16)	3.02E-16	5.14E-17	1.83E-17	8.20E-18	4.00E-18	2.60E-18	1.50E-18	1.10E-18
500	(6.46E-16)	2.80E-16	4.58E-17	1.63E-17	6.90E-18	3.20E-18	1.80E-18	1.20E-18	9.00E-19
700	(1.54E-15)	2.19E-16	3.52E-17	1.26E-17	4.41E-18	1.98E-18	1.02E-18	6.47E-19	4.45E-19
800	(2.38E-15)	(1.94E-16)	(3.09E-17)	(1.12E-17)	(3.53E-18)	(1.56E-18)	(7.69E-19)	(4.75E-19)	(3.13E-19)
900	(3.67E-15)	(1.71E-16)	(2.71E-17)	(9.74E-18)	(2.82E-18)	(1.22E-18)	(5.78E-19)	(3.49E-19)	(2.20E-19)

1000	(5.67E-15)	(1.51E-16)	(2.37E-17)	(8.56E-18)	(2.25E-18)	(9.64E-19)	(4.35E-19)	(2.56E-19)	(1.55E-19)	
2000	(2.56E-14)	(6.66E-17)	(9.81E-18)	(3.66E-18)	(5.09E-19)	(2.04E-19)	(6.70E-20)	(3.33E-20)	(1.54E-20)	
3000	(4.56E-14)	(4.12E-17)	(5.85E-18)	(2.22E-18)	(2.13E-19)	(8.27E-20)	(2.24E-20)	(1.01E-20)	(4.02E-21)	
4000	(6.56E-14)	(2.93E-17)	(4.06E-18)	(1.56E-18)	(1.15E-19)	(4.34E-20)	(1.03E-20)	(4.33E-21)	(1.54E-21)	
5000	(8.56E-14)	(2.25E-17)	(3.05E-18)	(1.19E-18)	(7.14E-20)	(2.64E-20)	(5.66E-21)	(2.25E-21)	(7.36E-22)	
6000	(1.05E-13)	(1.82E-17)	(2.42E-18)	(9.52E-19)	(4.83E-20)	(1.75E-20)	(3.46E-21)	(1.31E-21)	(4.01E-22)	
7000	(1.25E-13)	(1.51E-17)	(1.99E-18)	(7.88E-19)	(3.47E-20)	(1.24E-20)	(2.28E-21)	(8.36E-22)	(2.40E-22)	
8000	(1.45E-13)	(1.29E-17)	(1.68E-18)	(6.69E-19)	(2.61E-20)	(9.23E-21)	(1.59E-21)	(5.64E-22)	(1.54E-22)	
9000	(1.65E-13)	(1.12E-17)	(1.44E-18)	(5.79E-19)	(2.02E-20)	(7.09E-21)	(1.15E-21)	(3.99E-22)	(1.04E-22)	
10000	1.85E-13	(9.96E-18)	(1.26E-18)	(5.09E-19)	(1.61E-20)	(5.60E-21)	(8.72E-22)	(2.93E-22)	(7.35E-23)	

Energy	Angle (degree)									
(eV)	0	10	20	30	40	50	60	70	80	
3.2	8.30E-17	6.20E-17	3.40E-17	2.20E-17	2.00E-17	2.70E-17	(3.40E-17)	(4.10E-17)	(4.80E-17)	(5.50E-17)
4.2	1.01E-16	8.60E-17	7.30E-17	4.20E-17	2.50E-17	5.30E-17	(8.10E-17)	(1.09E-16)	(1.37E-16)	(1.65E-16)
5	1.19E-16	0.84E-16	0.50E-16	0.24E-16	0.18E-16	0.26E-16	0.36E-16	0.47E-16	0.60E-16	0.70E-16
6	1.18E-16	8.10E-17	4.10E-17	2.20E-17	4.00E-17	8.00E-17	(1.20E-16)	(1.60E-16)	(2.00E-16)	(2.40E-16)
7.9	9.80E-17	6.20E-17	2.70E-17	1.70E-17	4.60E-17	9.40E-17	(1.42E-16)	(1.90E-16)	(2.38E-16)	(2.86E-16)
10	0.55E-16	0.38E-16	0.24E-16	0.21E-16	0.31E-16	0.58E-16	0.83E-16	1.20E-16	1.60E-16	1.78E-16
15.4	4.00E-17	2.90E-17	2.70E-17	3.20E-17	4.30E-17	5.70E-17	(7.10E-17)	(8.50E-17)	(9.90E-17)	(1.13E-16)
20	0.26E-16	0.20E-16	0.19E-16	0.25E-16	0.32E-16	0.40E-16	0.49E-16	0.56E-16	0.62E-16	0.69E-16
30	0.12E-16	0.12E-16	0.13E-16	0.17E-16	0.21E-16	0.27E-16	0.30E-16	0.32E-16	0.33E-16	0.34E-16

50	0.05E-16	0.04E-16	0.06E-16	0.08E-16	0.10E-16	0.14E-16	0.16E-16	0.18E-16	0.19E-16	0.20E-16
100	0.02E-16	0.02E-16	0.03E-16	0.03E-16	0.04E-16	0.04E-16	0.05E-16	0.05E-16	0.05E-16	0.05E-16
200	2.80E-18	2.40E-18	2.20E-18	2.00E-18	(2.15E-18)	(2.25E-18)	(2.35E-18)	(2.45E-18)	(2.55E-18)	(2.65E-18)
300	1.40E-18	1.20E-18	1.10E-18	1.10E-18	(1.00E-18)	(1.00E-18)	(1.00E-18)	(1.00E-18)	(1.00E-18)	(1.00E-18)
400	9.00E-19	8.00E-19	6.00E-19	6.00E-19	(6.00E-19)	(6.00E-19)	(6.00E-19)	(6.00E-19)	(6.00E-19)	(6.00E-19)
500	7.00E-19	6.00E-19	5.00E-19	5.00E-19	4.00E-19	4.00E-19	4.00E-19	4.00E-19	4.00E-19	4.00E-19
700	3.07E-19	2.46E-19	1.96E-19	1.68E-19	1.59E-19	1.51E-19	1.42E-19	1.34E-19	1.25E-19	1.17E-19
800	(2.03E-19)	(1.57E-19)	(1.23E-19)	(9.74E-20)	(1.01E-19)	(9.28E-20)	(8.46E-20)	(7.75E-20)	(6.99E-20)	(6.33E-20)
900	(1.34E-19)	(1.01E-19)	(7.68E-20)	(5.64E-20)	(6.32E-20)	(5.70E-20)	(5.04E-20)	(4.49E-20)	(3.91E-20)	(3.42E-20)
1000	(8.92E-20)	(6.46E-20)	(4.81E-20)	(3.27E-20)	(3.98E-20)	(3.50E-20)	(3.00E-20)	(2.59E-20)	(2.18E-20)	(1.85E-20)
2000	(6.13E-21)	(3.41E-21)	(2.21E-21)	(9.06E-22)	(1.89E-21)	(1.41E-21)	(9.88E-22)	(6.93E-22)	(4.66E-22)	(3.24E-22)
3000	(1.28E-21)	(6.11E-22)	(3.65E-22)	(1.11E-22)	(3.20E-22)	(2.16E-22)	(1.34E-22)	(8.35E-23)	(4.93E-23)	(3.05E-23)
4000	(4.21E-22)	(1.80E-22)	(1.01E-22)	(2.51E-23)	(9.06E-23)	(5.71E-23)	(3.25E-23)	(1.85E-23)	(1.00E-23)	(5.70E-24)
5000	(1.78E-22)	(7.00E-23)	(3.78E-23)	(7.91E-24)	(3.40E-23)	(2.03E-23)	(1.08E-23)	(5.79E-24)	(2.90E-24)	(1.55E-24)
6000	(8.80E-23)	(3.23E-23)	(1.68E-23)	(3.08E-24)	(1.52E-23)	(8.75E-24)	(4.42E-24)	(2.23E-24)	(1.05E-24)	(5.35E-25)
7000	(4.85E-23)	(1.68E-23)	(8.49E-24)	(1.38E-24)	(7.77E-24)	(4.28E-24)	(2.06E-24)	(1.00E-24)	(4.49E-25)	(2.18E-25)
8000	(2.89E-23)	(9.54E-24)	(4.69E-24)	(6.95E-25)	(4.32E-24)	(2.31E-24)	(1.07E-24)	(4.98E-25)	(2.14E-25)	(1.00E-25)
9000	(1.83E-23)	(5.78E-24)	(2.78E-24)	(3.78E-25)	(2.58E-24)	(1.33E-24)	(6.00E-25)	(2.69E-25)	(1.11E-25)	(5.03E-26)
10000	(1.22E-23)	(3.70E-24)	(1.74E-24)	(2.19E-25)	(1.62E-24)	(8.22E-25)	(3.57E-25)	(1.55E-25)	(6.21E-26)	(2.72E-26)

3.3.5 Ionization

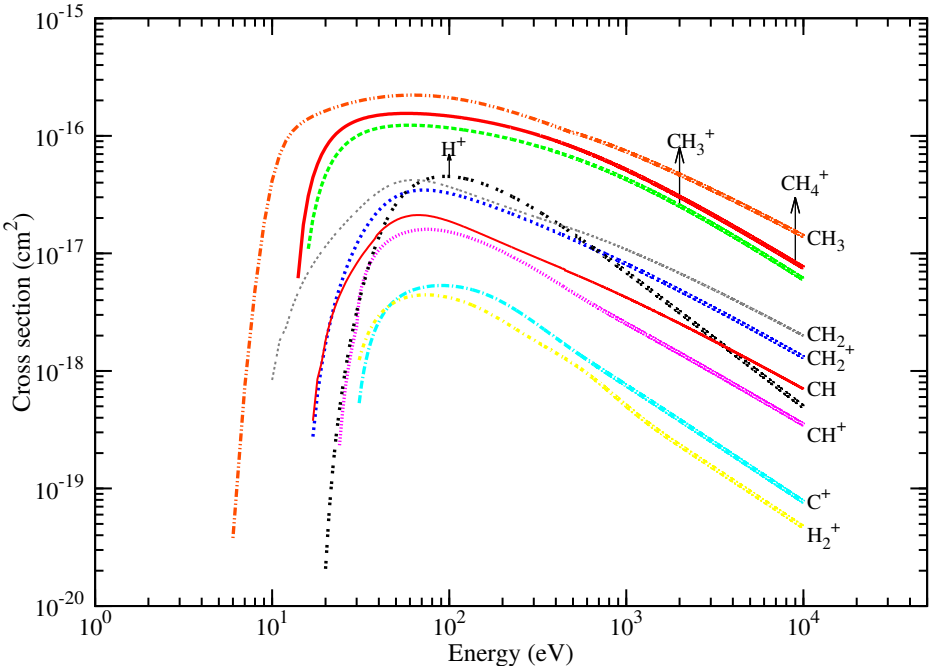

Figure 3.3: Electron impact cross sections of CH_4 for various ionization and dissociation channels.

Ionization and dissociative ionization of CH_4 result in the production of ions CH_4^+, CH_3^+, CH_2^+ , CH^+, C^+, H_2^+ and H^+. Cross section for these ionization processes have been measured by many authors, e.g., *Tian and Vidal* [1997], *Chatham et al.* [1984], *Adamczyk et al.* [1966] and *Straub et al.* [1997]. *Straub et al.* [1997] measured the cross sections in the energy range 15-1000 eV and it is found to be the most reliable among the various available measurements [*Liu and Shemansky*, 2006]. These measurements were later revised due to instrumental recalibration and was published in *Lindsay and Mangan* [2003] (hereafter referred to as Straub's revised measurements). *Liu and Shemansky* [2006] derived the oscillator strength and excitation functions for various ionization channels of CH_4 and calculated the cross section values. These cross sections are in good agreement with Straub's revised measurements. However, cross sections reported by *Liu and Shemansky* [2006] exclude the contribution by pair production (e.g. (CH_2^+, H^+), (C^+, H^+)). *Erwin and Kunc* [2008], using scaling law, developed analytical expressions for calculating cross sections for various ionization channels of methane, which are valid at all non-relativistic energies. These expressions allow the calculation of electron impact ionization cross sections in an easier, and more direct way than the functions derived by *Liu and Shemansky* [2006]. Good agreement is found between these theoretical ionization cross sections when compared with Straub's revised measurements and measurements of *Tian and Vidal* [1997]. Maximum deviation (∼20%) is found for H^+ production.

For the present work, the cross sections for CH_4^+ and CH_3^+ production are taken from *Liu and Shemansky* [2006]. For CH_2^+ production, the cross section for positive ion pair formation (CH_2^+, H^+), measured by *Lindsay et al.* [2001], is added with the values of *Liu and Shemansky* [2006] to account for the contribution via doubly ionized channels. These cross sections are fitted using analytical equation [*Shirai et al.*, 2002];

$$\sigma = \sigma_o a_1 (E/E_R)^{a_2} / [1 + (E/a_3)^{a_2+a_4} + (E/a_5)^{a_2+a_6}] \quad (3.1)$$

where $\sigma_o = 1 \times 10^{-16}$ cm^2, E_R is the Rydberg constant, and a_1, a_2, a_3, a_4, a_5 and a_6 are the fitting parameters whose values are given in Table 3.2. The analytical expression of *Erwin and Kunc* [2008] is used to calculate the cross sections for channels CH^+, C^+ and H_2^+. For H^+ production channel, the analytical expression of *Shirai et al.* [2002] is used, extending it to 10 keV to get cross section values at higher energies. Figure 3.3 shows the ionization and dissociative ionization cross sections used in the present study.

Table 3.2: Parameters for CH_4^+, CH_3^+ and CH_2^+ ionization cross section (equation (3.1))

Process	E_{th}(eV)	a_1	a_2	a_3	a_4	a_5	a_6
CH_4^+	12.99	4.40	1.627	7.720E-3	-4.50E-2	3.10E-2	0.93
CH_3^+	14.24	2.18	1.435	1.13E-2	7.4E-2	4.91E-2	1.01
CH_2^+	15.20	0.121	1.868	3.44E-2	3.00E-1	5.20E-2	0.91

3.3.6 Dissociation

Dissociation of methane by electron impact results in the production of neutral radicals CH_3, CH_2 and CH. Experimental cross sections for these processes are not available over a wide energy range, except for the CH_3 radical production where the measurements are made up to 500 eV [*Motlagh and Moore*, 1998]. *Erwin and Kunc* [2008] have given analytical expression for CH_4 dissociation cross sections which is valid at all non-relativistic energies. But the analytical expression does not account for the production of CH_3 radical through dissociative ionization channel $CH_3 + H^+$. For CH_3 radical production, we have used the analytical representation of *Motlagh and Moore* [1998] cross sections, as given by *Shirai et al.* [2002] and extended it to 10 keV. For CH_2 and CH radical production, cross sections are calculated using the analytical expression of *Erwin and Kunc* [2008]. Figure 3.3 shows the dissociation cross sections used in the study.

3.3.7 Emission

Electronically excited state of neutral CH_4 leads to the dissociation of the molecule resulting in the production of excited fragments [*Danko et al.*, 2011]. Cross sections for

hydrogen Lyman series and carbon lines for energies less than 400 eV were measured by *Pang et al.* [1987]. *Motohashi et al.* [1996] measured cross sections for the emission from various excited fragments: the hydrogen Lyman and Balmer series, CH band emission at 420-440 nm, line emissions from C at 165.7 nm and 156.1 nm and these cross sections are found to be in agreement with that of *Pang et al.* [1987]. The uncertainties in these cross sections were estimated to be ±20% for H Lyman-α, ±12% for H Balmer-α, ±20% for CH band, and ±50% for atomic carbon emission. Maximum energy of the experimentally measured cross sections are 1 keV, 6 keV, 5 keV and 1 keV for H Lyman-α, H Balmer-α, CH band, and C emissions, respectively. Analytic cross sections for these emission processes given by *Shirai et al.* [2002] are extended upto 10 keV and used in the current model. (cf. Figure 3.4 and 3.5).

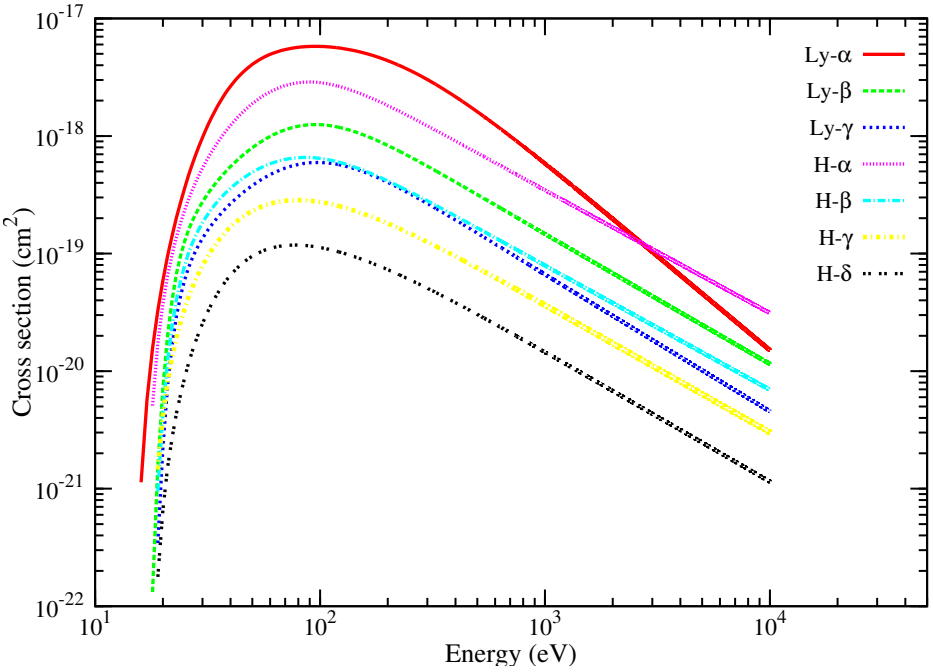

Figure 3.4: Electron impact cross sections for H Lyman and H Balmer emissions.

3.3.8 Total cross sections

The total inelastic cross section is obtained by adding the cross sections of above mentioned inelastic processes. Cross sections for the emission process and H^+ production channel are not taken into account while calculating the total inelastic cross section as they are already accounted in other channels. Figures 3.2-3.5 show the cross sections for elastic and various inelastic processes of methane that have been used in the present work.

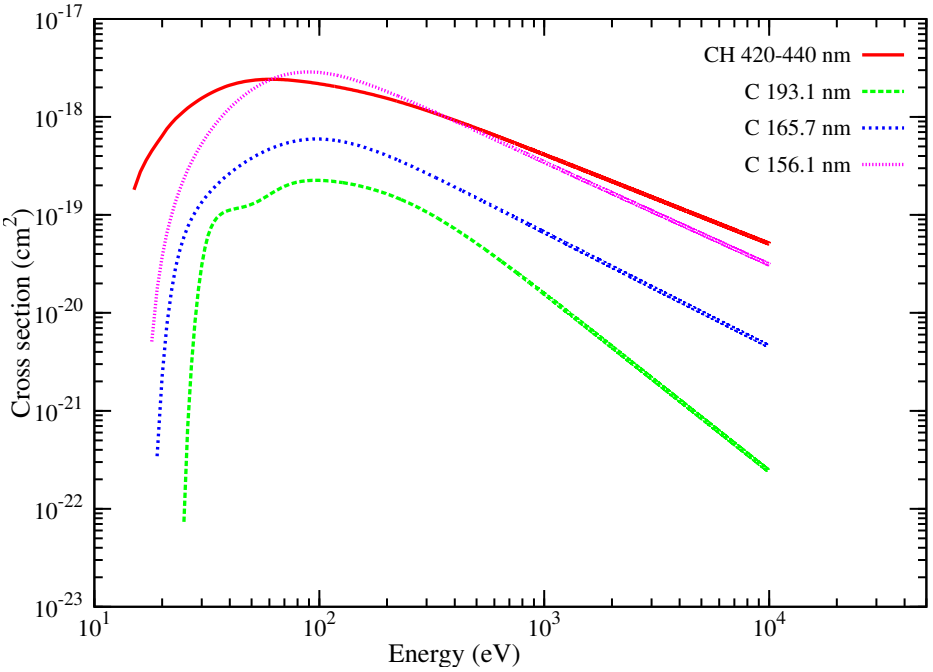

Figure 3.5: Electron impact cross sections of CH_4 for CH band and various CI line emissions.

3.4 Results

3.4.1 Yield Spectrum

As described in Chapter 2, the output of the Monte Carlo simulation is the numerical yield spectrum which is a basic distribution function that contains information regarding the degradation process and can be used to calculate the yield of any excited or ionized state (See equations 2.12 & 2.15). To obtain AYS, the numerical yield spectra are fitted analytically by using the analytical equation of *Green et al.* [1977a]:

$$U_a(E, E_0) = A_1 \xi_0^s + A_2(\xi_0^{1-t}/\epsilon^{3/2+r}) \tag{3.2}$$

where $\xi = E_0/1000$ and $\epsilon = E/I$ (I is the lowest ionization threshold which is equal to 12.99 eV for CH_4). The best fit parameters for methane gas are $A_1 = 0.024$, $A_2 = 4.40$, $t = 0$, $r = -0.27$, and $s = -0.085$. However, the above equation well represent the numerical yield spectrum only at energy values greater than the ionization threshold (13 eV). Unlike the case of xenon, a bulge is seen on the numerical yield at energies <10 eV. This is caused by the increase in the e-CH_4 collisions which in turn occur due to the large vibration cross sections in this energy regime (refer Figure 3.2). To improve AYS at lower energies, *Bhardwaj and Jain* [2009] used an additional function:

$$U_b(E, E_0) = \frac{E_0 A_0 e^{-x}/A_3}{(1 + e^x)^2}. \tag{3.3}$$

Here $x = (E - A_4)/A_3$, and A_0, A_3, and A_4 are the fitting parameters and they suggested best fit parameters for e-CO_2 collisions. To further improve the fit for e-CH_4 collisions, we introduced two more parameters, A_5 and A_6, and modified the above function as:

$$U_b(E, E_0) = \frac{E_0 A_0 e^{-A_5 x}/A_3}{(1 + e^{A_6 x})^2}. \tag{3.4}$$

The best fit parameters for e-CH_4 collisions are $A_0 = 0.9$, $A_3 = 8.5$, $A_4 = 7.0$, $A_5 = 0.001$ and $A_6 = 4.5$. The final AYS is the sum of equations (3.2) and (3.4). The numerical yield spectrum obtained from the model as well as the AYS are shown in Figure 3.6.

By employing AYS, the population or yield of any state j can be calculated using equation 2.15. This can be used for determining various properties of the gas, like mean energy per ion pair and efficiency.

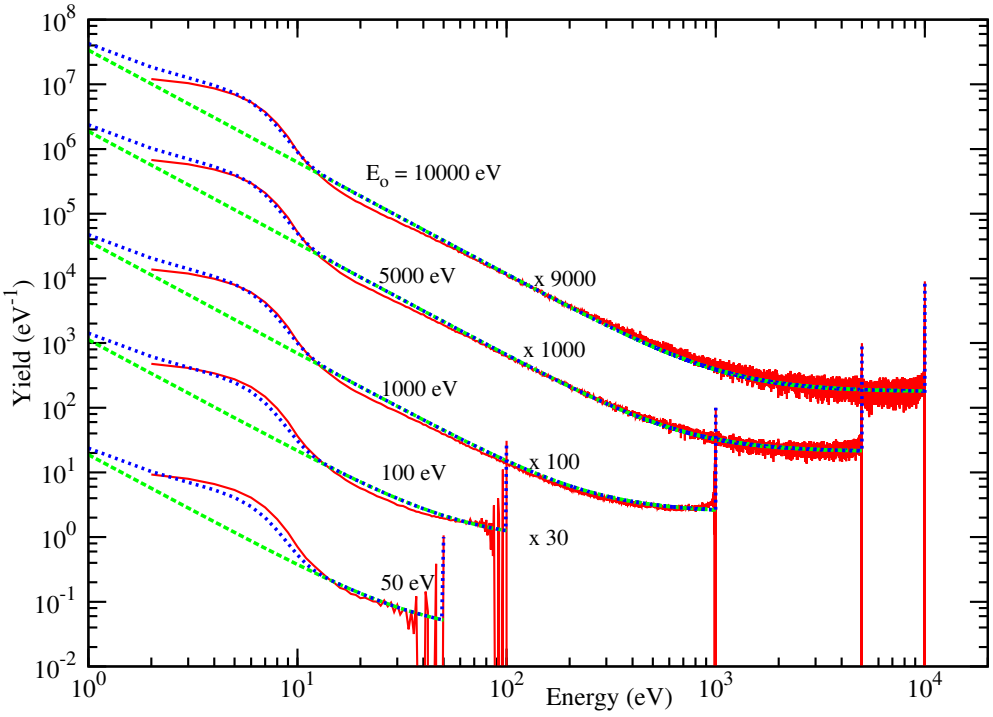

Figure 3.6: Yield spectra for different incident energies. Solid curve shows numerical yield spectra obtained using the model. Analytical Yield Spectrum (AYS), calculated using equation (3.2), is represented by dashed curves. Dotted curve shows improved AYS, obtained by summing equations (3.2) and (3.4). Yield Spectrum for 10000, 5000, 1000, 100 and 50 eV are shown after multiplying with scaling factors 9000, 1000, 100 and 30 and 1, respectively

3.4.2 Mean energy per ion pair

Figure 3.7 shows the mean energy per ion pair value calculated for neutral methane and for the various ionization channels of CH_4. The w-value at two different incident energies, 10 keV and 100 eV, are shown in Table 3.3. The w-value for neutral CH_4 is 26

eV at 10 keV and 27.8 eV at 100 eV. Experimentally determined value for mean energy per ion pair, as given in *ICRU* [1993], is 27.3±0.3 eV for incident energies ≥ 10 keV. *Fox et al.* [2008] reported a value of 31 eV, while *Wedlund et al.* [2011] computed a value of 28.0±1.2 eV at an incident electron energy of 2 keV. Our value of mean energy per ion pair is consistent with those reported in previous studies.

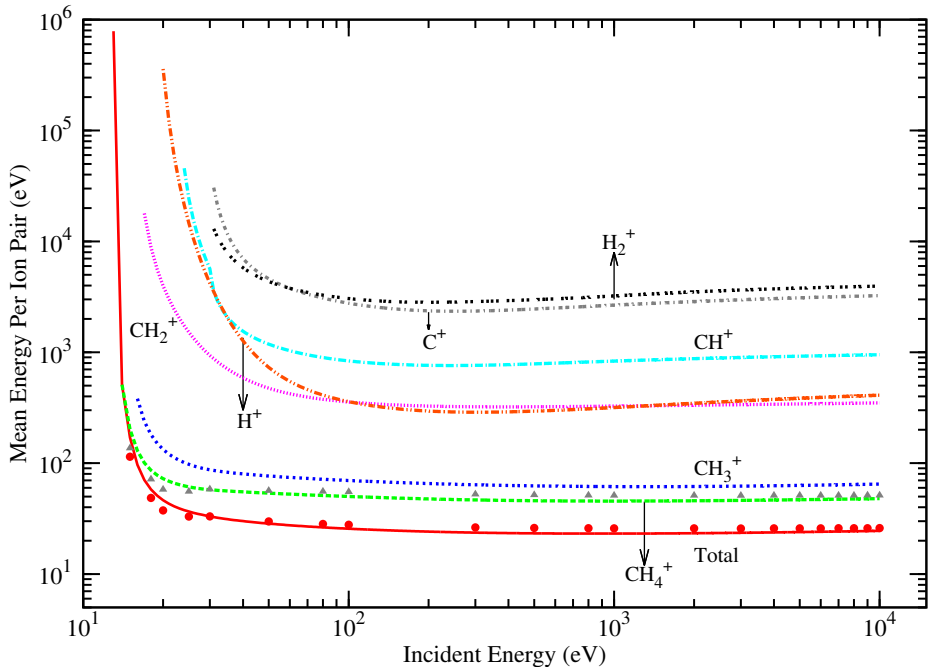

Figure 3.7: Mean energy per ion pair for ions CH_4^+, CH_3^+, CH_2^+, CH^+, C^+, H_2^+, H^+, and neutral CH_4 (shown as total). Symbols shows the values calculated using numerical yield spectrum for CH_4^+ and neutral CH_4

Table 3.3: Mean energy per ion pair (w-value) for neutral and different ionization states of methane for incident energies 100 eV and 10 keV.

	E_0 = 100 eV	E_0 = 10 keV
CH_4	27.8 eV	26 eV
CH_4^+	54.9 eV	51.2 eV
CH_3^+	75.8 eV	68.3 eV
CH_2^+	369.9 eV	357.09 eV
CH^+	855.7 eV	972.7 eV
C^+	43 keV	9.5 keV
H_2^+	3.1 keV	4.08 keV
H^+	358.16 eV	413.06 eV

3.4.3 Secondary Electron production

The energy distribution of secondary electrons is shown in Figure 3.8 at a few incident energies. Distributions of tertiary and quaternary electrons are also shown for incident energy of 10 keV. Figure 3.8 shows that, each incident electron of energy 10 keV, at some point of its energy degradation process, produces at least one secondary, or teritary or quaternary electron whose energy is <32 eV.

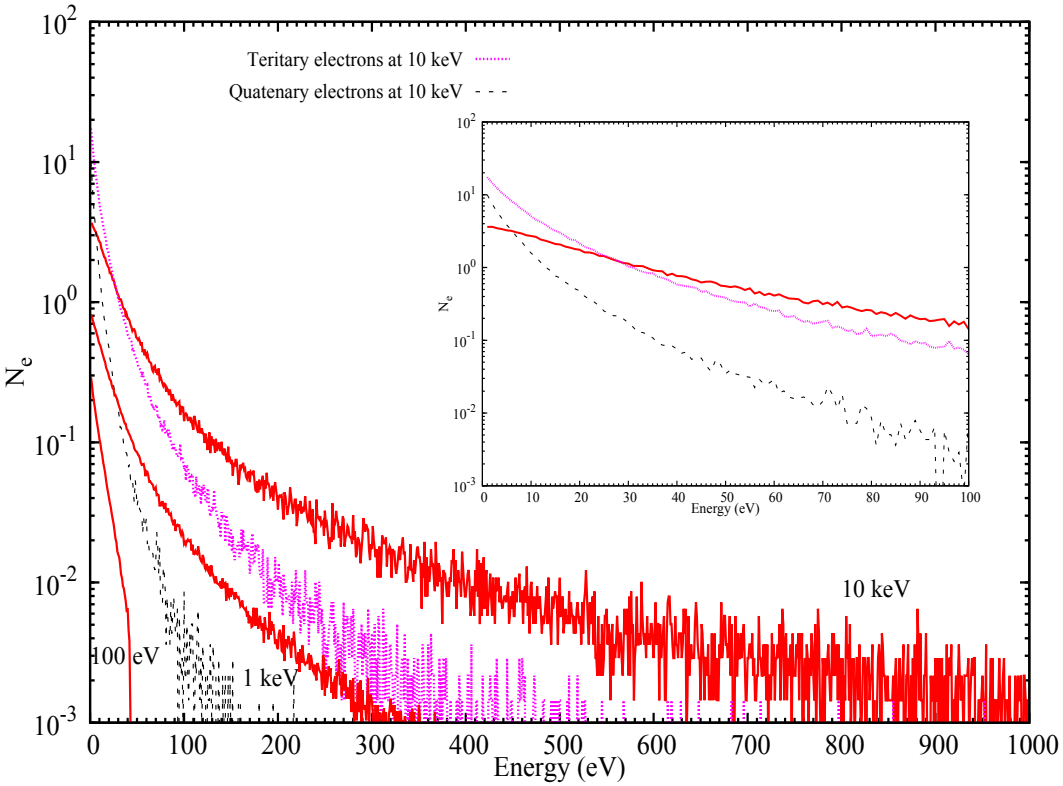

Figure 3.8: Energy Distribution of secondary electrons for incident energies 100 eV, 1 keV and 10 keV. Verical axis shows the number of secondary electrons produced per incident primary electron. Dotted and dashed curves show distribution of tertiary and quaternary electrons, respectively, for an incident energy of 1000 eV. The inset shows the energy distribution of secondary, teritary and quaternary electrons for an incident energy of 10 keV by zooming in the lower energy range.

3.4.4 Efficiency

The efficiency of various inelastic processes is calculated using numerical yield spectrum as well as AYS. Ionization efficiencies are shown in Figure 3.9. Because of its higher cross section, CH_4^+ production channel has the highest efficiency throughout the energy range, with an efficiency of 25.3% (23.6%) for an incident electron energy of 10 keV (100 eV). The other ionization channels CH_3^+, CH_2^+, CH^+, C^+, H_2^+ and H^+ have efficiencies of 20.8% (18.8%), 4.3% (4.1%), 2.5% (2.8%), 0.9% (1%), 0.5% (0.6%) and 4.4% (5%), respectively. At electron energies ≥100 eV, there is no significant variation in

these efficiencies. But at lower energies, especially near the threshold region, ionization efficiencies fall off very rapidly. At 18 eV, the efficiencies for the production of CH_4^+, CH_3^+ and CH_2^+ are 18.2%, 9.1% and 0.2%, respectively.

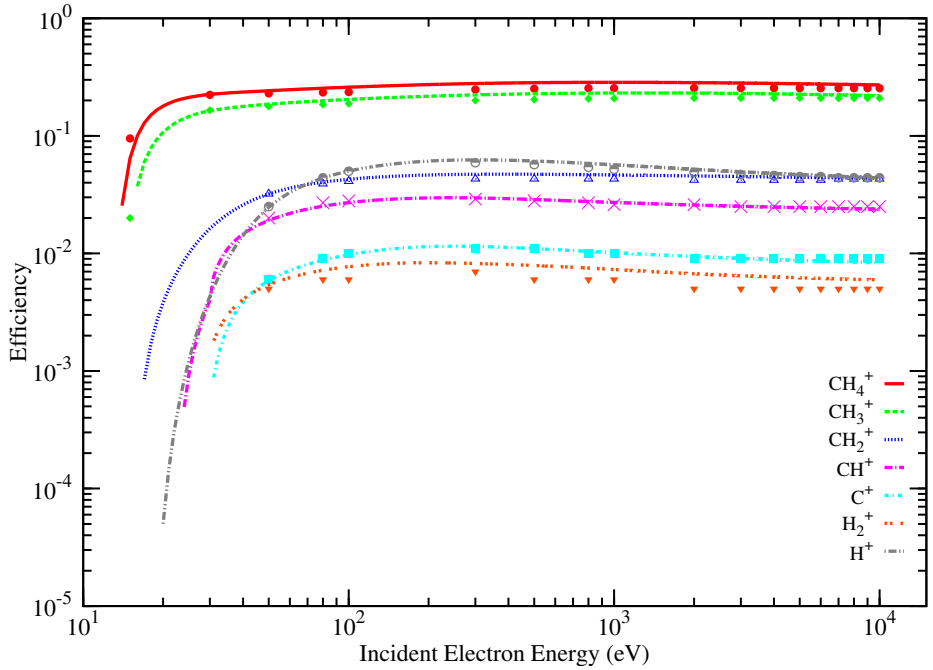

Figure 3.9: Efficiencies of various ionization processes. Symbols represent the efficiencies that are calculated using numerical yield spectra and solid lines are efficiencies calculated using AYS.

Figure 3.10 show efficiencies of various dissociation channels. Since the production of CH_3 radical has the highest cross section (cf. Figure 3.3), it has the highest efficiency with a value of 20.8% (21%) at 10 keV (100 eV). Efficiencies of CH_2 and CH production are 3.9% (3.7%) and 2.5%(2.6%) at 10 keV (100 eV). The dissociation efficiency is almost constant at energies >100 eV. At electron energy of 30 eV, CH_3, CH_2 and CH dissociation channels are having efficiencies 23.8%, 2.9% and 1.3%, respectively.

Efficiencies of various emission processes are shown in Figures 3.11. Only a small fraction of the incident electron energy goes to various emission channels with H Lyman-α emission having the highest efficiency of 0.43% (0.58%) at 10 keV (100 eV). For H Lyman-β and Lyman-γ emissions, efficiencies are 0.11% (0.14%) and 0.05% (0.06%) at 10 keV (100 eV). The CH band emission has an efficiency of 0.25% (0.28%) at 10 keV (100 eV). Among the various line emissions of atomic carbon, the 165.7 and 156.1 nm emissions have almost the same efficiencies at all energies, with a value of 0.033% (0.04%) and 0.031% (0.03%) at 10 keV (100 eV), respectively. The carbon 193.1 nm emission has an efficiency of 0.02% at 10 keV. As there is a large uncertainty in the value of C-line emission cross sections ($\pm$50%), the calculated value of efficiencies would also be uncertain by a similar amount.

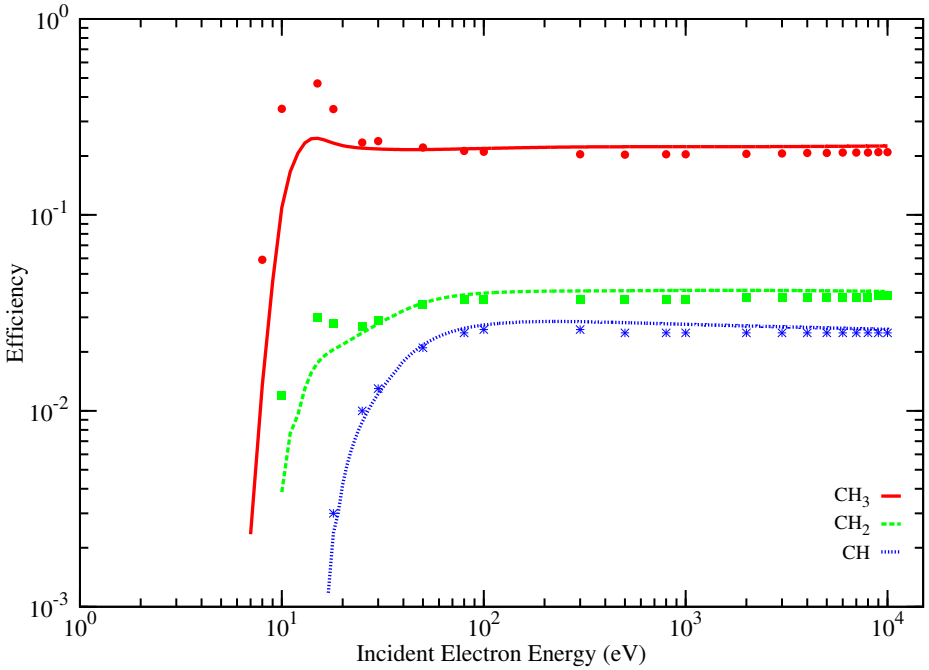

Figure 3.10: Efficiencies of various dissociation channels. Symbols represent the efficiencies that are calculated using numerical yield spectra and solid lines are efficiencies calculated using AYS.

In Figure 3.12 an overall picture of the efficiencies of various inelastic loss processes is presented. Efficiency values calculated using both the numerical yield spectrum as well as the AYS are shown; a good match is observed between the two efficiency values at energies greater than 10 eV. Efficiency calculated using the AYS for energy <10 eV would be only an approximate as the AYS is not able to represent well the numerical yield spectrum in this region. Hence, the efficiency of vibration process shown in Figure 3.12 is calculated only using the numerical yield spectrum. Among the different loss processes, ionization is found to be the dominant process above 30 eV. Above 100 eV, the ionization efficiency attains a constant value of 54%. The dissociation efficiency is constant at energies above 30 eV with a value of 27%. The emission efficiency is 1.2% (1.6%) at 10 keV (100 eV). All through the energy range, only a very small fraction of the incident electron energy is channelled into the attachment process. The attachment efficiency peaks at 10 eV and has a value of 0.14%.

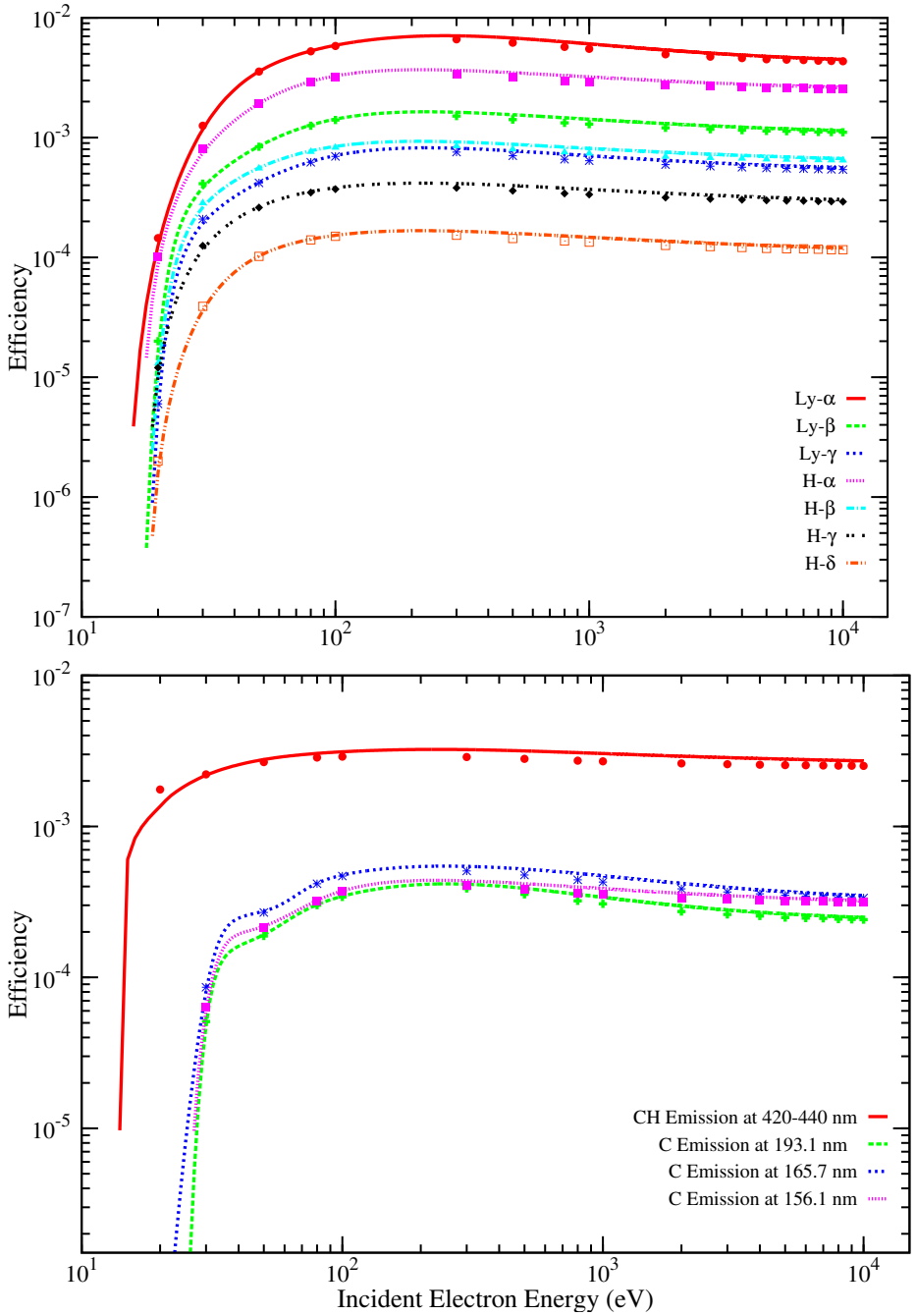

Figure 3.11: Efficiencies of various emission channels. Symbols represent the efficiencies that are calculated using numerical yield spectra and solid lines are efficiencies calculated using AYS.

3.5 Summary

In the present Chapter, a Monte Carlo model for studying the degradation of 1-10,000 eV electrons in methane gas in presented. Analytically fitted cross sections are used as input to the model. The numerical yield spectra obtained as the output of the Monte Carlo model includes non-spatial information about the degradation process. The numerical yield spectrum is analytically fitted using equations given by *Green et al.*

[1977a] and *Bhardwaj and Jain* [2009]. Two new parameters are introduced to better fit the low energy (<10 eV) region of the numerical yield as described in equation 3.4, thus obtaining the Analytical Yield Spectra. The AYS is used to calculate mean energy per ion pair and efficiency of various loss channels. The mean energy per ion pair for CH_4 has a value 26 (27.8) eV at 10 (0.1) keV. The energy distribution of secondary electrons for a few incident energies is presented in Figure 3.8.

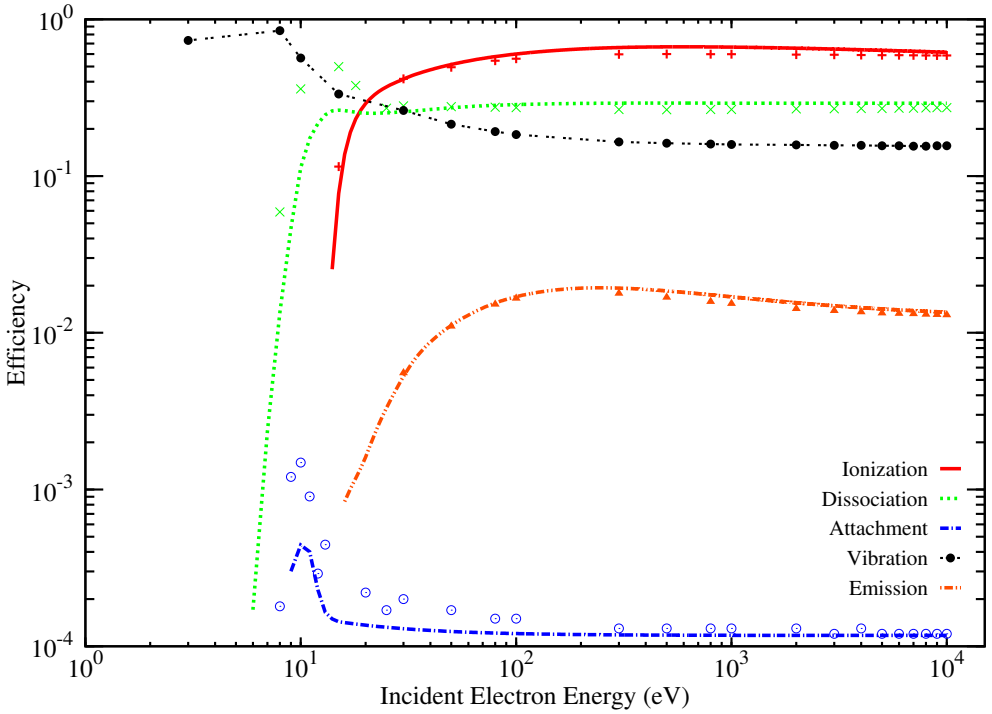

Figure 3.12: Efficiencies of various loss channels. Symbols represent the efficiencies that are calculated using numerical yield spectra and solid lines are efficiencies calculated using AYS. Vibrational efficiencies are calculated using numerical yield spectrum only.

Efficiency of a loss channel gives information on the amount of incident electron energy going into that loss process. Efficiencies are calculated using numerical yield spectrum as well as the AYS, and are found to be in good agreement for energy >10 eV. At energies <10 eV, vibration is the dominant loss process with an efficiency 80% at 8 eV. In this energy region, electron attachment process has an efficiency of 0.14%, which falls down to a very small value for energies >20 eV. From 25 eV onwards, dissociation process has an efficiency of 27%. At energies higher than 100 eV, ionization is the dominant loss process consuming more than 50% of the incident electron energy. In addition to the major inelastic processes, efficiencies are calculated for various emissions. The H Lyman-α emission has the highest efficiency among the various emission channels.

These efficiencies can be applied to planetary atmospheres for calculating volume production rates by multiplying with electron production rate and integrating over en-

ergy. These results will be useful for modeling of aeronomical processes in the planetary atmospheres where methane is a significant constituent.

Chapter 4

Photochemical model for the dayside ionosphere of Titan

4.1 Introduction

Energy degradation of electrons in CH_4 gas using Monte Carlo technique was discussed in the previous chapter. Yield spectrum, obtained as the output of the model, can be used to understand the e-CH_4 interactions in planetary atmospheres. As described in Section 3.2, CH_4 is a key constituent in the atmospheres of many outer solar system bodies, especially in the Saturnian moon Titan. Even though methane constitutes only 3-4% of Titan's atmosphere, the photochemistry in the upper atmosphere is largely governed by CH_4. When solar photons and other energetic particles collide with the major neutrals N_2 and CH_4 causing their photoionization or photodissociation, a suit of ions and radicals, like N_2^+, CH_4^+, CH_3^+, CH_3, etc, are formed. These products then start reacting with the background gases, thus initiating a chain of chemical reactions. The chemistry ultimately results in the formation of heavy hydrocarbon ions and neutrals along with free electrons. This has been discussed in detail in Chapter 1 (see section 1.3.1). In this chapter, a photochemical model for the dayside ionosphere of Titan is developed by using the yield spectrum generated for e-CH_4 collisions.

4.2 Model description

Photochemical models have been widely used for the study of upper atmospheric photochemistry in Titan's atmosphere (see section 1.4). The basic aim of these models is to calculate the densities of different chemical species and thus to have a better understanding of the atmospheric composition. The photochemical models for Titan's ionosphere can be classified into two:

(a) Models for calculating the plasma composition (ions and electrons) by considering a fixed background atmosphere and an extensive list of ion-molecule reactions [*Keller et al.*, 1992; *Vuitton et al.*, 2008]

(b) Models for calculating the neutral composition by considering neutral-neutral chem-

istry [*Dobrijevic et al.*, 2016].

The model that is developed in the present study belongs to the former category. Based on observations, the background neutral atmosphere and other physical parameters that control the chemistry are held fixed. Then, the one-dimensional continuity equation is solved for the species of interest. The rate of change of number density, n_i, of the i^{th} ion species is given by the continuity equation:

$$\frac{dn_i}{dt} + \bigtriangledown.\phi_i = P_i - L_i \tag{4.1}$$

where P_i and L_i are the production and loss rate of the ion per unit volume, and $\bigtriangledown.\phi_i$ represents the flux divergence due to ion transport. Under steady-state condition $dn_i/dt = 0$. The role of ionospheric transport (movement of plasma to the locations far from where they were created) and chemistry in controlling the ionospheric densities and composition has been studied by different authors, viz. *Ma et al.* [2006], *Cui et al.* [2010], and *Cravens et al.* [2010]. Their study showed that at altitudes less than 1400 km, the chemical life time of different ionic species is much less than their estimated transport time. Hence the transport is not important for estimating the plasma density in this regime. This region is known as photochemical equilibrium region. Thus, under steady-state condition, in the photochemical equilibrium region, the continuity equation reduces to:

$$P_i = L_i \tag{4.2}$$

As the constituents of the upper atmosphere are not well mixed, this equation is solved for each ion species at each altitude independently for calculating the densities.

The plasma within Titan's dayside ionosphere originates mainly from the ionization of atmospheric neutrals by solar UV photons and photoelectrons [*Cravens et al.*, 2005; *Robertson et al.*, 2009; *Galand et al.*, 2010]. Thus, to calculate the ion production rates, it is essential to know the available photon flux and photoelectron flux at each altitude. As the photons propagate through the atmosphere they get absorbed by atmospheric neutrals. The photoabsorption process include ionization, excitation and dissociation. Using Beer-Lambert law, the amount of available photon flux at each altitude can be obtained. The ionization rate or the photoelectron production rate is then calculated by multiplying the photon flux with the neutral density and their corresponding photoionization cross sections. The photoelectrons once generated in the atmosphere, degrade their energy by interacting with the atmospheric gases. The steady-state photoelectron flux is calculated by using the AYS approach. Once the photon and photoelectron fluxes are obtained, the ion production rates can be calculated.

The ion production rates through photon/photoelectron impact ionization, along with the neutral atmosphere and electron temperature profile, are used as input to a photochemical model which simulates the ion-neutral chemistry. The production and destruction reactions of different ionic species are described. In the photochemical

equilibrium region, the plasma is lost through ion-electron dissociative recombination reactions. During such reactions, an electron combines with an ion and result in the formation of neutrals. Although ions can get removed through chemical reactions, such reactions will cause the generation of another ion, and thus will not remove plasma from the atmosphere. While the primary ions such as N_2^+, N^+, CH_4^+, etc get converted to heavier ions through ion-neutral chemistry, the terminal ions, which are the byproducts of the chemistry, are depleted through recombination reactions. By balancing ion production rates and loss rates at each altitude, the model produces ion densities as a function of altitude.

The photochemical model that is developed to calculate the plasma density profiles on the dayside ionosphere of Titan is discussed in the present chapter. The Cassini mission made extensive measurements of Titan's ionosphere, both on dayside and nightside, and collected enormous data. This made it possible to use in-situ measured data as input to the model. Since the current study is on the dayside ionosphere, we initally focuses on the T40 flyby of Cassini orbiter that occurred on 5 January 2008. The T40 was a complete dayside flyby where both inbound and outbound legs of the flyby were on Titan's dayside. The altitude of closest approach was 1010 km above the surface with a SZA of 37.2°. The model calculated plasma density profiles are finally compared with the Cassini observations during T40. The model inputs are presented in section 4.3 and the model results are discussed in section 4.4.

4.3 Model inputs

4.3.1 Solar flux

Solar flux in the UV and X-ray regime is the basic driving force for the photoionization process. Hence solar flux forms a crucial input to any upper atmosphere models. The Extreme Ultraviolet Spectrometer (EUVS) on board the Atmospheric Explorer satellites was the first instrument to measure the solar flux in wavelength range 14-185 nm. Based on this measurements, *Hinteregger et al.* [1981] developed an aeronomic reference spectrum, F74113, for the day 23 April 1974, suitable for the solar minimum condition. But this reference spectrum was not able to reproduce the absolute values of the observed photoelectron fluxes at solar minimum [*Richards and Torr*, 1984, 1988]. *Richards et al.* [1994] developed a solar flux model called EUV flux model for Aeronomic Calculation (EUVAC) using this F74113 reference spectrum. In this model, the flux in the wavelength range 12-25 nm was increased by a factor of 2 and below 12 nm the flux was increased by a factor of 3 to have a better agreement between the calculated and observed photoelectron flux of *Winningham et al.* [1989] at solar minimum. The model provides flux for the wavelength range 50-1055 Å in 37 wavelength bins having a width of 50 Å and at a few important solar emission lines. EUVAC uses the 10.7 cm solar radio

flux (F10.7) and its 81-day average value ($F_{av}10.7$) as proxies. A new high resolution version of the EUVAC model called HEUVAC was published by *Richards et al.* [2005]. This version extended the EUV model below 5 nm. The current study uses the flux from HEUVAC model. The solar flux in the wavelength range 1 to 1055 Å is used for 5 January 2008, with an F10.7 value of 77.1 and $F_{av}10.7$ value of 69.4 [*Westlake et al.*, 2012] and with a bin resolution of 10 Å. The flux is reduced by $1/r^2$, where r is the mean Sun-Titan distance which is 9.5 AU to account for the weaker flux at Titan. Figure 4.1 shows the HEUVAC solar flux at 1 AU on 5 January 2008.

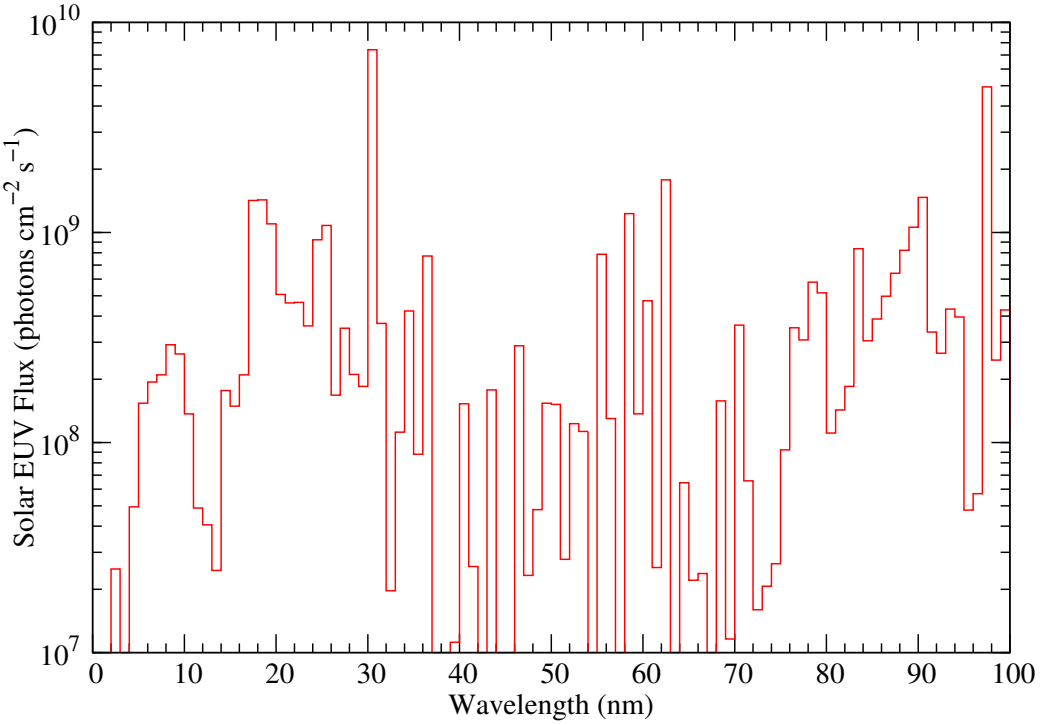

Figure 4.1: The HEUVAC model solar flux at 1 AU on 5 January 2008.

4.3.2 Neutral densities

As the solar radiation passes through the atmosphere, it is attenuated mainly by the absorption caused by the major atmospheric neutrals N_2 and CH_4. During the T40 flyby, the INMS measured the density profiles of major atmospheric gases N_2, CH_4, and H_2. In the present study, the density profiles of these gases are taken from *Mandt et al.* [2012] which are simulated using an ion neutral thermal model for the conditions relevant for T40. These densities are in good agreement with the neutral densities measured by INMS (see Figure 4.2). In addition to the major constituents, the photochemical model requires the density profiles of the minor atmospheric species as well. Following the methodology of *Richard et al.* [2015], we have used the mixing ratio profiles of 15 minor species given by *Krasnopolsky* [2009] (except for CH_2NH which is taken from *Lavvas et al.* [2008]) after shifting the profiles to make them consistent with the global average

mixing ratios as given by *Magee et al.* [2009], *Cui et al.* [2009] and *Robertson et al.* [2009] (See Figure 4.3).

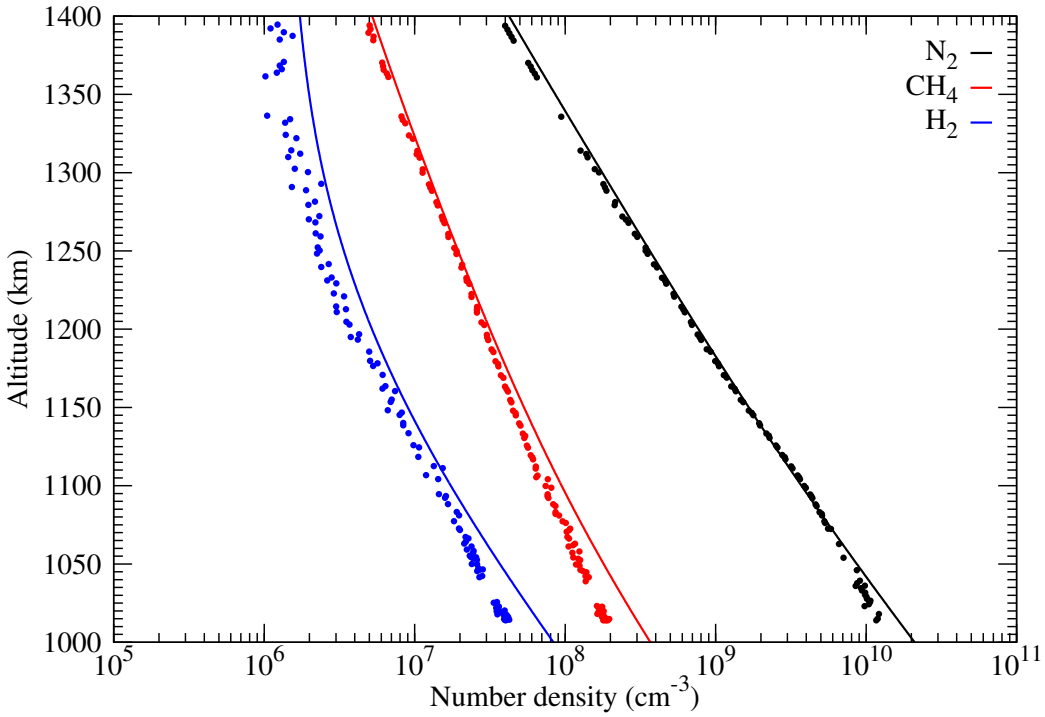

Figure 4.2: The density profiles of the major atmospheric species N_2, CH_4, and H_2 used in the model. The symbols show the profile measured by the INMS during T40 flyby.

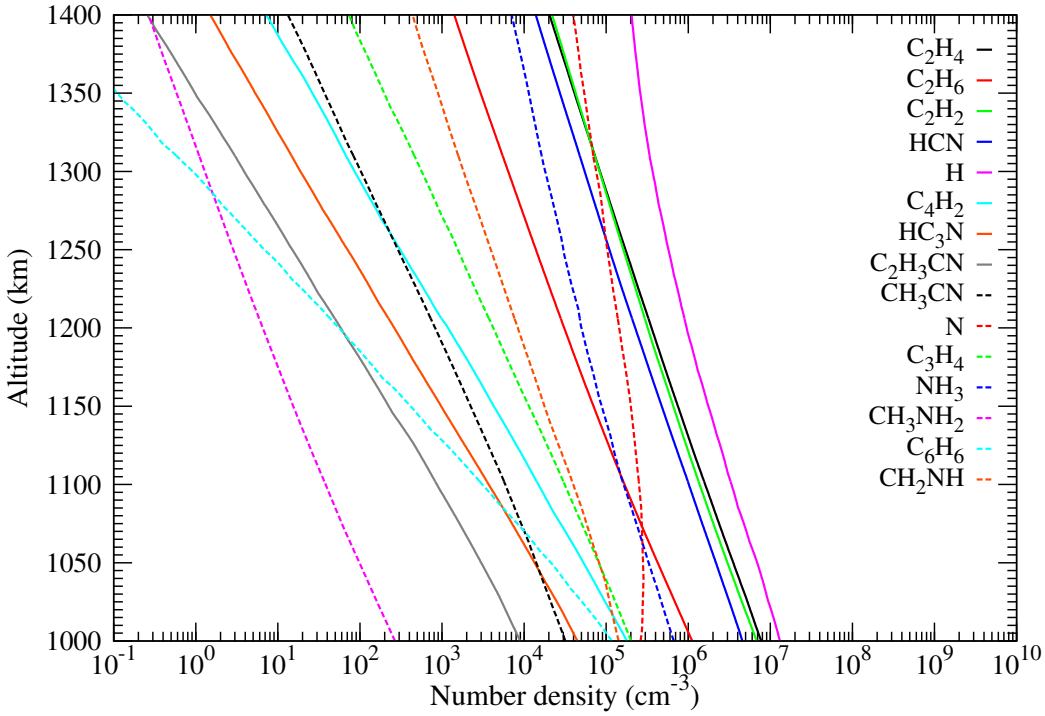

Figure 4.3: The density profiles of 15 minor species used in the model.

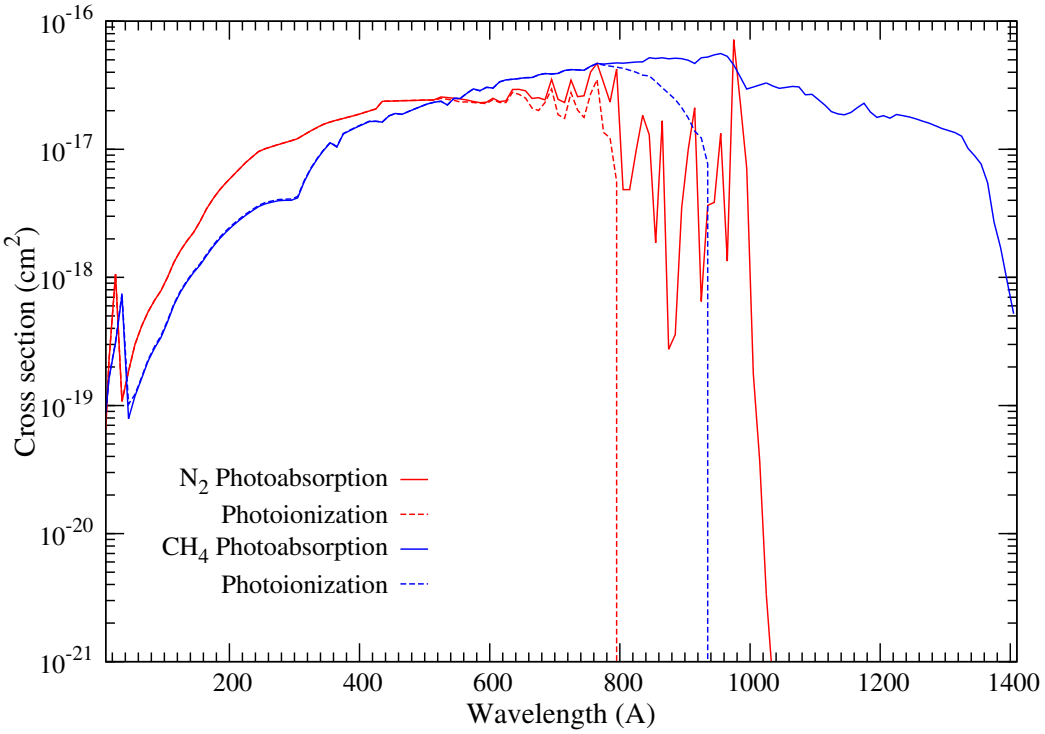

Figure 4.4: Photon impact cross sections of N_2 and CH_4 used in the model.

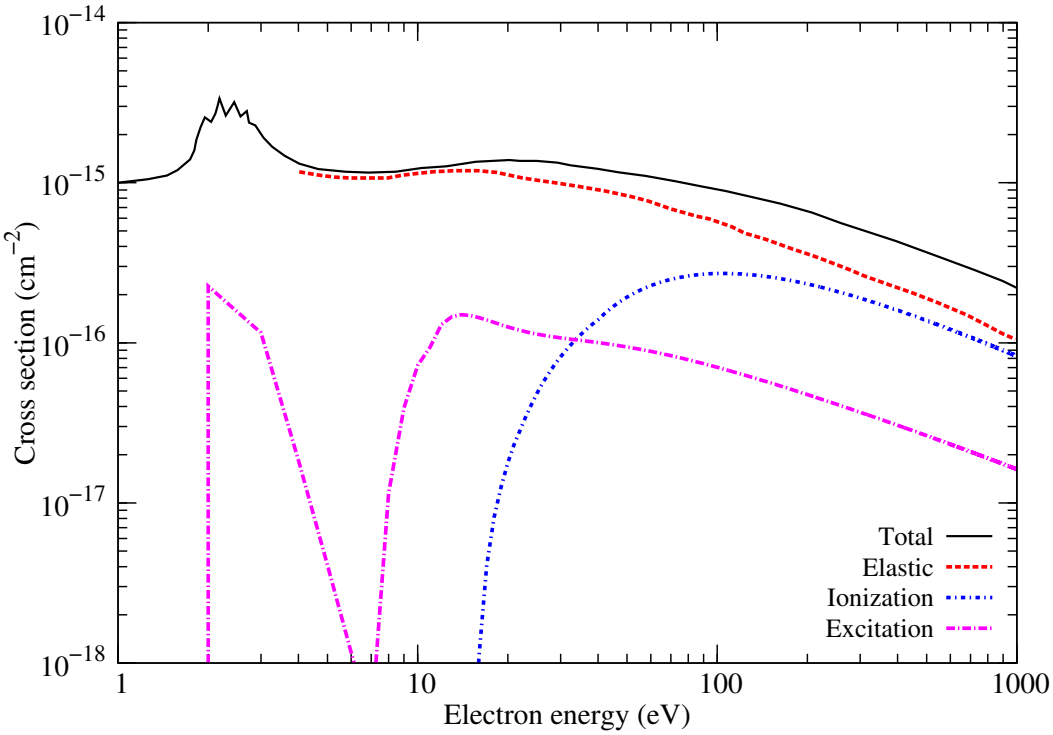

Figure 4.5: Electron impact cross sections of N_2 used in the model.

4.3.3 Cross sections

Cross sections of the major atmospheric constituents due to photon and electron impact are important inputs for calculating the attenuated solar flux and photoelectron

flux in Titan's upper atmosphere. Photoabsorption and photoionization cross sections of N_2 and CH_4 used in the model are the same as that in *Bhardwaj and Jain* [2012] in which photo-cross sections are taken from the database http://amop.space.swri.edu [*Huebner et al.*, 1992]. Photo cross sections for the H_2^+ and C^+ production channels of CH_4 are taken from *Lavvas et al.* [2011]. Inelastic cross sections for the electron impact on N_2 are taken from *Bhardwaj and Jain* [2012]. The electron impact cross sections of CH_4 are the same as that discussed in Chapter 3. The photon cross sections of N_2 and CH_4 and the electron impact cross sections of N_2 used in the present study are shown in Figures 4.4 and 4.5, respectively.

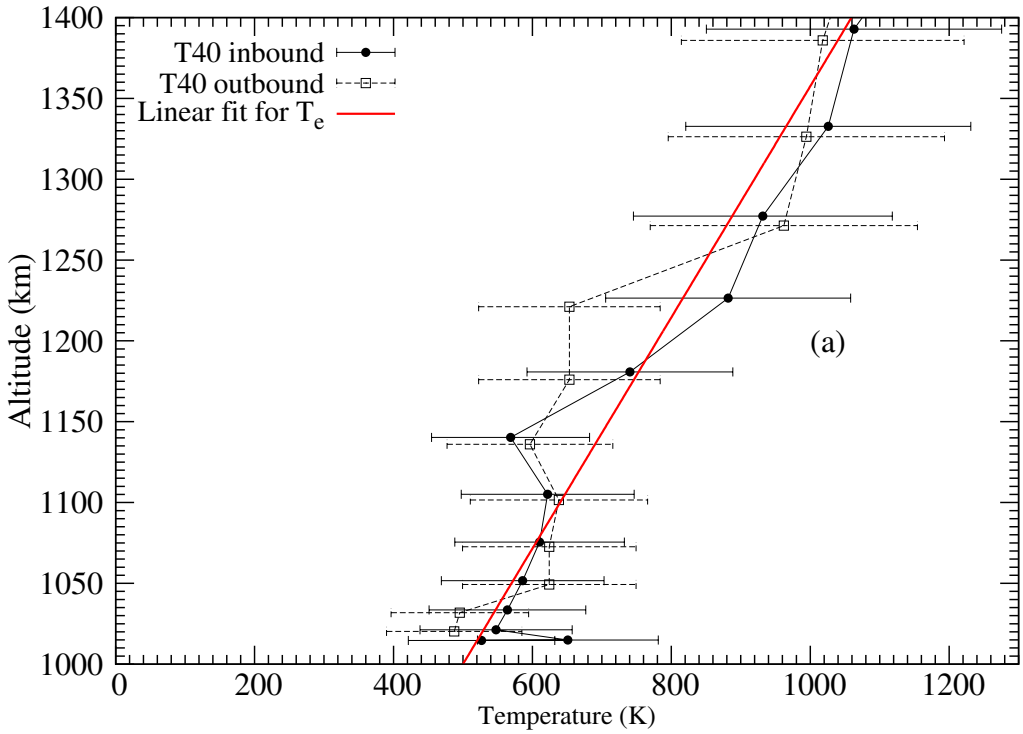

Figure 4.6: Electron temperature profile measured during T40 flyby. The solid line shows the linear fit for the electron temperature that is used in the current model.

4.3.4 Electron temperature

The electron temperature is required for calculating the loss rate of various ions via electron recombination reaction. Dissociative recombination reaction rate of an ion i at an altitude Z is calculated as:

$$R_{DR}(Z) = \alpha_i \, (\frac{300}{T_e(Z)})^{\beta} \tag{4.3}$$

where α_i is the dissociative recombination coefficient of the ion i, $T_e(Z)$ is the electron temperature at the altitude Z, and β is the temperature dependence factor. To obtain the electron temperature at each altitude, we have used the linear relation given by

Dobrijevic et al. [2016] as:

$$T_e(Z) = (1/0.715)(Z - 642.5) \tag{4.4}$$

where Z is the altitude in km. This linear relationship matches well with the RPWS/LP measured electron temperature during T40 flyby (see Figure 4.6).

4.3.5 Reaction rate coefficients

The reaction rate coefficients for the various ion-neutral reactions used in the model are primarily based on *McEwan and Anicich* [2007] and *Vuitton et al.* [2007]. The dissociative electron recombination coefficients and the temperature dependent factors are the same as that in *Richard* [2013]. The list of reactions, along with their rate coefficients that has been used in the present study is shown in the Appendix section.

4.4 Model results

4.4.1 Photoelectron production rate

The photoelectrons are produced in the atmosphere via photoionization process. The initial energy spectrum of the photoelectrons largely reflects the spectral distribution of solar flux. However, many distortions can be seen on the photoelectron energy spectrum due to the different ionization thresholds and energy states of atmospheric gases. The photoelectron production rate or the primary photoelectron energy spectrum at an altitude Z can be calculated as:

$$Q(Z, E) = \sum_l n_l(Z) \sum_{j,\lambda} \sigma_l^{ion}(j, \lambda)\ I(Z, \lambda) \tag{4.5}$$

Here $n_l(Z)$ is the density of the neutral constituent l at altitude Z, $\sigma_l^{ion}(j, \lambda)$ is the photoionization cross section of the j^{th} ionization state of the l^{th} constituent at wavelength λ and I(Z, λ) is the attenuated solar flux of wavelength λ available at altitude Z. It can be obtained using the Beer-Lambert law as:

$$I(Z, \lambda) = I(\infty, \lambda)\ exp[-\tau(\lambda, Z)] \tag{4.6}$$

where $I(\infty, \lambda)$ is the unattenuated solar flux of wavelength λ reaching the top of the atmosphere and τ is the optical depth. The optical depth is a measure of the degree of attenuation that has occurred when the radiation has reached the altitude Z after passing through the atmosphere. It is calculated as

$$\tau(\lambda, Z) = sec(\chi) \sum_l \sigma_l^a(\lambda) \int_Z^\infty n_l(Z')dZ', \tag{4.7}$$

where σ_l^a is the total photoabsorption cross section of the constituent l at λ, and χ is the SZA. In the above equation, $sec(\chi)$ is used instead of Chapman function $Ch(\chi)$ which is a valid approximation for zenith angles up to 75° [*Schunk and Nagy*, 2009].

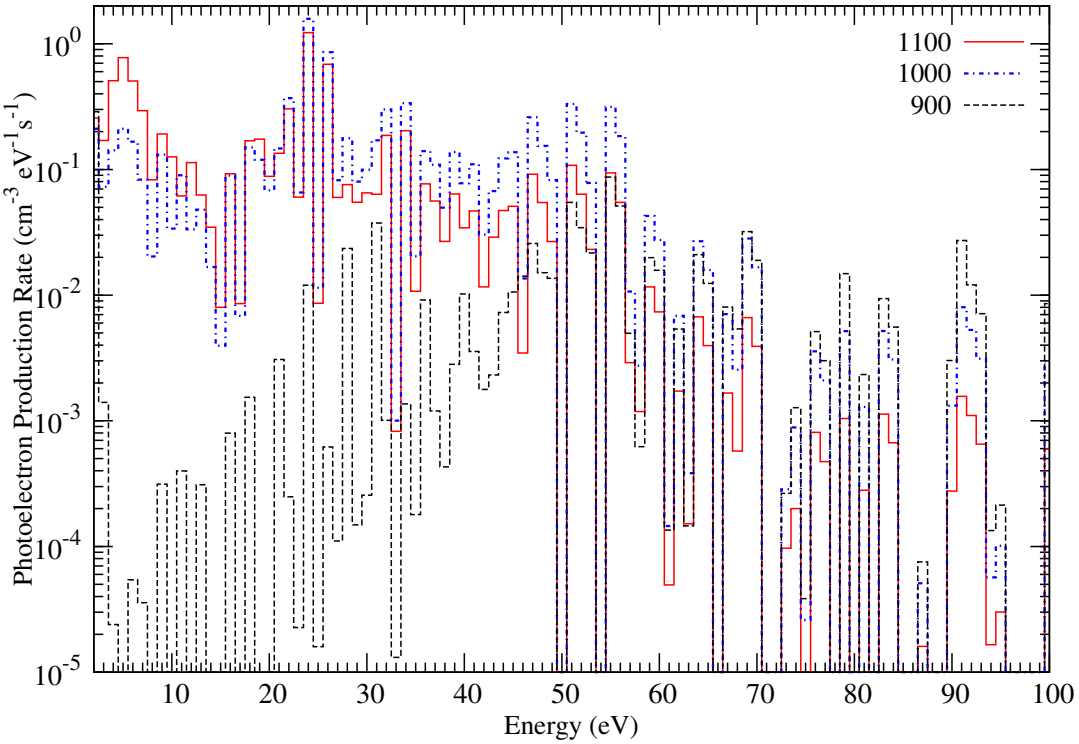

Figure 4.7: Calculated primary photoelectron energy spectra at three different altitudes of 900, 1000 and 1100 km, for a SZA of 37^o.

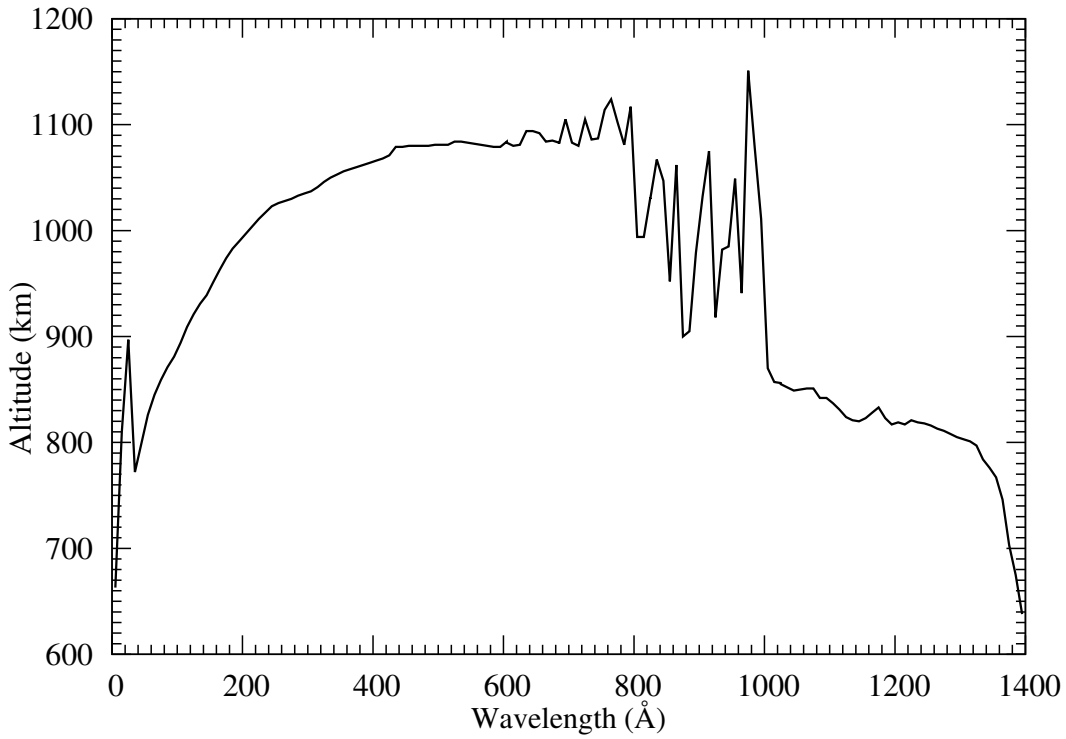

Figure 4.8: The altitude of unit optical depth for a SZA of 37° at different wavelengths in Titan's atmosphere.

Figure 4.7 shows the calculated photoelectron production rate for three different altitudes, for a SZA of 37^o. The photoelectrons are released at each altitude with a range of energies. The sharp peak at ∼24 eV is due to the ionization of N_2 by intense solar HeII lines at 303.8 Å. For a radiation of wavelength λ, the maximum absorption occurs at that altitude where the optical depth is unity. The altitude of unit optical depth for the solar flux wavelength range used in the current model is shown in Figure 4.8, for a SZA of 37°. The shape of the curve closely resembles the photoabsorption cross section of N_2 (refer Figure 4.4). The photoabsorption threshold of N_2 is 12.14 eV (1021 Å). The radiation larger than this wavelength is mainly absorbed by CH_4. The high energy photons (<200 Å) can penetrate deep into the atmosphere and thus have altitude of unit optical depth at <900 km. Ionization caused by these photons can generate photoelectrons having energy >50 eV. Hence, the high energy photoelectrons are more at lower altitudes. Low energy electrons (<30 eV) are more at higher altitudes as they are produced by photons of $\lambda > 275$ Å whose altitude of unit optical depth is above 1000 km.

4.4.2 Photoelectron flux

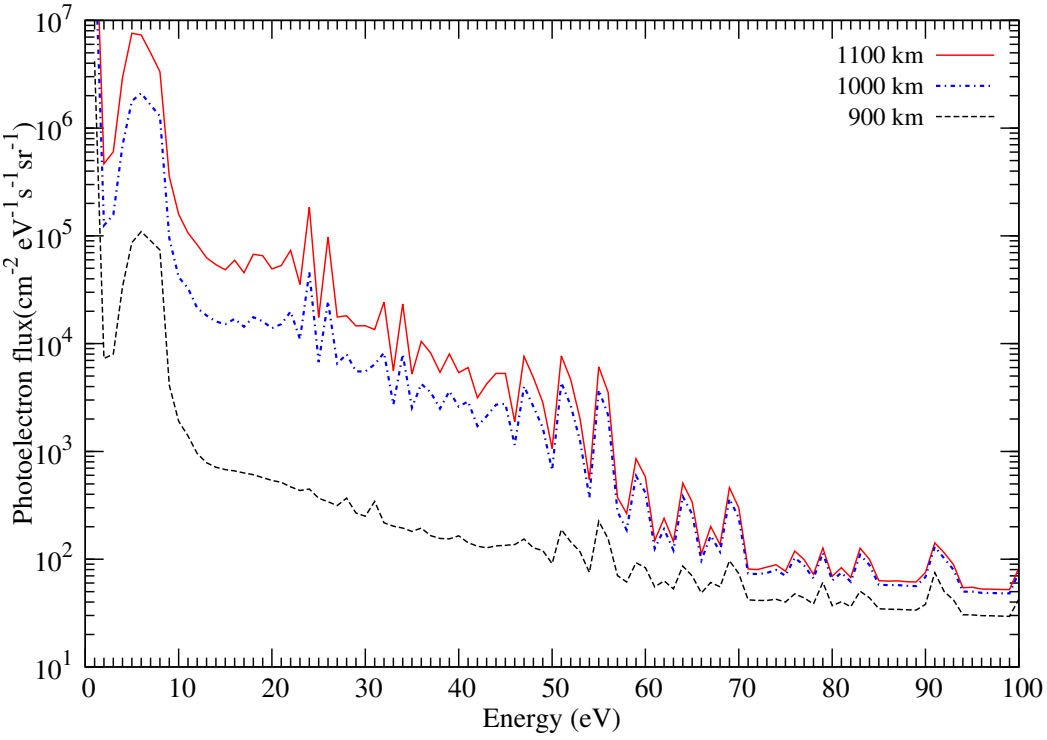

Figure 4.9: Calculated photoelectron flux at three different altitudes of 900, 1000 and 1100 km, for a SZA of 37^o.

The primary photoelectrons generated in the atmosphere during photoionization lose their energy by colliding with the background neutrals. Using the AYS approach, we

calculate the degraded electron spectrum. The photoelectron flux is calculated as:

$$\psi(Z,E) = \int_{E}^{500} \frac{Q(Z,E)\ U_c(E,E_0)}{\sum_l n_l(Z)\ \sigma_l(E)}\ dE_0 \tag{4.8}$$

Here Q(Z, E) is the photoelectron production rate at altitude Z which is calculated using equation (4.5). $U_c(E, E_0)$ is the composite yield spectrum, which is the yield spectrum of a mixture of gases. It is obtained as:

$$U_c(E,E_\circ) = \sum_l f_l\ U_l(E,E_\circ) \tag{4.9}$$

where

$$f_l = \frac{\rho_l n_l}{\sum_l\ \rho_l n_l} \tag{4.10}$$

Here U_l(E, $E_\circ$) is the yield spectrum for individual gases, n_l is the number density of l^{th} gas, and ρ_l is the average value of the total inelastic cross section of the l^{th} gas between E and E_0. The yield spectrum U(E, $E_\circ$) represents the equilibrium number of electrons per unit energy at an energy E resulting from the local degradation of an incident electron of energy E_0. Since the most abundant gases in the atmosphere of Titan are N_2 and CH_4, the yield spectrum of these gases are required to calculate the composite yield spectrum. For N_2, we have used the AYS given by *Singhal et al.* [1980] as:

$$U(E,E_0) = C_0 + C_1\ E_k + C_2\ E_k^2 \tag{4.11}$$

where

$$E_k = \frac{(E_0/1000)^\Omega}{E+L} \tag{4.12}$$

C_0, C_1, C_2, and Ω the fitted parameters which are independent of the energy and have values 0.0166, 5.04, 169.0, and 0.585, respectively. L is an intrinsic parameter and is set as 1 eV. The yield spectrum of methane has already been presented in Chapter 3. Once the composite yield spectrum is obtained, photoelectron flux is calculated using equation 4.8.

Figure 4.9 shows the calculated photoelectron flux for three different altitudes. For all altitudes, flux is maximum for electrons having energy <10 eV. The peak at ∼24 eV, which occurs due to the ionization of N_2 by HeII line, is seen in the degraded spectrum as well. At 900 km, this peak seems to be absent which indicates that the HeII photons at 303 Å get absorbed at higher altitudes. The decrease in the flux of photoelectrons having energy >50 eV is due to the corresponding decrease in the production rate of these high energy photoelectrons. This is caused by the drop in the solar EUV flux and the ionization cross sections at shorter wavelengths. Figure 4.10 shows a comparison of the photoelectron flux calculated using the current model with that of CAPS-ELS observations and previous models. Our calculated flux is consistent with the calculations

of *Lavvas et al.* [2011] and *Richard et al.* [2015]. The measured photoelectron flux peaks at an energy slightly lower than the modelled values. *Lavvas et al.* [2011] pointed out that this occurs due to the low value of the spacecraft potential (-0.5 V) used in the retrieval of photoelectron flux from CAPS/ELS observation. *Lavvas et al.* [2011] suggested a higher value of -1.2 eV for the spacecraft potential based on the location of HeII peak. If the CAPS/ELS observations are shifted by 1.2 eV to account for the spacecraft potential during the time of measurement, there is a better agreement between the peak of the modelled and measured photoelectron flux.

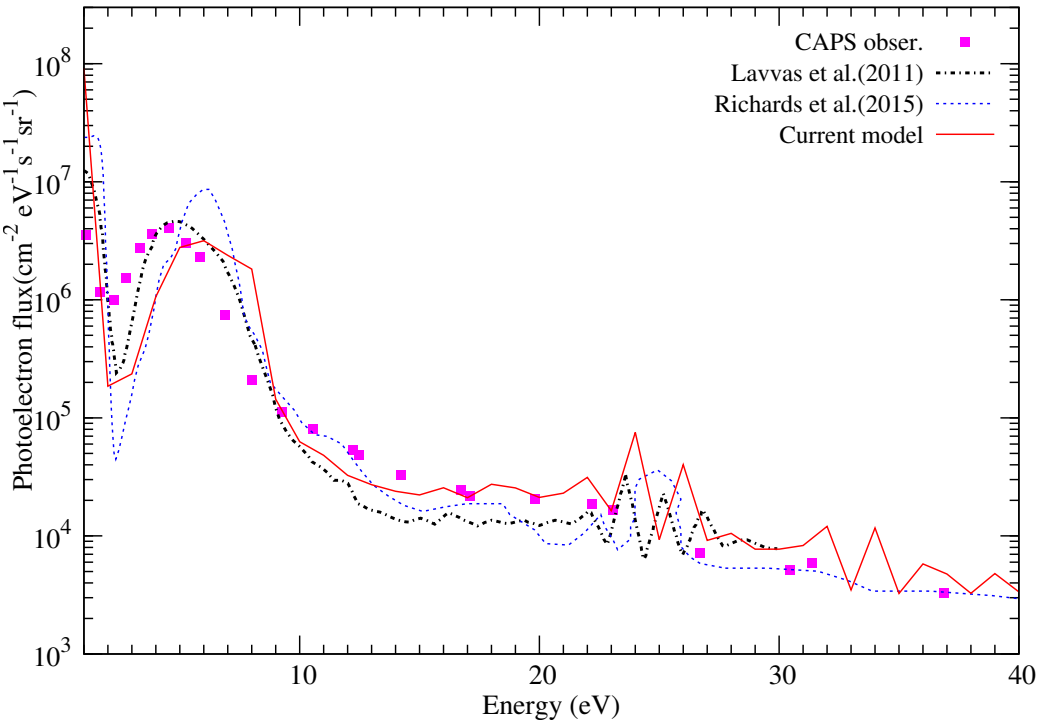

Figure 4.10: Calculated photoelectron flux at 1020 km compared with Cassini CAPS observation (obtained from *Richard et al.* [2015]) and calculations of *Lavvas et al.* [2011] and *Richard et al.* [2015] for the T40 flyby.

4.4.3 Volume Production Rates

The direct product of the photoionization in Titan's ionosphere are the ions N_2^+, N^+, CH_4^+, CH_3^+, CH_2^+, C^+, H_2^+, and H^+. These ions can be generated by electron impact ionization as well. Once produced, they are lost through ion-molecule reactions. The production rate of the primary ions through photon impact and photoelectron impact can be calculated as:

$$V_i(Z) = n_l(Z) \int \varphi(Z, E)\ \sigma_{il}(E)\ dE \tag{4.13}$$

where n_l(Z) is the density of the parent neutral species, φ(Z, E) is the photon/photoelectron flux at the altitude Z and energy E, and σ_{il} is the photoionization/electron impact

ionization cross section for ion species i being produced from neutral species l at energy E.

The production rates of the major primary ions N_2^+, N^+, CH_4^+, and CH_3^+ for a SZA of 37° are shown in Figure 4.11. For the major primary ion N_2^+, the maximum production rate (15 cm^{-3} s^{-1}) occurs at an altitude of ∼1040 km. Whereas for N^+, the peak production (2 cm^{-3} s^{-1}) occurs at lower altitudes (∼980 km) because the higher energy photons that are required to cause the dissociative ionization of N_2 can penetrate to these altitudes. The CH_4^+ production rate profile shows a flattened peak with a value of ∼0.4 cm^{-3} s^{-1} between 850 km and 1000 km, a feature which is also seen in the calculated production rate profile of *Richard et al.* [2015] and *Lavvas et al.* [2011]. This is because molecular nitrogen does not absorb much photons having wavelength ∼900 Å, the wavelength region where CH_4^+ production has maximum cross section. This allows more photons with energy near the ionization threshold of CH_4 to penetrate deeper into the atmosphere and produce an extended peak [*Richard*, 2013]. For CH_3^+, the peak production (0.2 cm^{-3} s^{-1}) occurs at around 1030 km. For the minor ions, viz. CH_2^+, CH^+, C^+, H_2^+, and H^+, which are produced through the dissociative ionization of methane by photon/photoelectron impact, the altitude of peak production occurs at 1036 km, 1009 km, 1009 km, 1011 km, and 1014 km with the peak values 0.02, 0.008, 0.001, 0.001, and 0.01 cm^{-3} s^{-1}, respectively (see Figure 4.12).

In Figure 4.13, we have compared the production rates of major primary ions N_2^+, N^+, CH_4^+ and CH_3^+ with the calculations of *Lavvas et al.* [2011] and *Richard et al.* [2015] for a SZA of 60^o. For N_2^+, the peak value of 9 cm^{-3} s^{-1} occurs at ∼1065 km which is consistent with the calculations of *Richard* [2013] who obtained a value of 8 cm^{-3} s^{-1} at ∼1070 km, whereas *Lavvas et al.* [2011] obtained a value of 5 cm^{-3} s^{-1} at the same altitude. The secondary peak at ∼900 km occurs due to the ionization caused by solar x-ray photons and photoelectrons having energy >100 eV, which is seen in all three profiles. For N^+, the peak value calculated by *Lavvas et al.* [2011] and *Richard* [2013] (1.4 cm^{-3} s^{-1}) are ∼40% higher than that of the current model. The altitude of peak production for N^+ is also slightly low as compared to the altitudes obtained by the other two models. The difference between the production rate values calculated by *Lavvas et al.* [2011], *Richard et al.* [2015] and the present study is mainly caused by the difference in the photoionization cross sections of N_2. The photo cross sections for N_2^+ production that we have used is around 10 to 20% higher than that of *Lavvas et al.* [2011] in the wavelength range 200-600 Å whereas as, those used by *Richard et al.* [2015] are in good agreement with our values. For N^+, our photo cross sections are lower than that of *Lavvas et al.* [2011] and *Richard et al.* [2015] up to a maximum of one order of magnitude at few energies. For the major ionization products of methane, viz. CH_4^+ and CH_3^+, the difference between our calculated peak values and that of *Lavvas et al.* [2011] and *Richard* [2013] is less than 20%. The higher value for the CH_4^+ production rate of *Lavvas*

et al. [2011] is due to the use of high resolution photoabsorption cross sections of N_2 in the wavelength range 840-1000 Å (The impact of high resolution photoabsorption cross sections of N_2 on the calculated volume production rates is discussed in the following section). Overall, our calculations are in agreement with the volume production rates calculated by models of *Richard* [2013] and *Lavvas et al.* [2011].

4.4.3.1 Impact of high resolution N_2 photo cross sections on volume production rate calculations

Many recent studies recommended the use of high resolution (HR) photoabsorption cross sections of N_2 in the wavelength range 845-1000 Å for the meticulous calculation of volume production rates [*Lavvas et al.*, 2011; *Mandt et al.*, 2012; *Sagnières et al.*, 2015]. Photons in this wavelength range are capable of ionizing CH_4 (whose ionization threshold is 945 Å or 13.12 eV) but have energies less than the ionization threshold of N_2 (796 Å or 15.57 eV). The fine structure of the HR cross sections of N_2 allows more photons in this wavelength region to pass through the atmosphere without getting absorbed by N_2. This enhances the ionization rate of CH_4 at lower altitudes as compared to the case when low resolution cross sections are used. To asses the impact of HR cross sections on our production rate calculations, we made test runs of the model using the HR N_2 cross sections derived by *Liang et al.* [2007] for the wavelength 840-1000 Å. We averaged these cross sections into 0.1 Å bins with appropriate solar flux taken from HEUVAC model.

The use of HR cross sections does not have any effect on the production rate of N_2^+ and N^+. However, enhancement in the CH_4^+ and CH_3^+ production rates are observed at altitudes below ∼1000 km as can be seen from the Figure 4.14a. Figure 4.14b shows a comparison between the CH_4^+ production rates calculated using the low resolution (LR) and HR photoabsorption cross sections of N_2 by *Lavvas et al.* [2011] and the current model for a SZA of 60^o. It can be seen that there is a closer match between our LR and HR profiles as compared to the profiles by *Lavvas et al.* [2011]. This occurs due to the difference in the LR photo cross sections adopted. *Lavvas et al.* [2011] have used the N_2 photoabsorption cross sections of *Samson et al.* [1987] while we used the photo cross sections by *Huebner et al.* [1992], the bin resolution being 10 Å in both studies. A comparison between these two cross sections, convolved into 10 Å bins, is shown in the Figure 4.14(c). The fine structures in the HR photoabsorption cross sections of N_2 are better represented by the LR 10 Å bin cross sections that we use as compared to the one used by *Lavvas et al.* [2011]. This explains the reason for the better agreement between our LR and HR profiles.

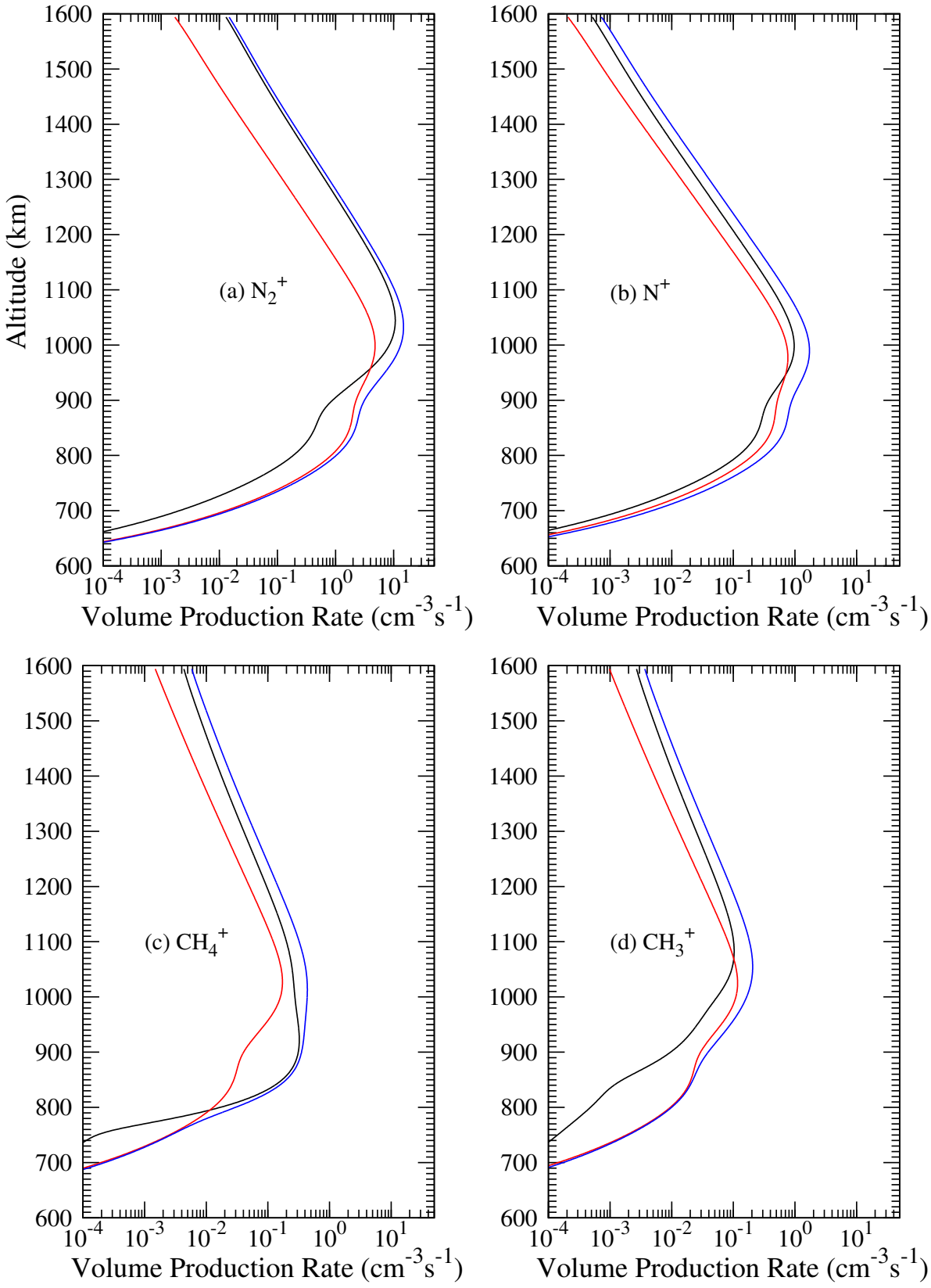

Figure 4.11: Volume production rates of the major primary ions N_2^+, N^+, CH_4^+, and CH_3^+ due to photon impact (black line) and photoelectron impact (red line) at a SZA of 37°. Blue line indicates the total ion production rates (photon + photoelectron).

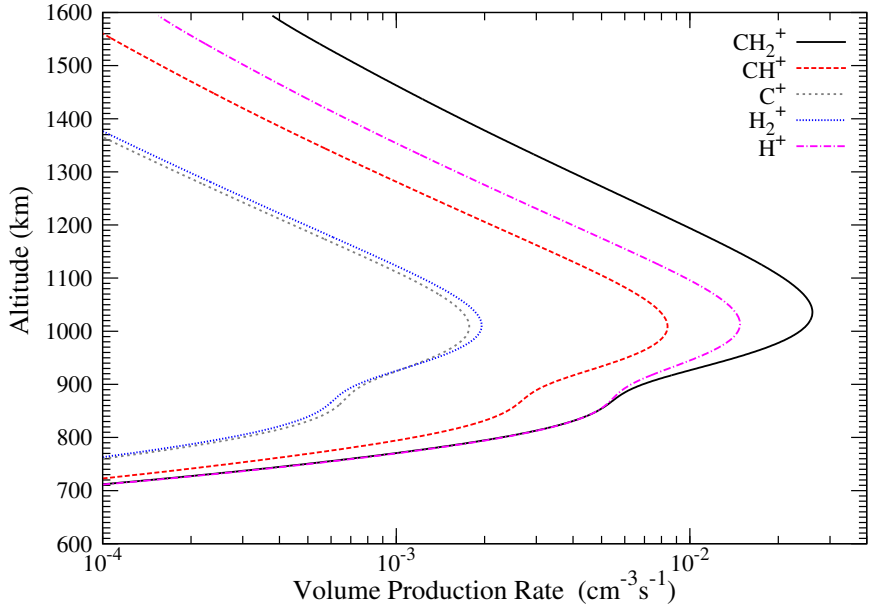

Figure 4.12: Total volume production rates of the minor primary ions CH_2^+, CH^+, C^+, H_2^+, and H^+ at a SZA of 37°.

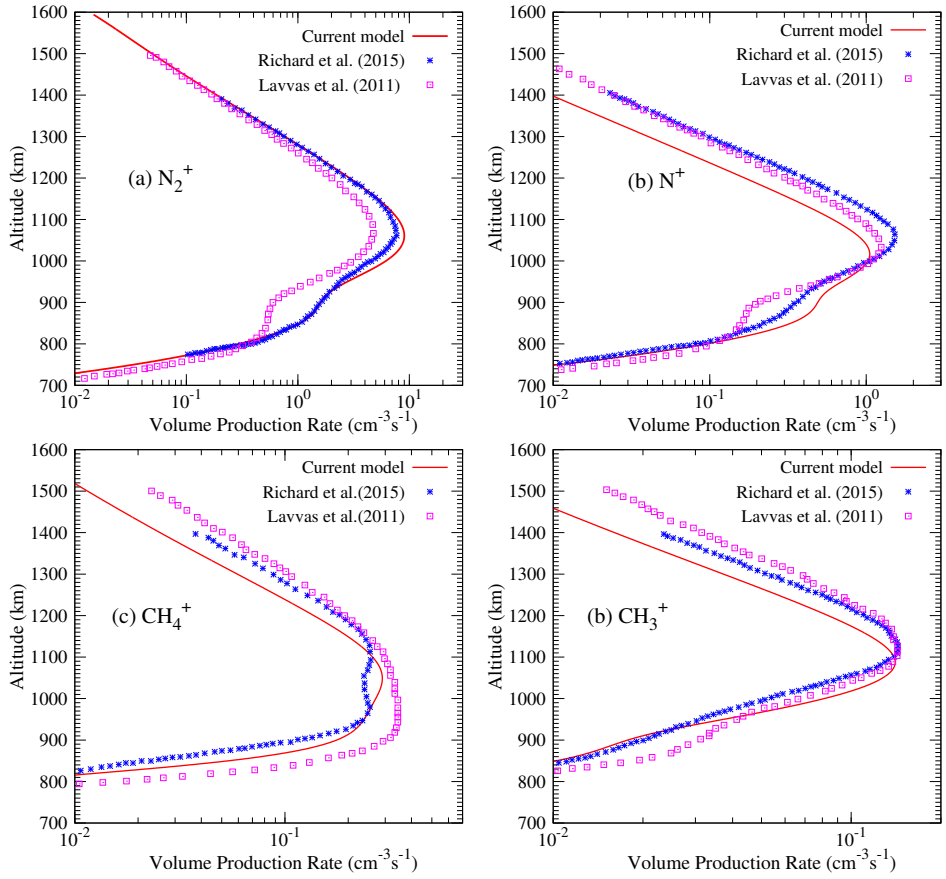

Figure 4.13: Volume production rates of major primary ions N_2^+, N^+, CH_4^+ and CH_3^+ calculated for a SZA of 60°. The symbols stars and open squares show the calculations of *Richard et al.* [2015] and *Lavvas et al.* [2011], respectively.

However, in the present study, the positive ion density profiles are calculated for altitudes above 1000 km. In this altitude regime the LR mode production rate values are consistent with those obtained in the HR mode. Hence, we continue using the volume production rates obtained in the LR mode itself for further calculations.

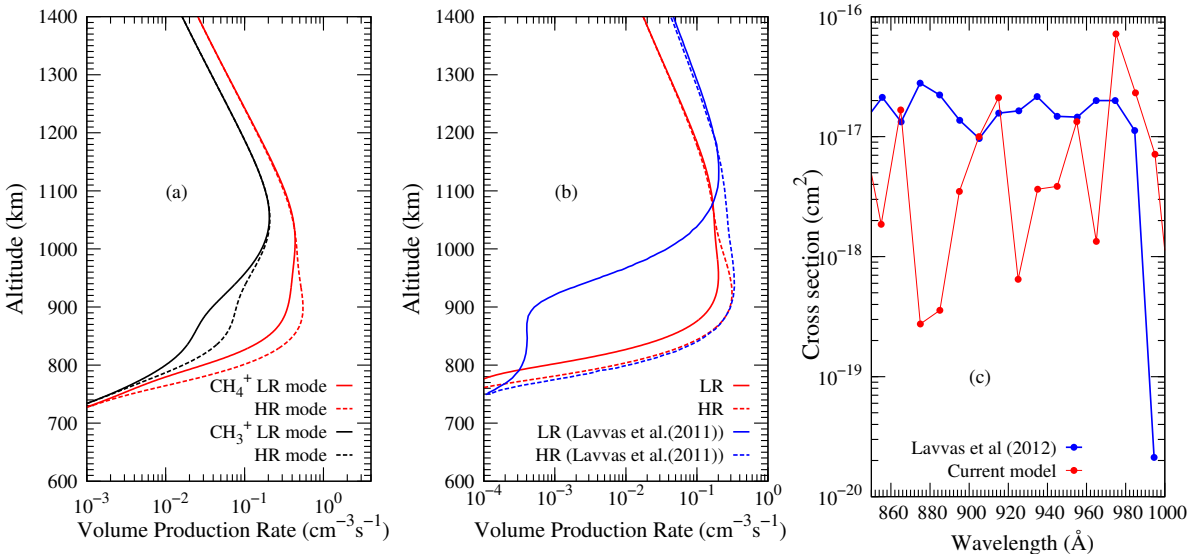

Figure 4.14: (a) Production rate of CH_4^+ and CH_3^+ ions for a SZA of 37°. Solid curves and dashed curves show the profiles obtained using low resolution (LR) and high resolution (HR) N_2 photoabsorption cross sections, respectively. (b) Comparison between CH_4^+ production rates calculated by *Lavvas et al.* [2011] (blue lines) and current model (red lines) at a SZA of 60^o. (c) Comparison between the low resolution (10 Å bins) photoabsorption cross sections of N_2 used by *Lavvas et al.* [2011] and by the current model.

4.4.4 Photochemical equilibrium model

To calculate the plasma densities on the dayside ionosphere, a photochemical equilibrium model is developed which includes the ion-neutral chemistry. The model does not consider ion transport for calculating the plasma densities and the production and loss processes of the ions are taken to be in equilibrium. The major production processes are photon/photoelectron impact ionization and chemical reactions. The loss processes include dissociative recombination and chemical reactions. The primary production rates of various ions discussed in the previous section are used as input to the model along with the background neutral densities and electron temperature. For the reaction between the ion species i and the neutral species l, having a rate coefficient of k_{il}, the reaction rate (in cm^3s^{-1}) at an altitude Z is calculated as:

$$Rate(Z) = K_{il}\ [i(Z)]\ [l(Z)] \tag{4.14}$$

where $[i(Z)]$ and $[l(Z)]$ indicates the concentration of the species at altitude Z. The production reaction of an ion species would act as the loss reaction of another ion species. Hence all the reactions in the chemical network are coupled. The loss rate through dissociative recombination is calculated using equation 4.3.

Table 4.1: List of neutrals and ions included in the model

N_2, CH_4, H_2, N, C_2H_2, C_2H_4, NH_3
C_2H_6, HCN, H, C_4H_2, HC_3N, C_2H_3CN,
CH_3CN, C_3H_4, C_4H_2, CH_2NH, C_6H_6
N_2^+, N^+, CH_4^+, CH_3^+, CH_2^+, H_2^+, H^+,
HN_2^+, CH_5^+, $C_2H_5^+$, $CHCCNH^+$, $HCNH^+$, HCN^+
CH_3CNH^+, $C_3H_5^+$, c-$C_3H_3^+$, $C_2H_3CNH^+$,
NH_4^+, $CH_3NH_3^+$, $C_4H_3^+$, $C_6H_5^+$, $C_6H_7^+$, $CH_2NH_2^+$

The plasma densities are calculated for the altitude region 1000-1400 km with an altitude resolution of 1 km. Table 4.1 gives the list of neutral and ion species that have been included in the model. The list of ion-neutral reactions along with the reaction rate coefficients are listed in the Appendix section. The dominant ions in Titan's ionosphere are $HCNH^+$, $C_2H_5^+$, and CH_5^+. In the altitude range 1050-1200 km, $HCNH^+$ constitutes about 40-50% of the total ion population measured by INMS. The ions $C_2H_5^+$ and CH_5^+ contributes ∼15% and ∼2%, respectively [*Cravens et al.*, 2006; *Westlake et al.*, 2012]. These ions, along with other ion species, like CH_3^+, $CH_2NH_2^+$, c-$C_3H_3^+$, $C_3H_5^+$, CH_3CNH^+, and $CHCCNH^+$, account for ∼80% of the INMS observed ion population [*Vigren et al.*, 2013]. Figure 4.15 shows the important reaction pathways of the major primary ions N_2^+, N^+, CH_4^+, and CH_3^+ and the dominant terminal ions $HCNH^+$, $C_2H_5^+$, and CH_5^+. All the primary ions actively involve in the chemistry and get converted either to the major terminal ions or to the source ions which triggers the formation of the terminal ions. The major loss reaction of the most dominant ion $HCNH^+$ is the dissociative recombination reaction, whereas $C_2H_5^+$ and CH_5^+ are lost in reactions with HCN through which they produce $HCNH^+$.

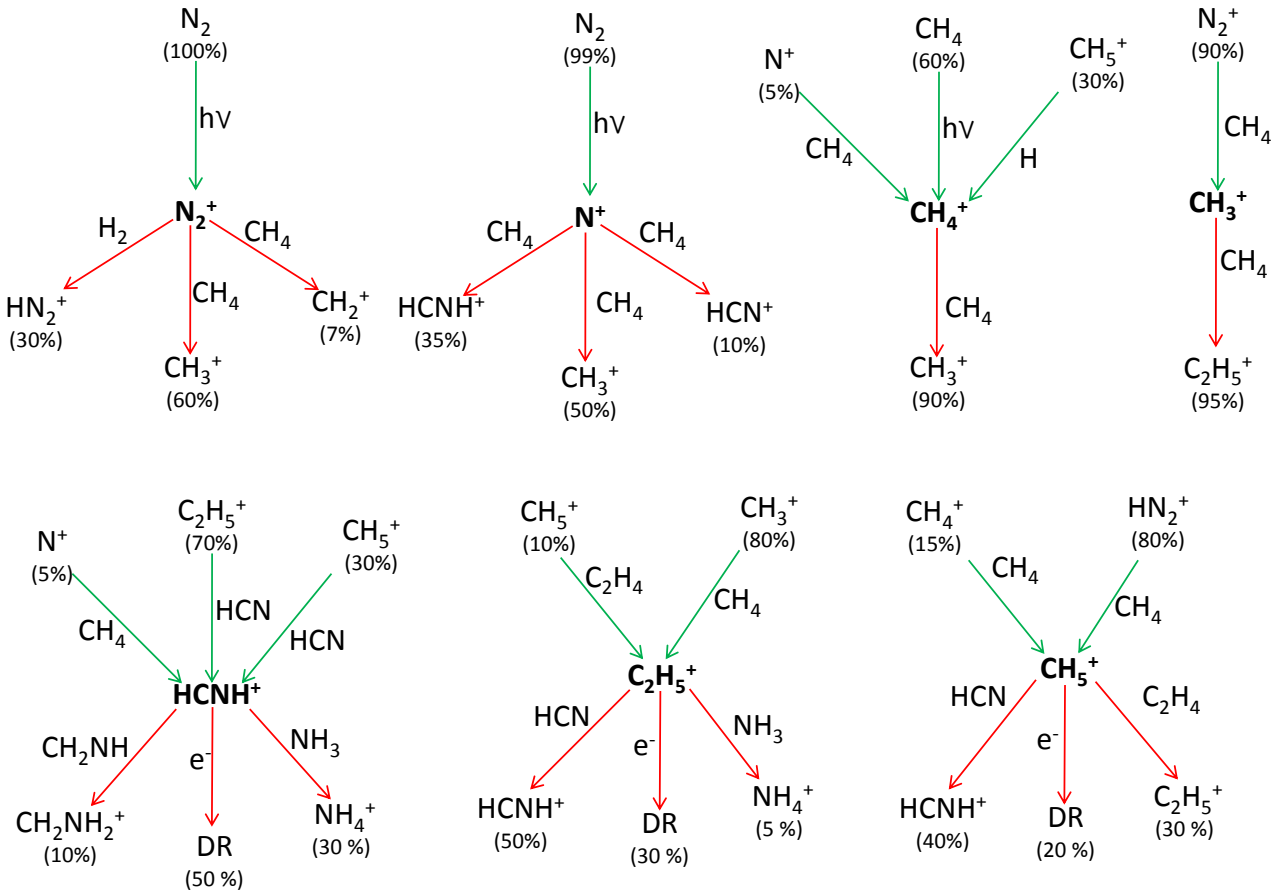

Figure 4.15: The reaction pathways of the major primary ions and terminal ions. The approximate percentage contribution to total production or loss for each reaction at altitudes near the ionospheric (∼1100 km) peak is indicated in parentheses.

The calculated density profiles of the three major ions $HCNH^+$, $C_2H_5^+$ and CH_5^+ for the T40 flyby condition are shown in Figure 4.16 along with those calculated by other photochemical models. The peak densities for $HCNH^+$, $C_2H_5^+$ and CH_5^+ calculated using the current model is higher than the corresponding INMS observed densities by a factor of 2 to 6. The $HCNH^+$ profile shows a good match with the profile of *Westlake et al.* [2012] at regions >1200 km. However, there is ∼30 km difference between altitude of peak production and our peak value is ∼40% higher than that of *Westlake et al.* [2012]. Profile of *Dobrijevic et al.* [2016] shows closest match with the observations as they have included the reaction $N(^2D) + HCN \rightarrow CH + N_2$ which consumes HCN thus lowering the production of $HCNH^+$, that is not included in any other model including the current model. For $C_2H_5^+$ and CH_5^+, the general shape of our profiles is consistent with those of *Westlake et al.* [2012] and *Dobrijevic et al.* [2016], but our calculated values are slightly higher.

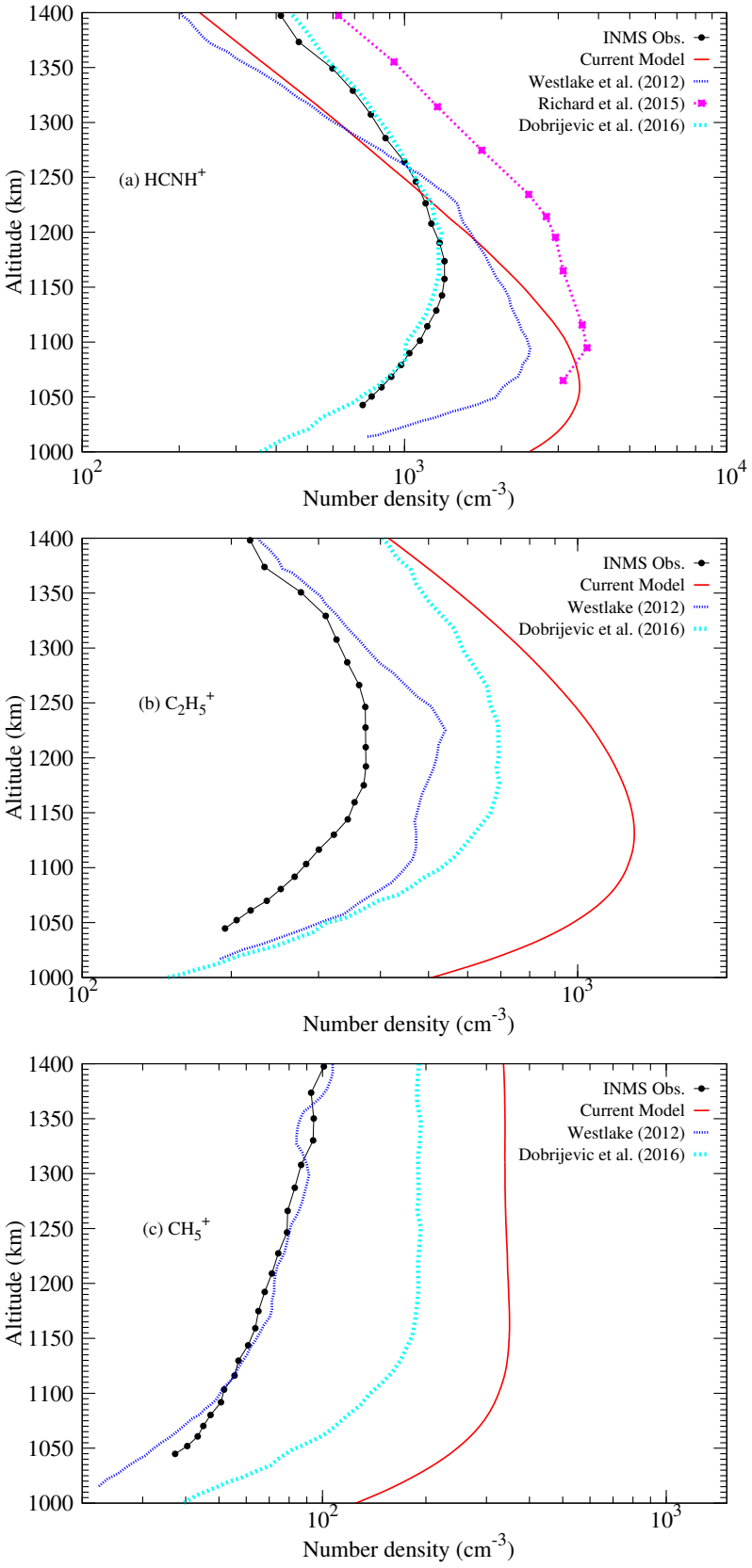

Figure 4.16: Calculated density profiles of three major ions, $HCNH^+$, $C_2H_5^+$ and CH_5^+, for a SZA of 37^o, compared with INMS observations for T40 flyby and model calculations of *Westlake et al.* [2012], *Richard et al.* [2015] and *Dobrijevic et al.* [2016].

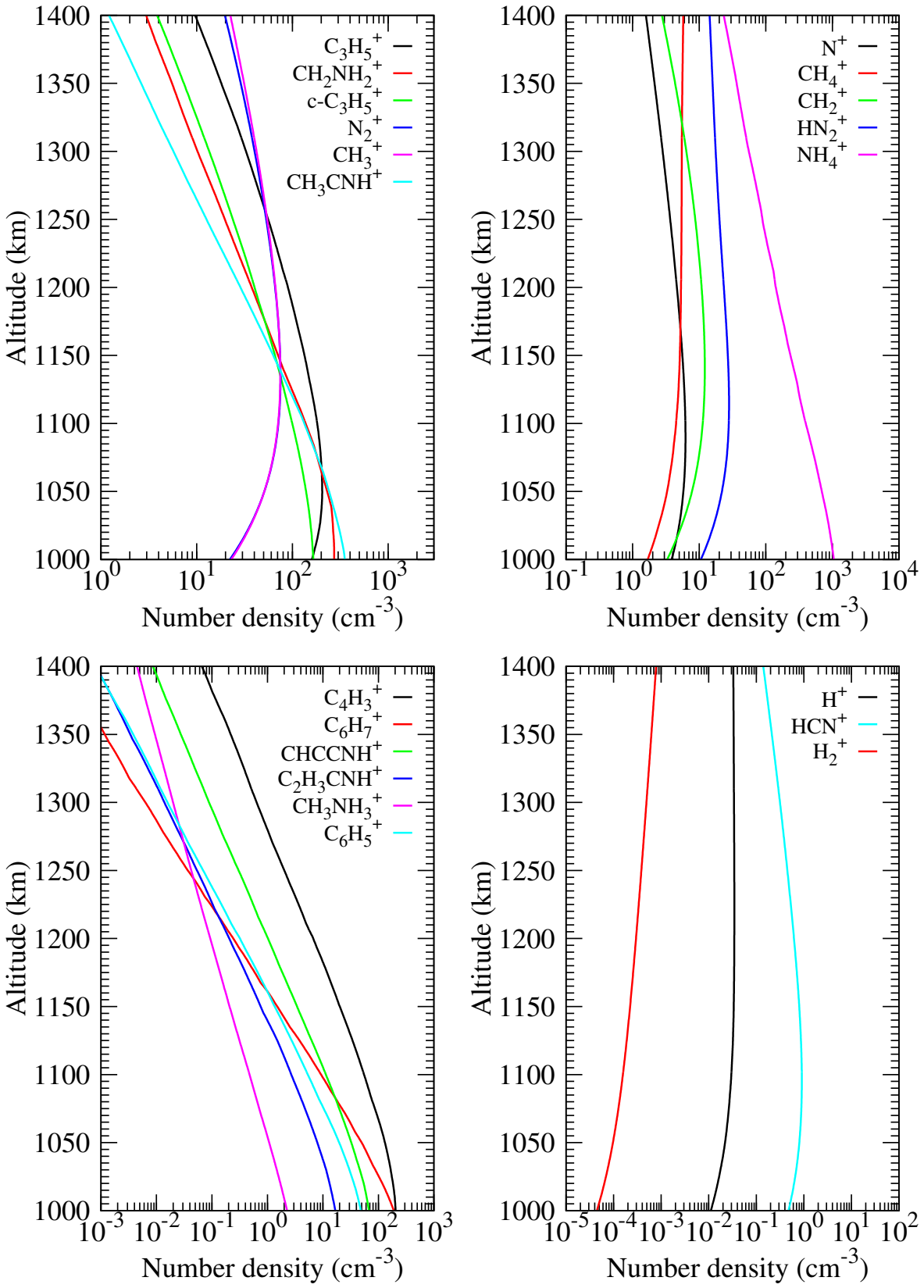

Figure 4.17: Density profiles of minor ions calculated using photochemical model for T40 flyby condition.

Figure 4.17 shows the density profiles of 20 other ions calculated using our photo-

chemical model. Densities of all the 23 ions are added to calculate the total electron density at each altitude. The electron density profile thus obtained is shown in Figure 4.18 along with the RPWS/LP measured electron density and from the calculations of other models [*Westlake et al.*, 2012; *Vigren et al.*, 2013; *Dobrijevic et al.*, 2016]. Though our calculated altitude of peak density is slightly lower (∼1050 km) as compared to other models, the calculated density profile is found to be consistent with other model results. The difference in the altitude of peak density is due to the difference in the calibration constant adopted by different models with which the neutral densities measured by INMS are multiplied to account for the recalibration of the instrument. *Westlake et al.* [2012] and *Vigren et al.* [2013] used a calibration factor of 3.0, whereas we adopted a value of 2.2 based on the recent study of *Teolis et al.* [2015]. A lower value for the calibration factor slenderize the atmosphere, thus allowing the UV radiation to penetrate to lower altitudes.

It is evident from the Figure 4.18 that our calculated peak value of electron density is around a factor of 2.5 higher than the observation. In fact, all the models overestimate the electron density by a factor of 2 to 3. We also modelled the electron density profile for a few more Cassini flybys on Titan's dayside viz. T48, T86, T95 and T104 (see Figure 4.19). The neutral densities for each of these flybys are taken from respective INMS measurements and electron temperature profiles are based on RPWS/LP observations. Details of all the five flybys that are considered in our study are given in Table 4.2. For all the flybys, our modeled electron density profiles are consistently higher than the measured values by a factor of 2 to 3.

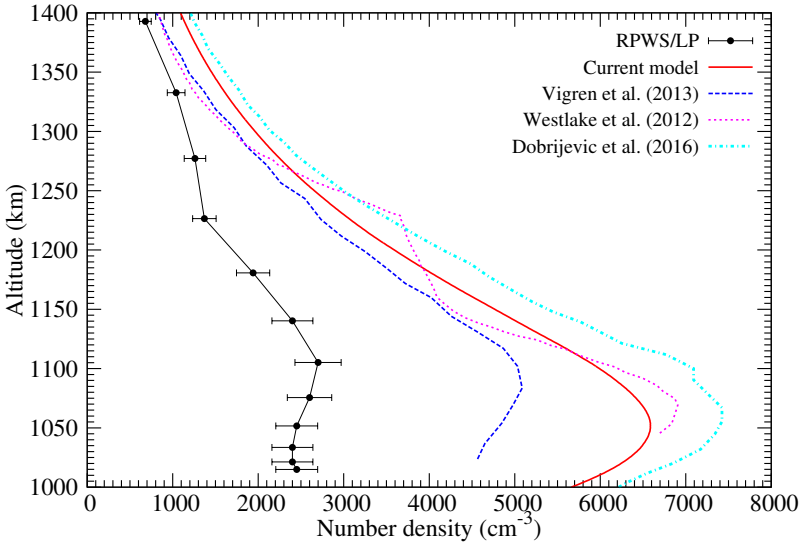

Figure 4.18: Calculated electron density profile for T40 flyby of Titan, compared with Cassini RPWS/LP observations and model calculations of *Vigren et al.* [2013], *Westlake et al.* [2012] and *Dobrijevic et al.* [2016].

Table 4.2: Information on the Cassini flybys used in our study

Flyby	Date	SZA
T40	5 January 2008	37
T48	5 December 2008	25.3
T86	26 September 2012	46.4
T95	14 October 2013	25
T104	21 August 2014	12.1

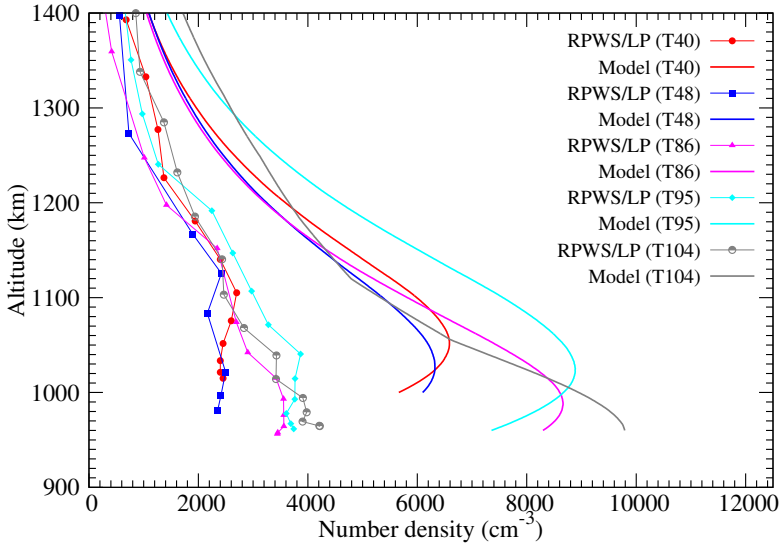

Figure 4.19: Calculated electron density profile for various Titan flybys compared with Cassini RPWS/LP observations.

Thus, it is seen that models are not able to reproduce the observed electron density on Titan's dayside ionosphere. Various factors can contribute towards this difference between calculated and measured electron density profile. In the following section, we study the impact of different model parameters on the calculated electron density to understand the possible reasons for this discrepancy. The overestimation in the modelled electron density can occur due to two reasons; either the models overestimate the production rate of plasma or the models underestimate the loss rate of plasma. We vary different model parameters that control the production/loss processes and make a comprehensive study of the impact on these variations on plasma densities.

4.5 Impact of model input parameters on the calculated ion and electron densities

Electron density profile obtained using parameters described in section 4.3 will be hereafter referred to as standard case.

4.5.1 Impact of photoelectron flux

On the dayside ionosphere of Titan, the main ionization sources are solar EUV photons and photoelectrons generated by EUV photons. Any overestimation in the photon flux or photoelectron flux will cause an aberrance in the value of ion production rates which will ultimately affect the electron density. Recently, *Vigren et al.* [2016] showed that the model derived photoelectron fluxes are higher than those measured by CAPS/ELS by a factor of ∼3±1 at electron energies less than 60 eV and suggested that this can be a probable reason for the higher electron densities predicted by the models. However, our calculated photoelectron flux are consistent with the model calculations of *Richard et al.* [2015] and *Lavvas et al.* [2011] as well as with the observations of CAPS/ELS at an altitude of 1020 km (see Figure 4.10). *Vigren et al.* [2016] pointed out that the better match of *Richard et al.* [2015] and *Lavvas et al.* [2011] calculations with the observation is due to the fact that they have used the photoelectron fluxes measured by the central anode of CAPS/ELS instrument for comparing with their calculations. The central anode CAPS/ELS measurements are found to be higher than those measured by the anode 2 of the same instrument which *Vigren et al.* [2016] have used in their study. However, this inconsistency in the measurement made by the two different anodes is seen only at altitude close to 1021 km. At higher altitudes, viz. 1056, 1121 and 1201 km, the measurements by central anodes match with the anode 2 measurements (differing only by <20% for the egress of T40 flyby).

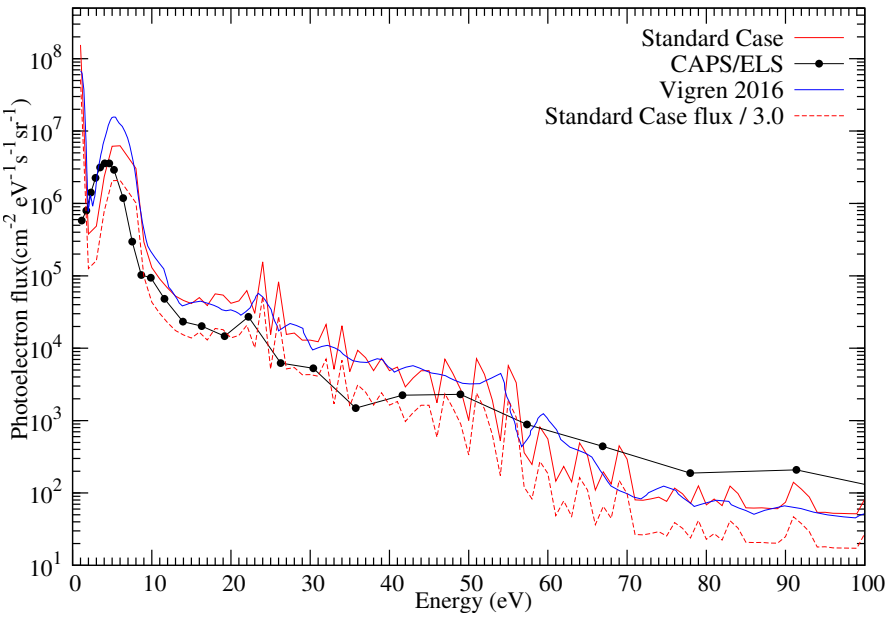

Figure 4.20: Calculated photoelectron flux at 1074 km compared with calculations of *Vigren et al.* [2016] and with Cassini CAPS observation (obtained from *Vigren et al.* [2016]). The dashed line indicates the case when the photoelectron flux is reduced by a factor of 3.0

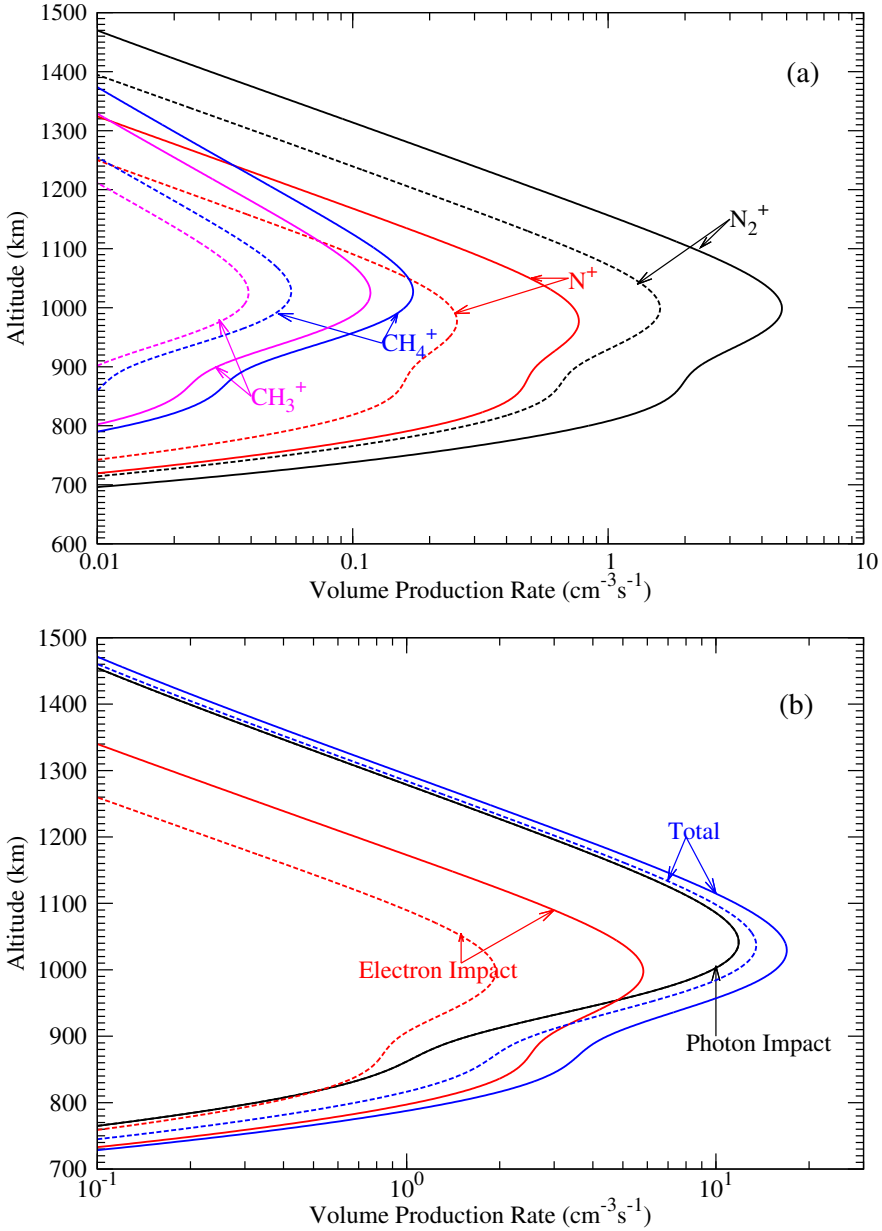

Figure 4.21: (a) Production rates of the major primary ions N_2^+, N^+, CH_4^+, and CH_3^+ due to electron impact. Solid curves show the electron impact production rate obtained in the standard case and dashed curves shows the production rates obtained when photoelectron flux is reduced by a factor of 3.0. (b) Total ion production rates due to photon and photoelectron impact. Solid blue curve shows the total ion production rates (photon + photoelectron) in the standard case and dashed blue curve shows the one obtained when the photoelectron flux is reduced by a factor of 3. Same is the case with the red curves which shows total ion production rates by electron impact.

We compared our calculated photoelectron flux with the calculation of *Vigren et al.* [2016] and the observation of CAPS/ELS (as given by Vigren et al. 2016) at an altitude of 1074 km. Our calculations are higher than the observation by a factor of ∼2 to 3 at electron energies <60 eV (see Figure 4.20). *Vigren et al.* [2016] calculated the electron

impact production rates using modeled photoelectron flux as well as using CAPS/ELS observed photoelectron flux at different altitudes for the dayside flybys T40, T41, T42 and T48. They used SEE/TIMED solar flux and adopted a calibration factor of 2.9 for the INMS measured neutral densities for their calculation. *Vigren et al.* [2016] found that the ratio of the ion production rates calculated using modeled fluxes to the one obtained using observed fluxes has a value of ∼3.0 for electron energy less than 60 eV. A comparison of our calculated electron impact ion production rates with that of the ion production rates calculated by *Vigren et al.* [2016] using the observed photoelectron fluxes also showed a similar result.

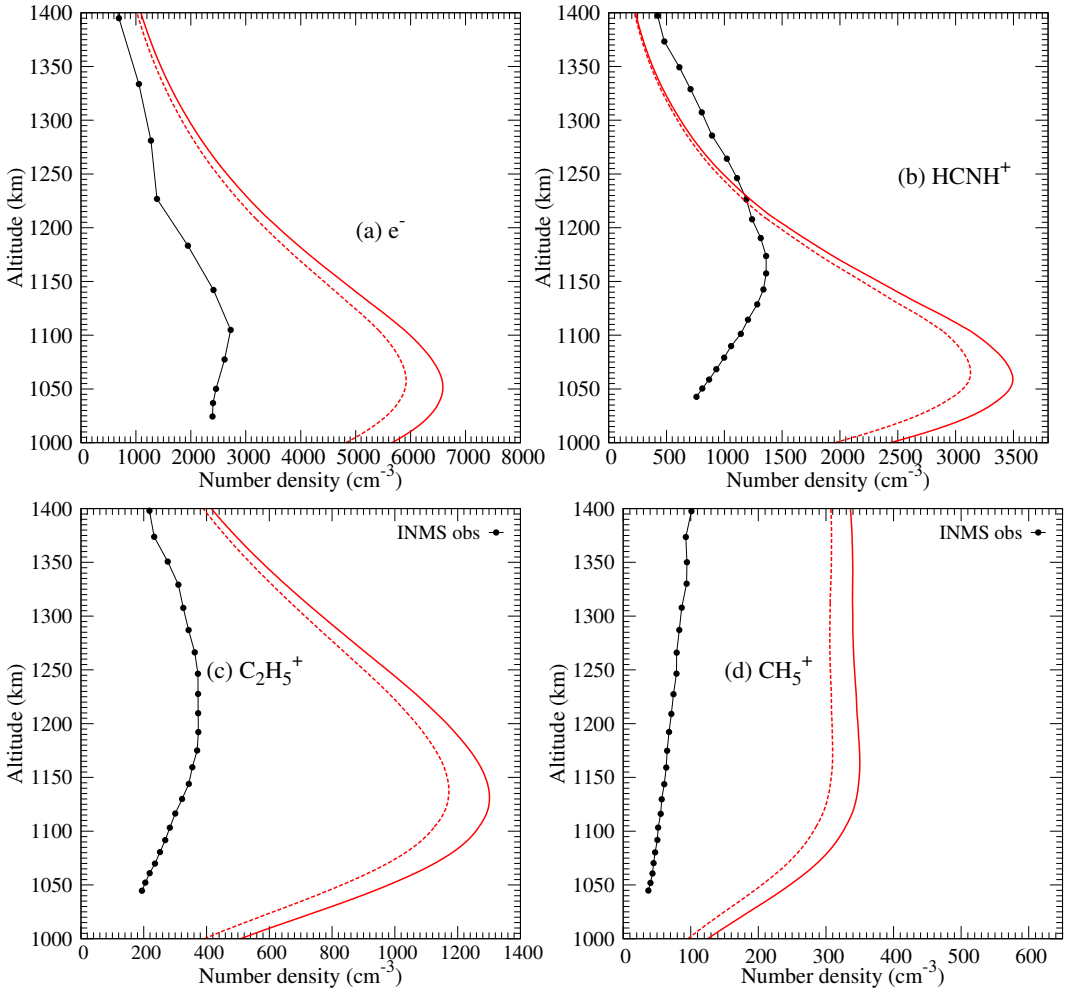

Figure 4.22: Density profiles of electrons and the major ions, $HCNH^+$, $C_2H_5^+$, and CH_5^+. Symbols show the Cassini observations. Solid red curve is the profile obtained in the standard case and dashed red curve shows the calculated density when the photoelectron flux is reduced by a factor of 3.0.

To understand the effect of this over-estimation of photoelectron flux on the plasma density calculation, we reduced the photoelectron flux by a factor of 3. Figure 4.21(a) shows the electron impact volume production rates of the major primary ions, N_2^+, N^+,

CH_4^+, and CH_3^+, obtained when the photoelectron flux is reduced by a factor of 3. The peak production rate of all the four ions is reduced by 60-70%. However, the electron impact ion production rates constitutes only ∼30% of the total volume production rates (see Figure 4.21(b)). Decreasing the photoelectron flux reduces this contribution to 15% and the total ion production rate is reduced by 20%. These modified ion production rates are used for calculating the electron and ion densities. It is found that reducing the photoelectron flux reduces the peak densities of major ions only by 10-15% and peak electron density by ∼10% (see Figure 4.22). This shows that an overestimation in photoelectron fluxes may not be an important factor in causing aberrance in the modelled electron density.

Table 4.3: A comparison between empirically calculated production rate of N_2^+ by *Madanian et al.* [2016] and the values calculated using the present model

Altitude	Empirical rates by *Madanian et al.* [2016] (cm^{-3} s^{-1})	Present model (cm^{-3} s^{-1})	Ratio
1014	8.43	14.27	1.69
1020	8.85	14.55	1.64
1024	7.51	14.68	1.96
1049	8.87	14.43	1.63
1056	8.09	14.08	1.74
1066	7.44	13.41	1.80
1076	6.92	12.60	1.82
1086	6.42	12.60	1.96
1097	5.85	10.64	1.82
1110	5.73	9.38	1.64
1124	5.27	8.08	1.53
1138	4.53	6.88	1.52
1152	3.89	5.81	1.49
1168	3.56	4.75	1.33
1184	2.85	3.86	1.35
1201	2.41	3.07	1.28
1220	1.70	2.37	1.39
1238	1.37	1.85	1.35
1257	0.95	1.42	1.50
1278	0.76	1.06	1.40
1298	0.58	0.80	1.37
1320	0.47	0.58	1.24
1343	0.36	0.42	1.17
1372	0.24	0.28	1.17
1397	0.19	0.20	1.01

4.5.2 N_2^+ ion production rates

N_2^+ is the most abundantly produced primary ion in Titan's ionosphere. However, the N_2^+ ion densities measured by INMS cannot be used directly for verifying the modelled ion production rates since the mass of N_2^+ coincides with the most abundant terminal ion $HCNH^+$ whose number density is around two to three orders of magnitude higher than that of N_2^+. However, INMS measured CH_3^+ density can be used as a proxy for verifying the calculated N_2^+ production rates. It is seen that 90-95% of CH_3^+ is produced from the reaction between N_2^+ and $CH_4$and most of the CH_3^+ that is produced is lost through the reaction with CH_4 (refer Figure 4.15). If we assume that all the N_2^+ that is produced is converted to CH_3^+ and all the CH_3^+ that is produced is lost through the reaction with CH_4, an empirical estimate of the N_2^+ ion production rate can be obtained from the INMS measured CH_3^+ densities as [*Richard et al.*, 2015]:

$$P_{N_2^+} = L_{CH_3^+} = k_{CH_3^+,CH_4}\,[CH_4]\,[CH_3^+] \tag{4.15}$$

$P_{N_2^+}$ and $L_{CH_3^+}$ represent the production and loss rate of N_2^+ and CH_3^+, $k_{CH_3^+,CH_4}$ is the reaction rate coefficient for the reaction between CH_4 and CH_3^+, and $[CH_4]$ and $[CH_3^+]$ are the INMS measured densities of CH_4 and CH_3^+.

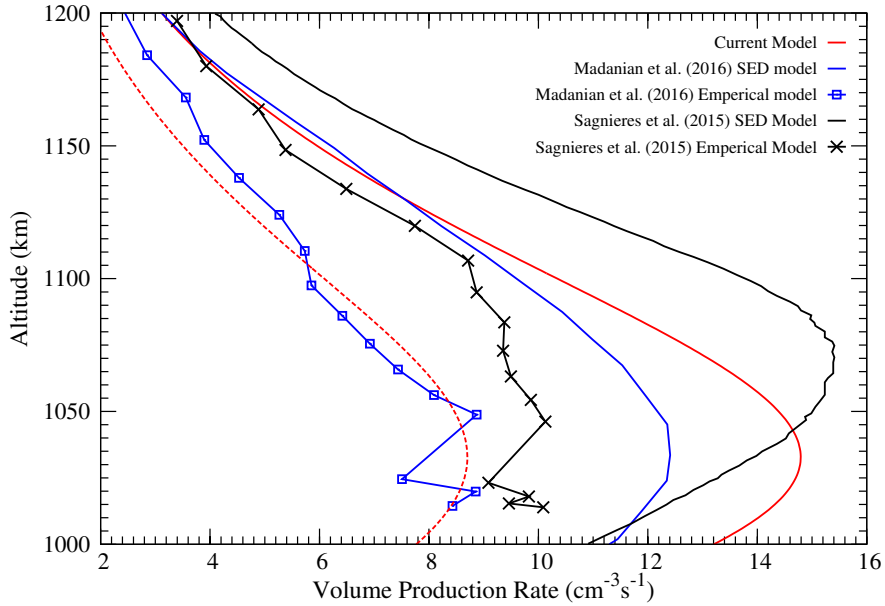

Figure 4.23: Comparison of volume production rate of N_2^+ calculated using the current study (solid red curve) with that of *Sagnières et al.* [2015] and *Madanian et al.* [2016]. Solid black curve and crosses show the calculation of *Sagnières et al.* [2015], using solar energy deposition model (SED) model and empirical model, respectively. Similarly, solid blue curve and open squares represent calculations of *Madanian et al.* [2016]. Red dashed curve shows the case where our calculated production rate values are adjusted to match with the empirical calculations of *Madanian et al.* [2016].

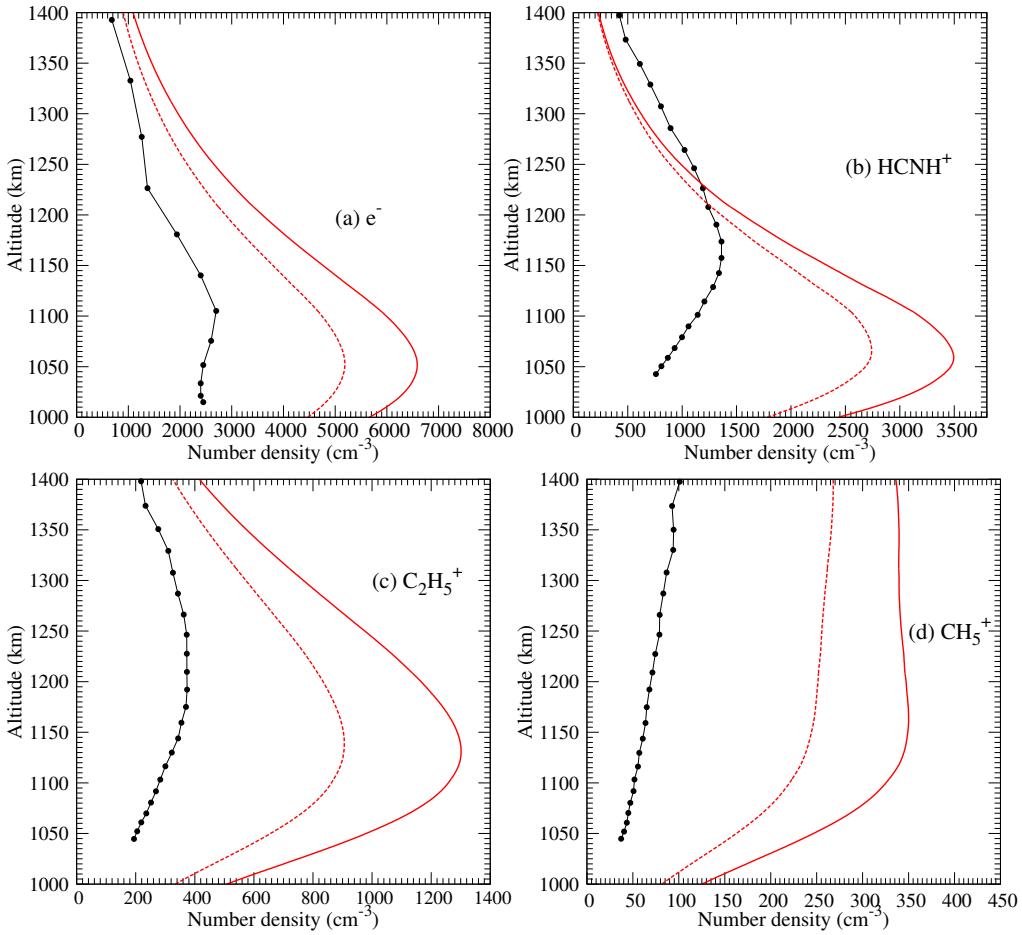

Figure 4.24: Density profiles of electrons and major ions, $HCNH^+$, $C_2H_5^+$, and CH_5^+, calculated using the empirical production rate of N_2^+. Solid curves show the standard case profiles. The dashed curves show the profiles obtained when our calculated production rate values of N_2^+ are adjusted to match with the empirical calculations of *Madanian et al.* [2016].

A recent study of *Sagnières et al.* [2015] showed that the primary production rate of N_2^+ calculated using solar energy deposition (SED) models are higher than the one which are derived empirically using INMS measured ion and neutral densities by a factor of two. To check whether the empirical volume production rates of N_2^+ could reduce the calculated plasma density, we made test runs of the model using the empirical N_2^+ production rates of *Madanian et al.* [2016]. These values are chosen over the empirical values of *Richard et al.* [2015] and *Sagnières et al.* [2015] as the former study uses the most recent INMS calibration factor for ion and neutral densities, based on the study of *Teolis et al.* [2015], which we have also adopted for the present work. Figure 4.23 shows a comparison between the production rate calculation of *Madanian et al.* [2016] and *Sagnières et al.* [2015]. The maximum difference of a factor of ∼1.5 between the SED and empirical values of *Sagnières et al.* [2015] occur at an altitude of ∼1080 km. Our model calculated values are in close agreement with the SED values of *Madanian et al.* [2016],

with a difference less than 12% at the peak. A ratio between our model calculated values and the empirical values of *Madanian et al.* [2016] for different altitudes is presented in Table 4.3. It is evident that in the altitude range 1050-1100 km (the altitude region where the electron density peaks) the model calculated values are around a factor of ∼2 higher than the empirical values. We adjusted our calculated volume production rate of N_2^+ in such a way that it matches with the empirical values of *Madanian et al.* [2016] (see Figure 4.23). These reduced N_2^+ ion production rates are used in the chemistry model. The density profiles of major ions and electrons thus obtained is shown in Figure 4.24. The peak density of electrons and $HCNH^+$ is decreased by 20% and that of CH_5^+ and $C_2H_5^+$ by ∼30%. This shows that, even though the over-estimation of ion production rate is contributing to the exaggerated plasma density to some extent, this alone is not sufficient to account for the inconsistency between the observed and modelled electron density profiles.

4.5.3 Electron Temperature

Dissociative ion-electron recombination reaction plays a major role in the loss of electrons and ions. This reaction inversely depends on electron temperatures, T_e. Higher the value of T_e, lower will be the rate of recombination, and hence higher will be the electron density (c.f. equation 4.3).

Theoretical studies suggest that on Titan's dayside ionosphere T_e should be close to neutral temperature at altitudes below 1050 km [*Richard et al.*, 2011]. However, observations revealed that T_e is higher than the modelled values. *Richard et al.* [2011] modelled the dayside electron temperature for the T18 flyby condition for different magnetic topologies. These modelled values were found to be smaller than that of the LP measurements. The magnitude of difference depends on the magnetic topology that is considered in each case. *Lavvas et al.* [2013] assumed a temperature profile for T40 which conciliate with both observations and theory. Modelled T_e for the outbound conditions of T40 flyby is given by *Richard* [2013]. Figure 4.25(a) shows each of these profiles along with the RPWS/LP observations for T40 and the linear relation for T_e given by *Dobrijevic et al.* [2016] which we have used in the standard case. The test runs of the model were performed with each of these T_e profiles, keeping all other parameters the same as that in the standard case. Three cases were considered.

Case 1 : T_e modelled for T40 outbound from *Richard* [2013]

Case 2 : T_e from *Lavvas et al.* [2013]

Case 3 : T_e from *Richard et al.* [2011]. We have extrapolated the T_e profile of *Richard et al.* [2011], taken from *Westlake et al.* [2012], for 1060 to 1000 km.

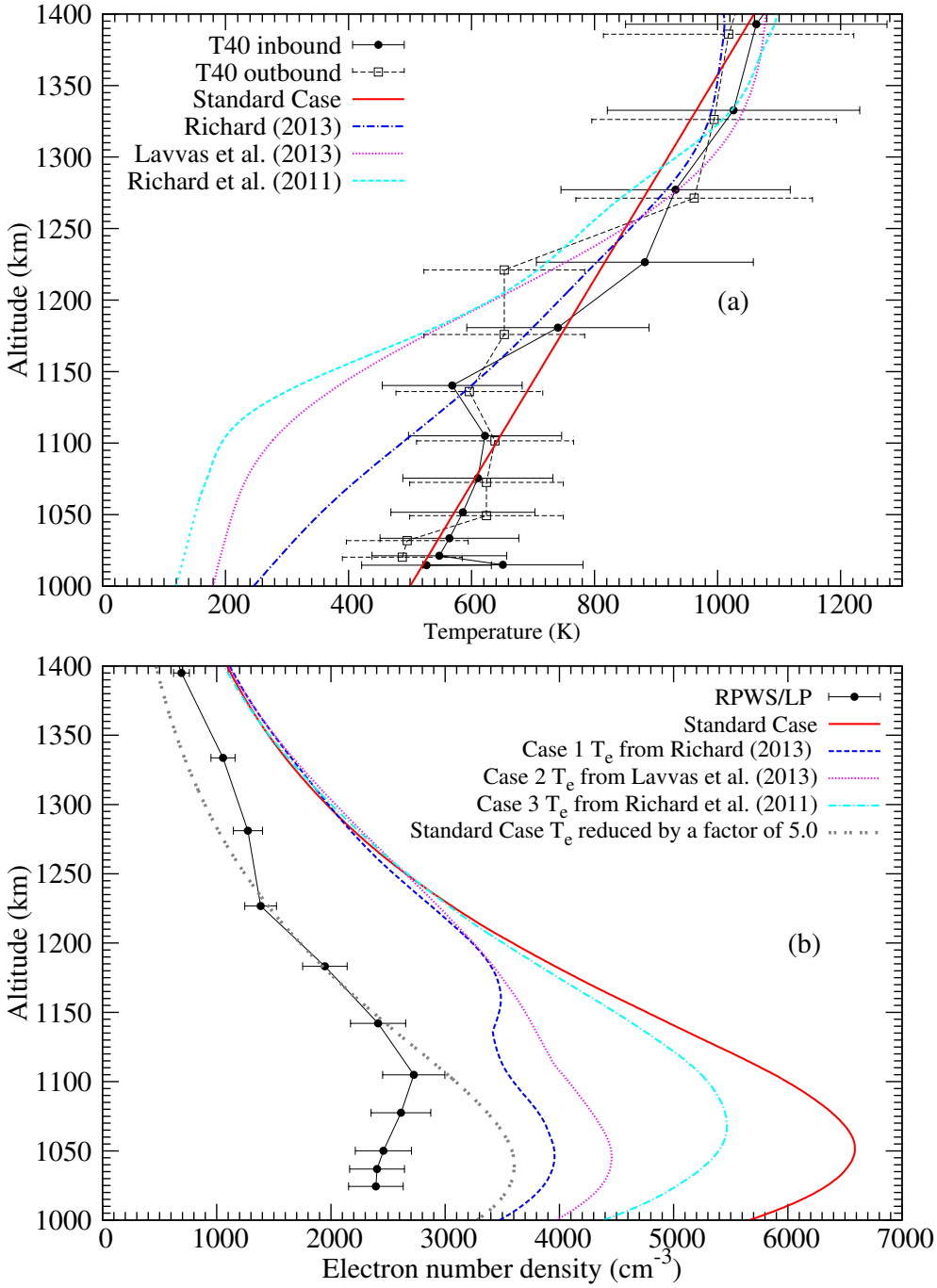

Figure 4.25: (a) Electron Temperature profiles used for testing model sensitivity. The symbols circles and squares represents the T_e measured by Langmuir probe during the T40 inbound and outbound conditions, respectively. Electron temperature of *Richard et al.* [2011] (from *Westlake et al.* [2012]) has been extrapolated from 1060-1000 km. Extrapolated region is represented by dotted line. (b) Electron density profile calculated using different electron temperatures profiles.

Figure 4.25(b) shows the electron densities obtained in each case. All profiles agree with each other for altitudes above 1250 km. The profile obtained in case 1 coincides with the standard case profile at heights greater than 1200 km. However, the electron

density peak is reduced by ∼15% of the standard peak for ∼30% decrease in T_e at 1050 km. The T_e value at this altitude for the case 2 and case 3 are, respectively, ∼60% and ∼70% less than that of the standard case profile. Correspondingly, electron densities are reduced by ∼30% and ∼40%.

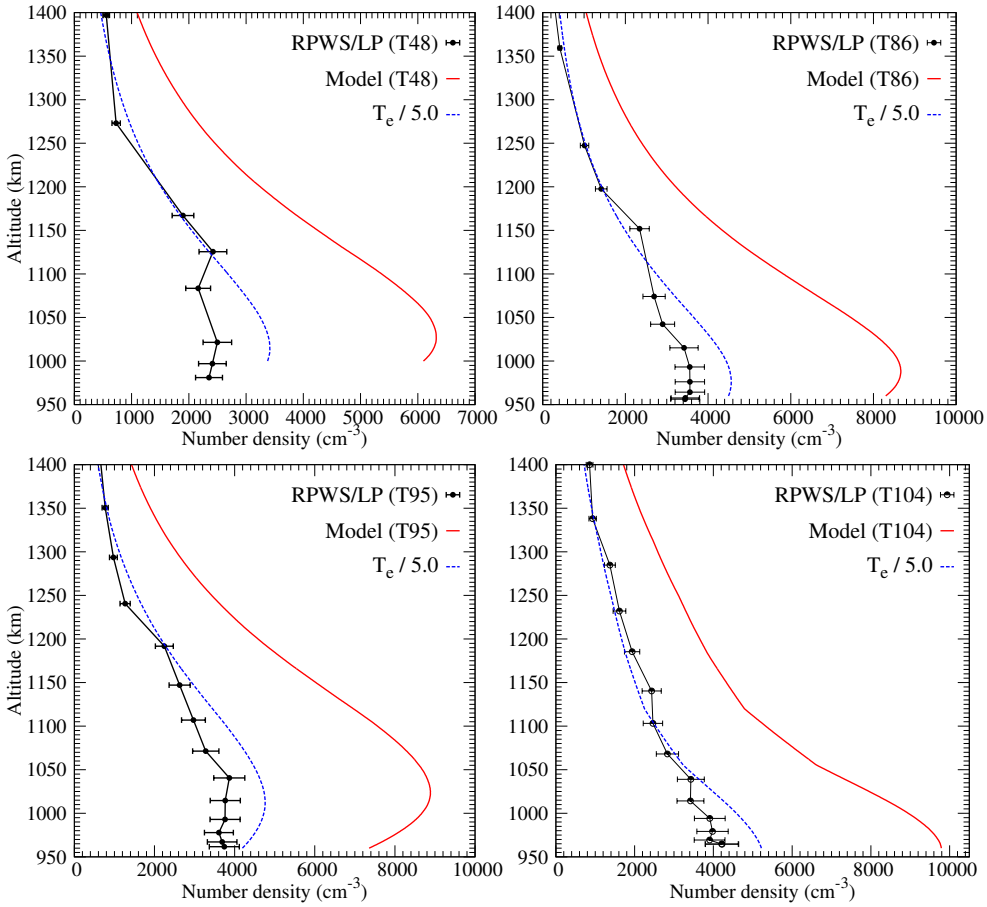

Figure 4.26: Electron density profile calculated for the dayside flybys T48, T86, T95 and T104. Solid red curves shows the standard case profiles and blue dashed curves show the profiles obtained when the RPWS/LP measured electron temperature is reduced by a factor of 5 for each flyby.

Also, it is observed that when T_e used in the standard case is reduced by a factor of 5, the modelled electron density profile shows better agreement with the observed values at altitudes >1150 km. Figure 4.26 shows the modelled electron density profile when the electron temperature is reduced by a factor of 5 for the flybys, T48, T86, T95, and T104. At altitudes below ∼1050 km, the modelled value is still higher than the observed value by ∼ 30-40% which suggests that T_e has to be still lower in this region for the calculated electron density to agree with the observation. There is a possibility that the actual T_e is less than the observed value in this region as *Vigren et al.* [2013] has pointed out that it is difficult for the Langmuir probe to measure T_e below 300 K

due to instrumental properties though the instrument is sensitive enough to measure T_e less than 400 K.

4.5.4 HCN density

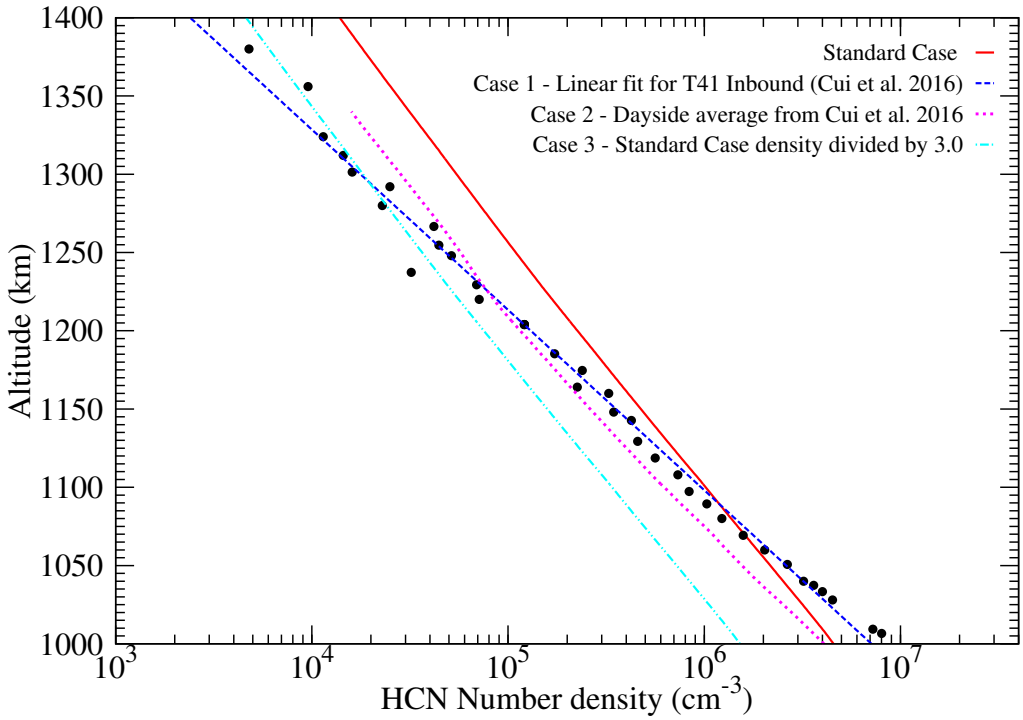

Figure 4.27: HCN density profiles used for different model runs. Symbols represent the density measured by INMS during the inbound leg of T41 flyby.

In the photochemical model, HCN density is crucial for determining the density profiles of the three major ions $HCNH^+$, $C_2H_5^+$ and CH_5^+ as their densities are largely influenced by the reactions

$$CH_5^+ + HCN \rightarrow HCNH^+ \ (3.0 \times 10^{-9} \text{ cm}^3 \text{ s}^{-1}) \tag{4.16}$$

$$C_2H_5^+ + HCN \rightarrow HCNH^+ \ (2.7 \times 10^{-9} \text{ cm}^3 \text{ s}^{-1}) \tag{4.17}$$

In the standard case we have used the mixing ratio profile of HCN given by *Krasnopolsky* [2009] which was anchored to the mixing ratio reported by *Magee et al.* [2009] (see section 4.3.2). Recently, *Cui et al.* [2016] derived the HCN abundance for the altitude range 960–1400 km by using the INMS data obtained during several flybys of Titan. They also deduced an average dayside mixing ratio profile for HCN. We have run the model by using different density profiles of HCN to see how the electron and the major ion densities will vary in each case. Three different model runs were carried out:
Case 1 : HCN density measured during the inbound part of the T41 flyby (as given by Cui et al. 2016) is fitted. (T41 flyby occurred on 22 February 2008 with a SZA of 30^o,

conditions which are quite similar to T40.)

Case 2 : Dayside average mixing ratio profile of HCN as given by *Cui et al.* [2016].

Case 3 : Reducing the density of HCN used in the standard case by a factor of 3.

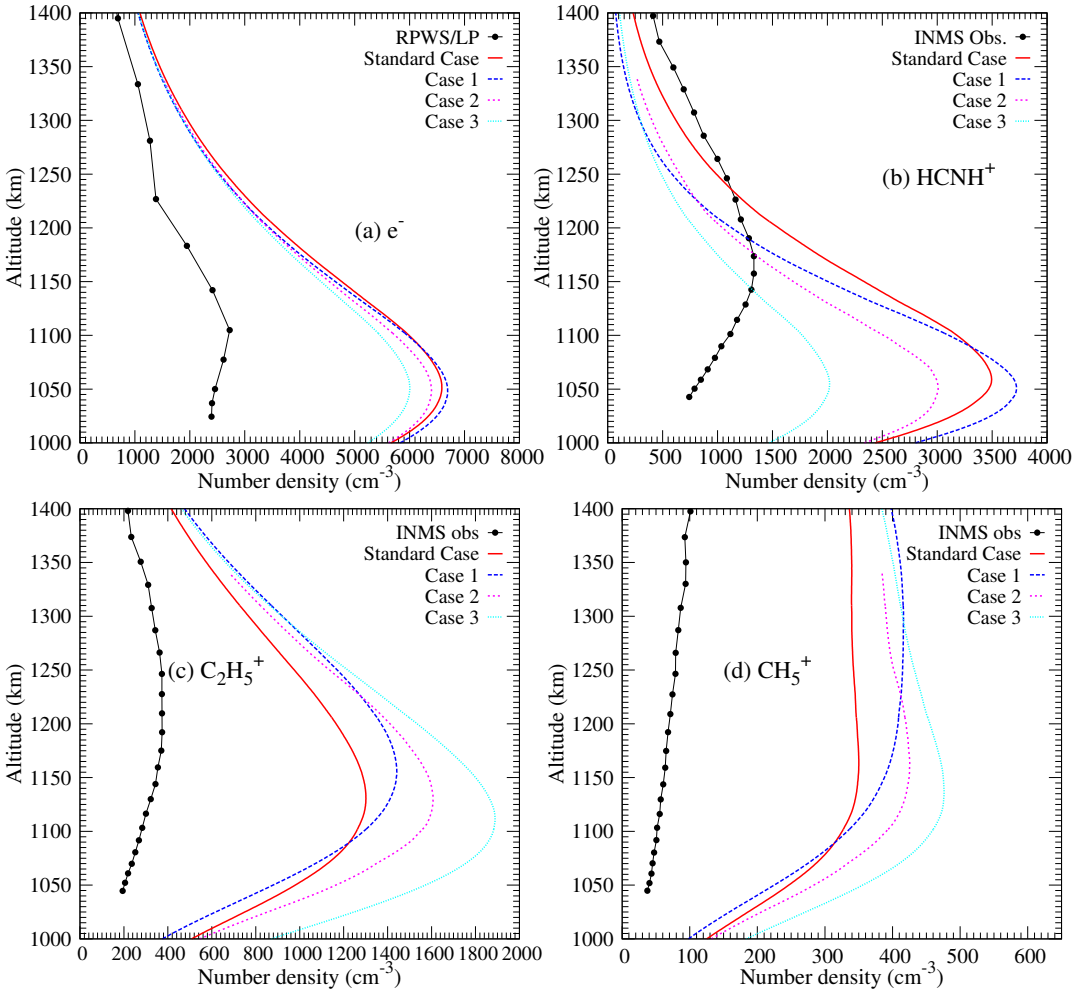

Figure 4.28: Density profiles of electron and major ions, $HCNH^+$, $C_2H_5^+$ and CH_5^+, obtained using different density profiles of HCN shown in Figure 4.27. Case 1: HCN density measured during the inbound part of the T41 flyby fitted linearly. Case 2: Dayside average mixing ratio profile of HCN as given by *Cui et al.* [2016]. Case 3: Reducing the density of HCN used in standard case by a factor of 3.

Figure 4.27 shows the different HCN profiles that we have used for model runs. In case 1, the HCN density is larger than that in the standard case at altitudes <1100 km but at higher altitudes it is lower by a factor of ∼10 at the maximum. Correspondingly, the peak densities of electrons as well as $HCNH^+$ is higher at altitudes <1100 km and are lower than the standard profile at upper region (see Figure 4.28). The observed effect is just opposite for $C_2H_5^+$ and CH_5^+. The maximum decrease in the peak electron density occurs in case 3, i.e, when HCN density in the standard case is reduced by a factor of 3. Decreasing the HCN density by a factor of 3 was suggested by *Westlake*

et al. [2012] in accordance with the uncertainties in the mixing ratio reported by *Magee et al.* [2009]. The peak electron density in this case is ∼10% less than the standard peak. There occurs a drastic decrease in the $HCNH^+$ peak (by a factor of ∼1.75) but at the cost of $C_2H_5^+$ and CH_5^+ density profiles, which is also suggested by *Westlake et al.* [2012]. In case 2, the dayside average mixing ratio of HCN reported by *Cui et al.* [2016] is ∼80% higher than that of the mixing ratio given by *Magee et al.* [2009] at an altitude of 1050 km. However, using this dayside average profile causes a decrease in the peak electron and $HCNH^+$ densities with a reasonable shift in the $C_2H_5^+$ and CH_5^+ profiles.

4.5.5 Dissociative electron recombination coefficient (DRC) of $C_2H_5^+$ and CH_5^+

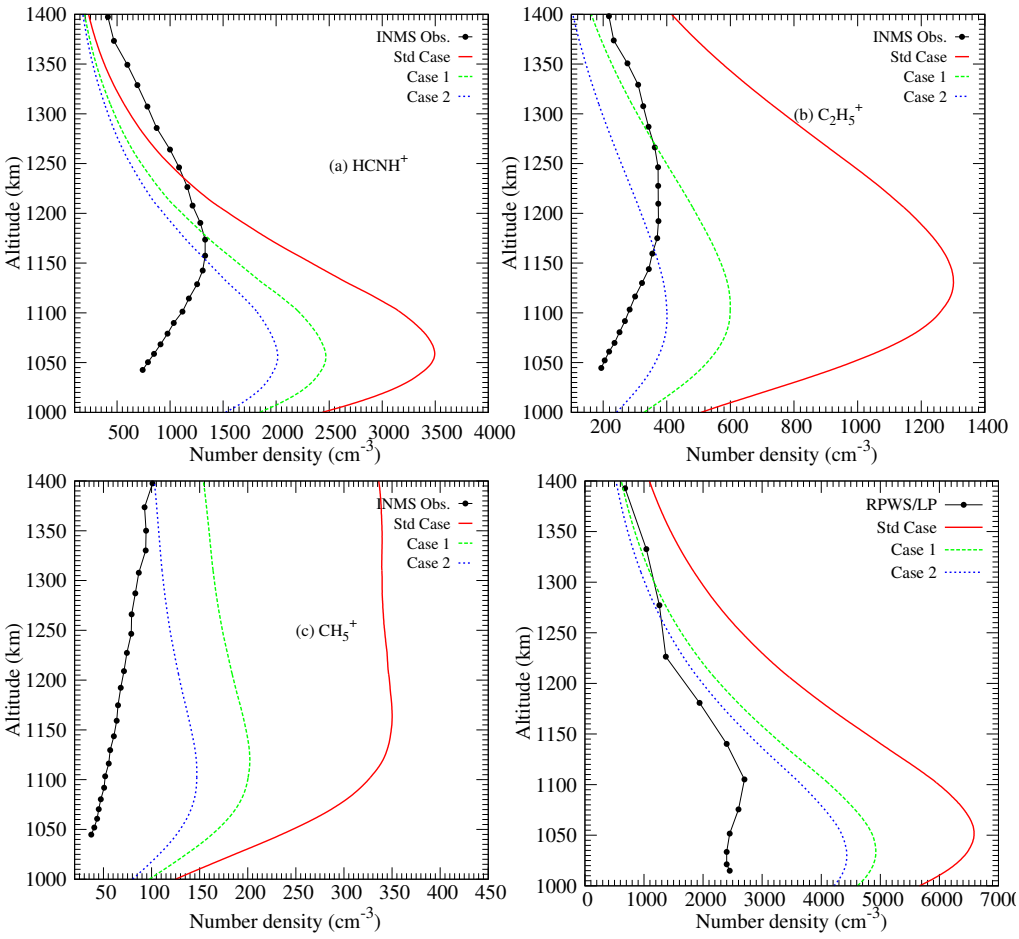

Figure 4.29: Density profiles of major ions and electrons obtained by varying the dissociative recombination coefficient (DRC) of CH_5^+ and $C_2H_5^+$. Black circles represents the INMS observations. Red solid curve indicates the profile calculated in the standard case. Green dashed curve represent case 1 where the DRC of CH_5^+ and $C_2H_5^+$ is increased by a factor 5. Blue dotted curves show case 2 where the DRC of CH_5^+ and $C_2H_5^+$ is increased by a factor 10.

Dissociative electron recombination reaction of ions is the major loss channel through which the plasma is removed from the ionosphere. As shown in Figure 4.16, there is a large overestimation in the densities of major ions which ultimately reflects as an overvaluation in the calculated electron density. If the DRC for these ions were higher it would have caused the loss of these ions at a higher rate and hence a lesser value of electron density.

For CH_5^+ we have used a DRC of 1.1×10^{-6} cm^3 s^{-1} [*McLain et al.*, 2004]. Several authors have reported different values, e.g., 2.9×10^{-7} cm^3 s^{-1} [*Sheehan and St.-Maurice*, 2004], 7.0×10^{-7} cm^3 s^{-1} [*Lehfaoui et al.*, 1997], and 1.4×10^{-7} cm^3 s^{-1} [*Smith and Spanel*, 1993]. Similarly for $C_2H_5^+$, the DRC value used in the standard case is 1.2×10^{-6} cm^3 s^{-1} [*McLain et al.*, 2004]. For this ion also DRC has been reported by *Lehfaoui et al.* [1997] (6.0×10^{-7} cm^3 s^{-1}) and *Adams and Smith* [1988] (7.4×10^{-7} cm^3 s^{-1}). It is evident that there are considerable differences between various reported values of DRC.

To reduce the densities of major ions and electrons, we tried increasing the DRC of CH_5^+ and $C_2H_5^+$ by keeping the DRC of $HCNH^+$ same as that in the standard case. Increasing the DRC of $C_2H_5^+$ and CH_5^+ simultaneously by a factor of 5(10) reduces the difference between the observations and modeled profile from a factor 7 to a factor of 4(3) for CH_5^+ and from 7 to 3(2) for $C_2H_5^+$ (see Figure 4.29). The $HCNH^+$ profile also improved with the peak value in the standard case $\sim$3500 cm^{-3} reducing to 2500 cm^{-3} ($\sim$2300 cm^{-3}). The peak electron density also decreased to 5000 cm^{-3} (4500 cm^{-3}) from the standard case peak of 6500 cm^{-3}. Even though increasing the DRC improved the calculated densities, the modelled profiles are still higher than the observations which suggests that there may be some chemical reactions involving the major ions $HCNH^+$, $C_2H_5^+$ and CH_5^+ which are not identified so far that could account for the additional loss of these ions.

4.5.6 Additional reactions proposed by *Westlake et al.* [2012]

Westlake et al. [2012] proposed that there can be additional loss channels for $HCNH^+$ that can consume the ion and reduce the density. They suggested the following loss reactions for $HCNH^+$:

$$HCNH^+ + C_2H_2 \rightarrow CHCCNH^+ + H_2 \; (2.0 \times 10^{-10} \text{ cm}^3 \text{ s}^{-1}) \tag{4.18}$$

$$HCNH^+ + C_2H_4 \rightarrow C_2H_3CNH^+ \; (2.0 \times 10^{-9} \text{ cm}^3 \text{ s}^{-1}) \tag{4.19}$$

However, there was no experimental evidence that such reactions could exist. To test the impact on the model results, we made a test run by including these two reaction. Figure 4.30 shows the electron and $HCNH^+$ density thus obtained in these case along with the standard case profile and measured densities. New profiles agree with standard

case profile at altitudes above 1250 km. Inclusion of these reactions reduced the peak value of $HCNH^+$ density by ∼30% and that of electron density by ∼8%.

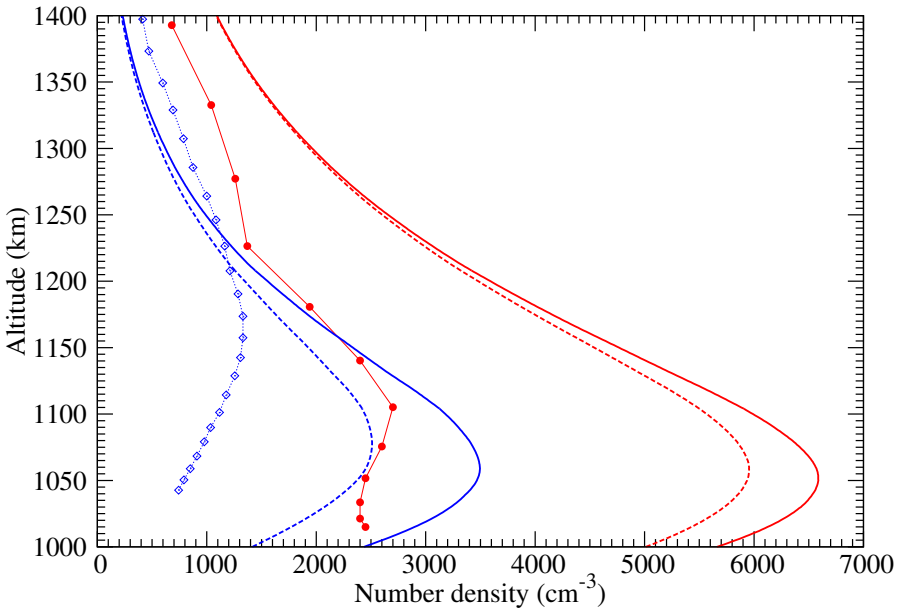

Figure 4.30: Density profiles of $HCNH^+$ and electron obtained by adding theoretical reactions proposed by *Westlake et al.* [2012]. Solid circles and open squares represent RPWS/LP measured electron density and INMS measured $HCNH^+$ density, respectively. Red and blue curves show the calculated density profiles of electron and $HCNH^+$ with solid lines representing the standard case profiles and dashed lines representing the profiles obtained when the theoretical reactions were included.

Demarais et al. [2013] investigated the chemistry of $HCNH^+$ with C_2H_2 and C_2H_4 using the flowing afterglow-selected ion flow tube technique. They concluded that the large energy barriers will inhibit these reaction pathways and they will not contribute significantly to the depletion of $HCNH^+$ and the suggested ionic products will not be formed from these reaction unless the energy barrier is overcome.

4.5.7 NH_3 density

Our photochemical model overestimates the density of NH_4^+ ion by 2 orders of magnitude (see Figure 4.31). Similar result was reported by *Richard* [2013] whose modelled NH_4^+ value was around a factor of 50 larger than the observation. The NH_3^+ density depends on the density of NH_3. Higher the NH_3 density, higher will be the abundance of NH_4^+ and vice versa. *Yelle et al.* [2010] and *Dobrijevic et al.* [2016] modelled the density of NH_3 by considering a coupled ion-neutral chemistry scheme. Their profiles seem to be lower than that of our standard case by a factor 75 and 20, respectively (see Figure 4.31). The test runs of the model using each of these density profiles were performed to assess how the NH_4^+ density varies. Using the profile of *Dobrijevic et al.*

[2016] we could reduce the difference between the model and observation to a factor of 10 or less. When the NH_3 profile of *Yelle et al.* [2010] is used, the agreement between observation and model further improved, reducing the maximum difference from an order of magnitude to 60% at maximum. However, improving the NH_4^+ density had a noticeable impact on $HCNH^+$ density profile (and hence on electron density) as reaction of $HCNH^+$ with NH_3 to form NH_4^+ is an important loss channel for this ion. Using the NH_3 profile from *Yelle et al.* [2010] or *Dobrijevic et al.* [2016] increased the peak value of $HCNH^+$ (electron) by ∼33% (15%) of the standard case peak value.

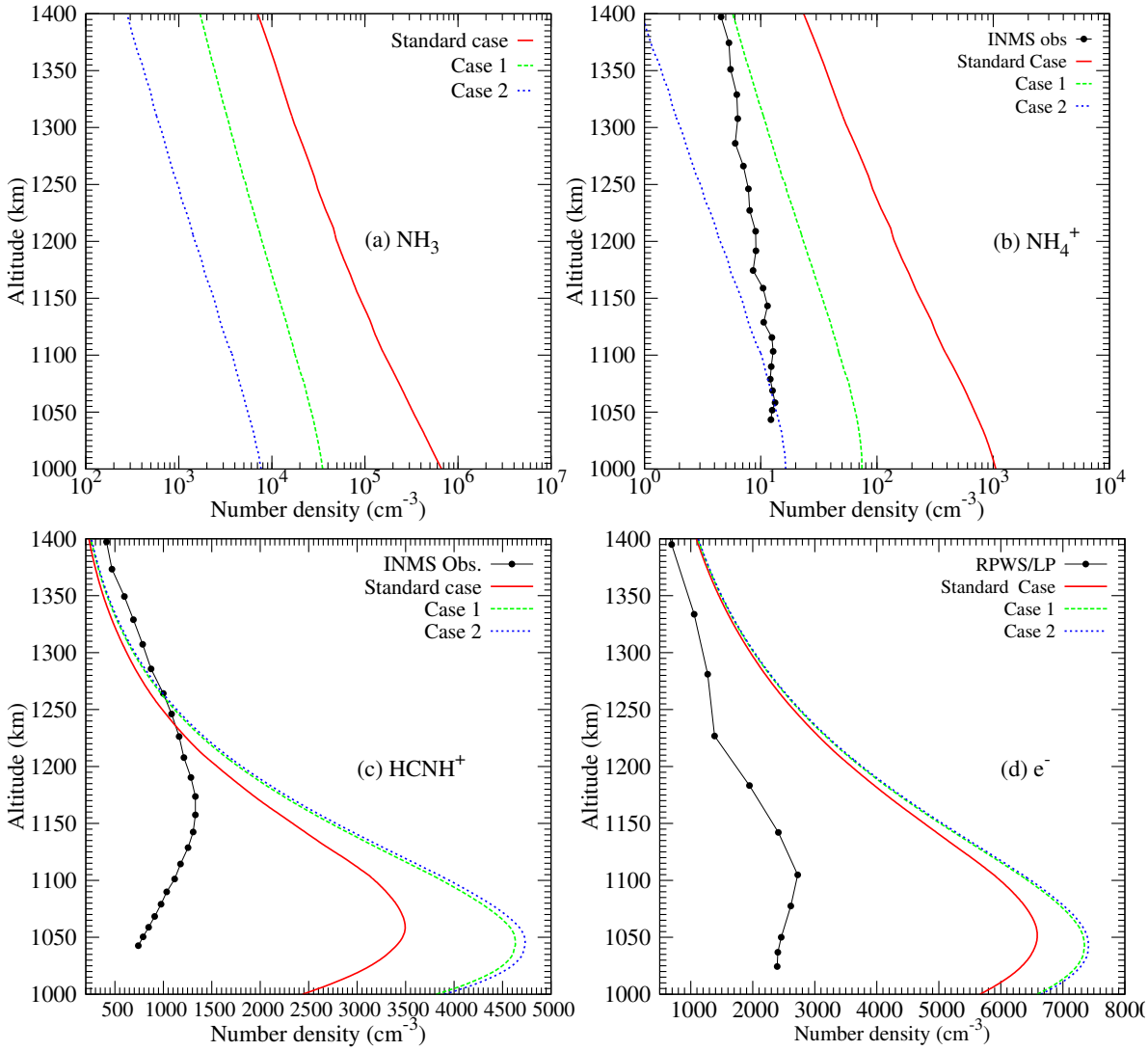

Figure 4.31: NH_3 densities used in the standard case along with the modelled profiles of *Dobrijevic et al.* [2016] (Case 1) and *Yelle et al.* [2010] (Case 2). The profiles for NH_4^+, $HCNH^+$, and electrons obtained by using each of these NH_3 profiles are also shown.

The sensitivity test of HCN and NH_3, presented in Section 4.5.4 and 4.5.7, respectively, suggests the importance of these minor species in determining the densities of major ions $HCNH^+$, $C_2H_5^+$, and CH_5^+. However, due to coupled chemistry, the overall

impact on the modelled electron density is not appreciable as the decrease in the density of $HCNH^+$ is compensated by the increase in the density of $C_2H_5^+$ and CH_5^+ and vice versa.

4.5.8 Solar flux models

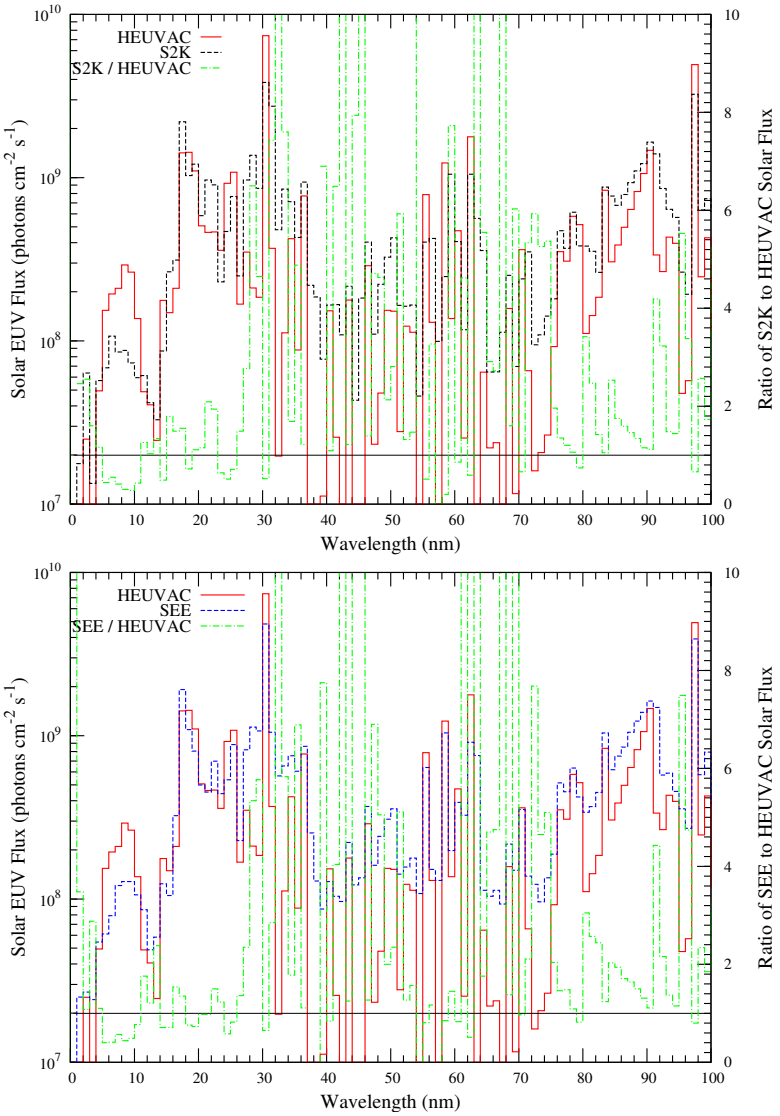

Figure 4.32: Comparison between S2K, SEE and HEUVAC solar flux models for 5 January 2008. The magnitude of the ratio between the solar fluxes is indicated on the right side vertical axis. The horizontal line shows the point where the ratio S2K/HEUVAC and SEE/HEUVAC equals 1.

In the standard case, HEUVAC flux model has been used for the calculation of plasma density. To see how the model results vary with input solar flux models, we did test runs using different solar flux models, viz. SOLAR2000 (S2K) model v.2.38 [*Tobiska et al.*, 2000] and Solar EUV Experiment (SEE, Version 11.0) [*Woods et al.*, 2005] flux. The S2K model is based on measured solar irradiance and gives flux for the

wavelength range 0.1 to 100000 Å. The SEE gives the solar irradiance measured at Earth by NASA's Thermospheric Ionospheric Mesospheric Energy and Dynamics (TIMED) for the wavelength 1-2000 Å. Figure 4.32 shows the solar EUV fluxes at 1 AU generated using S2K and SEE for the day 5 January 2008 along with HEUVAC flux which we have used in the standard case. It is seen that S2K and SEE fluxes are generally higher than that of the HEUVAC with noticeable difference in the wavelength range 30-70 nm where N_2^+, CH_4^+ and CH_3^+ photoionization cross sections are high. Increased flux in this wavelength regime would cause higher volume production rates leading to increased electron densities. Figure 4.33 shows electron density profiles obtained by using different flux models. Profiles calculated using S2K and SEE match with each other at altitudes above 1200 km. At the altitude of peak production (∼1050 km) the S2K and SEE profiles are higher than that of the standard case profile by ∼17% and 10%, respectively. Overall, the difference between the standard case profile and profile obtained using SEE and S2K is only ∼15%. This suggest that input solar flux model does not make any significant impact on the electron density profiles.

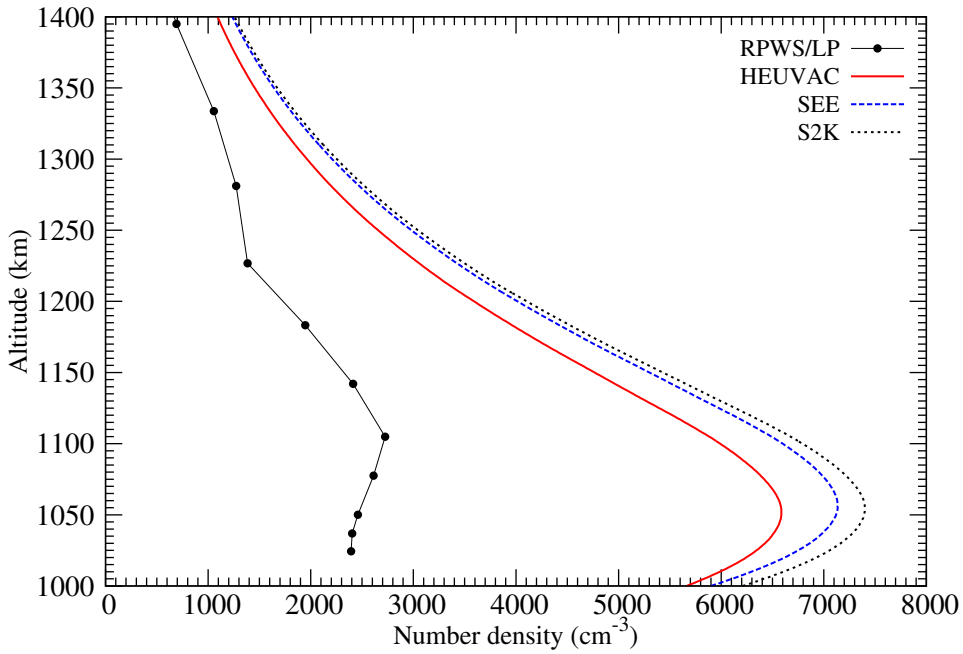

Figure 4.33: Electron density profile obtained using three different solar flux models.

4.6 Summary

In the present chapter, a one dimensional photochemical model for the dayside ionosphere of Titan has been developed for computing the density profiles of ions and electrons under steady-state photochemical equilibrium condition. The study concentrated on the T40 flyby of Cassini orbiter and used the in-situ measurements from instruments onboard Cassini as input to the model. An energy deposition model is

employed for calculating the attenuated photon flux and photoelectron flux at different altitudes in Titan's ionosphere. The Analytical Yield Spectrum approach has been used for calculating the photoelectron fluxes. Volume production rates of major primary ions, like, N_2^+, N^+, CH_4^+, CH_3^+, etc due to photon and photoelectron impact are calculated. The modelled ion production rates are found to be in good agreement with the calculations of *Lavvas et al.* [2011] and *Richard et al.* [2015]. It is used as input to the model where ion-neutral chemistry is described. The densities of 23 ions were calculated. The ion densities are added together to obtain the total electron density. The calculated plasma density profiles are compared with the Cassini observations as well as previous model calculations. It is seen that the modelled electron density profile in Titan's ionosphere is larger than that measured by Cassini by a factor of 2 to 3 around the peak. We also modelled the electron density profiles of four other dayside flybys, viz. T48, T86, T95, and T104 and compared them with observations. In all these cases, model overestimated the electron density at the ionospheric peak as compared to the observations.

We have made a comprehensive assessment of various model parameters to understand their impact on the calculated plasma densities. Following are observations of the present study:

1. Following the suggestion of *Vigren et al.* [2016], we reduced the model calculated photoelectron flux by a factor of 3 to evaluate the impact of the exaggerated photoelectron flux on the calculated plasma density. The peak electron density is found to decrease by only ∼10%.

2. Use of the empirical production rate of N_2^+ ion, calculated by *Madanian et al.* [2016], also could make a difference of not more than 20% in the peak electron density.

3. Our model calculations suggest that the use of model electron temperature profile, instead of the measured one, can improve the density calculations.

4. The electron temperature measured by Cassini RPWS/LP has to be reduced by a factor of 5 to bring the modelled electron densities come closer to the LP observations.

5. Even though increasing the dissociative recombination rate coefficients of the ions $C_2H_5^+$ and CH_5^+ by a factor of 10 could bring the calculated major ion densities ($C_2H_5^+$, CH_5^+ and $HCNH^+$) closer to the observations, the modelled electron densities are higher than the observation by ∼60% near the peak.

6. The use of different available density profiles of minor neutral species, HCN and NH_3, have noticeable impact on the profiles of $C_2H_5^+$, CH_5^+ and $HCNH^+$. However,

the decrease in the peak electron density is <20% due to the coupled chemistry between these three ions.

7. We show that the use of different solar flux models (HEUVAC, SEE and S2K) can cause only about 15% change on the modelled electron densities.

The Cassini observed density profiles are consistent with model calculations when we varied the parameters which influence the loss of ions and electrons, viz. electron temperature and dissociative electron recombination rate coefficients. This shows that even though the overestimation in the production parameters, namely photoelectron flux and primary production rate of N_2^+, may contribute towards the disagreement between the modelled and observed plasma density profiles to some extent, a more significant role is played by the loss processes, in agreement with the study of *Richard et al.* [2015], *Westlake et al.* [2012] and *Vigren et al.* [2013]. It is probable that some important chemical reactions are missing that may account for the additional loss of ions and electrons.

In the subsequent chapter, we extend the photochemical model further to address the chemistry of negative ions and to calculate the density profiles of anions on the dayside of Titan's ionosphere.

Chapter 5

Modelling the negative ion chemistry on Titan's dayside ionopshere

5.1 Introduction

Even though there have been a number of models which studied the positive ion chemistry in Titan's ionosphere (refer Section 1.4.1), there are only two studies so far which attempted to model the anion chemistry [*Vuitton et al.*, 2009; *Dobrijevic et al.*, 2016]. These models considered anions of masses up to 75 amu and modelled the profiles of anions of the form $C_{n-1}N$ and C_nH, where n=2–6. By considering radiative electron attachment, dissociative electron attachment, and ion–pair formation as the main production processes, and photodetachement, ion–ion recombination, and ion–neutral associative detachment as the main loss processes, *Vuitton et al.* [2009] calculated the densities of anions CN^-, C_3N^-, C_5N^-, C_4H^-, C_6H^-, C_2H^-, CH_3^-, CH_2^-, H^-, OH^-, and O^-. The DEA to neutral molecules, especially to HCN, was proposed by *Vuitton et al.* [2009] as the most important production process of anions and the associative detachment with radicals H and CH_3 as the major loss channel. The most dominant negative ion in Titan's ionosphere was identified as CN^-, followed by C_3N^- with a peak density of 1 cm^{-3} and 0.1 cm^{-3}, respectively. The anions C_4H^- and C_6H^- were found to contribute significantly to the total anion density in the lower altitudes (<800 km) with densities in the range 10^{-3} to 10^{-2} cm^{-3}. The densities of all other anions were found to be negligible ($< 2 \times 10^{-3}$ cm^{-3}) at all altitudes.

The model of *Dobrijevic et al.* [2016] was a one dimensional photochemical model with vertical transport coupling neutral species with cations and anions. They updated the DEA cross sections used by *Vuitton et al.* [2009] and calculated the densities of the negative ions CN^-, C_3N^-, H^-, C_2H^-, C_3^-, and C_4H^-. The anions C_5N^-, C_6H^-, CH_3^-, CH_2^-, OH^-, and O^- were not included their study. They also suggested CN^- as the most dominant negative ion in Titan, followed by C_3N^-. However, noticeable differences were seen when the profiles were compared with that of *Vuitton et al.* [2009]. At the peak, the density of CN^- calculated by *Dobrijevic et al.* [2016] was a factor of two lower and

C_4H^- density a factor of 10 higher than those calculated by *Vuitton et al.* [2009]. The dissociative electron attachment to CH_4 was found to be the main source of anions. All this differences were attributed to the use of updated DEA cross sections in the model of *Dobrijevic et al.* [2016].

In the present study, by using the negative ion chemistry scheme of *Vuitton et al.* [2009] and the state-of-the-art DEA cross sections and reaction rate coefficients, we extent the photochemical model presented in the previous chapter to calculate the density profiles of 10 anions on Titan's dayside ionosphere. *Dobrijevic et al.* [2016] have shown how the updated DEA cross sections affect the densities of a few selected anions. We extend this further and include rest of the anions as in *Vuitton et al.* [2009] model. The chemistry of anions is discussed in detail and we point out the most important production and loss reactions of all the ten ions at the ionospheric peak. We present a comparison between the density profiles obtained by *Vuitton et al.* [2009], *Dobrijevic et al.* [2016], and the present study. Recently, *Desai et al.* [2017] reported the detection of consistent peaks between 25.8 and 26.0 m/q and between 49.0 and 50.1 m/q in the mass/charge spectrum recorded by CAPS-ELS of the Cassini mission. A relative density profiles for these mass peaks were also depicted. We present a comparison between our modelled profiles with these recent profiles derived from observations.

5.2 Formation and destruction processes of anions

Vuitton et al. [2009] selected the plausible candidates for negative ions in Titan's ionosphere based on the gas phase acidity and electron affinity of the parent neutral species. The higher the electron affinity of the parent species, the more stable will be the negative ion formed. They considered the formation of negative ions only from deprotonated neutrals as anions formed by attaching an electron to a molecule with a filled valance shell quickly undergo auto-detachment. Gas phase acidity characterises how easily a molecule can be deprotonated. The anions chosen by *Vuitton et al.* [2009], CN^-, C_3N^-, C_5N^-, C_4H^-, C_6H^-, C_2H^-, CH_3^-, OH^-, and O^- are formed from molecules having high to moderate electron affinity (∼1-4 eV) and gas phase acidity (∼1400-1600 kJ/mol). They also considered the anions H^- and CH_2^- in the model even though H and CH_2 are having low electron affinity, since they are formed from CH_4 which is the second dominant gas in Titan's atmosphere. The following are the major production processes of anions in Titan's ionosphere:

1. **Radiative Electron Attachment (REA)**: During REA, a thermal electron gets attached to an atom or radical resulting in the formation of negative ion.

$$A + e_T \rightarrow A^- + h\nu \tag{5.1}$$

Vuitton et al. [2009] (hereafter referred to as V09) considered REA reactions to the radicals C_2H, C_4H, C_6H, and C_3N, resulting in the formation of negative ions

C_2H^-, C_4H^-, C_6H^-, and C_3N^-. Only theoretically calculated rate coefficients are available for these reactions [*Herbst and Osamura*, 2008]. For the formation of the anions H^-, CH_2^-, OH^-, and CN^- via the thermal electron capture by the corresponding neutral species, they adopted a rate coefficient of 10^{-14} cm^3s^{-1}, following the suggestion of *Petrie* [1996]. *Dobrijevic et al.* [2016] (hereafter referred to as D16) pointed out that REA processes are relatively inefficient in Titan's ionosphere either due to the very low abundance of the radicals involved in the reaction or due to very low reaction rate coefficients involved.

In the present model, we have considered only three REA reactions:

$$C_3N + e_T \rightarrow C_3N^- + h\nu \ (2.6 \times 10^{-10} \ cm^3s^{-1}) \tag{5.2}$$

$$C_4H + e_T \rightarrow C_4H^- + h\nu \ (1.1 \times 10^{-8} \ cm^3s^{-1}) \tag{5.3}$$

$$C_6H + e_T \rightarrow C_6H^- + h\nu \ (6.2 \times 10^{-8} \ cm^3s^{-1}) \tag{5.4}$$

The rate coefficients are taken from the theoretical study of *Herbst and Osamura* [2008]. Our model does not include any other REA reactions suggested by V09 as they have very low rate coefficients (of the order of 10^{-14} to 10^{-16} cm^3s^{-1}).

2. **Dissociative Electron Attachment (DEA)**: In DEA reactions, a suprathermal electron dissociates a molecule into two or more atoms or radicals and attaches itself to one of the fragments formed.

$$AB + e_s \rightarrow A^- + B \tag{5.5}$$

In the photochemical model the rate of a DEA reaction at an altitude Z is calculated as:

$$[AB(Z)] \int \varphi(Z,E) \ \sigma(E) \ dE \tag{5.6}$$

where [AB(Z)] is the concentration of parent neutral molecule AB at altitude Z, $\varphi(Z,E)$ is the photoelectron flux calculated using equation (4.8) and $\sigma(E)$ is the DEA cross section of the molecule AB.

Cross sections for DEA reactions relevant for Titan's atmosphere have been re-measured recently [*Rawat et al.*, 2007; *Rawat et al.*, 2008; *May et al.*, 2008, 2010; *Krishnakumar et al.*, 2011; *Gilmore and Field*, 2015]. We have used the latest DEA measurements available for our calculations. For those molecules whose DEA cross sections are not available (HC_5N and C_6H_6), we assumed it to be equal to that of some structurally similar molecules, as done by *Vuitton et al.* [2009]. The list of dissociative attachment cross sections that we have used for the calculations are shown in Figure 5.1 and references are provided in Table 5.1.

Table 5.1: List of dissociative electron attachment processes considered in the model.

Reaction	References
$HCN + e_s \rightarrow CN^- + H$	*May et al.* [2010]
$HC_3N + e_s \rightarrow CN^- + C_2H$	*Gilmore and Field* [2015]
$HC_3N + e_s \rightarrow C_3N^- + H$	*Gilmore and Field* [2015]
$C_4H_2 + e_s \rightarrow C_4H^- + H$	*May et al.* [2008]
$C_2H_2 + e_s \rightarrow C_2H^- + H$	*Song et al.* [2017]
$C_2H_2 + e_s \rightarrow H^- + C_2H$	*Song et al.* [2015]
$CH_4 + e_s \rightarrow H^- + CH_3$	*Rawat et al.* [2008]
$CH_4 + e_s \rightarrow CH_2^- + H_2$	*Rawat et al.* [2008]
$NH_3 + e_s \rightarrow H^- + NH_2$	*Rawat et al.* [2008]
$H_2O + e_s \rightarrow OH^- + H$	*Itikawa and Mason* [2005]
$H_2O + e_s \rightarrow O^- + H_2$	*Rawat et al.* [2007]
$H_2 + e_s \rightarrow H^- + H$	*Krishnakumar et al.* [2011]

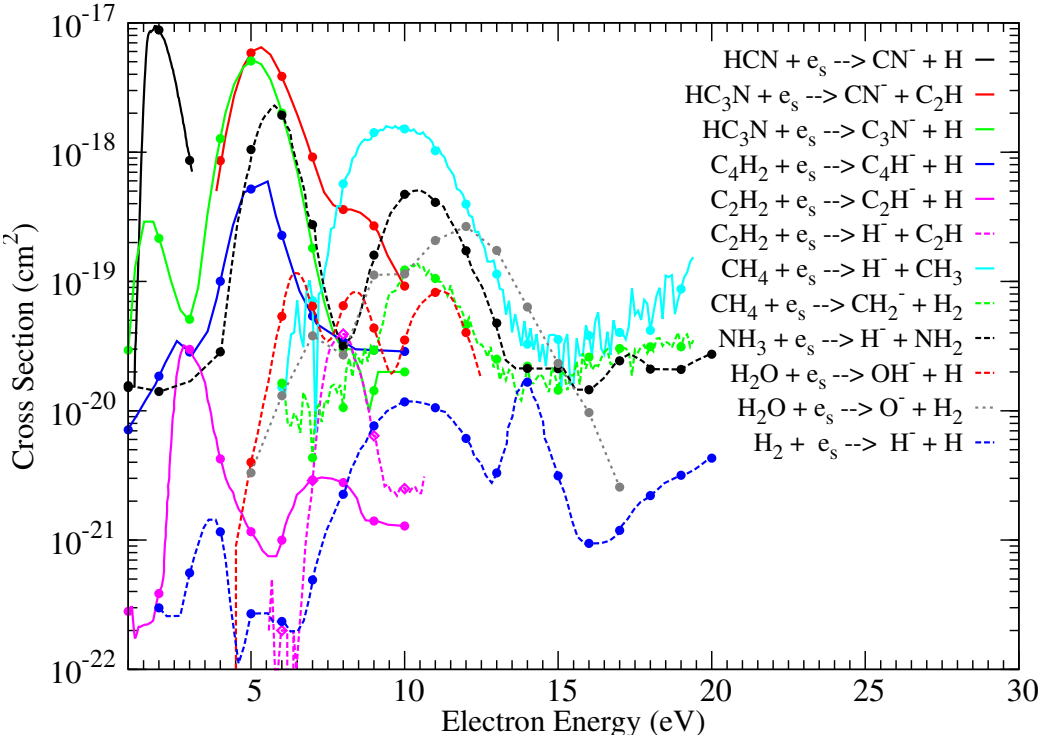

Figure 5.1: Dissociative electron attachment cross sections used in the model. References are given in Table 5.1

3. **Ion-pair formation**: Sometimes photoionization of a molecule can result in the

formation of a pair of positive and negative ions.

$$AB + h\nu \rightarrow A^- + B \tag{5.7}$$

Ion-pair formation is not an effective process as the cross section of the process is very low ($\sim 10^{-21}$) cm^2 and hence has not been considered in the current model.

The major loss processes of anions are:

1. **Photodetachment**: Upon photon impact, the electron gets detached from the anion resulting in the formation of a neutral atom and free electron.

$$A^- + h\nu \rightarrow A + e^- \tag{5.8}$$

The photodetachment rates (in unit of s^{-1}) can be calculated as:

$$\int \psi(Z, E)\ \sigma_{phd}(E)\ dE \tag{5.9}$$

where $\psi(Z, E)$ is the photon flux at altitude Z calculated using the Beer-Lambert law and $\sigma_{phd}(E)$ is the photodetachment cross section of the neutral species. Measured cross sections are not available for photodetachment processes.

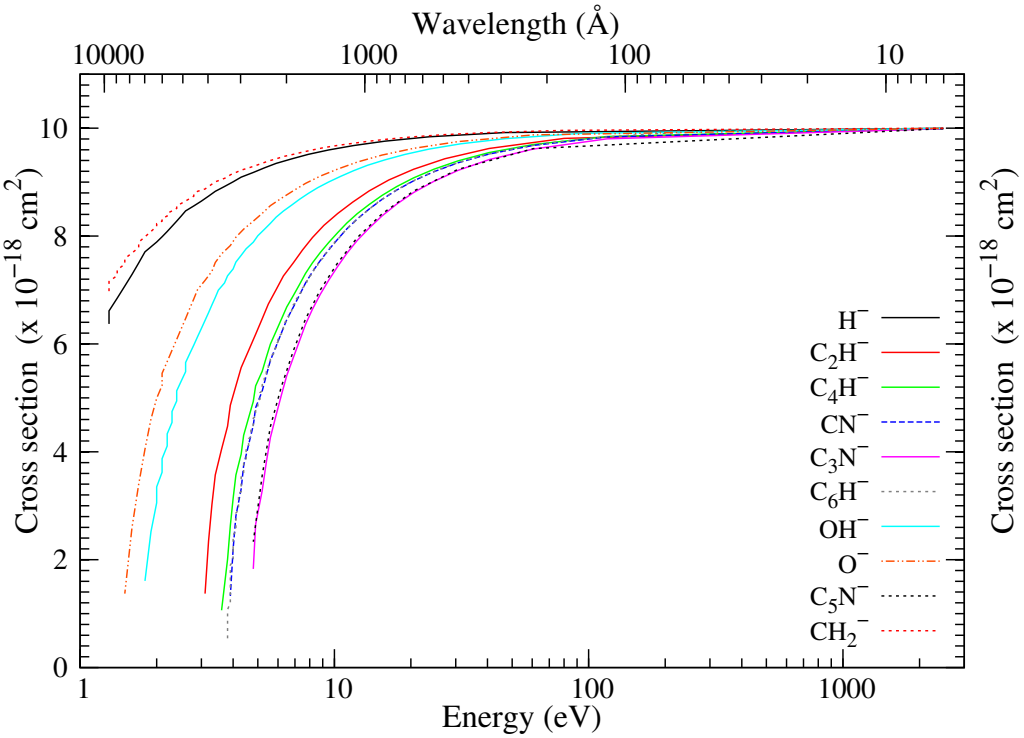

Figure 5.2: Photodetachment cross sections of anions calculated using Miller-Threshold law.

Millar et al. [2007] in their theoretical study on hydrocarbon anions in interstellar clouds and circumstellar envelopes, assumed that the photodetachment cross

sections depend upon the photon energy through the relation

$$\sigma = \sigma_0(1 - EA/\varepsilon)^{0.5},\ \varepsilon > EA \tag{5.10}$$

where EA is the electron affinity and ϵ is the photon energy in eV. Similar to V09 and D16, we also adopted the Miller-threshold law to calculate the photodetachment cross sections in our model. Figure 5.2 shows the photodetachment cross sections calculated for the 10 anions included in our study.

2. **Ion-ion recombination**: These are reactions of the form:

$$A^- + B^+ \rightarrow A + B \tag{5.11}$$

Much information is not available on ion-ion recombination reactions. Using a complex potential model, *Hickman* [1979] calculated the rate coefficients of ion-ion recombination reactions using an approximate scaling formula based on the reduced mass of the colliding particles and electron affinity of the electron donor. *Smith et al.* [1978] showed that this formula could reproduce the measured coefficients for the reaction between NH_4^+ and Cl^- ions with an accuracy of $\pm$30%. V09, using the same formula, obtained a rate coefficient of 10^{-7} cm^3s^{-1} at room temperatures for the mutual neutrilisation reactions valid in Titan's ionosphere. We have adopted the same rate value in our model as no other measured rate coefficients are available. We considered the mutual-neutrilisation reactions only with the most dominant positive ions $HCNH^+$ and $C_2H_5^+$.

3. **Ion-neutral associative detachment**: These are the reverse reactions of DEA processes where an anion combines with a neutral forming a neutral molecule and an electron:

$$A^- + B \rightarrow AB + e^- \tag{5.12}$$

The reactant neutral involved in such reactions are radical species since such reactions are possible only if the electron detachment energy is less than the energy of the bond that is produced. The most abundant radicals in Titan's ionosphere are H and CH_3 [*Yelle et al.*, 2010]. There are measurements/calculations of rate coefficients for the reactions of anions with H atom [*Martinez et al.*, 2009; *Barckholtz et al.*, 2001; *Yang et al.*, 2011; *Howard et al.*, 1974; *Adams*, 2006]. However, no rate coeffcients are available for reactions with CH_3 radical. Following the methodology of V09, for the associative detachment reactions of anions with CH_3 radical, we adopted the same rate coefficients as that for the reaction with H atom.

4. **Chemical reactions**: These are ion-neutral reactions through which anion of one form is converted into another anion. They can be proton transfer reactions or

polymerization reactions. For proton transfer reactions V09 calculated the rates using Langevin theory. Similarly, for polymerization reactions, as no measured rate coefficients are available, the rate constants were set to 10^{-12} cm^3 s^{-1} based on the study of *Howling et al.* [1994] and *Perrin et al.* [1994]. For these reactions we adopted the same rate coefficients as that of V09.

5.3 Model inputs

The photochemical model that is presented in Chapter 4 is extended further by adding the chemistry of negative ions. The model inputs are more or less the same as described in Section 4.3 with the following changes.

5.3.1 Solar flux

For calculating densities of positive ions, we used the HEUVAC solar flux in the wavelength range 1 to 1055 Å. The flux has to be extended in case of negative ions as the photodetachment cross sections are considerably high at higher wavelength (refer Figure 5.2). Above 1055 Å, we used the flux from Solar2000 model (version 2.38) of *Tobiska et al.* [2000] and considered flux up to 10000 Å.

5.3.2 Neutral Densities

Neutral densities used in the model remain the same as that described in Section 4.3.2. In addition to these neutrals, density profiles of the radicals C_4H, C_6H, and CH_3 are required as the reactions involving these radicals form an important production/loss channel for many anions (refer Table 5.2). For the radicals C_4H and C_6H, the profiles given by *Krasnopolsky* [2009] are used, after multiplying with the scaling factor used for their parent neutral species. CH_3 density profile is taken from *Krasnopolsky* [2009] without applying any correction factor, since the CH_4 profile of *Krasnopolsky* [2009] and the one that we have used in the model from *Mandt et al.* [2012] are in close agreement.

5.3.3 Cross sections

The photo cross sections and electron impact cross sections of N_2 and CH_4 used in the model have been described in Section 4.3.3. Dissociative electron attachment cross sections of minor species are required to calculate the production rate of anions through DEA. The list of dissociative attachment cross sections that we have used for the calculations are shown Figure 5.1 and references are provided in Table 5.1. Photodetachment cross sections are calculated theoretically using Miller-Threshold law and are shown in Figure 5.2.

5.3.4 Reaction rate coefficients

A list of ion-neutral reactions involving negative ions are added to the model for calculating the anion density profiles. The reaction rate coefficients of different reactions involving negative ions, available till then, have been reviewed by V09. For those reactions for which measured rate coefficients were not available, V09 calculated them using Langevin theory. For most of the reactions considered in the current model, we used the rate coefficients as in V09. However, we have incorporated changes in the rate coefficients reported post the model of V09 as follows.

1. For the reaction of the anions CN^-, C_3N^-, and C_5N^- with H atom, we used the rate coefficient measurements of *Yang et al.* [2011] which was also used by D16 in their study.

2. For the reactions of H^- with H and C_2H_2, the rate coefficients measurements of *Martinez et al.* [2009] and *Martinez et al.* [2010] have been used.

3. We also incorporated the reaction of hydride anion with H_2O molecule, the rate coefficient for which was measured by *Martinez et al.* [2010]. This particular reaction was not considered in the model of V09.

4. For the reaction of CN^- with HC_3N, we used the measurement of *Biennier et al.* [2014], whereas the models of V09 and D16 have used theoretical value.

Table A.3 in the Appendix shows the reactions of anions along with their rate coefficients used in the model.

5.4 Results and Discussion

The density profiles of the 10 anions calculated using the current model are shown in Figure 5.3. The major production and loss processes of different anions at the ionospheric peak are listed in Table 5.2. In the following sections, we present the results of model calculations for each negative ion and also show a comparison of our calculated profile with that of *Vuitton et al.* [2009] and *Dobrijevic et al.* [2016].

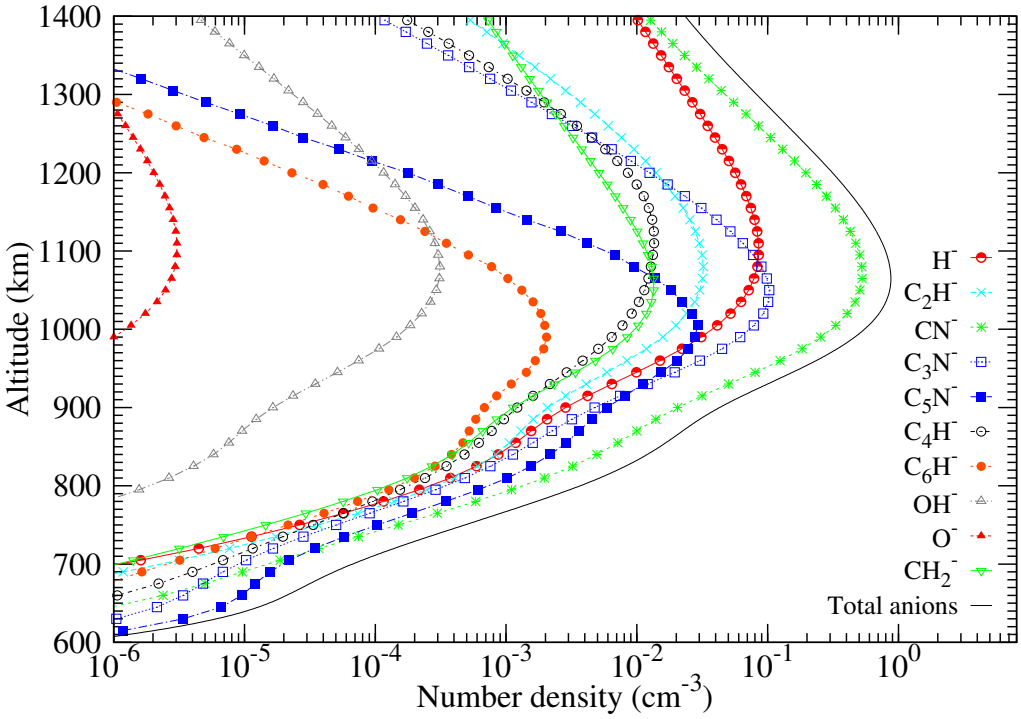

Figure 5.3: The density profiles of 10 negative ions calculated in the present model, along with the total anion density.

5.4.1 H^- and CH_2^-

The maximum density of H^- is $\sim$0.1 cm^{-3}, which is around two orders of magnitude higher than the value obtained by V09 (see Figure 5.4a). This difference is due to the difference in the DEA cross sections of CH_4 adopted in the two studies. V09 used the DEA cross sections of methane measured by *Sharp and Dowell* [1967] whereas we have used the recent measurements of *Rawat et al.* [2008]. The DEA cross sections of *Sharp and Dowell* [1967] are around a factor of 20 lower than those of *Rawat et al.* [2008]. The recent review article by *Song et al.* [2015] recommends the use of the DEA cross sections of *Rawat et al.* [2008] as these measurements are more recent and obtained using an advanced apparatus. The overall uncertainty in the measurements was estimated to be a maximum of $\pm$15%. D16 also used the cross section measurements by *Rawat et al.* [2008] in their calculations. Our peak H^- density is around a factor of 3 higher than the peak value of D16. The model of D16 differs from our model mainly in the fact that our model parameters, viz. the neutral density, solar flux, and solar zenith angle, are for the condition that prevailed on Titan during the T40 flyby of Cassini, while the model of *Dobrijevic et al.* [2016] is a global mean model for a solar zenith angle of 60^o. However, our calculated profile falls within the uncertainty limits of *Dobrijevic et al.* [2016].

Table 5.2: Major production and loss processes of anions at 1100 km and their relative contribution.

Reaction	Rates (cm^3 s^{-1}) or s^{-1}	References for Cross sections/ Rate Coefficients	% Contribution
	(1) H^-		
Production:			
$CH_4 + e_s \rightarrow H^- + CH_3$	(4.13×10^{-11}) †	*Rawat et al.* [2008]	98
Loss:			
$H^- + h\nu \rightarrow H + e$	(1.81×10^{-02})	Miller Threshold Law	40
$H^- + HCN \rightarrow CN^- + H_2$	1.5×10^{-08}	*Mackay et al.* [1976]	32
$H^- + H \rightarrow H_2 + e$	2.0×10^{-09}	*Martinez et al.* [2009]	16
$H^- + C_2H_2 \rightarrow C_2H^- + H_2$	3.1×10^{-09}	*Martinez et al.* [2010]	10
	(2) CN^-		
Production:			
$H^- + HCN \rightarrow CN^- + H_2$	1.50×10^{-08}	*Mackay et al.* [1976]	83
$C_2H^- + HCN \rightarrow C_2H_2 + CN^-$	3.90×10^{-09}	*Mackay et al.* [1976]	8
$HCN + e_s \rightarrow CN^- + H$	(9.0×10^{-11})	*May et al.* [2010]	5
Loss:			
$CN^- + H \rightarrow HCN + e$	6.30×10^{-10}	*Yang et al.* [2011]	84
$CN^- + CH_3 \rightarrow CH_3CN + e$	6.3×10^{-10}	idem as $CN^- + H$	6
	(3) C_2H^-		
Production:			
$H^- + C_2H_2 \rightarrow C_2H^- + H_2$	3.1×10^{-09}	*Martinez et al.* [2010]	99
Loss:			
$C_2H^- + H \rightarrow C_2H_2 + e$	1.6×10^{-09}	*Barckholtz et al.* [2001]	53
$C_2H^- + HCN \rightarrow C_2H_2 + CN^-$	3.9×10^{-09}	*Mackay et al.* [1976]	34
$C_2H^- + hv \rightarrow C_2H + e$	(8.23×10^{-4})	Miller-Threshold Law	7
	(4) C_3N^-		
Production:			
$C_3N + e_T \rightarrow C_3N^- + h\nu$	2.63×10^{-10}	*Herbst and Osamura* [2008]	91
Loss:			
$C_3N^- + H \rightarrow HC_3N$	5.4×10^{-10}	*Yang et al.* [2011]	90
	(5) C_5N^-		
Production:			
$CN^- + HC_5N \rightarrow C_5N^- + HCN$	5.4×10^{-09}	*Vuitton et al.* [2009]	58

Table 5.2 – *Continued from previous page*

Reaction	Rates ($cm^3\ s^{-1}$) or s^{-1}	References for Cross sections/ Rate Coefficients	% Contribution
$H^- + HC_5N \rightarrow C_5N^- + H_2$	1.0×10^{-08}	*Vuitton et al.* [2009]	20
$HC_5N + e_s \rightarrow C_5N^- + H$	$(8.0 \times 10^{-10}$)	*Gilmore and Field* [2015]	18
Loss :			
$C_5N^- + H \rightarrow HC_5N$	5.8×10^{-10}	*Yang et al.* [2011]	90
	(6) C_4H^-		
Production:			
$C_4H + e_T \rightarrow C_4H^- + h\nu$	1.1×10^{-08}	*Herbst and Osamura* [2008]	86
$H^- + C_4H_2 \rightarrow C_4H^- + H_2$	6.4×10^{-09}	*Vuitton et al.* [2009]	10
Loss:			
$C_4H^- + H \rightarrow C_2H_2 + E$	8.3×10^{-09}	*Barckholtz et al.* [2001]	56
$C_4H^- + HCN \rightarrow CN^- + C_2H_2$	2.0×10^{-09}	*Vuitton et al.* [2009]	36
	(7) C_6H^-		
Production:			
$H^- + C_6H_2 \rightarrow C_6H^- + H_2$	6.3×10^{-09}	*Vuitton et al.* [2009]	83
$C_2H^- + C_6H_2 \rightarrow C_6H^- + C_2H_2$	2.3×10^{-09}	*Vuitton et al.* [2009]	11
Loss:			
$C_6H^- + H \rightarrow$ Products	5.0×10^{-10}	*Barckholtz et al.* [2001]	48
$C_6H^- + HCN \rightarrow CN^- + C_2H_2$	1.9×10^{-09}	*Vuitton et al.* [2009]	45
	(8) OH^-		
Production:			
$H^- + H_2O \rightarrow OH^- + H_2$	4.8×10^{-09}	*Martinez et al.* [2010]	96
Loss :			
$OH^- + hv \rightarrow OH + e$	7.4×10^{-03}	Miller-Threshold Law	37
$OH^- + H \rightarrow H_2O + e_T$	1.4×10^{-9}	*Howard et al.* [1974]	26
$OH^- + HCN \rightarrow CN^- + H_2O$	3.7×10^{-9}	*Raksit and Bohme* [1983]	17
$OH^- + C_2H_2 \rightarrow C_2H^- + H_2O$	2.2×10^{-9}	*Raksit and Bohme* [1983]	15
	(9) O^-		

Table 5.2 – *Continued from previous page*

Reaction	Rates ($cm^3\ s^{-1}$) or s^{-1}	References for Cross sections/ Rate Coefficients	% Contribution
Production:			
$H_2O + e_s \rightarrow O^- + H_2$	$(6.56 \times 10^{-12}$)	*Itikawa and Mason* [2005]	100
Loss:			
$O^- + hv \rightarrow O + e$	$(1.04 \times 10^{-02}$)	Miller-threshold law	34
$O^- + CH_4 \rightarrow OH^- + CH_3$	1.0×10^{-10}	UMIST database	31
$O^- + HCN \rightarrow CN^- + OH$	3.7×10^{-9}	*Bohme* [1975]	12
	(10) CH_2^-		
Production:			
$CH_4 + e_s \rightarrow CH_2^- + C_2$	$(2.93 \times 10^{-12}$)	*Rawat et al.* [2008]	100
Loss :			
$CH_2^- + hv \rightarrow CH_2 + e$	$(1.89 \times 10^{-02}$)	Miller-Threshold Law	81
$CH_2^- + H \rightarrow$ Products	1.0×10^{-9}	*Adams* [2006]	16

†Value inside the bracket is rate (unit: s^{-1}) calculated as $\int \varphi(Z,E)\,\sigma(E)\,dE$ where $\varphi(Z,E)$ is the photon (photoelectron) flux and $\sigma(E)$ is the photodetachment (dissociative electron attachment) cross sections.

The CH_2^- is another anion, other than H^-, that is produced through the DEA of CH_4. As in the case of the hydride anion, the use of the DEA cross sections of *Sharp and Dowell* [1967] makes the density of CH_2^- calculated by V09 almost two orders of magnitude less than that in our model (see Figure 5.4b). D16 did not include CH_2^- in their calculations; the reasons for the exclusion they cited are the low electron affinity of CH_2 and that CH_2^- is only a minor product of the dissociative electron attachment of methane as compared to H^-. However, our calculations show that, the CH_2^- density can be comparable to other anions, like C_2H^-, C_4H^-, and C_5N^- (see Figure 5.3).

5.4.2 CN^- and C_3N^-

We found CN^- as the dominant negative ion in Titan's ionosphere, agreeing with the results of V09 and D16. However, the process through which this ion is produced is different in the current model and V09. In the V09 model, CN^- is mainly produced through the DEA of HCN where they used the cross sections of *Inoue* [1966]. These cross sections are around one order of magnitude higher than the recent DEA cross sections of HCN measured by *May et al.* [2010] and used in our model calculations. The major production process of CN^- in our model is the reaction of H^- with HCN, constituting around 83% of the total production rate at 1100 km. The DEA of HCN

become important only at altitude greater than 1150 km and that too only as the second major production channel. Our CN^- profile is generally in good agreement with the calculations of D16 although differences are seen at lower altitudes (see Figure 5.5a).

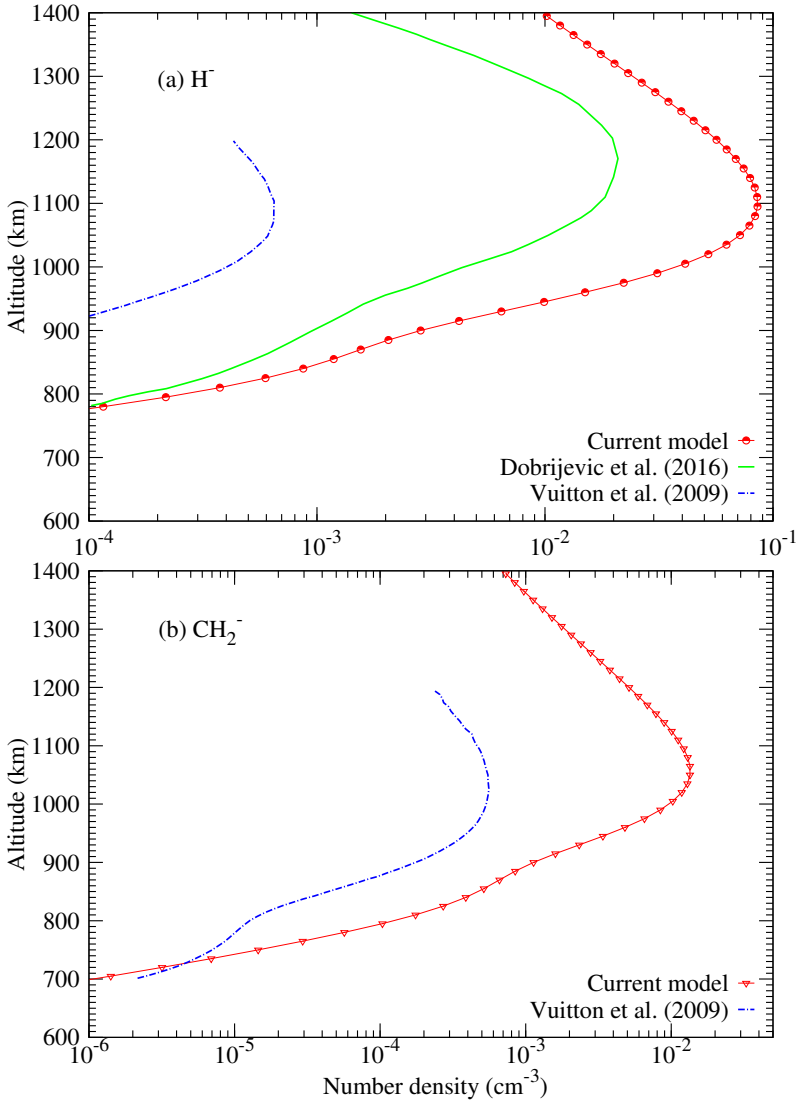

Figure 5.4: The density profiles of (a) H^- and (b) CH_2^- calculated using the current model compared with the calculations of *Vuitton et al.* [2009] and *Dobrijevic et al.* [2016].

All three models suggest C_3N^- as the second most dominant ion near the ionospheric peak. However, as discussed in Chapter 4, our model overestimates the thermal electron density by a factor of 2 compared to the observations of Langmuir probe onboard Cassini orbiter, a common issue reported by different authors in literature, e.g. *Robertson et al.* [2009]; *Westlake et al.* [2012]; *Vigren et al.* [2013]; *Mukundan and Bhardwaj* [2018]. To understand the impact of this overestimation on our calculated C_3N^- density, we reduced the thermal electron density by a factor of 2. This reduced the peak C_3N^- density roughly by a factor of 3 (cf. Figure 5.5) though it continues to be the second

most abundant ion in the range 1000-1100 km, the region where the negative ion density peaks. The hydride anion overtakes C_3N^- density at altitudes greater than 1100 km (cf. Figure 5.3).

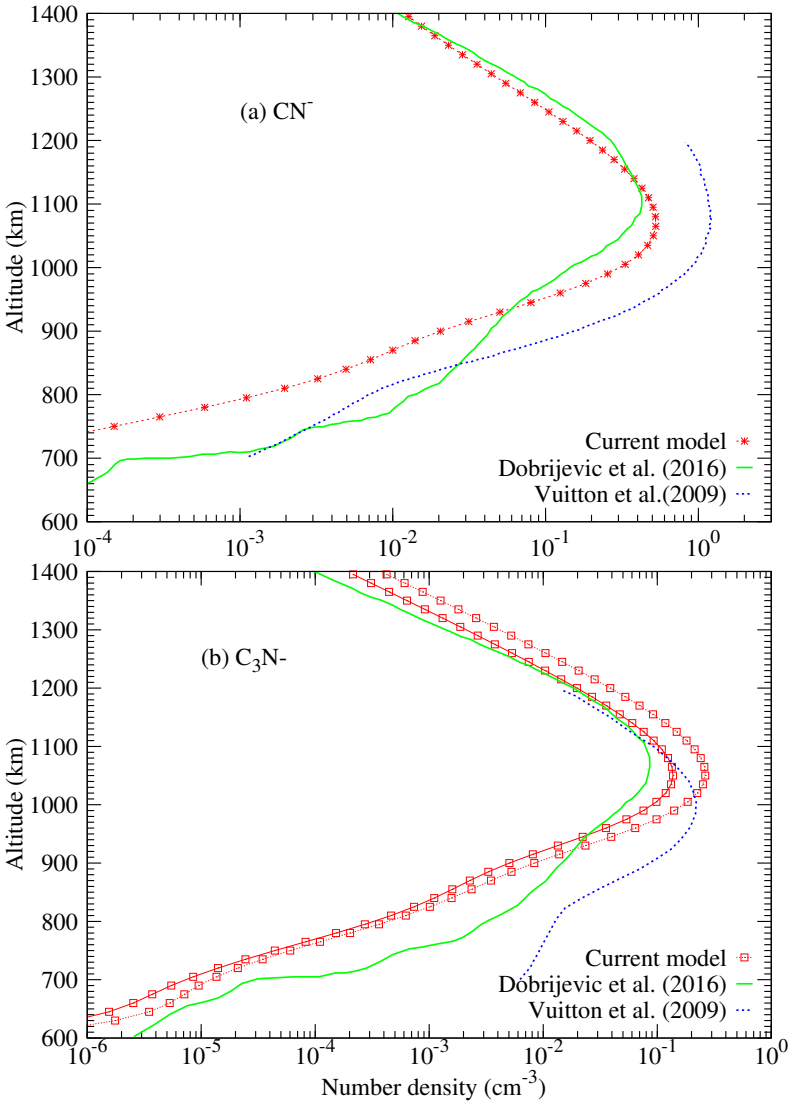

Figure 5.5: The density profiles of (a) CN^- and (b) C_3N^- calculated using the current model compared with the calculations of *Vuitton et al.* [2009] and *Dobrijevic et al.* [2016]. In the bottom panel, symbols connected by solid line shows the profile of C_3N^- obtained when electron density was reduced by half to nullify the effect of overestimation in the electron density. See the text for more details.

5.4.3 C_4H^- and C_5N^-

For the anion C_4H^- also, radiative electron attachment to C_4H radical is the major production process. As in the case of C_3N^- ion, reducing the modelled thermal electron density by a factor of 2 decreases the peak of C_4H^- density by ∼50%. The maximum density obtained for C_4H^- (0.01 cm^{-3}) is lesser than the peak density obtained by V09

by a factor of 5 and D16 by a factor of 4 (see Figure 5.6a). These could be due to the differences in the C_4H radical densities used in these studies. We have scaled the C_4H_2 profile of *Krasnopolsky* [2009] to make it consistent with the global average mixing ratio of C_4H_2 reported by *Magee et al.* [2009]. The C_4H radical is produced via the dissociation of C_4H_2. Hence, the C_4H profile also has been multiplied by the same scaling factor. D16 used the C_4H radical profile which they generated using their model. V09 tuned their C_4H_2 density, and hence the C_4H density, in such a way that they would be able to reproduce the density of the associated protonated species $C_4H_3^+$ observed during the T40 flyby. Our C_4H radical density is lower than those adopted by V09 and D16, thus reducing our C_4H^- peak density. In addition, the model of D16 is a coupled model in which the ions and neutrals are coupled. Their study has shown that the coupling has a significant impact on the calculated C_4H^- density. The density of C_4H^- obtained using coupled model was a factor of 4 more than that obtained using a decoupled model. Thus, when the C_4H^- profile of D16 is reduced by a factor of 4, the profile shows a good agreement with the one obtained using the current study.

The C_5N^- ion was not included in the model of D16, the reason being the very low abundance of the parent neutral HC_5N which is not yet detected in Titan's atmosphere. As many models strongly support the presence of HC_5N in Titan [*Couturier-Tamburelli et al.*, 2015; *Krasnopolsky*, 2009; *Coupeaud et al.*, 2005] we have included the C_5N^- ion in our calculations following the chemistry scheme of V09. Study of V09 showed that C_5N^- is the third most dominant anion and is formed mainly through the DEA of HC_5N. As the DEA cross sections of HC_5N was not available, they assumed the cross sections to be equal to that of the DEA cross sections of HC_3N to produce C_3N^-. Following this methodology, we calculated the production rate of C_5N^- through the DEA of HC_5N using the recent cross sections of *Gilmore and Field* [2015]. But in our model, the main production channel is the reaction of CN^- with HC_5N. This reaction has a rate coefficient of 5.4×10^{-9} cm^3 s^{-1} which is a theoretically calculated rate by V09. Reactions with the radicals H and CH_3 and the ion-ion recombination reactions are the only loss processes of C_5N^- among which the former dominates constituting ∼90% of the total loss rate at 1100 km. We used the reaction rate coefficient of 5.8×10^{-10} cm^3 s^{-1} measured by *Yang et al.* [2011], whereas V09 used a value of 1×10^{-7} cm^3 s^{-1}. With these modifications, the profile of C_5N^- that we obtained is approximately 80% lesser than that of V09 (see Figure 5.6b). However, both models agree that C_5N^- is the third most dominant anion at ∼1000 km.

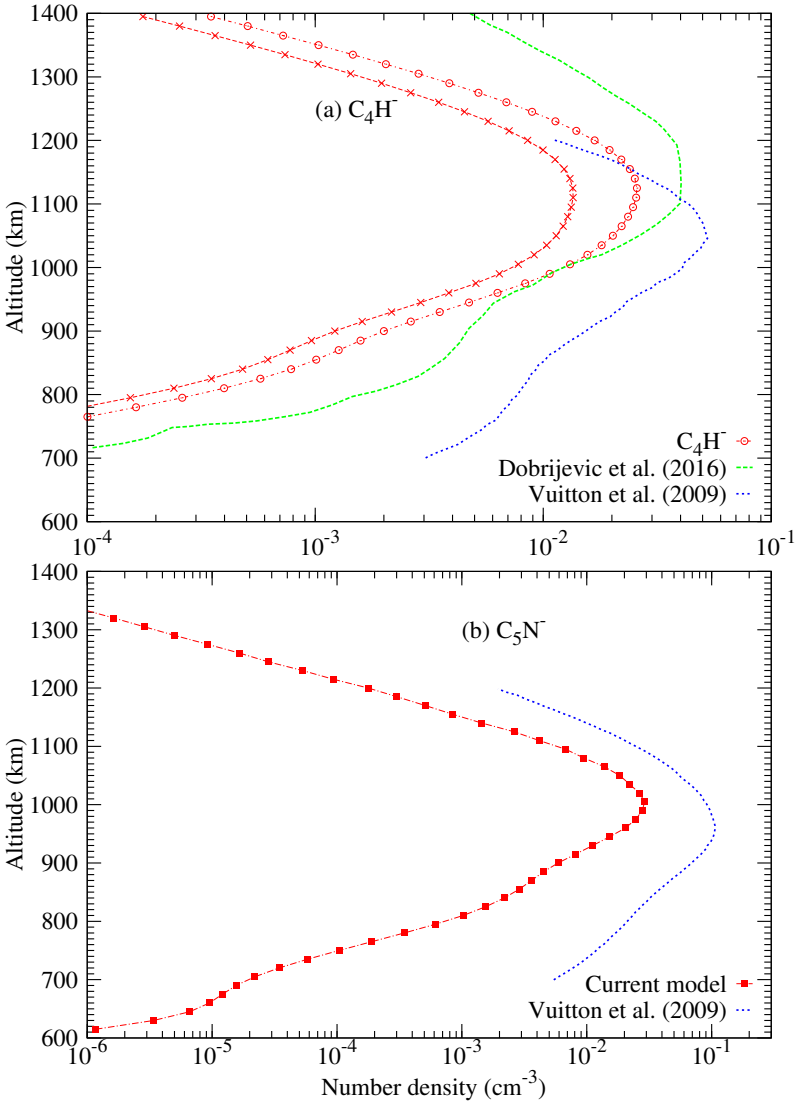

Figure 5.6: The density profiles of (a) C_4H^- and (b) C_5N^- calculated using the current model compared with the calculations of *Vuitton et al.* [2009] and *Dobrijevic et al.* [2016]. In the top panel, symbols connected by solid line shows the profile of C_3N^- obtained when electron density was reduced by half to nullify the effect of overestimation in the electron density. See the text for more details.

5.4.4 C_2H^- and C_6H^-

As per our model, the hydrocarbon anion C_2H^- has peak density that is comparable to C_5N^- even though C_5N^- peaks at still lower altitude (see Figure 5.3). D16 predicted a peak density of 0.02 cm^{-3} for C_2H^- which is in good agreement with our calculated peak of 0.03 cm^{-3} (see Figure 5.7a). But the peak value suggested by V09 is lesser by around one order of magnitude, a difference that is caused by the reaction pathways through which C_2H^- is formed in the two models. As per V09 the major production channel for the ion is the DEA of C_2H_2, whereas our calculations suggest the reaction between H^- and C_2H_2 as the main production channel. As our H^- densities are significantly higher

than those of V09 due to the usage of recent DEA cross sections of methane, C_2H^- density also increased accordingly.

For C_6H^-, our peak density is a factor of 5 less than that predicted by the model of V09. This could be due to the difference in C_6H_2 density and the DEA cross sections adopted in the two studies. As the DEA cross sections of C_6H_2 is not available, it is assumed to be equal to that of the structurally similar molecule C_2H_2. While V09 used the cross section measurements of *Rutkowsky et al.* [1980], we used the recent cross sections of *Song et al.* [2017].

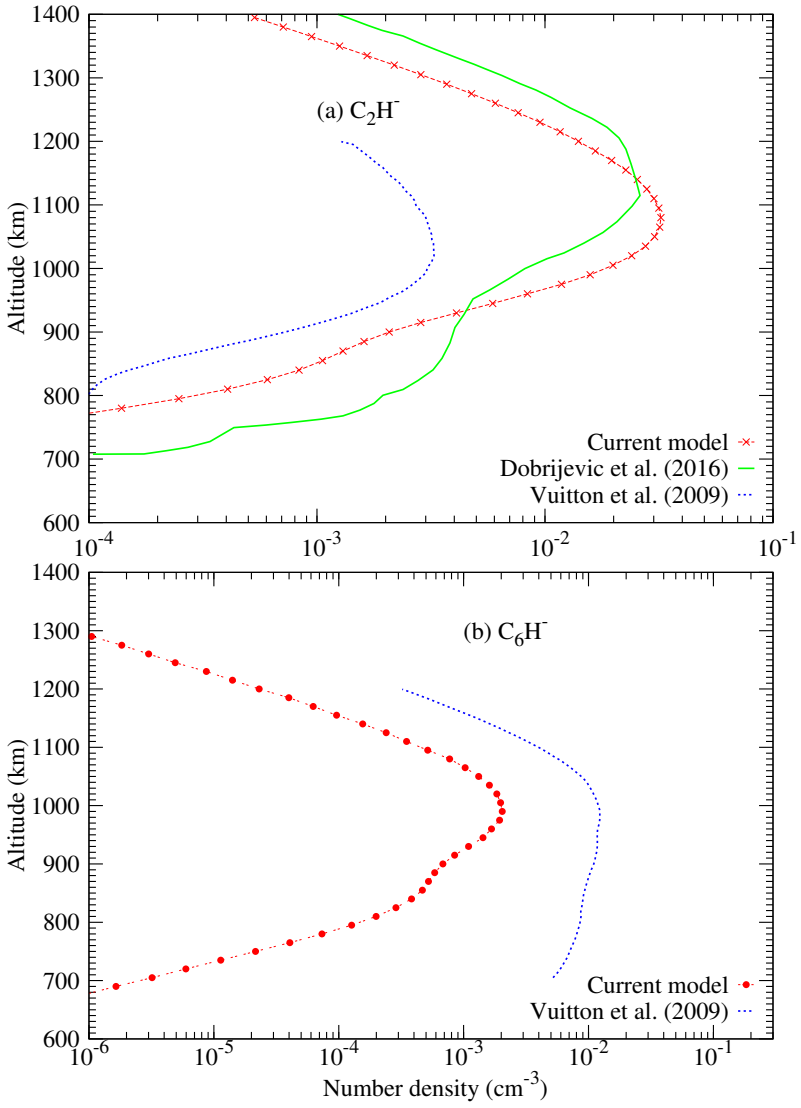

Figure 5.7: The density profiles of (a) C_2H^- and (b) C_6H^- calculated using the current model compared with the calculations of *Vuitton et al.* [2009] and *Dobrijevic et al.* [2016].

5.4.5 O^- and OH^-

The DEA of H_2O is the sole process through which O^- ion is formed in Titan's ionosphere. Once formed, O^- immediately reacts with CH_4 and HCN and get converted

to OH^- and CN^-, respectively. At altitudes greater than 1050 km it is mainly the photodetachment process that causes the depletion of O^- ion. The peak O^- density obtained by V09 is around 70% lower than our peak value (see Figure 5.8a). V09 have used the DEA cross sections of H_2O calculated by *Haxton et al.* [2007] for calculating the O^- density. These theoretical cross sections are found to be generally lower than the values available in literature. We used the DEA cross sections reported by *Rawat et al.* [2007]. Though *Rawat et al.* [2007] could not discriminate between OH^- and O^- due to the low mass resolution of their mass spectrometer, the relative yield of OH^- anion is very low as compared to the O^-. However, O^- seems to be a minor ion in the ionosphere of Titan (peak density $\sim 3 \times 10^{-6}$ cm^{-3}) as the dissociative electron attachment to H_2O favors the formation of H^- rather than O^- ion.

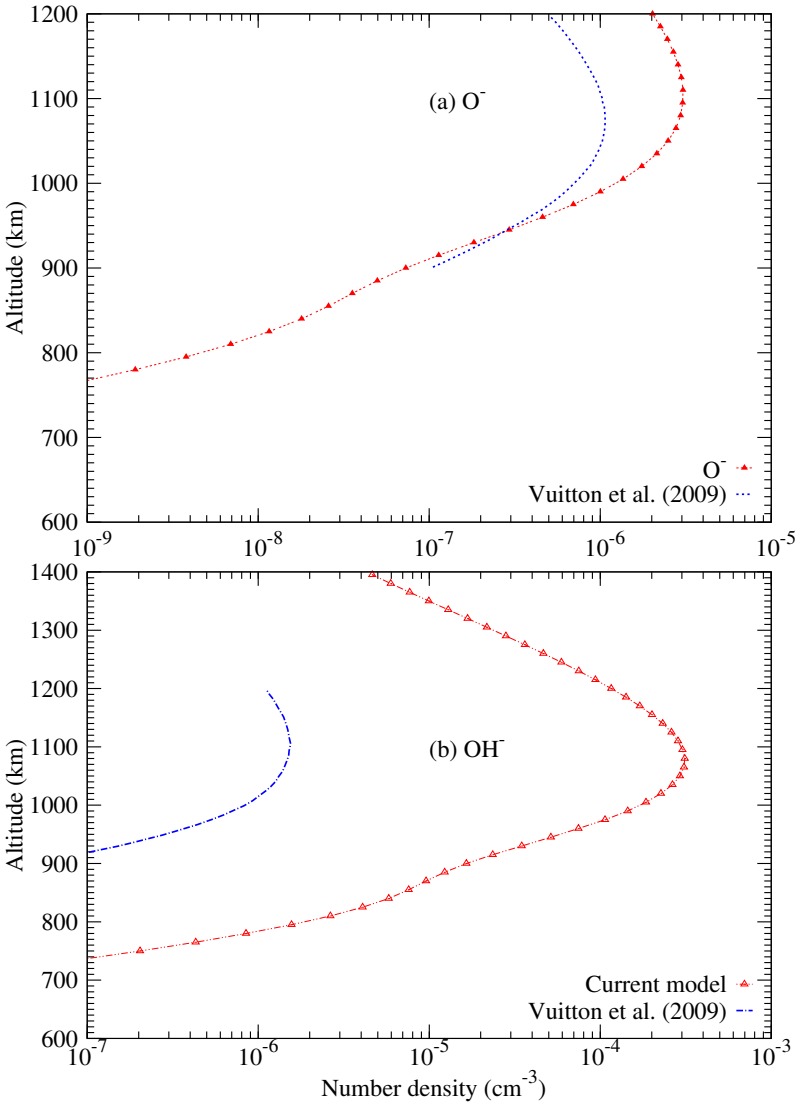

Figure 5.8: The density profiles of (a) O^- and (b) OH^- calculated using the current model compared with the calculations of *Vuitton et al.* [2009].

For OH^-, the peak density that we could get is two orders of magnitude higher than

that of V09 (see Figure 5.8b). The main production process of OH^- in our model is the reaction between H^- and H_2O for which we used a rate coefficient of 4.8×10^{-9} cm^3 s^{-1} measured by *Martinez et al.* [2010]. This particular reaction was not considered in the model of V09. As per their calculation, the main production process of OH^- was DEA of H_2O. However, the inclusion of this reaction would not have caused a noticeable difference in their OH^- density as their peak H^- density is of the order of 10^{-4} cm^{-3}.

5.5 Comparison of model results with the recent observations

Wellbrock et al. [2013], using the data from 34 Titan flybys of the Cassini orbiter, suggested seven different mass groups of negative ions that are present in Titan's ionosphere. The suggested mass ranges were 12-30, 30-55, 55-95, 95-130, 130-190, 190-652, and 625+ m/q. The ions that we considered in our study constitutes the first three mass ranges (12-30: CN^-, C_2H^-, O^-, OH^-, CH_2^-; 30-55: C_3N^- and C_4H^-; and 55-95: C_5N^- and C_6H^-). The maximum density of negative ions that we obtained is close to 1 cm^{-3}.

Recently, *Desai et al.* [2017] reported an updated analysis of the negatively charged ions measured by the Cassini CAPS-ELS instrument. They used a fitting procedure to show how the ELS mass spectrum, which was previously classified into five broad mass groups by *Wellbrock et al.* [2013], can be resolved in to specific peaks for anion species up to over 100 m/q. They reported the consistent detection of mass peaks centered between 25.8-26.0 m/q and between 49-50.1 m/q (hereafter referred to as peak 1 and peak 2, respectively) during the flybys T40, T16, T18, T32, and T48. These peaks were attributed to the carbon chain anions CN^-/C_2H^- and C_3N^-/C_4H^-, respectively, even though they were not able to differentiate between these nitrile and hydrocarbon compounds. At lower altitudes, the detection of three more broad mass groups were reported with masses in the range 71-94, 117-124 and 146-166 m/q during the T40 flyby.

Desai et al. [2017] presented the relative density profiles for the different mass peaks mentioned above, observed during T40 flyby. Relative density of an ion at an altitude is the ratio between the local abundance of the ion at that altitude and the maximum observed abundance of the ion. Using the number densities obtained as the model results, we also calculated the relative densities of the anions CN^-, C_2H^-, C_3N^- and C_4H^- and compared them with the profiles given by *Desai et al.* [2017]. Figure 5.9a shows the profile for peak 1 anions. *Desai et al.* [2017] proposed that this peak could be caused either by CN^- or by C_2H^-. A good agreement is seen when the model calculated relative density profiles of these two anions were compared with the peak 1 profile. Except at the altitude of 1250 km, our model values are in agreement with the value reported by *Desai et al.* [2017]. Our model shows that the altitude of peak production for CN^- and C_2H^-

occurs close to 1075 km. The maximum of peak 1 profile occurs near the same altitude. As per our model, the main production channels of CN^- and C_2H^- are the reactions of the hydride anion with HCN and C_2H_2, respectively. In the altitude range 1000-1300 km, HCN and C_2H_2 have comparable abundance. But the rate coefficient of the reaction between H^- with HCN is an order of magnitude higher than that between H^- and C_2H_2, which makes CN^- number density around two orders of magnitude higher than C_2H^-. Hence, we suggest that it should be CN^-, rather than C_2H^-, that is constituting the peak at 25.8-26.0 m/q.

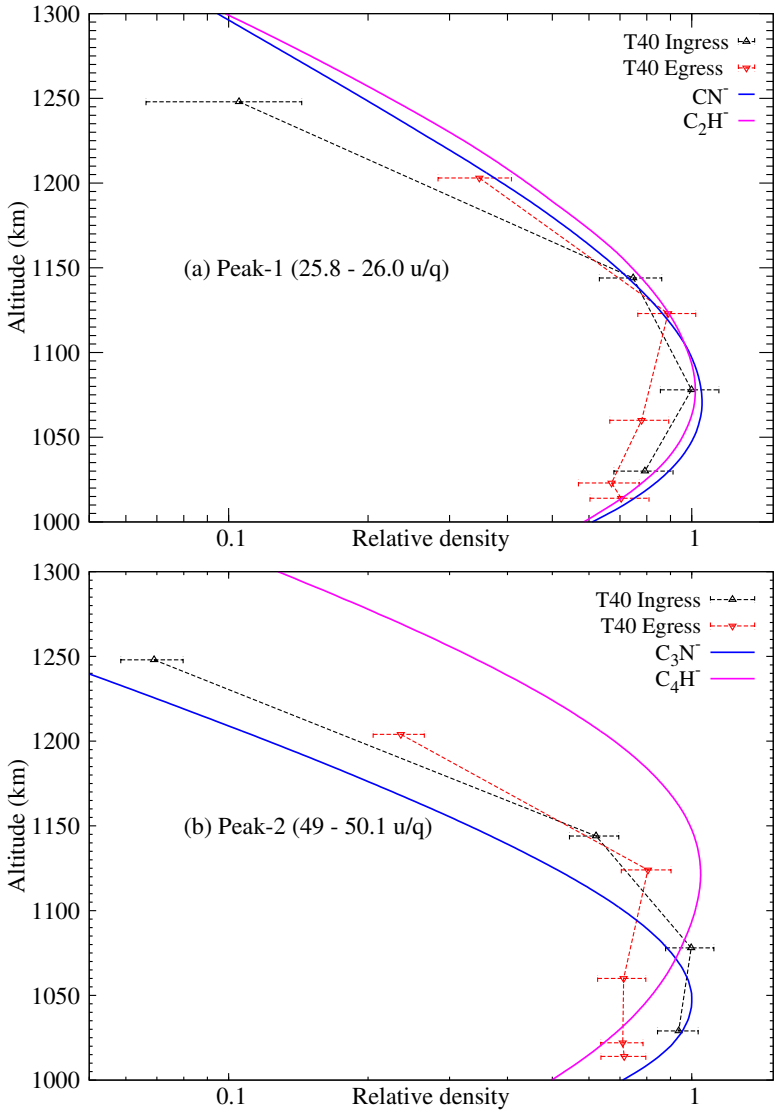

Figure 5.9: The relative model density profiles of the anions CN^-, C_2H^- (top panel), and C_3N^- and C_4H^- (bottom panel) compared with the profiles obtained by *Desai et al.* [2017] at the mass peaks 25.8-26.0 u/q and 49-50.1 m/q during the ingress and egress of the T40 flyby

The relative density of Peak 2 (49-50.1 m/q) profile as given by *Desai et al.* [2017] peaks at an altitude between 1000-1100 km (Figure 5.9). They suggested C_3N^- and/or

C_4H^- as the plausible species producing peak 2. We compared our calculated relative density profiles of C_3N^- and C_4H^- with the peak 2 profile of *Desai et al.* [2017]. The C_3N^- profile shows a better agreement with the peak 2 profile rather than C_4H^-. The profile for C_4H^- peaks at altitude >1100 km whereas the maximum of peak 2 profile occurs at altitudes below 1100 km. Even though our calculated relative density of C_3N^- is outside the error bars of the peaks 2 profile at most of the altitudes, the altitude of peak production and the shape of the profile is consistent with each other. In addition, our calculated peak density of C_3N^- is around an order of magnitude higher than that of C_4H^- ion (c.f. Figure 5.3). Hence, we suggest C_3N^- as the potential anion that causes the peak at 49-50.1 m/q.

Desai et al. [2017] depicted the relative density profiles of two more mass groups 71-94 and 117-124 m/q (hereafter referred to as group 3 and group 4, respectively) which are quite broad as compared to the mass bins 25.8-26 m/q and 49.0-50.1 m/q. They suggested that there are several possible heavy carbon chain anions that might be contributing towards group 3, like C_5N^-, C_6H^-, $C_6H_7^-$, $C_6H_5^-$ etc. The C_5N^- and C_6H^- are the only two anions considered in our model that could belong to group 3. A reliable comparison with the relative density profile of group 3 is possible only if the model includes more anions having mass in the group 3 bin. But the unavailability of the chemical reaction pathways and the reaction rates of these heavy anions hinders the inclusion of these heavy ions in to the chemical models.

5.6 Conclusion

We extended the one dimensional photochemical model by adding the reactions involving anions for calculating the density profiles of negative ions in the dayside ionosphere of Titan. The chemistry scheme of anions proposed by *Vuitton et al.* [2009] has been used with the most recent cross sections and reaction rate coefficients. Our study shows CN^- to be the dominant negative ion in Titan's ionosphere, in agreement with the calculations of *Vuitton et al.* [2009] and *Dobrijevic et al.* [2016]. The second most dominant ion is found to vary with altitude. In the region 900-1100 km, C_3N^- is the second most abundant ion and above this altitude region, the H^- takes over. The C_5N^- and C_2H^- show the same peak density (0.03 cm^{-3}) even though they peak at two different altitudes, 1000 and 1070 km, respectively. Similarly, CH_2^- and C_4H^- ions have peak magnitude of 0.01 cm^{-3}, but they peaks at 1050 and 1120 km, respectively. Even though the electron affinity of H^- and CH_2^- are low, our model shows that these anions can have considerable densities because of the abundance of the parent neutral CH_4. The density of C_6H^- is one order of magnitude low as compared to other hydrocarbon anions. Our model predicted OH^- density is two orders of magnitude higher than that of *Vuitton et al.* [2009]. The O^- seems to be a very minor ion in the upper atmosphere of Titan.

The main difference between our model results and the calculations of *Vuitton et al.* [2009] is the abundance of hydride anion. The H^- is widely known to be an important negative ion in astrophysical environments [*Millar et al.*, 2017; *Ross et al.*, 2008]. Our model suggests that it could be an important ion in Titan's ionosphere also, due to the abundance of the parent neutral molecule CH_4 and its relatively high dissociative electron attachment cross section. The hydride anion also plays a major role in the negative ion chemistry. Our model shows that at the ionospheric peak, it should be the reactions of H^- with the respective neutrals that contributes significantly to the production of anions CN^-, C_2H^-, and C_6H^- and not the dissociative electron attachment process as suggested by *Vuitton et al.* [2009]. Although the CAPS/ELS instrument has not reported the detection of anions whose mass agree with H^-, *Desai et al.* [2017] has pointed out that H^- cannot be measured by the instrument because of the limitation caused by the spacecraft velocity.

We identified the dominant production and loss reactions of each anion included in our study at the ionospheric peak (∼1100 km) along with the most recent cross sections/rate coefficients wherever available (Tables 5.2). The rate coefficients available for some of these reactions are more than 40 years old, e.g. *Mackay et al.* [1976]. Most of the reaction rate coefficients for the ion-neutral reactions involving the HC_5N are theoretically calculated by *Vuitton et al.* [2009] using Langevin theory. Similarly, the dissociative electron attachment cross sections are not available for the neutrals HC_5N and C_6H_2, which are required to calculate the production rates of the anions C_5N^- and C_6H^-. Thus, there is a requirement to measure the reaction rate coefficients and dissociative electron attachment cross sections of hydrocarbon molecules for improved modelling of the anion chemistry in Titan's atmosphere.

We present a comparison between the modelled anion abundance with the CAPS/ELS observations, recently reported by *Desai et al.* [2017]. Our calculated relative density profiles of CN^- and C_2H^- shows a good agreement with the profile for 25.8-26.0 m/q reported by *Desai et al.* [2017]. We suggest CN^- to be the anion which causes the peak at 26 amu. For the profile in the mass bin 49-50.1 m/q, the modelled profile of C_3N^- is more consistent rather than of C_4H^-. The observations clearly indicates the presence of negative anions with masses >200 m/q in the lower altitudes. The highest mass that has been considered in the models so far is only ∼75 amu. Experimental studies for determining the possible reaction pathways and the reaction rate coefficient of heavy negative ions, like $C_6H_5CH_2^-$, $C_6H_5NH_2^-$, $C_6H_5O^-$, which could be present in Titan's atmosphere [*Wang and Bierbaum*, 2016] is highly appreciable.

Chapter 6

Summary and future scope

The Cassini-Huygens mission thoroughly measured the ionosphere of the Saturnian moon Titan and revealed the complexity of the ionospheric chemistry which results in the formation of positive ions, negative ions, and free electrons. Even though many models have been developed to calculate the plasma density which is formed as a byproduct of the chemistry, none of them were able to reproduce the Cassini measured electron density. The models overestimated the electron density by a factor of 2 to 3 near the ionospheric peak which has prompted to explore the possible reasons for this disagreement. Also, there exist only limited discussions on modelling the chemistry of negative ions which are recently discovered by the Cassini mission. In this thesis, a one dimensional photochemical model for the dayside ionosphere of Titan is developed for calculating the density profiles of cations, anions, and free electrons under steady-state photochemical equilibrium condition.

The photoelectrons generated in the atmosphere is an important source of ionization on the dayside ionosphere of Titan. Once generated, they degrade their energy by colliding with the atmospheric neutrals. To understand the electron interaction with the neutrals in Titan's atmosphere we developed an energy deposition model based on Monte Carlo technique which describes the degradation of electron with energy in the range 1 eV–10 keV. We began by developing an energy degradation model for an atomic gas xenon since electron-atom interactions are easier to deal with as compared to electron-molecule interactions as atomic targets offer only two possible energy loss channels, viz. ionization and excitation, for the electron to degrade its energy. Out of the several available techniques for studying electron degradation we used Monte Carlo method as it is the most realistic simulation possible for studying electron energy deposition. This model was then extended further to study the electron interaction with the molecular gas methane, the gas which plays a significant role in Titan's ionospheric chemistry. Molecular targets add more intricacies to electron degradation process due to the presence of additional loss channels, such as electron attachment, rotational and vibrational exciations, neutral dissociation, dissociative ionization, dissociative excitation, etc.

The output of the Monte Carlo simulation is the numerical yield spectrum which is a basic distribution function that contain information regarding the degradation process and can be used to calculate the yield of any excited or ionized states. The numerical yield spectra are then fitted analytically, thus generating analytical yield spectra (AYS). Mean energy per ion pair and efficiencies of various inelastic processes are calculated, using numerical yield as well as analytical yield and are found to be in good agreement. The mean energy per ion pair for neutral CH_4 is found to have a value 26 (27.8) eV at 10 keV (100 eV). Efficiency calculations showed that at energies <10 eV, vibration is the dominant loss process with an efficiency of 80% at 8 eV, whereas at energies greater than 100 eV ionization dominates consuming more than 50% of the incident electron energy. The electron attachment process has an efficiency of 0.14%, which falls down to a very small value for energies >20 eV. From 25 eV onwards, dissociation process has an efficiency of 27%. The AYS generated is used for calculating steady-state photoelectron flux in Titan's atmosphere.

By considering solar photons and photoelectrons as the major source of ionization, a photochemical model was developed. Initially, the study concentrated on the T40 flyby of Cassini orbiter which was a complete dayside flyby and used the in-situ measurements from instruments onboard Cassini as input to the model. The density profiles of 23 positive ions and free electrons are calculated. The modelled profiles are compared with the Cassini INMS and RPWS/LP observations and also with the calculations of other models. At the ionospheric peak, the calculated electron density is higher by a factor of 2 to 3 as compared to the observations. We also made calculations for four additional dayside Titan flyby conditions and compared with the observations. In all cases, disagreement between the modelled and observed profiles were evident. The present thesis investigated the impact of different model parameters, viz. photoelectron flux, ion production rates, electron temperature, dissociative recombination rate coefficients, neutral densities of minor species, and solar flux on the calculated electron density to understand the possible reasons for this discrepancy. Recent studies have shown that there is an overestimation in the modelled photoelectron flux and N_2^+ ion production rates which may contribute towards this disagreement. The present study has found that accounting for the over estimation in these parameters will not improve the electron density by more than 20%. The modelled plasma densities are found to be very sensitive to electron temperature and dissociative recombination rate coefficients and improvements in these parameters can help in reducing the differences between observed and calculated electron densities. Reduction in the measured electron temperature by a factor of 5 provides a good agreement between the modelled and observed electron density. The change in HCN and NH_3 densities affects the calculated densities of the major ions ($HCNH^+$, $C_2H_5^+$, and CH_5^+); however the overall impact on electron density is not appreciable (<20 %). Though increasing the dissociative recombination rate

coefficients of the ions $C_2H_5^+$ and CH_5^+ by a factor of 10 reduces the difference between modelled and observed densities of the major ions, the modelled electron density is still higher than the observation by ∼60% at the peak. The present study suggests that even though the overestimation in the production parameters may contribute towards the disagreement between the modelled and observed plasma density profiles to some extent, a more significant role is played by the loss processes. It is possible that there might be some unidentified chemical reactions that may account for the additional loss of plasma in Titan's ionosphere.

To address the negative ions in Titan's ionosphere, the photochemical model is extended further to include anion chemistry. Using the state-of-the-art cross sections and rate coefficients, the density profiles of anions are computed and compared with previous model results. Significant differences in the profiles were seen which show the importance of having updated parameters for modelling anion density profiles. The use of updated cross sections increased the maximum density of the anions H^-, OH^-, and CH_2^- by two orders of magnitude than what was previously suggested. The study shows that H^- could be important anion in Titan's ionosphere due to the abundance of parent neutral molecule methane and its relatively large dissociative electron attachment cross section. We identified the dominant production and loss reactions of each anion considered in the model at the ionospheric peak and suggested that it should be the reactions of H^- with the neutrals HCN, C_2H_2, and C_6H_2 that contribute significantly to the production of anions CN^-, C_2H^-, and C_6H^- and not the dissociative electron attachment process as suggested by the previous models. We also presented a comparison between the modelled anion abundance with the relative density profiles of anions recently derived using the Cassini observations. Our calculated relative density profiles of CN^- and C_2H^- show a good agreement with the profile for 25.8-26.0 m/q reported from the Cassini observations. The present study has suggested CN^- to be the anion which causes the peak at 26 amu. For the mass bin 49-50.1 m/q profile, the modelled profile of C_3N^- is more consistent rather than that of C_4H^-.

The model developed in the thesis is useful to understand the photochemistry in the ionospheric region of Titan and can provide a quantitative information on the controlling parameters of plasma density in the ionosphere. The study also highlights the requirement of having updated cross sections and rate coefficients for modelling the chemistry of negative ions in the upper atmosphere. The results of the study are useful for resolving the inconsistency between the modelled and observed plasma density on Titan's dayside ionosphere.

6.1 Future Scope

The work presented in this thesis demonstrates the impact various crucial input parameters have on modelling the ionospheric chemistry of Titan. The results brought

out from this work point to the necessity of further modelling studies which would be carried out in near future.

The Monte Carlo model for electron degradation presented in this thesis is a local degradation model where the electron loses its energy locally and does not include the electron transport effects. So the results are applicable to those region of the atmosphere where the neutral densities are high enough so that there occurs rapid collisions between energetic electrons and neutrals, thus spatially constraining the energy degradation. However, at much higher altitudes the collision frequency decreases due to the decrease in the atmospheric density and hence the energetic electrons can diffuse to higher altitudes. Thus, the energy deposition model has to be improved for accounting the spatial degradation of electrons so that it can be applied to the high altitude regime where electron transport effect becomes prominent.

The electron temperature (T_e) is a vital parameter for modelling the plasma densities. The present study showed that using modelled T_e profiles helps to generate electron density profiles which shows a better agreement with the observations as compared to the one obtained using RPWS/LP measured T_e profiles. Near the ionospheric peak, models suggest a lower T_e which is close to the neutral temperature whereas measurements showed that T_e is much higher than the neutral temperature in this region. Electron temperature modelling has to be done to explain this difference.

The photochemical model presented in this thesis is a decoupled model where we used a fixed background neutral atmosphere as input to the model to generate the plasma densities. To make the model fully self consistent, the neutral densities should also be computed by including the neutral-neutral chemistry. The present study showed that there are differences between various reported profiles of minor neutrals, such as HCN and NH_3, which are of extreme relevance in the ionospheric chemistry of Titan. Modelling the plasma chemistry using self-consistently generated neutral densities could improve the difference between model and observations and need to be explored. This would also help in a better understanding of the coupling between neutrals and ions.

The basic models for electron degradation and ionospheric chemistry developed in this thesis can be applied to other planetary bodies having an atmosphere by changing input model parameters and related chemical reactions.

Appendix A

Reactions and Rate Coefficients

Table A.1: List of ion-neutral reactions considered in the model

Reaction	**Rate Coefficient** ($cm^3\ s^{-1}$)	**Reference**
$N_2^+ + CH_4 \rightarrow CH_3^+ + N_2 + H$	1.04×10^{-09}	*Anicich et al.* [2006]
$N_2^+ + CH_4 \rightarrow CH_2^+ + N_2 + H_2$	1.03×10^{-10}	*Anicich et al.* [2006]
$N_2^+ + H_2 \rightarrow HN_2^+ + H$	2.00×10^{-09}	*Anicich* [1993]
$N_2^+ + C_2H_2 \rightarrow N_2H^+ + C_2H$	2.4×10^{-10}	*McEwan and Anicich* [2007]
$N_2^+ + C_2H_2 \rightarrow HCN^+ + HCN$	1.2×10^{-11}	*McEwan and Anicich* [2007]
$N_2^+ + C_2H_6 \rightarrow C_2H_5^+ + N_2 + H$	2.16×10^{-10}	*Vuitton et al.* [2007]
$N_2^+ + C_2H_4 \rightarrow HCNH^+ + HCN + H$	1.3×10^{-10}	*Richard* [2013]
$N_2^+ + C_2H_4 \rightarrow N_2H^+ + C_2H_3$	1.3×10^{-10}	*Richard* [2013]
$N_2^+ + N \rightarrow N^+ + N_2$	1.00×10^{-11}	*Vuitton et al.* [2007]
$N_2^+ + HCN \rightarrow HCN^+ + N_2$	3.9×10^{-10}	*Richard* [2013]
$N_2^+ + H \rightarrow H^+ + N_2$	1.00×10^{-11}	*Vuitton et al.* [2007]
$N_2^+ + C_6H_6 \rightarrow C_6H_5^+ + N_2 + H$	3.84×10^{-10}	*Vuitton et al.* [2007]
$N_2^+ + CH_3NH_2 \rightarrow CH_2NH_2^+ + N_2 + H$	8.17×10^{-10}	*Vuitton et al.* [2007]
$N^+ + CH_4 \rightarrow CH_3^+ + NH$	5.75×10^{-10}	*Anicich* [1993]
$N^+ + CH_4 \rightarrow CH_4^+ + N$	5.75×10^{-11}	*Anicich* [1993]
$N^+ + CH_4 \rightarrow HCNH^+ + H_2$	4.14×10^{-10}	*Anicich* [1993]
$N^+ + CH_4 \rightarrow HCN^+ + H_2 + H$	1.15×10^{-10}	*Anicich* [1993]
$N^+ + C_2H_4 \rightarrow HCN^+ + CH_3$	1.30×10^{-10}	*Anicich and McEwan* [1997]
$N^+ + C_2H_4 \rightarrow HCNH^+ + CH_2$	1.95×10^{-10}	*Anicich and McEwan* [1997]
$N^+ + C_2H_6 \rightarrow HCNH^+ + CH_4$	1.00×10^{-10}	*Anicich and McEwan* [1997]
$N^+ + HCN \rightarrow HCN^+ + N$	2.41×10^{-09}	*Anicich and McEwan* [1997]
$N^+ + C_2H_6 \rightarrow C_2H_5^+ + NH$	1.00×10^{-10}	*Anicich and McEwan* [1997]
$N^+ + C_2H_3CN \rightarrow c\text{-}C_3H_3^+ + N_2$	1.20×10^{-10}	*Anicich and McEwan* [1997]
$N^+ + C_6H_6 \rightarrow C_6H_5^+ + NH$	1.40×10^{-10}	*Anicich and McEwan* [1997]

Table A.1 – *Continued from previous page*

Reaction	**Rate coefficient** ($cm^3\ s^{-1}$ **or** s^{-1})	**Reference**
$N^+ + CH_3NH_2 \rightarrow CH_2NH_2^+ + N + H$	1.59×10^{-09}	*Vuitton et al.* [2007]
$CH_4^+ + H_2 \rightarrow CH_5^+ + H$	3.50×10^{-11}	*McEwan and Anicich* [2007]
$CH_4^+ + CH_4 \rightarrow CH_5^+ + CH_3$	1.14×10^{-09}	*McEwan and Anicich* [2007]
$CH_4^+ + C_2H_4 \rightarrow C_2H_5^+ + CH_3$	2.60×10^{-10}	*McEwan and Anicich* [2007]
$CH_4^+ + HCN \rightarrow HCNH^+ + CH_3$	3.23×10^{-09}	*McEwan and Anicich* [2007]
$CH_4^+ + HC_3N \rightarrow CHCCNH^+ + CH_3$	2.50×10^{-09}	*McEwan and Anicich* [2007]
$CH_4^+ + HCN \rightarrow CH_3CNH^+ + H$	6.60×10^{-11}	*McEwan and Anicich* [2007]
$CH_4^+ + C_2H_4 \rightarrow C_3H_5^+ + H_2 + H$	6.00×10^{-11}	*McEwan and Anicich* [2007]
$CH_4^+ + C_2H_2 \rightarrow$ c-$C_3H_3^+$ $H_2 + H$	1.63×10^{-09}	*Anicich and McEwan* [1997]
$CH_4^+ + NH_3 \rightarrow NH_4^+ + CH_3$	1.35×10^{-09}	*Anicich and McEwan* [1997]
$CH_3^+ + H_2 \rightarrow CH_5^+ + h\nu$	5.00×10^{-13}	*McEwan and Anicich* [2007]
$CH_3^+ + CH_4 \rightarrow C_2H_5^+ + H_2$	1.10×10^{-09}	*McEwan and Anicich* [2007]
$CH_3^+ + C_2H_6 \rightarrow C_2H_5^+ + CH_4$	1.48×10^{-09}	*McEwan and Anicich* [2007]
$CH_3^+ + C_2H_6 \rightarrow C_3H_5^+ + 2H_2$	1.57×10^{-10}	*McEwan and Anicich* [2007]
$CH_3^+ + N \rightarrow HCN^+ + H_2$	3.35×10^{-11}	*McEwan and Anicich* [2007]
$CH_3^+ + N \rightarrow HCNH^+ + H$	3.35×10^{-11}	*McEwan and Anicich* [2007]
$CH_3^+ + HCN \rightarrow CH_3CNH^+ + h\nu$	2.00×10^{-10}	*McEwan and Anicich* [2007]
$CH_3^+ + CH_3CN \rightarrow C_2H_5^+ + HCN$	6.66×10^{-10}	*McEwan and Anicich* [2007]
$CH_3^+ + CH_3CN \rightarrow HCNH^+ + C_2H_4$	1.04×10^{-09}	*McEwan and Anicich* [2007]
$CH_3^+ + C_2H_4 \rightarrow C_3H_5^+ + H_2$	5.41×10^{-10}	*McEwan and Anicich* [2007]
$CH_3^+ + C_2H_2 \rightarrow$ c-$C_3H_3^+ + H_2$	1.15×10^{-09}	*McEwan and Anicich* [2007]
$CH_3^+ + C_2H_4 \rightarrow$ c-$C_3H_3^+ + 2H_2$	4.24×10^{-11}	*Anicich and McEwan* [1997]
$CH_3^+ + C_4H_2 \rightarrow$ c-$C_3H_3^+ + C_2H_2$	1.17×10^{-09}	*Vuitton et al.* [2007]
$CH_3^+ + HC_3N \rightarrow$ c-$C_3H_3^+ + HCN$	2.10×10^{-09}	*Vuitton et al.* [2007]
$CH_3^+ + NH_3 \rightarrow NH_4^+ + CH_2$	2.63×10^{-10}	*Anicich and McEwan* [1997]
$CH_3^+ + CH_3NH_2 \rightarrow CH_2NH_2^+$	1.44×10^{-09}	*Anicich and McEwan* [1997]
$CH_3^+ + NH_3 \rightarrow CH_2NH_2^+ + H_2$	1.49×10^{-09}	*Anicich and McEwan* [1997]
$CH_2^+ + H_2 \rightarrow CH_3^+ + H$	1.16×10^{-09}	*McEwan and Anicich* [2007]
$CH_2^+ + CH_4 \rightarrow C_2H_5^+ + H$	3.90×10^{-10}	*McEwan and Anicich* [2007]
$CH_2^+ + N \rightarrow HCN^+ + H$	1.10×10^{-10}	*McEwan and Anicich* [2007]
$CH_2^+ + HC_3N \rightarrow CHCCNH^+ + CH$	4.10×10^{-09}	*McEwan and Anicich* [2007]
$CH_2^+ + C_2H_2 \rightarrow$ c-$C_3H_3^+ + H$	2.50×10^{-09}	*McEwan and Anicich* [2007]
$CH_2^+ + NH_3 \rightarrow NH_4^+ + CH$	8.78×10^{-10}	*Anicich and McEwan* [1997]
$CH_2^+ + CH_3NH_2 \rightarrow CH_3NH_3^+ + CH$	2.10×10^{-10}	*Vuitton et al.* [2007]
$CH_2^+ + NH_3 \rightarrow CH_2NH_2^+ + H$	1.78×10^{-09}	*Anicich and McEwan* [1997]

Table A.1 – *Continued from previous page*

Reaction	**Rate coefficient (cm^3 s^{-1} or s^{-1})**	**Reference**
$CH_2^+ + CH_3NH_2 \rightarrow CH_2NH_2^+ + CH_3$	1.15×10^{-09}	*Vuitton et al.* [2007]
$H^+ + CH_4 \rightarrow CH_4^+ + H$	7.47×10^{-10}	*McEwan and Anicich* [2007]
$H^+ + CH_4 \rightarrow CH_3^+ + H_2$	3.40×10^{-09}	*McEwan and Anicich* [2007]
$H^+ + C_2H_6 \rightarrow CH_3^+ + CH_4$	2.35×10^{-10}	*McEwan and Anicich* [2007]
$H^+ + C_2H_6 \rightarrow C_2H_5^+ + H$	2.35×10^{-10}	*McEwan and Anicich* [2007]
$H^+ + HCN \rightarrow HCN^+ + H$	1.10×10^{-08}	*McEwan and Anicich* [2007]
$H_2^+ + CH_4 \rightarrow CH_3^+ + H_2 + H$	2.28×10^{-09}	*McEwan and Anicich* [2007]
$H_2^+ + H \rightarrow H^+ + H_2$	6.40×10^{-10}	*McEwan and Anicich* [2007]
$H_2^+ + CH_4 \rightarrow CH_5^+ + H$	1.14×10^{-10}	*McEwan and Anicich* [2007]
$H_2^+ + CH_4 \rightarrow CH_4^+ + H_2$	1.41×10^{-09}	*McEwan and Anicich* [2007]
$H_2^+ + C_2H_6 \rightarrow C_2H_5^+ + H_2 + H$	1.37×10^{-09}	*McEwan and Anicich* [2007]
$H_2^+ + N_2 \rightarrow N_2H^+ + H$	2.00×10^{-09}	*McEwan and Anicich* [2007]
$HN_2^+ + CH_4 \rightarrow CH_5^+ + N_2$	8.90×10^{-10}	*McEwan and Anicich* [2007]
$HN_2^+ + C_2H_4 \rightarrow C_2H_5^+ + N_2$	1.00×10^{-09}	*McEwan and Anicich* [2007]
$HN_2^+ + C_2H_6 \rightarrow C_2H_5^+ + N_2 + H_2$	1.13×10^{-09}	*McEwan and Anicich* [2007]
$HN_2^+ + HCN \rightarrow HCNH^+ + N_2$	3.20×10^{-09}	*McEwan and Anicich* [2007]
$HN_2^+ + HC_3N \rightarrow CHCCNH^+ + N_2$	4.20×10^{-09}	*McEwan and Anicich* [2007]
$HN_2^+ + CH_3CN \rightarrow CH_3CNH^+ + N_2$	4.10×10^{-09}	*McEwan and Anicich* [2007]
$HN_2^+ + C_4H_2 \rightarrow C_4H_3^+ + N_2$	1.10×10^{-09}	*Vuitton et al.* [2007]
$HN_2^+ + C_6H_6 \rightarrow C_6H_7^+ + N_2$	1.50×10^{-09}	*Vuitton et al.* [2007]
$CH_5^+ + H \rightarrow CH_4^+ + H_2$	1.50×10^{-10}	*McEwan and Anicich* [2007]
$CH_5^+ + C_2H_4 \rightarrow C_2H_5^+ + CH_4$	1.50×10^{-09}	*McEwan and Anicich* [2007]
$CH_5^+ + C_2H_6 \rightarrow C_2H_5^+ + CH_4 + H_2$	2.03×10^{-10}	*McEwan and Anicich* [2007]
$CH_5^+ + HC_3N \rightarrow CHCCNH^+ + CH_4$	4.50×10^{-09}	*McEwan and Anicich* [2007]
$CH_5^+ + HCN \rightarrow HCNH^+ + CH_4$	3.00×10^{-09}	*Vuitton et al.* [2007]
$CH_5^+ + CH_3CN \rightarrow CH_3CNH^+ + CH_4$	4.90×10^{-09}	*Vuitton et al.* [2007]
$CH_5^+ + NH_3 \rightarrow NH_4^+ + CH_4$	2.30×10^{-09}	*Vuitton et al.* [2007]
$CH_5^+ + CH_3NH_2 \rightarrow CH_3NH_2^+ + CH_4$	2.25×10^{-09}	*Vuitton et al.* [2007]
$CH_5^+ + C_4H_2 \rightarrow C_4H_3^+ + CH_4$	3.00×10^{-09}	*Vuitton et al.* [2007]
$CH_5^+ + C_6H_6 \rightarrow C_6H_7^+ + CH_4$	2.00×10^{-09}	*Vuitton et al.* [2007]
$CH_5^+ + CH_2NH \rightarrow CH_2NH_2^+ + CH_4$	3.00×10^{-09}	*Vuitton et al.* [2007]
$C_2H_5^+ + HCN \rightarrow HCNH^+ + C_2H_4$	2.70×10^{-09}	*Vuitton et al.* [2007]
$C_2H_5^+ + HC_3N \rightarrow CHCCNH^+ + C_2H_4$	3.55×10^{-09}	*McEwan and Anicich* [2007]
$C_2H_5^+ + CH_3CN \rightarrow CH3CNH^+ + C_2H_4$	3.80×10^{-09}	*McEwan and Anicich* [2007]
$C_2H_5^+ + C_2H_4 \rightarrow C_3H_5^+ + CH_4$	3.55×10^{-10}	*McEwan and Anicich* [2007]

Table A.1 – *Continued from previous page*

Reaction	**Rate coefficient** ($cm^3\ s^{-1}$ **or** s^{-1})	**Reference**
$C_2H_5^+ + CH_3CCH \rightarrow C_3H_5^+ + C_2H_4$	1.26×10^{-09}	*McEwan and Anicich* [2007]
$C_2H_5^+ + C_2H_2 \rightarrow$ c-C3H$_3^+ + CH_4$	6.84×10^{-11}	*Vuitton et al.* [2007]
$C_2H_5^+ + C_2H_3CN \rightarrow C_2H_3CNH^+$	3.00×10^{-09}	*Vuitton et al.* [2007]
$C_2H_5^+ + NH_3 \rightarrow NH_4^+ + C_2H_4$	2.09×10^{-09}	*Anicich* [1993]
$C_2H_5^+ + CH_3NH_2 \rightarrow CH_3NH_3^+ + C_2H_4$	1.87×10^{-09}	*Vuitton et al.* [2007]
$C_2H_5^+ + C_4H_2 \rightarrow C_4H_3^+ + C_2H_4$	3.00×10^{-09}	*Vuitton et al.* [2007]
$C_2H_5^+ + C_6H_6 \rightarrow C_6H_7^+ + C_2H_4$	3.00×10^{-09}	*Vuitton et al.* [2007]
$C_2H_5^+ + CH_2NH \rightarrow CH_2NH_2^+ + C_2H_4$	2.70×10^{-09}	*Vuitton et al.* [2007]
$CHCCNH^+ + CH_3CN \rightarrow CH_3CNH^+$ HC_3N	1.28×10^{-09}	*McEwan and Anicich* [2007]
$CHCCNH^+ + NH_3 \rightarrow NH_4^+ + HC_3N$	2.00×10^{-09}	*Vuitton et al.* [2007]
$HCNH^+ + HC_3N \rightarrow CHCCNH^+ + HCN$	3.40×10^{-09}	*McEwan and Anicich* [2007]
$HCNH^+ + CH_3CN \rightarrow$ CH3CNH$^+ +$ HCN	3.80×10^{-09}	*McEwan and Anicich* [2007]
$HCNH^+ + C_2H_3CN \rightarrow C_2H_3CNH^+ +$ HCN	4.50×10^{-09}	*Vuitton et al.* [2007]
$HCNH^+ + NH_3 \rightarrow NH_4^+ +$ HCN	2.30×10^{-09}	*Vuitton et al.* [2007]
$HCNH^+ + CH_3NH_2 \rightarrow CH_3NH_3^+ +$ HCN	3.00×10^{-09}	*Vuitton et al.* [2007]
$HCNH^+ + C_6H_6 \rightarrow C_6H_7^+ +$ HCN	3.00×10^{-09}	*Vuitton et al.* [2007]
$HCNH^+ + CH_2NH \rightarrow CH_2NH_2^+ +$ HCN	2.70×10^{-09}	*Vuitton et al.* [2007]
$HCN^+ + C_2H_2 \rightarrow CHCCNH^+ +$ H	1.35×10^{-10}	*McEwan and Anicich* [2007]
$HCN^+ + HC_3N \rightarrow CHCCNH^+ +$ CN	2.21×10^{-09}	*McEwan and Anicich* [2007]
$HCN^+ + CH_4 \rightarrow HCNH^+ + CH_3$	1.41×10^{-09}	*McEwan and Anicich* [2007]
$HCN^+ + H_2 \rightarrow HCNH^+ +$ H	8.80×10^{-10}	*McEwan and Anicich* [2007]
$HCN^+ +$ HCN $\rightarrow HCNH^+ +$ CN	1.45×10^{-09}	*McEwan and Anicich* [2007]
$C_3H_5^+ + HC_3N \rightarrow CHCCNH^+ + CH_3C_2H$	3.80×10^{-10}	*Vuitton et al.* [2007]
$C_3H_5^+ + NH_3 \rightarrow NH_4^+ + CH_3C_2H$	9.00×10^{-09}	*Vuitton et al.* [2007]
$C_3H_5^+ + C_6H_6 \rightarrow C_6H_7^+ + CH_3C_2H$	1.15×10^{-10}	*Vuitton et al.* [2007]
$NH_4^+ + CH_3NH_2 \rightarrow CH_3NH_3^+ + NH_3$	1.40×10^{-09}	*Vuitton et al.* [2007]
$C_4H_3^+ + C_2H_2 \rightarrow C_6H_5^+ + h\nu$	2.20×10^{-10}	*Vuitton et al.* [2007]
$C_4H_3^+ + C_2H_4 \rightarrow C_6H_5^+ + H_2$	1.20×10^{-10}	*Vuitton et al.* [2007]
$C_4H_3^+ + NH_3 \rightarrow NH_4^+ + C_4H_2$	9.90×10^{-10}	*Vuitton et al.* [2007]
$C_6H_5^+ + NH_3 \rightarrow NH_4^+ + C_6H_4$	7.48×10^{-11}	*Vuitton et al.* [2007]
$C_6H_5^+ + C_2H_6 \rightarrow C_6H_7^+ + CH_4$	1.26×10^{-10}	*Vuitton et al.* [2007]
$C_6H_5^+ + C_2H_4 \rightarrow C_6H_7^+ + C_2H_2$	1.02×10^{-10}	*Vuitton et al.* [2007]
$C_6H_5^+ + H_2 \rightarrow C_6H_7^+ + h\nu$	6.00×10^{-11}	*Vuitton et al.* [2007]
$C_6H_7^+ + NH_3 \rightarrow NH_4^+ + C_6H_6$	2.20×10^{-10}	*Vuitton et al.* [2007]
$CH_2NH_2^+ + NH_3 \rightarrow NH_4^+ + CH_2NH$	1.10×10^{-10}	*Vuitton et al.* [2007]

Table A.2: Dissociative recombination rate coefficients used in the model (from *Richard* [2013])

Ion	α (cm^3 s^{-1})	β
N_2^+	1.70×10^{-07}	0.3
N^+	4.00×10^{-12}	0.58
CH_4^+	3.50×10^{-07}	0.5
CH_3^+	2.97×10^{-07}	0.53
CH_2^+	6.40×10^{-07}	0.6
H^+	3.50×10^{-12}	0.75
H_2^+	1.60×10^{-08}	0.43
HN_2^+	1.70×10^{-07}	0.92
CH_5^+	1.10×10^{-06}	0.7 if $T_e < 300$
		1.5 if $T_e > 300$
$C_2H_5^+$	1.20×10^{-06}	0.8 if $T_e < 300$
		1.2 if $T_e > 300$
$CHCCNH^+$	1.38×10^{-06}	0.6
$HCNH^+$	2.80×10^{-07}	0.65
HCN^+	2.00×10^{-07}	0.5
CH_3CNH^+	3.40×10^{-07}	1.03
$C_3H_5^+$	1.50×10^{-06}	0.7 if $T_e < 300$
		1.4 if $T_e > 300$
C-$C_3H_3^+$	7.00×10^{-07}	0.5
$C_2H_3CNH^+$	1.78×10^{-06}	0.8
NH_4^+	1.34×10^{-06}	0.6
$CH_3NH_3^+$	3.00×10^{-07}	0.7
$C_4H_3^+$	6.20×10^{-07}	0.7
$C_6H_5^+$	1.10×10^{-06}	0.7
$C_6H_7^+$	2.40×10^{-06}	1.3
$CH_2NH_2^+$	1.10×10^{-06}	0.7

Table A.3: List of anion-neutral reactions considered in the model

Reaction	**Rate Coefficient** ($cm^3\ s^{-1}$)	**Reference**
$H^- + H \rightarrow H_2 + e$	2.0×10^{-09}	*Martinez et al.* [2009]
$H^- + CH_3 \rightarrow CH_4 + e$	1.8×10^{-09}	Idem as $H^- + H$
$H^- + C_2H_2 \rightarrow C_2H^- + H_2$	3.1×10^{-10}	*Martinez et al.* [2010]
$H^- + C_4H_2 \rightarrow C_4H^- + H_2$	6.4×10^{-09}	*Vuitton et al.* [2009]
$H^- + HCN \rightarrow CN^- + H_2$	1.5×10^{-08}	*Mackay et al.* [1976]
$H^- + HC_3N \rightarrow C_3N^- + H_2$	1.0×10^{-08}	*Vuitton et al.* [2009]
$H^- + HCNH^+ \rightarrow HCN + H + H$	1.0×10^{-07}	*Hickman* [1979]
$H^- + C_2H_5^+ \rightarrow C_2H_4 + H + H$	1.0×10^{-07}	*Hickman* [1979]
$H^- + C_6H_2 \rightarrow C_6H^- + H_2$	6.3×10^{-09}	*Vuitton et al.* [2009]
$H^- + HC_5N \rightarrow C_5N^- + H_2$	1.0×10^{-08}	*Vuitton et al.* [2009]
$H^- + h\nu \rightarrow H + e$	2.3×10^{-02}	Miller Threshold Law
$C_2H^- + H \rightarrow C_2H_2 + e$	1.6×10^{-09}	*Barckholtz et al.* [2001]
$C_2H^- + CH_3 \rightarrow CH_3C_2H + e$	1.6×10^{-09}	idem as $C_2H^- + H$
$C_2H^- + C_4H_2 \rightarrow C_2H_2 + C_4H^-$	1.5×10^{-09}	*Mackay et al.* [1976]
$C_2H^- + HCN \rightarrow C_2H_2 + CN^-$	3.9×10^{-09}	*Mackay et al.* [1976]
$C_2H^- + HC_3N \rightarrow C_2H_2 + C_3N^-$	2.5×10^{-09}	*Vuitton et al.* [2009]
$C_2H^- + HCNH^+ \rightarrow C_2H + HCN + H$	1.0×10^{-07}	*Hickman* [1979]
$C_2H^- + C_2H_5^+ \rightarrow C_2H + H + C2H4$	1.0×10^{-07}	*Hickman* [1979]
$C_2H^- + HC_5N \rightarrow C_5N^- + C2H2$	2.9×10^{-09}	*Vuitton et al.* [2009]
$C_2H^- + C_6H_2 \rightarrow C_6H^- + C2H2$	2.3×10^{-09}	*Vuitton et al.* [2009]
$C_2H^- + hv \rightarrow C_2H + e$	8.2×10^{-04}	Miller-Threshold Law
$CN^- + H \rightarrow HCN + e$	6.3×10^{-10}	*Yang et al.* [2011]
$CN^- + HCNH^+ \rightarrow CN + H + HCN$	1.0×10^{-07}	*Hickman* [1979]
$CN^- + C_2H_5^+ \rightarrow CN + H + C_2H_4$	1.0×10^{-07}	*Hickman* [1979]
$CN^- + HC_3N \rightarrow HCN + C_3N^-$	4.3×10^{-09}	*Biennier et al.* [2014]
$CN^- + CH_3 \rightarrow CH_3CN + e$	6.3×10^{-10}	idem as $CN^- + H$
$CN^- + HC_5N \rightarrow C_5N^- + HCN$	5.4×10^{-09}	*Vuitton et al.* [2009]
$CN^- + hv \rightarrow CN + e$	1.3×10^{-04}	Miller Threshold Law
$C_3N^- + H \rightarrow HC_3N + e$	5.4×10^{-10}	*Yang et al.* [2011]
$C_3N^- + CH_3 \rightarrow CH_3C_3N + e$	5.4×10^{-10}	Idem as $C_3N^- + H$
$C_3N^- + HCNH^+ \rightarrow C_3N + HCN + H$	1.0×10^{-07}	*Hickman* [1979]
$C_3N^- + C_2H_5^+ \rightarrow C_3N + H + C_2H_4$	1.0×10^{-07}	*Hickman* [1979]
$C_3N^- + hv \rightarrow C_3N$	1.53×10^{-05}	Miller-Threshold Law
$C_5N^- + H \rightarrow$ Products	5.8×10^{-10}	*Yang et al.* [2011]
$C_5N^- + CH_3 \rightarrow$ Products	5.8×10^{-10}	Idem as $C_5N^- + H$

Table A.3 – *Continued from previous page*

Reaction	**Rate coefficient (cm^3 s^{-1} or s^{-1})**	**Reference**
$C_5N^- + HCNH^+ \rightarrow C_5N + HCN + H$	3.76×10^{-08}	*Harada and Herbst* [2008]
$C_5N^- + C_2H_5^+ \rightarrow$ Products	3.76×10^{-08}	*Harada and Herbst* [2008]
$C_4H^- + H \rightarrow C_4H_2 + e$	8.30×10^{-10}	*Barckholtz et al.* [2001]
$C_4H^- + CH_3 \rightarrow$ Soot + e	8.30×10^{-10}	Idem as $C_4H^- + H$
$C_4H^- + HCN \rightarrow C_4H_2 + CN^-$	2.00×10^{-09}	*Vuitton et al.* [2009]
$C_4H^- + HCNH^+ \rightarrow C_4H + H + HCN$	1.00×10^{-07}	*Hickman* [1979]
$C_4H^- + C_2H_5^+ \rightarrow C_4H + H$	1.00×10^{-07}	*Hickman* [1979]
$C_4H^- + HC_3N \rightarrow C_4H_2 + C_3N^-$	2.00×10^{-09}	*Vuitton et al.* [2009]
$C_4H^- + HC_5N \rightarrow C_5N^- + C_2H_2$	2.3×10^{-09}	*Vuitton et al.* [2009]
$C_4H^- + C_6H_2 \rightarrow C_6H^- + C_2H_2$	1.8×10^{-09}	*Vuitton et al.* [2009]
$C_4H^- + C_2H_2 \rightarrow C_6H^- + H_2$	1.0×10^{-12}	*De Bleecker et al.* [2006]
$C_4H^- + hv \rightarrow C_4H + e$	2.3×10^{-04}	Miller-Threshold Law
$C_6H^- + C_2H_2 \rightarrow$ CxHyNz-	1.0×10^{-12}	*De Bleecker et al.* [2006]
$C_6H^- + HC_5N \rightarrow C_5N^- + C_2H_2$	2.1×10^{-09}	*Vuitton et al.* [2009]
$C_6H^- + HC_3N \rightarrow C_3N^- + C_2H_2$	1.8×10^{-09}	*Vuitton et al.* [2009]
$C_6H^- + HCN \rightarrow CN^- + C_2H_2$	1.9×10^{-09}	*Vuitton et al.* [2009]
$C_6H^- + H \rightarrow$ Products	5.0×10^{-10}	*Barckholtz et al.* [2001]
$C_6H^- + CH_3 \rightarrow$ Products	5.0×10^{-10}	Idem as $C_6H^- + H$
$C_6H^- + HCNH^+ \rightarrow C_6H + HCN + H$	3.7×10^{-08}	UMIST database
$C_6H^- + C_2H_5^+ \rightarrow$ Products	3.70×10^{-08}	UMIST database
$C_6H^- + hv \rightarrow C_6H$	2.31×10^{-04}	Miller Threshold Law
$OH^- + H \rightarrow H_2O + e_T$	1.4×10^{-09}	*Howard et al.* [1974]
$OH^- + CH_3 \rightarrow H_2O + e_T$	1.4×10^{-09}	Idem as $OH^- + H$
$OH^- + C_2H_2 \rightarrow C_2H^- + H_2O$	2.2×10^{-09}	*Raksit and Bohme* [1983]
$OH^- + HCN \rightarrow CN^- + H2O$	3.5×10^{-09}	*Raksit and Bohme* [1983]
$OH^- + HCNH^+ \rightarrow$ Products	1.0×10^{-07}	*Hickman* [1979]
$OH^- + C_2H_5^+ \rightarrow$ Products	1.0×10^{-07}	*Hickman* [1979]
$OH^- + hv \rightarrow OH + e$	7.4×10^{-03}	Miller-Threshold Law
$O^- + HCNH^+ \rightarrow$ Products	1.0×10^{-07}	*Hickman* [1979]
$O^- + C_2H_5^+ \rightarrow$ Products	1.0×10^{-07}	*Hickman* [1979]
$O^- + H \rightarrow OH + e$	5.0×10^{-10}	UMIST database
$O^- + CH_3 \rightarrow$ Products	5.0×10^{-10}	Idem as $O^- + H$
$O^- + CH_4 \rightarrow$ OH- + CH3	1.0×10^{-10}	UMIST database
$O^- + C_2H_2 \rightarrow$ products	1.1×10^{-09}	*Viggiano and Paulson* [1983]
$O^- + C_2H_4 \rightarrow$ products	9.0×10^{-10}	*Viggiano and Paulson* [1983]

Table A.3 – *Continued from previous page*

Reaction	**Rate coefficient (cm^3 s^{-1} or s^{-1})**	**Reference**
$O^- + C_4H_2 \rightarrow C_4H^- + OH$	1.6×10^{-09}	*Vuitton et al.* [2009]
$O^- + C_6H_2 \rightarrow C_6H^- + OH$	1.6×10^{-09}	*Vuitton et al.* [2009]
$O^- + HCN \rightarrow CN- + OH$	3.7×10^{-09}	*Bohme* [1975]
$O^- + HC_3N \rightarrow C3N- + OH$	2.9×10^{-09}	*Vuitton et al.* [2009]
$O^- + HC_5N \rightarrow C5N- + OH$	2.8×10^{-09}	*Vuitton et al.* [2009]
$O^- + hv \rightarrow O + e$	1.0×10^{-02}	Miller-threshold law
$CH_2^- + HCNH^+ \rightarrow$ Products	1.0E-07	*Hickman* [1979]
$CH_2^- + C_2H_5^+ \rightarrow$ Products	1.0×10^{-07}	*Hickman* [1979]
$CH_2^- + H \rightarrow$ Products	1.0×10^{-09}	*Adams* [2006]
$CH_2^- + CH_3 \rightarrow$ Products	1.0×10^{-09}	*Adams* [2006]
$CH_2^- + hv \rightarrow CH_2 + e$	1.89×10^{-02}	Miller-Threshold Law

References

Adamczyk, B., J. H. Boerboom, B. L. Schram, and J. Kistemaker (1966), Partial ionization cross sections of He, Ne, H_2 and CH_4 for electrons from 20 to 500 eV, *Journal of Chemical Physics*, *44*, 4640 – 4642, doi:10.1063/1.1726690.

Adams, N. (2006), *Gas Phase Ionic Reactions*, pp. 575–587, Springer, New York.

Adams, N. G., and D. Smith (1988), Measurements of the dissociative recombination coefficients for several polyatomic ion species at 300K, *Chemical Physics Letters*, *144*, 11–14.

Adibzadeh, M., and C. E. Theodosiou (2005), Elastic electron scattering from inert-gas atoms, *Atomic Data and Nuclear Data Tables*, *91*, 8–76, doi:10.1016/j.adt.2005.07.004.

Almeida, D. P. (2002), Electron-impact multiple ionization of xenon (σ^{n^+}, n=2–9), *Journal of Electron Spectroscopy and Related Phenomena*, *122*, 1 – 9.

Anicich, V. G. (1993), Evaluated bimolecular ion-molecule gas phase kinetics of positive ions for use in modeling planetary atmospheres/cometary comae/interstellar clouds, *Journal of Physical and Chemical Reference Data*, *22*.

Anicich, V. G., and M. J. McEwan (1997), Ion-molecule chemistry in Titan's ionosphere, *Planetary and Space Science*, *45*, 897–921.

Anicich, V. G., P. F. Wilson, and M. J. McEwan (2006), An ICR study of ion-molecules reactions relevant to Titan's Atmosphere: An investigation of binary hydrocarbon mixtures up to 1 micron, *Journal of the American Society for Mass Spectrometry*, *17*(4), 544 – 561, doi:10.1016/j.jasms.2005.11.022.

Appleton, E. V., and M. A. F. Barnett (1925), Local reflection of wireless waves from the upper atmosphere, *Nature*, *115*.

Ashihara, O. (1978), Photoelectron fluxes in the cometary atmosphere, *Icarus*, *35*, 369.

Bakes, E. L. O., C. P. McKay, and C. W. Bauschlicher (2002), Photoelectric Charging of Submicron Aerosols and Macromolecules in the Titan Haze, *Icarus*, *157*, 464–475, doi:10.1006/icar.2002.6843.

Banaszkiewicz, M., L. M. Lara, R. Rodrigo, J. J. Lopez-Moreno, and G. J. Molina-Cuberos (2000), A coupled model of Titan's atmosphere and ionosphere, *Icarus*, *147*, 386, doi:10.1006/icar.2000.6448.

Banks, P., R. Schunk, and W. Raitt (1976), The topside ionosphere: A region of dynamic transition, *Annual Review of Earth and Planetary Sciences*, *4*(1), 381–440.

Banks, P. M. (1969), The thermal structure of the ionosphere, *IEEE Proceedings*, *57*, 258–281.

Banks, P. M., and A. F. Nagy (1970), Concerning the influence of elastic scattering upon photoelectron transport and escape, *Journal of Geophysical Research*, *75*, 1902–1910, doi:10.1029/JA075i01.

Banks, P. M., C. R. Chappell, and A. F. Nagy (1974), A new model for the interaction of auroral electrons with the atmosphere: Spectral degradation, backscatter, optical emission, and ionization, *Journal of Geophysical Research*, *79*(10), 1459–1470, doi:10.1029/JA079i010p01459.

Barckholtz, C., T. P. Snow, and V. M. Bierbaum (2001), Reactions of C_n^- and C_nH^- with atomic and molecular hydrogen, *The Astrophysical Journal Letters*, *547*(2), L171.

Bergstralh, J. T., E. D. Miner, and M. S. Matthews (1991), *Uranus*, University of Arizona Press.

Bhardwaj, A., and G. R. Gladstone (2000), Auroral emissions of the giant planets, *Reviews of Geophysics*, *38*(3), 295–353, doi:10.1029/1998RG000046.

Bhardwaj, A., and S. K. Jain (2009), Monte Carlo model of electron energy degradation in a CO_2 atmosphere, *Journal of Geophysical Research*, *114*, A11,309, doi:10.1029/2009JA014298.

Bhardwaj, A., and S. K. Jain (2012), Production of N_2 Vegard-Kaplan and other triplet band emissions in the dayglow of Titan, *Icarus*, *218*, 989–1005, doi:10.1016/j.icarus.2012.01.019.

Bhardwaj, A., and S. K. Jain (2013), CO Cameron band and CO_2^+ UV doublet emissions in the dayglow of Venus: Role of CO in the Cameron band production, *Journal of Geophysical Research (Space Physics)*, *118*, 3660–3671, doi:10.1002/jgra.50345.

Bhardwaj, A., and M. Michael (1999), Monte Carlo model for electron degradation in SO_2 gas: cross sections, yield spectra and efficiencies, *Journal of Geophysical Research*, *104*(10), 24,713 – 24,728, doi:10.1029/1999JA900283.

Bhardwaj, A., and M. Micheal (1999), On the excitation of Io's atmosphere by the photoelectrons: Application of the analytical yield spectral model of SO_2, *Geophysical Research Letters*, *26*, 393, doi:10.1029/1998GL900320.

Bhardwaj, A., and V. Mukundan (2015), Monte Carlo model for electron degradation in methane gas, *Planetary and Space Science*, *111*, 34–43, doi:10.1016/j.pss.2015.03.008.

Bhardwaj, A., and S. Raghuram (2011), Model for Cameron-band emission in comets: A case for the EPOXI mission target comet 103P/Hartley 2, *Monthly Notices of Royal Astronomical Society Letters*, *412*, L25 – L29.

Bhardwaj, A., and S. Raghuram (2012), Coupled Chemistry-Emission Model for Atomic Oxygen Green and Red-doublet Emissions in Comet C/1996 B2 Hyakutake, *Astrophysical Journal*, *748*(1), 13.

Bhardwaj, A., and R. P. Singhal (1990), Auroral and dayglow processes on Neptune, *Indian Journal of Radio and Space Physics*, *19*, 171 – 176.

Bhardwaj, A., and R. P. Singhal (1993), Optically thin H Lyman alpha production on outer planets: Low-energy proton acceleration in parallel electric fields and neutral

H atom precipitation from ring current, *Journal of Geophysical Research*, *98*, 9473, doi:10.1029/92JA02400.

Bhardwaj, A., S. A. Haider, and R. P. Singhal (1990), Auroral and Photoelectron Fluxes in Cometary Ionospheres, *Icarus*, *85*, 216 – 228.

Bhardwaj, A., S. A. Haider, and R. P. Singhal (1996), Production and Emissions of Atomic Carbon and Oxygen in the Inner Coma of Comet Halley: Role of Electron Impact, *Icarus*, *120*(0061), 412 – 430.

Biennier, L., S. Carles, D. Cordier, J.-C. Guillemin, S. D. L. Picard, and A. Faure (2014), Low temperature reaction kinetics of CN^- + HC_3N and implications for the growth of anions in Titans atmosphere, *Science*, *227*, 123 – 131, doi:10.1016/j.icarus.2013.09.004.

Bird, M., R. Dutta-Roy, S. Asmar, and T. Rebold (1997), Detection of Titan's ionosphere from Voyager 1 radio occultation observations, *Icarus*, *130*(2), 426 – 436, doi:10.1006/icar.1997.5831.

Boesten, L., and H. Tanaka (1991), Elastic DCS for e+CH_4 collisions, 1.5 to 100 eV, *Journal of Physics B: Atomic Molecular and Optical Physics*, *24*, 821.

Bohme, D. (1975), The kinetics and energetics of proton transfer, *Interactions Between Ions and Molecules*, pp. 489–504.

Borucki, W. J., R. C. Whitten, E. L. O. Bakes, E. Barth, and S. Tripathi (2006), Predictions of the electrical conductivity and charging of the aerosols in Titan's atmosphere, *Icarus*, *181*, 527–544, doi:10.1016/j.icarus.2005.10.030.

Breit, G., and M. A. Tuve (1925), A Radio Method of Estimating the Height of the Conducting Layer, *Nature*, *116*, 357, doi:10.1038/116357a0.

Brown, R., J. Lebreton, and H. Waite (2009), *Titan from Cassini-Huygens*, Springer Netherlands.

Bundschu, C. T., J. C. Gibsony, R. J. Gulleyz, M. J. Brungerx, S. J. Buckmany, N. Sannak, and F. A. Gianturco (1997), Low-energy electron scattering from methane, *Journal of Physics B: Atomic Molecular and Optical Physics*, *30*, 2239.

Campbell, L., and M. Brunger (2016), Electron collisions in atmospheres, *International Reviews in Physical Chemistry*, *35*(2), 297–351, doi:10.1080/0144235X.2016.1179002.

Campbell, L., and M. J. Brunger (2009), On the role of electron-driven processes in planetary atmospheres and comets, *Journal of Physics*, *80*.

Capone, L., R. Whitten, J. Dubach, S. Prasad, and W. Huntress (1976), The lower ionosphere of Titan, *Icarus*, *28*(3), 367 – 378.

Chamberlain, J. W. (1961), *Physics of the Aurora and Airglow: International Geophysics Series*, Elsevier Science, Netherlands.

Chatham, H., D. Hils, R. Robertson, and A. Gallagher (1984), Total and partial electron collisional ionization cross sections for CH_4, C_2H_6, SiH_4, and Si_2H_6, *Journal of Chemical Physics*, *81*, 1770 – 1777, doi:10.1063/1.447848.

Chen, R. H., and A. F. Nagy (1978), A comprehensive model of the Venus ionosphere, *Journal of Geophysical Research*, *83*, 1133–1140, doi:10.1029/JA083iA03p01133.

Cho, H., Y. S. Park, E. A. y Castro, G. L. C. de Souza, I. Iga, L. E. Machado, and M.-T. Lee (2008), A comparative experimental - theoretical study on elastic electron

scattering by methane, *Journal of Physics B: Atomic Molecular and Optical Physics*, *41*, 045,203.

Cicerone, R. J., and S. A. Bowhill (1970), Photoelectron escape fluxes obtained by a Monte Carlo technique, *Radio Science*, *5*, 49, doi:10.1029/RS005i001p00049.

Cicerone, R. J., and S. A. Bowhill (1971), Photoelectron fluxes in the ionosphere computed by a Monte Carlo method, *Journal of Geophysical Research*, *76*, 8299, doi:10.1029/JA076i034p08299.

Coates, A. J., F. J. Crary, G. R. Lewis, D. T. Young, J. H. Waite, and E. C. Sittler (2007), Discovery of heavy negative ions in Titan's ionosphere, *Geophysical Research Letters*, *34*, L22103, doi:10.1029/2007GL030978.

Coates, A. J., A. Wellbrock, G. R. Lewis, G. H. Jones, D. T. Young, F. J. Crary, and J. H. Waite (2009), Heavy negative ions in Titan's ionosphere: Altitude and latitude dependence, *Planetary and Space Science*, *57*, 1866–1871, doi:10.1016/j.pss.2009.05.009.

Coates, A. J., et al. (2010), Negative ions at Titan and Enceladus: recent results, *Faraday Discussions*, *147*, 293, doi:10.1039/c004700g.

Combecher, D. (1980), Measurement of W Values of Low-Energy Electrons in Several Gases, *Radiation Research*, *84*(2), 189 – 218.

Cordier, D., O. Mousis, J. I. Lunine, P. Lavvas, and V. Vuitton (2009), An estimate of the chemical composition of Titan's lakes, *The Astrophysical Journal Letters*, *707*(2), L128.

Coupeaud, A., N. Pietri, I. Couturier-Tamburelli, and J.-P. Aycard (2005), Laboratory study of the Titan's atmosphere chemistry: Formation and characterization of HC_5N, in *IAU Symposium*, *IAU Symposium*, vol. 235, p. 92.

Coustenis, A. (2008), *Titan: Exploring an Earthlike World*, Series on atmospheric, oceanic and planetary physics, World Scientific Publishing Company, Singapore.

Coustenis, A. (2015), Titan's organic chemistry: A planetary-scale laboratory to study primitive earth, *Mètode Science Studies Journal - Annual Review*, *0*(6), doi:10.7203/metode.6.4999.

Coustenis, A., and T. Encrenaz (2013), *Life Beyond Earth: The Search for Habitable Worlds in the Universe*, Cambridge University Press.

Couturier-Tamburelli, I., N. Piétri, and M. S. Gudipati (2015), Simulation of Titan's atmospheric photochemistry. Formation of non-volatile residue from polar nitrile ices, *Astronomy & Astrophysics*, *578*, A111.

Cravens, T., et al. (2006), Composition of Titan's ionosphere, *Geophysical Research Letters*, *33*(7), L07,105, doi:10.1029/2005GL025575.

Cravens, T. E., G. A. Victor, and A. Dalgarno (1975), The absorption of energetic electrons by molecular hydrogen gas, *Planetary and Space Science*, *23*, 1059.

Cravens, T. E., J. U. Kozyra, A. F. Nagy, T. I. Gombosi, and M. Kurtz (1987), Electron impact ionization in the vicinity of comets, *Journal of Geophysical Research*, *92*, 7341–7353, doi:10.1029/JA092iA07p07341.

Cravens, T. E., et al. (2005), Titan′s ionosphere: Model comparisons with Cassini Ta data, *Geophysical Research Letters*, *32*, L12108, doi:10.1029/2005GL023249.

Cravens, T. E., R. V. Yelle, J.-E. Wahlund, D. E. Shemansky, and A. F. Nagy (2009), *Titan from Cassini Huygens*, chap. Composition and structure of the ionosphere and thermosphere, pp. 259 – 296, Springer, Newyork.

Cravens, T. E., et al. (2010), Dynamical and magnetic field time constants for Titan's ionosphere: Empirical estimates and comparisons with venus, *Journal of Geophysical Research: Space Physics*, *115*(A8), doi:10.1029/2009JA015050, a08319.

Cui, J., et al. (2009), Analysis of Titan's neutral upper atmosphere from Cassini Ion Neutral Mass Spectrometer measurements, *Icarus*, *200*, 581 – 615, doi:10.1016/j.icarus.2008.12.005.

Cui, J., M. Galand, R. V. Yelle, J. E. Wahlund, K. Agren, J. H. W. Jr, and M. K. Dougherty (2010), Ion transport in Titan's upper atmosphere, *Advances in Space Research*, *115*(82), 82 – 84, doi:10.1029/2009JA014563.

Cui, J., Y.-T. Cao, P. P. Lavvas, and T. T. Koskinen (2016), The Variability of HCN in Titan's Upper Atmosphere as Implied by the Cassini Ion-Neutral Mass Spectrometer Measurements, *The Astrophysical Journal Letters*, *826*, L5.

Danko, M., J. Országh, M. Lacko, Š. Matejčík, J. Fedor, and S. Denifl (2011), Electron Induced Fluorescence Spectra of Methane, *WDS'11 Proceedings of Contributed Papers, Part II*, pp. 192 – 197.

Date, H., Y. Ishimaru, and M. Shimozuma (2003), Electron collision processes in gaseous xenon, *Radiation Research*, *207*(1), 373 – 380.

Davies, D. K., L. E. Kline, W. E, and Bies (1988), Measurements of swarm parameters and derived electron collision cross sections in methane, *Journal of Applied Physics*, *65*, 3311, doi:10.1063/1.342642.

Dayashankar (1982), Ionization yield in xenon due to electron impact, *Physica B+C*, *113*, 237–243.

De Bleecker, K., A. Bogaerts, and W. Goedheer (2006), Detailed modeling of hydrocarbon nanoparticle nucleation in acetylene discharges, *Physical Review E*, *73*, 026,405, doi:10.1103/PhysRevE.73.026405.

Demarais, N., Z. Yang, T. Snow, and V. Bierbaum (2013), Chemistry of $HCNH^+$: Mechanisms, structures, and relevance to Titan's atmosphere, *Structural Chemistry*, *24*(6), 1957–1963.

Desai, R. T., et al. (2017), Carbon chain anions and the growth of complex organic molecules in Titan's ionosphere, *The Astrophysical Journal Letters*, *844*(2), L18.

Dias, T. H. V. T., F. P. Santos, A. D. Stauffer, and C. A. N. Conde (1993), Monte Carlo simulation of x-ray absorption and electron drift in gaseous xenon, *Physical Review*, *48*(4), 2887 – 2902.

Dobrijevic, M., J. C. Loison, K. M. Hickson, and G. Gronoff (2016), 1D-coupled photochemical model of neutrals, cations and anions in the atmosphere of Titan, *Icarus*, *268*, 313–339, doi:10.1016/j.icarus.2015.12.045.

Donahue, T. M., J. H. Hoffman, and R. R. Hodges (1981), Krypton and xenon in the atmosphere of Venus, *Geophysical Research Letters*, *8*, 513–516, doi:10.1029/GL008i005p00513.

Douthat, D. A. (1975), Electron degradation spectra in helium, *Radiation Research*, *61*(1), 141–152.

Erwin, D. A., and J. A. Kunc (2008), Dissociation and ionization of the methane molecule by nonrelativistic electrons including the near threshold region, *Journal of Applied Physics*, *103*(6), 064,906, doi:10.1063/1.2891694.

Feulner, G. (2012), The faint young Sun problem, *Reviews of Geophysics*, *50*, RG2006, doi:10.1029/2011RG000375.

Fleagle, R. G., and J. A. Businger (1980), *An introduction to atmospheric physics.*, Academic Press.

Fons, J. T., and C. C. Lin (1998), Measurement of the cross sections for electron-impact excitation into the $5p^5 6p$ levels of xenon, *Physcial Review A*, *58*, 4603–4615, doi:10.1103/PhysRevA.58.4603.

Fox, J. (2004), Advances in the aeronomy of Venus and Mars, *Advances in Space Research*, *33*(2), 132 – 139, doi:10.1016/j.asr.2003.08.014.

Fox, J. L., and G. A. Victor (1988), Electron energy deposition in N_2 gas, *Planetary and Space Science*, *36*(4), 329 – 352.

Fox, J. L., and R. V. Yelle (1997), Hydrocarbon ions in the ionosphere of Titan, *Geophysical Research Letters*, *24*, 2179, doi:10.1029/97GL02051.

Fox, J. L., M. I. Galand, and R. E. Johnson (2008), Energy deposition in planetary atmospheres by charged particles and solar photons, *Space Science Reviews*, *139*, 3.

Fulchignoni, M., F. Ferri, F. Angrilli, A. Ball, et al. (2005), In situ measurements of the physical characteristics of Titan's environment, *Nature*, *438*(7069), 785.

Galand, M., R. Yelle, J. Cui, J. E. Wahlund, V. Vuitton, A. Wellbrock, and A. Coates (2010), Ionization sources in Titan's deep ionosphere, *Journal of Geophysical Research*, *115*, 10 – 17, doi:10.1029/2009JA015100.

Gan, L., C. N. Keller, and T. E. Cravens (1992), Electrons in the Ionosphere of Titan, *Journal of Geophysical Research*, *97*(9), 12.

Garcia, G., J. L. de Pablos, F. Blanco, and A. Williart (2002), Total and elastic electron scattering cross sections from Xe at intermediate and high energies, *Journal of Physics B Atomic Molecular and Optical Physics*, *35*, 4657 – 4667.

Gibson, J. C., D. R. Lun, L. J. Allen, R. P. McEachran, L. A. Parcell, and S. J. Buckman (1998), Low-energy electron scattering from xenon, *Journal of Physics B Atomic Molecular and Optical Physics*, *31*, 3949–3964.

Gilmore, T., and T. Field (2015), Absolute cross sections for dissociative electron attachment to HCCCN, *Journal of Physics B Atomic Molecular Physics*, *48*(3), 035,201.

Gladstone, G. R., et al. (2016), The atmosphere of Pluto as observed by New Horizons, *Science*, *351*, aad8866, doi:10.1126/science.aad8866.

Green, A. E. S., and C. A. Barth (1965), Calculations of Ultraviolet molecular nitrogen emissions from the Aurora, *Journal of Geophysical Research*, *70*(5), 1083 – 1092, doi:10.1029/JZ070i005p01083.

Green, A. E. S., and C. A. Barth (1967), Calculations of the photoelectron excitation of the dayglow, *Journal of Geophysical Research*, *72*(15), 3975 – 3986, doi:10.1029/JZ072i015p03975.

Green, A. E. S., and T. Sawada (1972), Ionization cross sections and secondary electron distributions, *Journal of Atmospheric and Terrestrial Physics*, *34*, 1719 – 1728.

Green, A. E. S., and R. P. Singhal (1979), Microplume model of spatial–yield spectra, *Geophysical Research Letters*, *6*(7), 625 – 628.

Green, A. E. S., C. H. Jackman, and R. H. Garvey (1977a), Electron impact on atmospheric gases: 2. Yield spectra, *Journal of Geophysical Research*, *82*, 5104, doi:10.1029/JA082i032p05104.

Green, A. E. S., R. H. Garvey, and C. H. Jackman (1977b), Analytic yield spectra for electrons on H_2, *International Journal of Quantum Chemistry*, *12*(S11), 97–103, doi:10.1002/qua.560120815.

Green, A. E. S., Dayashankar, and P. F. Schippnick (1985), Yield and concentration microplumes for electron impact on water, *Radiation Research*, *104*, 1 – 14.

Gregersen, E. (2010), *Outer Solar System: Jupiter, Saturn, Uranus, Neptune, and the Dwarf Planets*, Explorer's guide to the universe, Britannica Educational Publishing, Newyork.

Grodent, D. (2015), A brief review of ultraviolet auroral emissions on giant planets, *Space Science Reviews*, *187*(1), 23–50.

Haider, S. A., and R. P. Singhal (1983), Analytical yield spectrum approach to electron energy degradation in Earth's atmosphere, *Journal of Geophysical Research*, *88*, 7185–7189, doi:10.1029/JA088iA09p07185.

Haider, S. A., M. A. Abdu, I. S. Batista, J. H. Sobral, X. Luan, E. Kallio, W. C. Maguire, M. I. Verigin, and V. Singh (2009), D, E, and F layers in the daytime at high-latitude terminator ionosphere of Mars: Comparison with Earth's ionosphere using cosmic data, *Journal of Geophysical Research: Space Physics*, *114*(A3), A03,311, doi:10.1029/2008JA013709, a03311.

Harada, N., and E. Herbst (2008), Modeling carbon chain anions in l1527, *The Astrophysical Journal*, *685*(1), 272.

Haxton, D. J., C. W. McCurdy, and T. N. Rescigno (2007), Dissociative electron attachment to the H_2O molecule I. Complex-valued potential-energy surfaces for the B12 , A12 , and B22 metastable states of the water anion, *Physical Review A*, *75*(1), 012710, doi:10.1103/PhysRevA.75.012710.

Heaps, M. G., and A. E. S. Green (1974), Monte Carlo approach to the spatial deposition of energy by electrons in molecular hydrogen, *Journal of Applied Physics*, *45*, 3183–3188, doi:10.1063/1.1663745.

Herbst, E., and Y. Osamura (2008), Calculations on the formation rates and mechanisms for C_nH anions in interstellar and circumstellar media, *The Astrophysical Journal*, *679*, 1670-1679, doi:10.1086/587803.

Hickman, A. P. (1979), Approximate scaling formula for ion-ion mutual neutralization rates, *The Journal of Chemical Physics*, *70*, 4872–4878, doi:10.1063/1.437364.

Hinson, D., F. Flasar, A. Kliore, P. Schinder, J. Twicken, and R. Herrera (1997), Jupiter's ionosphere: Results from the first galileo radio occultation experiment, *Geophysical Research Letters*, *24*(17), 2107–2110.

Hinteregger, H. E., K. Fukui, and B. R. Gilson (1981), Observational, reference and model data on solar EUV, from measurements on AE-E, *Geophysical Research Letters*, *8*(11), 1147 – 1150, doi:10.1029/GL008i011p01147.

Hörst, S. M. (2017), Titan's atmosphere and climate, *Journal of Geophysical Research: Planets*, *122*(3), 432–482, doi:10.1002/2016JE005240, 2016JE005240.

Howard, C. J., F. C. Fehsenfeld, and M. McFarland (1974), Negative ion-molecule reactions with atomic hydrogen in the gas phase at 296 K, *Journal of Chemical Physics*, *60*, 5086–5089.

Howling, A. A., L. Sansonnens, J. Dorier, and C. Hollenstein (1994), Time-resolved measurements of highly polymerized negative ions in radio frequency silane plasma deposition experiments, *Journal of Applied Physics*, *75*(3), 1340–1353, doi:10.1063/1.356413.

Huebner, W. F., J. J. Keady, and S. P. Lyon (1992), Solar photorates for planetary atmospheres and atmospheric pollutants, *Astrophysics and Space Science*, *195*(1), 1 – 289, doi:10.1007/BF00644558.

ICRU (1993), Average energy required to produce an ion pair, Report No. 31, International Commission on Radiation Units and Measurements, Washington, D.C., *ICRU Publications,ISBN 0-913394-25-4*.

Iga, I., M.-T. Lee, M. G. P. Homem, L. E. Machado, and L. M. Brescansin (1999), Elastic cross sections for e-CH_4 collisions at intermediate energies, *Physical Review A*, *21*, 12, doi:10.1103/PhysRevA.61.022708.

Imanaka, H., B. N. Khare, J. E. Elsila, E. L. Bakes, C. P. McKay, D. P. Cruikshank, S. Sugita, T. Matsui, and R. N. Zare (2004), Laboratory experiments of Titan tholin formed in cold plasma at various pressures: implications for nitrogen-containing polycyclic aromatic compounds in Titan haze, *Icarus*, *168*(2), 344 – 366, doi:10.1016/j.icarus.2003.12.014.

Inoue, M. (1966), Ions negatifs formes dans le cyanogene et lacide cyanhydrique, *Journal de Chimie Physique*, *63*(7-8), 1061.

Ionov, D. E., V. I. Shematovich, and Y. N. Pavlyuchenkov (2017), Influence of photoelectrons on the structure and dynamics of the upper atmosphere of a hot Jupiter, *Astronomy Reports*, *61*, 387–392, doi:10.1134/S1063772917050018.

Ip, W.-H. (1990), Titan's upper ionosphere, *Astrophysical Journal*, *362*, 354–363, doi:10.1086/169271.

Itikawa, Y., and N. Mason (2005), Cross sections for electron collisions with water molecules, *Journal of Physical and Chemical Reference Data*, *34*, 1, doi:10.1063/1.1799251.

Jackman, C. H., and A. E. S. Green (1979), Electron impact on atmospheric gases. III – Spatial yield spectra for N_2, *Journal of Geophysical Research*, *84*, 2715–2724, doi:10.1029/JA084iA06p02715.

Jain, S. K., and A. Bhardwaj (2015), Production of N_2 Vegard-Kaplan and Lyman-Birge-Hopefield emissions on Pluto, *Icarus*, *247*, 285 – 290, doi:10.1016/j.icarus.2014.08.032.

Johnson, R. E., D. Schnellenberger, and M. C. Wong (2000), The sputtering of an oxygen thermosphere by energetic O^+, *Journal of Geophysical Research*, *105*, 1659–1670, doi: 10.1029/1999JE001058.

Jolitz, R. D., C. F. Dong, C. O. Lee, R. J. Lillis, D. A. Brain, S. M. Curry, S. Bougher, C. D. Parkinson, and B. M. Jakosky (2017), A monte carlo model of crustal field influences on solar energetic particle precipitation into the martian atmosphere, *Journal of Geophysical Research: Space Physics*, *122*(5), 5653–5669, doi: 10.1002/2016JA023781, 2016JA023781.

Jonathan, I. L., and S. K. Atreya (2008), The methane cycle on Titan, *Nature Geoscience*, *1*, 159, doi:10.1038/ngeo12510.1038/ngeo125.

Jung, R. O., J. B. Boffard, L. W. Anderson, and C. C. Lin (2009), Excitation into $5p^5 7p$ levels from the ground level and the J=2 metastable level of Xe, *Physical Review A*, *2*, 10 – 20, doi:10.1103/PhysRevA.80.062708.

Kallenrode, M.-B. (2004), *An Introduction to Plasmas and Particles in the Heliosphere and Magnetospheres*, 3, 3 ed., Springer-Verlag, Berlin, Heidelberg.

Kanik, I., S. Trajmar, and J. C. Nickel (1993), Total Electron Scattering and Electronic State Excitations Cross Sections for O_2, CO, and CH_4, *Journal of Geophysical Research*, *98*, 7447, doi:10.1029/92JE02811.

Keller, C. N., T. E. Cravens, and L. Gan (1992), A model of the ionosphere of Titan, *Journal of Geophysical Research*, *97*, 12, doi:10.1029/92JA00231.

Keller, C. N., V. G. Anicich, and T. E. Cravens (1998), Model of Titan's ionosphere with detailed hydrocarbon ion chemistry, *Planetary and Space Science*, *46*, 1157–1174.

Knoll, G. F. (2000), *Radiation detection and measurement*, 3 ed., Wiley India.

Korosmezey, A., et al. (1987), A new model of cometary ionospheres, *Journal of Geophysical Research: Space Physics*, *92*(A7), 7331–7340, doi:10.1029/JA092iA07p07331.

Krasnopolsky, V. A. (2009), A photochemical model of Titan's atmosphere and ionosphere, *Icarus*, *201*, 226–256, doi:10.1016/j.icarus.2008.12.038.

Krishnakumar, E., and S. K. Srivastava (1988), Ionisation cross sections of rare-gas atoms by electron impact, *Journal of Physics B Atomic Molecular Physics*, *21*, 1055–1082.

Krishnakumar, E., S. Denifl, I. Cadez, S. Markelj, and N. J. Mason (2011), Dissociative Electron Attachment Cross Sections for H_2 and D_2, *Physical Review A*, *106*(34), 243,201, doi:10.1103/PhysRevLett.106.243201.

Kurokawa, M., M. Kitajima, K. Toyoshima, T. Kishino, T. Odagiri, H. Kato, M. Hoshino, H. Tanaka, and K. Ito (2011), High-resolution total-cross-section measurements for electron scattering from Ar, Kr, and Xe employing a threshold-photoelectron source, *Physical Review A*, *84*, 062,717, doi:10.1103/PhysRevA.84.062717.

Lara, L. M., E. Lellouch, J. J. López-Moreno, and R. Rodrigo (1996), Vertical distribution of Titan's atmospheric neutral constituents, *Journal of Geophysical Research*, *101*, 23,261–23,283, doi:10.1029/96JE02036.

Lavvas, P., M. Galand, R. V. Yelle, A. N. Heays, B. R. Lewis, G. R. Lewis, and A. J. Coates (2011), Energy deposition and primary chemical products in Titan's upper atmosphere, *Icarus*, *213*, 233 – 251, doi:10.1016/j.icarus.2011.03.001.

Lavvas, P. P., A. Coustenis, and I. M. Vardavas (2008), Coupling photochemistry with haze formation in Titan's atmosphere, Part II: Results and validation with Cassini/Huygens data, *Planetary and Space Science*, *56*, 67–99, doi:10.1016/j.pss.2007.05.027.

Lavvas, P. P., R. V. Yelle, and V. Vuitton (2009), The detached haze layer in Titan's mesosphere, *Icarus*, *201*(2), 626 – 633, doi:10.1016/j.icarus.2009.01.004.

Lavvas, P. P., et al. (2013), Aerosol growth in Titan's ionosphere, *Proceedings of the National Academy of Science*, *110*, 2729–2734, doi:10.1073/pnas.1217059110.

Lebius, H., J. Binder, H. R. Koslowski, K. Wiesemann, and B. A. Huber (1989), Partial and state-selective cross sections for multiple ionisation of rare-gas atoms by electron impact, *Journal of Physics B Atomic Molecular Physics*, *22*, 83–97.

Lebonnois, S., E. L. O. Bakes, and C. P. McKay (2002), Transition from Gaseous Compounds to Aerosols in Titan's Atmosphere, *Icarus*, *159*, 505–517, doi:10.1006/icar.2002.6943.

Lehfaoui, L., C. Rebrion-Rowe, S. Laubé, J. B. A. Mitchell, and B. R. Rowe (1997), The dissociative recombination of hydrocarbon ions. I. Light alkanes, *Journal of Chemical Physics*, *106*, 5406–5412, doi:10.1063/1.473566.

Liang, M.-C., A. N. Heays, B. R. Lewis, S. T. Gibson, and Y. L. Yung (2007), Source of nitrogen isotope anomaly in HCN in the atmosphere of Titan, *The Astrophysical Journal Letters*, *664*(2), L115.

Lindal, G. F., G. E. Wood, H. B. Hotz, D. N. Sweetnam, V. R. Eshleman, and G. L. Tyler (1983), The atmosphere of Titan - an analysis of the Voyager 1 radio occultation measurements, *Icarus*, *53*, 348–363.

Lindsay, B. G., and A. M. Mangan (2003), Cross sections for ion production by electron collision with molecules, in *Landolt-Bornstein, Photon and Electron-Interaction With Molecules: Ionization and Dissociation, New Ser.*, vol. I/17C, edited by Y. Itikawa, pp. 5–1–5–77, Springer, New York.

Lindsay, B. G., R. Rejoub, and R. F. Stebbings (2001), Production of positive ion pairs by electron-impact ionization of CH_4, *Journal of Chemical Physics*, *114*, 10,225, doi:10.1063/1.1371479.

Liu, X., and D. E. Shemansky (2006), Analysis of electron impact ionization properties of methane, *Journal of Geophysical Research*, *111*, A04,303, doi:10.1029/2005JA011454.

Lyons, J. R. (1995), Metal ions in the atmosphere of Neptune, *Science*, *267*(5198), 648–651.

Ma, Y. J., A. F. Nagy, T. E. Cravens, I. V. Sokolov, K. C. Hansen, J. E. Wahlund, F. J. Crary, A. J. Coates, and M. K. Dougherty (2006), Comparisons between MHD model calculations and observations of Cassini flybys of Titan, *Journal of Geophysical Research*, *111*, A05,207.

Mackay, G. I., L. D. Betowski, J. D. Payzant, H. I. Schiff, and D. K. Bohme (1976), Rate constant at 297K for proton-transfer reactions with hydrocyanic acid and acetonitrile.Comparisons with classical theories and exothermicity, *Journal of Physical Chemistry*, *80*, 2919 – 2922.

Madanian, H., T. E. Cravens, M. S. Richard, J. H. Waite, N. J. T. Edberg, J. H. Westlake, and J.-E. Wahlund (2016), Solar cycle variations in ion composition in the dayside

ionosphere of Titan, *Journal of Geophysical Research*, *121*, 8013–8037, doi:10.1002/2015JA022274.

Magee, B. A., J. H. Waite, K. E. Mandt, J. Westlake, J. Bell, and D. A. Gell (2009), INMS-derived composition of Titan's upper atmosphere: Analysis methods and model comparison, *Planetary and Space Science*, *57*(1415), 1895 – 1916, doi:10.1016/j.pss.2009.06.016.

Mahaffy, P. R., H. B. Niemann, A. Alpert, S. K. Atreya, J. Demick, T. M. Donahue, D. N. Harpold, and T. C. Owen (2000), Noble gas abundance and isotope ratios in the atmosphere of Jupiter from the Galileo Probe Mass Spectrometer atmosphere, *Journal of Geophysical Research*, *105*, 15.

Mandt, K. E., et al. (2012), Ion densities and composition of Titan's upper atmosphere derived from the Cassini Ion Neutral Mass Spectrometer: Analysis methods and comparison of measured ion densities to photochemical model simulations, *Journal of Geophysical Research*, *117*(E10006), 259 – 295, doi:10.1029/2012JE004139.

Mantas, G. P., and S. A. Bowhill (1975), Calculated photoelectron pitch angle and energy spectra, *Planetary and Space Science*, *24*, 355–375.

Mapstone, B., and W. R. Newell (1992), Elastic differential electron scattering from CH_4, C_2H_4 and C_2H_6, *Journal of Physics B: Atomic Molecular and Optical Physics*, *25*, 491.

Martinez, O., Z. Yang, N. B. Betts, T. P. Snow, and V. M. Bierbaum (2009), Experimental Determination of the Rate Constant for the Associative Detachment Reaction $H^- + H \rightarrow H_2 + e^-$ at 300 K, *The Astrophysical Journal*, *705*, L172–L175.

Martinez, O., Jr., Z. Yang, N. J. Demarais, T. P. Snow, and V. M. Bierbaum (2010), Gas-phase Reactions of Hydride Anion, *Astrophysical Journal*, *720*, 173–177.

Matson, D. L., L. J. Spilker, and J.-P. Lebreton (2002), The Cassini/Huygens Mission to the Saturnian System, *Space Science Reviews*, *104*, 1–58, doi:10.1023/A:1023609211620.

May, O., J. Fedor, B. C. Ibănescu, and M. Allan (2008), Absolute cross sections for dissociative electron attachment to acetylene and diacetylene, *Physical Review A*, *77*(4), 040701, doi:10.1103/PhysRevA.77.040701.

May, O., D. Kubala, and M. Allan (2010), Absolute cross sections for dissociative electron attachment to HCN and DCN, *Physical Review A*, *82*(1), 010,701, doi:10.1103/PhysRevA.82.010701.

Mayol, R., and F. Salvat (1997), Total and Transport Cross Sections for Elastic Scattering of Electrons by Atoms, *Atomic Data and Nuclear Data Tables*, *65*, 55, doi:10.1006/adnd.1997.0734.

McEachran, R. P., and A. D. Stauffer (1984), Elastic scattering of electrons from krypton and xenon, *Journal of Physics B Atomic Molecular Physics*, *17*, 2507–2518.

McEachran, R. P., and A. D. Stauffer (2014), Momentum transfer cross sections for the heavy noble gases, *European Physical Journal D*, *68*, 153.

McEwan, M. J., and V. G. Anicich (2007), Titan's ion chemistry: A laboratory perspective, *Mass Spectrometry Reviews*, *26*, 281–319, doi:10.1002/mas.20117.

McFadden, L., T. Johnson, and P. Weissman (2006), *Encyclopedia of the Solar System*, Encyclopedia of the Solar System Series, Elsevier Science, Newyork.

McLain, J. L., V. Poterya, C. D. Molek, L. M. Babcock, and N. G. Adams (2004), Flowing Afterglow Studies of the Temperature Dependencies for Dissociative Recombination of O_2^+, CH_5^+, $C_2H_5^+$, and $C_6H_7^+$ with Electrons, *Journal of Physical Chemistry A*, *108*, 6704–6708, doi:10.1021/jp040215l.

Millar, T. J., C. Walsh, M. A. Cordiner, R. N. Chuimn, and E. Herbst (2007), Hydrocarbon anions in interstellar clouds and circumstellar envelopes, *The Astrophysical Journal Letters*, *662*(2), L87.

Millar, T. J., C. Walsh, and T. A. Field (2017), Negative ions in space, *Chemical reviews*, *117*(3), 1765–1795.

Miller, S. L., and H. C. Urey (1959), Organic compound synthesis on the primitive earth, *Science*, *130*(3370), 245–251.

Molina-Cuberos, G. J., J. J. López-Moreno, and R. Rodrigo (2000), Influence of electrophilic species on the lower ionosphere of Titan, *Geophysical Research Letters*, *27*, 1351–1354, doi:10.1029/1999GL010771.

Motlagh, S., and J. H. Moore (1998), Cross sections for radicals from electron impact on methane and fluoroalkanes, *Journal of Chemical Physics*, *109*, 432, doi:10.1063/1.476580.

Motohashi, K., H. Soshi, M. Ukai, and S. Tsurubuchi (1996), Dissociative excitation of CH_4 by electron impact: Emission cross sections for the fragment species, *Chemical Physics*, *213*, 369.

Mueller-Wodarg, I. C. F., D. F. Strobel, J. I. Moses, J. H. Waite, J. Crovisier, R. V. Yelle, S. W. Bougher, and R. G. Roble (2008), Neutral Atmospheres, *Space Science Reviews*, *139*, 191 – 234.

Mukundan, V., and A. Bhardwaj (2016), Monte Carlo model for electron degradation in xenon gas, *Proceedings of the Royal Society of London Series A*, *472*, 20150,727, doi:10.1098/rspa.2015.0727.

Mukundan, V., and A. Bhardwaj (2018), Dayside ionosphere of titan: Impact on calculated plasma densities due to variations in the model parameters, *Icarus*, *299*, 222 – 239, doi:10.1016/j.icarus.2017.07.022.

Müller-Wodarg, I., C. A. Griffith, E. Lellouch, and T. E. Cravens (2014), *Titan: Interior, surface, atmosphere, and space environment*, vol. 14, Cambridge University Press.

Nagy, A. F., and P. M. Banks (1970), Photoelectron fluxes in the ionosphere, *Journal of Geophysical Research*, *75*, 6260–6270, doi:10.1029/JA075i031p06260.

Nagy, A. F., A. J. Kliore, M. Mendillo, S. Miller, L. Moore, J. I. Moses, I. Müller-wodarg, and D. Shemansky (2009), *Saturn from Cassini-Huygens*, 181 - 201 pp., Springer Netherlands, Dordrecht.

Nagy, P., A. Skutlartz, and V. Schmidt (1980), Absolute ionisation cross sections for electron impact in rare gases, *Journal of Physics B Atomic Molecular Physics*, *13*, 1249–1267.

Neish, C. D., Á. Somogyi, and M. A. Smith (2010), Titan's primordial soup: formation of amino acids via low-temperature hydrolysis of tholins, *Astrobiology*, *10*, 337–347, doi:10.1089/ast.2009.0402.

Nisbet, J. S. (1968), Photoelectron escape from the ionosphere, *Journal of Atmosheric and Terrestrial Physics*, *30*, 1257–1278.

Noël, S. (1997), Decay of the magnetospheric ring current: A Monte Carlo simulation, *Journal of Geophysical Research*, *102*, 2301–2308, doi:10.1029/96JA03275.

Oran, E. S., and D. J. Strickland (1978), Photoelectron flux in the Earth′s ionosphere, *Planetary and Space Science*, *26*, 1161–1177.

Palmer, M. Y., M. A. Cordiner, C. A. Nixon, S. B. Charnley, N. A. Teanby, Z. Kisiel, P. G. J. Irwin, and M. J. Mumma (2017), ALMA detection and astrobiological potential of vinyl cyanide on Titan, *Science Advances*, *3*, e1700,022, doi:10.1126/sciadv.1700022.

Pang, K. D., J. M. Ajello, B. Franklin, and D. E. Shemansky (1987), Electron impact excitation cross section studies of methane and acetylene, *Journal of Chemical Physics*, *86*, 2750–2764, doi:10.1063/1.452077.

Perrin, J., C. Bohm, R. Etemadi, and A. Lloret (1994), Possible routes for cluster growth and particle formation in rf silane discharges, *Plasma Sources Science and Technology*, *3*(3), 252.

Peterson, L. R. (1969), Discrete deposition of energy by electrons in gases, *Phys. Rev.*, *187*, 105–111, doi:10.1103/PhysRev.187.105.

Petrie, S. (1996), Novel pathways to CN^- within interstellar clouds and circumstellar envelopes: Implications for IS and CS chemistry, *Monthy Notices of the Royal Astronomical Society*, *281*, 137 – 144.

Pospieszalska, M. K., and R. E. Johnson (1996), Monte Carlo calculations of plasma ion-induced sputtering of an atmosphere: SO_2 ejected from Io, *Journal of Geophysical Research*, *101*, 7565, doi:10.1029/95JE03650.

Puech, V., and S. Mizzi (1991), Collision cross sections and transport parameters in neon and xenon, *Journal of Physics D Applied Physics*, *24*, 1974–1985.

Rachinhas, P. J. B. M., T. H. V. T. Dias, F. P. Santos, C. A. N. Conde, and A. D. Stauffer (1999), Absorption of electrons for energies up to 200keV; a Monte Carlo simulation model, *IEEE Transactions on Nuclear Science*, *46*(6), 1898–1900.

Raksit, A. B., and D. K. Bohme (1983), An experimental study of the influence of hydration on the reactivity of the hydroxide anion in the gas phase at room temperature, *Canadian Journal of Chemistry*, *61*(7), 1683–1689.

Rapp, D., and P. Englander-Golden (1965), Total Cross Sections for Ionization and Attachment in Gases by Electron Impact. I. Positive Ionization, *Journal of Chemical Physics*, *43*, 1464–1479, doi:10.1063/1.1696957.

Raulin, F., and Gpcos Team (2006), From Titan to the primitive Earth, in *European Planetary Science Congress 2006*, p. 329.

Rawat, P., V. S. Prabhudesai, G. Aravind, M. A. Rahman, and E. Krishnakumar (2007), Absolute cross sections for dissociative electron attachment to H_2O and D_2O, *Journal of Physics B: Atomic, Molecular and Optical Physics*, *40*, 4625–4636.

Rawat, P., V. S. Prabhudesai, M. A. Rahman, N. B. Ram, and E. Krishnakumar (2008), Absolute cross sections for dissociative electron attachment to NH_3 and CH_4,

International Journal of Mass Spectrometry, *277*, 96–102, doi:10.1016/j.ijms.2008.05.015.

Rayman, M. D., P. A. Chadbourne, J. S. Culwell, and S. N. Williams (1999), Mission design for Deep Space 1: A low-thrust technology validation mission, *Acta Astronautica*, *45*, 381–388.

Rayman, M. D., T. C. Fraschetti, C. A. Raymond, and C. T. Russell (2006), Dawn: A mission in development for exploration of main belt asteroids Vesta and Ceres, *Acta Astronautica*, *58*, 605–616, doi:10.1016/j.actaastro.2006.01.014.

Rees, M. H. (1972), *Physics and Chemistry of Upper Atmosphere*, 397 pp., Springer Netherlands.

Rejoub, R., B. G. Lindsay, and R. F. Stebbings (2002), Determination of the absolute partial and total cross sections for electron-impact ionization of the rare gases, *Physical Review A*, *65*(9726498), 232, doi:10.1103/PhysRevA.65.042713.

Richard, M. S. (2013), Plasma interactions in Titan's ionosphere, Ph.D. thesis, University of Kansas.

Richard, M. S., T. E. Cravens, I. P. Robertson, J. H. Waite, J.-E. Wahlund, F. J. Crary, and A. J. Coates (2011), Energetics of Titan's ionosphere: Model comparisons with Cassini data, *Journal of Geophysical Research*, *116*, A09310, doi:10.1029/2011JA016603.

Richard, M. S., et al. (2015), An empirical approach to modeling ion production rates in Titan′s ionosphere I: Ion production rates on the dayside and globally, *Journal of Geophysical Research*, *120*, 1264–1280, doi:10.1002/2013JA019706.

Richards, P. G., and D. G. Torr (1984), An investigation of the consistency of the ionospheric measurements of the photoelectron flux and solar euv flux, *Journal of Geophysical Research*, *89*, 5625–5635, doi:10.1029/JA089iA07p05625.

Richards, P. G., and D. G. Torr (1988), Ratios of photoelectron to euv ionization rates for aeronomic studies, *Journal of Geophysical Research*, *93*, 4060–4066, doi:10.1029/JA093iA05p04060.

Richards, P. G., J. A. Fennelly, and D. G. Torr (1994), EUVAC: A solar EUV flux model for aeronomic calculations, *Journal of Geophysical Reserch*, *99*(94), 8981 – 8992.

Richards, P. G., T. N. Woods, and W. K. Peterson (2005), HEUVAC: A new high resolution solar EUV proxy model, *Advances in Space Research*, *2003*(2006), 2004, doi:10.1016/j.asr.2005.06.031.

Robertson, I. P., et al. (2009), Structure of Titan′s ionosphere: Model comparisons with Cassini data, *Planetary and Space Science*, *57*, 1834–1846, doi:10.1016/j.pss.2009.07.011.

Romani, P. N., J. Bishop, B. Bezard, and S. Atreya (1993), Methane photochemistry on Neptune - Ethane and acetylene mixing ratios and haze production, *Icarus*, *106*, 442, doi:10.1006/icar.1993.1184.

Romanzin, C., M.-C. Gazeau, Y. Bnilan, E. Hbrard, A. Jolly, F. Raulin, S. Boy-Pronne, S. Douin, and D. Gauyacq (2005), Methane photochemistry: A brief review in the frame of a new experimental program of Titan's atmosphere simulations, *Advances in Space Research*, *36*(2), 258, doi:10.1016/j.asr.2005.03.079.

Ross, T., E. J. Baker, T. P. Snow, J. D. Destree, B. L. Rachford, M. M. Drosback, and A. G. Jensen (2008), The Search for H^- in Astrophysical Environments, *The Astrophysical Journal*, *684*, 358-363, doi:10.1086/590242.

Rutkowsky, J., H. Drost, and H.-J. Spangenberg (1980), Investigation of the Inelastic Interaction of Slowly Monoenergetic Electrons with Simple Hydrocarbon Molecules I. Electron Attachment Cross-sections as a Function of Electron Energy and Molecular Structure, *Annalen der Physik*, *492*, 259–270, doi:10.1002/andp.19804920404.

Sagnières, L. B. M., M. Galand, J. Cui, P. P. Lavvas, E. Vigren, V. Vuitton, R. V. Yelle, A. Wellbrock, and A. J. Coates (2015), Influence of local ionization on ionospheric densities in Titan's upper atmosphere, *Journal of Geophysical Research: Space Physics*, *120*(7), 5899–5921, doi:10.1002/2014JA020890, 2014JA020890.

Sakae, T., S. Sumiyoshi, E. Murakami, Y. Matsumoto, K. Ishibashi, and A. Katase (1989), Scattering of electrons by CH_4, CF_4, and SF_6, in the 75-700 eV range, *Journal of Physics B: Atomic Molecular and Optical Physics*, *22*, 1385.

Samson, J. A. R., T. Masuoka, P. N. Pareek, and G. C. Angel (1987), Total and dissociative photoionization cross sections of N_2 from threshold to 107 eV, *The Journal of Chemical Physics*, *86*, 6128 – 6132.

Santos, F. P., T. H. V. T. Dias, A. D. Stauffer, and C. A. N. Conde (1994), Three-dimensional Monte Carlo calculation of the VUV electroluminescence and other electron transport parameters in xenon, *Journal of Physics D Applied Physics*, *27*, 42 – 48.

Schram, B. L. (1966), Partial ionization cross sections of noble gases for electrons with energy 0.5-18 keV : II. Argon, Krypton and Xenon, *Physica*, *32*, 197–208.

Schunk, R., and A. Nagy (2009), *Ionospheres: Physics, Plasma Physics, and Chemistry*, Cambridge Atmospheric and Space Science Series, Cambridge University Press.

Sharma, L., R. Srivastava, and A. D. Stauffer (2011), Excitation of the $5p^5 7p$ levels of xenon by electron impact, *European Physical Journal D*, *62*, 399 – 403.

Sharp, T. E., and J. T. Dowell (1967), Isotope effects in dissociative attachment of electrons in methane, *The Journal of Chemical Physics*, *46*, 1530, doi:10.1063/1.1840885.

Sheehan, C. H., and J.-P. St.-Maurice (2004), Dissociative recombination of the methane family ions: rate coefficients and implications, *Advances in Space Research*, *33*, 216–220, doi:10.1016/j.asr.2003.07.019.

Shematovich, V. I., D. V. Bisikalo, J.-C. Grard, C. Cox, S. W. Bougher, and F. Leblanc (2008), Monte carlo model of electron transport for the calculation of Mars dayglow emissions, *Journal of Geophysical Research: Planets*, *113*(E2), E02,011, doi:10.1029/2007JE002938, e02011.

Shirai, T., T. Tabata, H. Tawara, and Y. Itikawa (2002), Analytic cross sections for electron collisions with hydrocarbons: CH_4, C_2H_6, C_2H_4, C_2H_2, C_3H_8, and C_3H_6, *Atomic Data and Nuclear Data Tables*, *80*, 147, doi:10.1006/adnd.2001.0878.

Shyn, T. W. (1991), Vibrational excitation cross sections of methane by electron impact, *Journal of Physics B: Atomic, Molecular and Optical Physics*, *24*, 5169.

Sienkiewicz, J. E., and W. E. Baylis (1989), Low energy elastic scattering e-Xe: the effect of exchange in the polarization potential, *Journal of Physics B*, *22*, 3733.

Singhal, R., and A. Green (1981), Spatial Aspects of Electron Energy Degradation in Atomic Oxygen, *Journal of Geophysical Research*, *86*(A6), 4776 – 4780.

Singhal, R. P., and A. Bhardwaj (1991), Monte Carlo simulation of photoelectron energization in parallel electric fields: Electroglow on Uranus, *J. Geophys. Res*, *96*, 15,963, doi:10.1029/90JA02749.

Singhal, R. P., and S. A. Haider (1984), Analytical Yield Spectrum approach to photoelectron fluxes in the Earth's atmosphere, *Jornal of Geophysical Research*, *89*(A8), 6847 – 6852, doi:10.1029/JA089iA08p06847.

Singhal, R. P., and S. A. Haider (1986), Some molecular nitrogen emissions from Titan-solar EUV and magnetospheric interaction., *Indian Journal of Radio and Space Physics*, *15*, 46–52.

Singhal, R. P., C. Jackman, and A. E. S. Green (1980), Spatial aspects of low and medium energy electron degradation in N_2, *Journal of Geophysical Research*, *85*(A3), 1246 – 1254, doi:10.1029/JA085iA03p01246.

Singhal, R. P., D. E. Rio, P. F. Schippnick, and A. E. S. Green (1983), Electron energy degradation in neon, *Radiation Research*, *95*(01), 32–44, doi:10.2307/3576069.

Singhal, R. P., S. C. Chakravarty, A. Bhardwaj, and B. Prasad (1992), Energetic electron precipitation in Jupiter's upper atmosphere, *Journal of Geophysical Research*, *97*, 18,245, doi:10.1029/92JE01894.

Smith, D., and P. Spanel (1993), Dissociative recombination of H_3^+ and some other interstellar ions: a controversy resolved, *International Journal of Mass Spectrometry and Ion Processes*, *129*, 163–182.

Smith, D., M. J. Church, and T. M. Miller (1978), Mutual neutralization of simple and clustered positive and negative ions, *The Journal of Chemical Physics*, *68*, 1224, doi: 10.1063/1.435842.

Solomon, S. C. (1993), Auroral electron transport using the Monte Carlo method, *Geophysical Research Letters*, *20*, 185–188, doi:10.1029/93GL00081.

Solomon, S. C. (2001), Auroral Paricle transport using Monte Carlo and hybrid methods, *Journal of Geophysical Research*, *106*(A1), 107, doi:10.1029/2000JA002011.

Song, M.-Y., J.-S. Yoon, H. Cho, Y. Itikawa, G. P. Karwasz, V. Kokoouline, Y. Nakamura, and J. Tennyson (2015), Cross Sections for Electron Collisions with Methane, *Journal of Physical and Chemical Reference Data*, *44*(2), 023101, doi:10.1063/1.4918630.

Song, M.-Y., J.-S. Yoon, H. Cho, G. P. Karwasz, V. Kokoouline, Y. Nakamura, and J. Tennyson (2017), Cross Sections for Electron Collisions with Acetylene, *Journal of Physical and Chemical Reference Data*, *46*(1), 013106, doi:10.1063/1.4976569.

Sorokin, A. R. (1986), Population processes in high-pressure inert-gas-mixture lasers, *Journal of Soviet Laser Research*, *7*(4), 332 – 345, doi:10.1007/BF01120145.

Srivastava, R. (2007), Electron impact excitation cross sections of xenon for optical plasma diagnostic, *Tech. rep.*, Indian Institute of Technology, Roorke.

Stephan, K., and T. D. Märk (1984), Absolute partial electron impact ionization cross sections of Xe from threshold up to 180 eV, *Journal of Chemical Physics*, *81*, 3116, doi:10.1063/1.448013.

Stolarski, R. S., and A. E. S. Green (1967), Calculations of auroral intensities from electron impact, *Journal of Geophyical Research*, *72*(15), 3967 – 3974, doi:10.1029/JZ072i015p03967.

Straub, H. C., D. Lin, B. G. Lindsay, K. A. Smith, and R. F. Stebbings (1997), Absolute partial cross sections for electron-impact ionization of CH_4 from threshold to 1000 eV, *Journal of Chemical Physics*, *106*, 4430, doi:10.1063/1.473468.

Strobel, D. F. (2004), Photochemistry in Outer Solar System Atmospheres, *Space Science Reviews*, *116*, 155.

Strobel, D. F., and D. E. Shemansky (1982), EUV emission from Titans upper atmosphere Voyager I encounter, *Journal of Geophysical Research*, *87*, 1361.

Strobel, D. F., M. E. Summers, and X. Zhu (1992), Titan′s upper atmosphere - Structure and ultraviolet emissions, *Icarus*, *100*, 512–526.

Summers, M. E., and D. F. Strobel (1989), Photochemistry of the atmosphere of Uranus, *Astrophysical Journal*, *346*, 495–508, doi:10.1086/168031.

Swartz, W. E. (1972), Electron production, recombination, and heating in the F region of the ionosphere, *Sci. Rep.*, *381*.

Tawara, H. (1992), Atomic and Molecular Processes in Fusion Edge Plasmas, *Journal Nuclear Fusion*, *2*, 41.

Teolis, B. D., et al. (2015), A Revised Sensitivity Model for Cassini INMS: Results at Titan, *Space Science Reviews*, *190*, 47–84.

Tian, C., and C. R. Vidal (1997), Electron impact dissociative ionization and the subsequent ion-molecule reactions in a methane beam, *Chemical Physics*, *222*, 105 – 112.

Tobiska, W. K., T. Woods, F. G. Eparvier, R. Viereck, L. Floyd, D. Bouwer, G. Rottman, and O. R. White (2000), The SOLAR2000 empirical solar irradiance model and forecast tool, *Journal of Atmospheric and Solar Terrestrial Physics*, *62*(14), 1233.

Toublanc, D., J. P. Parisot, J. Brillet, D. Gautier, F. Raulin, and C. P. McKay (1995), Photochemical Modeling of Titan's Atmosphere, *Icarus*, *113*, 2–26, doi:10.1006/icar.1995.1002.

Trajmar, S., W. McConkey, and I. Kanik (2006), Electron-Atom and Electron-Molecule Collisions, in *Springer Handbook of Atomic, Molecular, and Optical Physics*, edited by G. Drake, pp. 929 – 941, Springer New York.

Verchovsky, A. B., and M. A. Sephton (2005), A noble record, *Astronomy & Geophysics*, *46*(2), 2.12–2.14.

Viggiano, A. A., and J. F. Paulson (1983), Temperature dependence of associative detachment reactions, *The Journal of Chemical Physics*, *79*, 2241, doi:10.1063/1.446073.

Vigren, E., et al. (2013), On the thermal electron balance in Titan's sunlit upper atmosphere, *Icarus*, *223*, 234–251, doi:10.1016/j.icarus.2012.12.010.

Vigren, E., et al. (2016), Suprathermal electrons in titans sunlit ionosphere: Modelobservation comparisons, *Astrophysical Journal*, *826*, 131.

Vinodkumar, M., C. Limbachiya, B. Antony, and K. N. Joshipura (2007), Calculations of elastic, ionization and total cross sections for inert gases upon electron impact: threshold to 2 keV, *Journal of Physics B Atomic Molecular Physics*, *40*, 3259–3271.

Vuitton, V., R. V. Yelle, and V. G. Anicich (2006), The nitrogen chemistry of Titan′s upper atmosphere revealed, *The Astrophysical Journal Letters*, *647*(2), L175, doi: 10.1086/507467.

Vuitton, V., R. V. Yelle, and M. J. McEwan (2007), Ion chemistry and N-containing molecules in Titan′s upper atmosphere, *Icarus*, *191*, 722–742, doi:10.1016/j.icarus. 2007.06.023.

Vuitton, V., R. V. Yelle, and J. Cui (2008), Formation and distribution of benzene on Titan, *Journal of Geophysical Research: Planets*, *113*(E5), E05,007, doi:10.1029/ 2007JE002997.

Vuitton, V., P. Lavvas, R. V. Yelle, M. Galand, A. Wellbrock, G. R. Lewis, A. J. Coates, and J.-E. Wahlund (2009), Negative ion chemistry in Titan's upper atmosphere, *Planetary and Space Science*, *57*, 1558–1572, doi:10.1016/j.pss.2009.04.004.

Vuitton, V., O. Dutuit, M. A. Smith, and N. Balucani (2014), *Titan: Interior, surface, atmosphere, and space environment*, chap. Chemistry of Titan's atmosphere, p. 224.

Wahlund, J.-E., et al. (2005), Cassini Measurements of Cold Plasma in the Ionosphere of Titan, *Science*, *308*, 986–989, doi:10.1126/science.1109807.

Wahlund, J.-E., et al. (2009), On the amount of heavy molecular ions in Titan's ionosphere, *Planetary and Space Science*, *57*, 1857–1865, doi:10.1016/j.pss.2009.07. 014.

Waite, J. H., T. E. Cravens, J. Kozyra, A. F. Nagy, S. K. Atreya, and R. H. Chen (1983), Electron precipitation and related aeronomy of the Jovian thermosphere and ionosphere, *J. Geophys. Res.*, *88*, 6143–6163, doi:10.1029/JA088iA08p06143.

Waite, J. H., D. T. Young, T. E. Cravens, A. J. Coates, F. J. Crary, B. Magee, and J. Westlake (2007), The Process of Tholin Formation in Titan's Upper Atmosphere, *Science*, *316*, 870, doi:10.1126/science.1139727.

Waite, J. H., D. T. Young, A. J. Coates, F. J. Crary, B. A. Magee, K. E. Mandt, and J. H. Westlake (2008), The source of heavy organics and aerosols in Titan's atmosphere, in *Organic Matter in Space*, *IAU Symposium*, vol. 251, edited by S. Kwok and S. Sanford, pp. 321–326, doi:10.1017/S1743921308021844.

Walt, M., W. M. McDonald, and W. E. Francis (1969), Penetration of auroral electrons into the atmosphere, in *Physics of the magnetosphere*, edited by R. L. Carovillano, pp. 534–555.

Wang, Z.-C., and V. M. Bierbaum (2016), Reactions of substituted benzene anions with N and O atoms: Chemistry in Titans upper atmosphere and the interstellar medium, *Journal of Chemical Physics*, *144*, 214,304, doi:10.1063/1.4952454.

Wedlund, C. S., G. Gronoff, J. Lilensten, H. Menager, and M. Barthelemy (2011), Comprehensive calculation of the energy per ion pair or W values for five major planetary upper atmospheres, *Physica E*, *29*, 187.

Wellbrock, A., A. J. Coates, G. H. Jones, G. R. Lewis, and J. H. Waite (2013), Cassini CAPS-ELS observations of negative ions in Titans ionosphere: Trends of density with altitude, *Geophysical Research Letters*, *40*, 4481–4485, doi:10.1002/grl.50751.

Westlake, J. H., J. H. Waite, Jr., K. E. Mandt, N. Carrasco, J. M. Bell, B. A. Magee, and J.-E. Wahlund (2012), Titan′s ionospheric composition and structure: Photochemical modeling of Cassini INMS data, *Journal of Geophysical Research*, *117*, E01003, doi: 10.1029/2011JE003883.

Wetzel, R. C., F. A. Baiocchi, T. R. Hayes, and R. S. Freund (1987), Absolute cross sections for electron-impact ionization of the rare-gas atoms by the fast-neutral-beam method, *Phys. Rev.*, *35*(2), 559.

Wilson, E. H., and S. K. Atreya (2003), Chemical sources of haze formation in Titan's atmosphere, *Planetary nad Space Science*, *51*, 1017–1033, doi:10.1016/j.pss.2003.06.003.

Wilson, E. H., and S. K. Atreya (2004), Current state of modeling the photochemistry of Titan's mutually dependent atmosphere and ionosphere, *Journal of Geophysical Research (Planets)*, *109*, E06002, doi:10.1029/2003JE002181.

Winningham, J. D., D. T. Decker, J. U. Kozyra, J. R. Jasperse, and A. F. Nagy (1989), Energetic (¿60 ev) atmospheric photoelectrons, *Journal of Geophysical Research: Space Physics*, *94*(A11), 15,335–15,348, doi:10.1029/JA094iA11p15335.

Woods, T. N., F. G. Eparvier, S. M. Bailey, P. C. Chamberlin, J. Lean, G. J. Rottman, S. C. Solomon, W. K. Tobiska, and D. L. Woodraska (2005), Solar EUV Experiment (SEE): Mission overview and first results, *Journal of Geophysical Research*, *110*, A01,312, doi:10.1029/2004JA010765.

Yang, Z., C. A. Cole, O. M. Jr, M. Y. Carpenter, T. P. Snow, and V. M. Bierbaum (2011), Experimental and theoretical studies of reactions between H atoms and nitrogen-containing carbanions, *The Astrophysical Journal*, *739*(1988), 2 – 3.

Yelle, R. V., V. Vuitton, P. Lavvas, S. J. Klippenstein, M. A. Smith, S. M. Hörst, and J. Cui (2010), Formation of NH_3 and CH_2NH in Titan's upper atmosphere, *Faraday Discussions*, *147*, 31, doi:10.1039/c004787m.

Yung, Y. L. (1987), An update of nitrile photochemistry on Titan, *Icarus*, *72*, 468–472.

Yung, Y. L., M. Allen, and J. P. Pinto (1984), Photochemistry of the atmosphere of Titan - Comparison between model and observations, *Astrophysical Journal Supplement Series*, *55*, 465–506, doi:10.1086/190963.

Zecca, A., G. Karwaszt, R. S. Brusa, and R. Grisenti (1991), Absolute total cross section measurements for intermediate-energy electron scattering: IV. Kr and Xe, *Journal of Physics B*, *24*, 2737 – 2146.